ABSTRACT

Title of Dissertation:	OPTICAL AND ELECTRICAL RESPONSE OF SUPERCONDUCTING RESONATORS FOR A HYBRID QUANTUM SYSTEM
	Kristen Danielle Voigt Doctor of Philosophy, 2021
Dissertation directed by:	Professor Frederick Wellstood Department of Physics

I describe my contributions towards a hybrid quantum system that would have coupled ^{87}Rb atoms to a superconducting device. I first discuss my work coupling an optical fiber to a translatable thin-film LC lumped-element superconducting Al microwave resonator operating at 100 mK in a dilution refrigerator. The LC resonators had resonance frequencies f_0 of 6.15 GHz, quality factors Q of 1.5 x 10^5 to 6.5 x 10^5 at high powers, and were mounted inside a superconducting aluminum 3D cavity with a resonance frequency of 7.5 GHz and Q of 8 x 10^3. An optical microfiber (60 μm diameter) passed through a hole in the 3D cavity near the LC resonator. The 3D cavity was mounted on an x-z attocube-translation stage that allowed the LC resonator to be moved relative to the fiber.

The resonator's f_0 and Q were affected both by the fiber dielectric perturbing the resonator's electric field and from scattered light from the fiber. I measured both effects as a function of fiber-resonator position. I modeled the resonator's optical

response by accounting for optical production, recombination, and diffusion of quasiparticles and the non-uniform position-dependent illumination of the resonator. Using the model, I extracted key parameters describing quasiparticles in the resonator.

The hybrid quantum system requires the ^{87}Rb and LC resonator resonance to be tuned to the same frequency. I describe our LC resonator tuning method which moves a superconducting Al pin into the resonator's electric field, decreasing the resonator capacitance and increasing its resonance frequency up to 137 MHz. This was done at 15 mK using an attocube translation stage. I also investigated two-level system (TLS) defects in an LC resonator by applying a dc voltage. I describe a model in which the TLS causes a capacitive perturbation to the resonator rather than the 'standard' electric-dipole coupling model. I use this model of a capacitive TLS or cTLS, to describe intermittent telegraph noise measured in the transmission S_{21} through the resonator. I measured shifts in f_0 of more than 6 kHz corresponding to a cTLS fluctuating its capacitance contribution by 430 zF.

OPTICAL AND ELECTRICAL RESPONSE OF SUPERCONDUCTING RESONATORS FOR A HYBRID QUANTUM SYSTEM

by

Kristen Danielle Voigt

Dissertation submitted to the Faculty of the Graduate School of the
University of Maryland, College Park, in partial fulfillment
of the requirements for the degree of
Doctor of Philosophy
2021

Advisory Committee:
Professor Frederick Wellstood, Chair
Professor Christopher Lobb
Professor Steven Rolston
Dr. Benjamin Palmer
Professor Ichiro Takeuchi

Acknowledgements

Over the course of writing this thesis, I have reflected frequently on the help I received from people along the way. As I did, I composed thoughtful and witty prose that fully and completely conveyed my deep gratitude. But I forgot to write them down. So this is just a tribute.

I first have to say that I owe so much to my advisor Fred Wellstood. From my first semester in grad school when I was the sole TA for 180 students (and therefore graded all 180N documents, where N was the number of assignments plus tests), through the following years of my work on the "Atoms-on-Squids" project, he has always been supportive, fair, and practical. He has been hands on and engaged. His guidance on the project was indispensable. He has patiently explained (and re-explained) many physics concepts to me. I have always been astounded by his physical intuition and have been lucky to have him help shape mine. I have a rule of thumb that if it seems like Fred is wrong about something (physics-related) he probably isn't. He is devoted to his principles and doesn't take shortcuts even when you really really wish he would. I've received hundreds of pages of corrections from Fred, full of red ink (imagine Jackson Pollock ran out of all colors except red). If his thoughtful and very thorough insights haven't made me a better writer and scientist, implementing them built more character in me than laying bricks would have.

As part of "Atoms-on-Squids", I had the unique opportunity to be part of a multidisciplinary collaboration between multiple professors. Chris Lobb always brought levity and humor to group meetings. He once challenged the team to a "high-Q haiku" writing competition and scholarly hilarity ensued. Not only does he have a

gift for explaining things clearly but he has been personable, supportive, generous with his time, and just generally a cool dude. He gets an extra thanks for serving on my committee. Luis Orozco, on the AMO side of the experiment, was a pleasure to work with because of his clear passion for physics. He has always shown tremendous hospitality to his students with delicious self-catered dinner parties and outings to fine restaurants (if you're not his student I highly recommend dating/marrying one as I did to get in on this action). Steve Rolston, also on the AMO side of the collaboration, was always easy going and full of insightful feedback. I must also thank him for taking the time to serve on my thesis committee. Bob Anderson, who sadly passed away in 2018, was always quick with a pun and always greeted me with a smile. Thank you also to Ben Palmer and Ichiro Takeuchi for taking the time to serve on my thesis committee and for their patience with coordinating and rescheduling.

I owe a huge thank you to Zaeill Kim, the postdoc who started the superconducting side of the experiment. It was so great to join a lab with a fully functioning experiment that was already producing data. He taught me so much in my first year on the project. He inspired me because he was one of the most productive and prolific humans I've ever met. I would not have gotten half as far if he had not laid the groundwork.

Jared Hertzberg, our second postdoc on the project, was as dedicated as he was caffeinated. I learned the so much from him. He is a living encyclopedia of physics, dilution fridges, MATLAB, microwave cabling, device fabrication, machining, and just making things in general. He happily and patiently taught me as much as I could cram in my head or scribble on notes. His "postdoc humor", which involved plastic

cockroaches placed strategically on unsuspecting graduate students' desks, kept things interesting. I couldn't have asked for a better mentor.

Sudeep Dutta acted as an "adopted post-doc" on our project and was always happy to help no matter how much I asked of him. He spent many hours helping me painstakingly assemble the experiment around the delicate microfiber. Even if we executed everything perfectly, all our efforts would go up in smoke if the fiber gods were in a bad mood that day. But he'd be ready to start again nevertheless. He made working in the lab enjoyable with his dry witty humor, sarcasm, and involuntary fits of laughter and mirth. I learned a lot about physics from him as well as the value of 'respecting your elders'. He gets bonus points for being my 'elevator buddy' while I gradually learned to trust the undeniably suspicious-looking freight elevator to the sub-basement.

I am indebted to the AMO grad students on the project. Jeff Grover was an endless source of entertainment. Our friendship grew from a mutual love of lunch and curating the best cute animal pics for each other. He was the first person I would go to for AMO questions not only because I did not have to get out of my chair to speak to him (our desks were next to each other) but because he usually knew the answer or knew where to look. I am grateful for the many times he set up, relocked, and realigned the laser after my failed efforts only made matters worse. Pablo Solano, whose deep love of physics is evident, was always helpful and kind. His zen nature was contagious. It was a great attitude to have when he took over for Jon and helped me with the process of fabricating microfibers, a task that anyone other than Pablo would find trying. Pablo's catch phrase was 'should be fine' and if Pablo said it should be fine, it probably

was.

I know I shouldn't pick favorites, but I can't deny that I owe more to one graduate student than all others: Jonathan Hoffman. Maybe I'm biased though because he has been such a good partner and husband to me over the years. I could not have done this without his support both in and out of the lab. His hard work combined with his irreverent humor and boisterous laugh made working in the lab both fun and productive. His love and support made my life outside the lab full and beautiful. Even after he graduated and began his career, his mantra has still been "how can I help?". Whenever I come to him with a physics question, he is always enthusiastic to help. He is a genuinely selfless person and brilliant and creative scientist.

Rangga Budoyo and Cody Ballard, students on one of Fred's other projects, were always available to be the 'muscle' when I needed help putting the cans on the dil fridge. Rangga was an honorary member of our group for a while and made significant contributions to our understanding of the optical quasiparticle model. Cody Ballard, was always upbeat and eager to help. He fabricated devices for me and entertained me with his skilled sleight-of-hand tricks. I am very grateful to Ben Cooper who gave lots of advice and reassurance in the beginning when I was flying solo and afraid of breaking the half-million-dollar dilution refrigerator.

I also received great support from people at the Laboratory for Physical Sciences. Ben Palmer was always helpful: advising on intricacies of dilution refrigerator operations, resonator measurements, letting us borrow equipment, and helping us get cleanroom entry. I have to thank Moe Khalil, Vitaley Zaretsky, Sergey Novikov, Baladitya Suri, and Bahman Sarabi at LPS for sharing code and many helpful

discussions.

There were multiple staff members in the physics department, QMC, and JQI that I relied on during my time as a grad student. Dave Cogswell and Bruce Rowly in the Physics Machine Shop have been a tremendous source of knowledge, made all the hardware I designed for the experiment, and helped me in the student machine shop. Their class on machining was not only fun but the knowledge I gained there proved to be repeatedly helpful. If anything went wrong in the building or with equipment, I knew I could always count on Doug Benson and Brian Straughn to fix it. I especially appreciated the friendly chats I had with Doug whenever I bumped into him in the hallways. Early on he gave me some of the most applicable advice to the project: “If you can’t make it right, make it adjustable”. Alessandro Restelli was a great resource when I was designing the spiral resonator sensors.

Life has thrown some curve balls at me, but I have some great friends who have given so much time and energy to help me. I am forever indebted to Alex Jeffers for his help, encouragement, and generosity. He has repeatedly helped me during the writing process. When I was repeatedly pulled into perfectionism, he was there with sound advice, guiding me back to reality with the gentleness that one usually reserves for a toddler. Every time I hit a coding wall, I’d go to Alex, my MATLAB guru. He also introduced me to a surprising source of motivation: the govenator (who knew Mr. Schwarzenegger was such a gifted motivational speaker?).

Sometimes you just need a safe-space to be your true self (i.e. eat an entire pint of Ben and Jerry’s in a sitting) without judgment. That safe space for me has been wherever Dina Genkina is. She’s been a great friend and I know she always has my

back. Dina supported me with whatever I needed whether it be part of the writing process, thinking through a physics concept, or officiating my wedding.

Caeli Tracy has been especially helpful in the last few years of graduate school. Working with her is fun and easy and she has the uncanny ability to read my mind. Jiehang Zhang has also been helpful and supportive especially while I was writing my thesis. Briana Alterman has been great at moral support and has always been understanding and encouraging. A special thank you to Matt, Kumbhel, David, and Susannah whose companionship acted as a salve for the mental and emotional burns of grad school. I thank Zoom, which allowed me to defend my thesis in sweatpants without anyone knowing.

I am so grateful to my parents for all of their love and support and all the opportunities they gave me to get to this point. I always felt supported and knew that if grad school didn't work out, I could always live in their basement. I have also gotten so much love and support from my extended family and in-laws, thank you all.

I could not have gotten here without all of the support from everyone mentioned above (and to all the people I forgot to mention I am sorry). I am truly grateful for your help. Finally, I acknowledge funding from the NSF through the Physics Frontier Center at the Joint Quantum Institute, the Quantum Materials Center (formerly Center for Nanophysics and Advanced Materials) at University of Maryland, and the Laboratory for Physical Sciences.

Table of Contents

List of Tables

List of Figures

Chapter 1: Introduction

1.1 Background and Motivation

Accurately simulating the behavior of multiple coupled quantum systems has proven to be extremely challenging using conventional computers. Fundamentally, this is because the computational resources required will grow exponentially with the number of systems. In 1982, Richard Feynman proposed using the quantum behavior of atoms instead of classical bits to efficiently simulate quantum processes [1.1]. In particular, he argued that a quantum computer that was an analog of another quantum system could efficiently simulate the other system. Simulating quantum systems has been suggested to have practical applications such as efficiently simulating complex chemical reactions, and related processes such as protein folding. Ultimately, this could have a profound effect on medicine [1.2] and material science.

In fact, Feynman had a long-standing and deep interest in computation, from WW2-era human computers and punch-card systems, to parallel computing and reversible computation. It is this background that perhaps led him to a key insight—quantum processes could not only be used for simulations, but they could also be used for performing calculations with fundamental operations that were impossible in a conventional computer.

Since Feynman's original proposal, other potential applications of quantum computers have been proposed. One of the most important advances in quantum computing was Shor's discovery that a quantum computer could be used to efficiently factor large numbers, allowing RSA encryption to be broken [1.3]. Classical computers can already

factor numbers, but it becomes much more difficult as the number of digits increases [1.4]. Shor's quantum factoring routine turned out to be exponentially faster than the fastest known classical routine. Another important early advance was a quantum search routine proposed by Lov Grover [1.5]. For a database of size *N*, Grover's quantum search routine was $\sqrt{N}$ faster than the fastest known classical search routine. Although this was not an exponential increase in speed, it nevertheless again showed that a quantum computer could outperform classical computer in certain types of calculations.

Of course, these potential applications were merely theoretical proposals. To apply a quantum algorithm that could factor a large number or search a large database, one would need to construct an actual working quantum computer. As with a conventional computer, a quantum computer needs to store and manipulate information. In a conventional computer, information is stored as bits in memory and manipulated in a processor. In a quantum computer, the information will be stored in the quantum coherent state of a quantum system that is made by coupling together smaller two-level quantum systems called qubits (from combining the words quantum and bit). There may be a separate memory, although this is not required and most current implementations of quantum computers do not have a separate quantum memory. Quantum operations are then performed by reversibly and coherently manipulating the state of the qubits—the equivalent of running a program in a classical computer.

The state of a qubit or quantum two-level system can be specified by two numbers: θ and ϕ, which determine the relative amplitude and phase of the two states in the superposition. To visualize the state of a qubit, θ and ϕ can be thought of as angles that specify a point on the surface of a sphere with unit radius, called the Bloch sphere (see

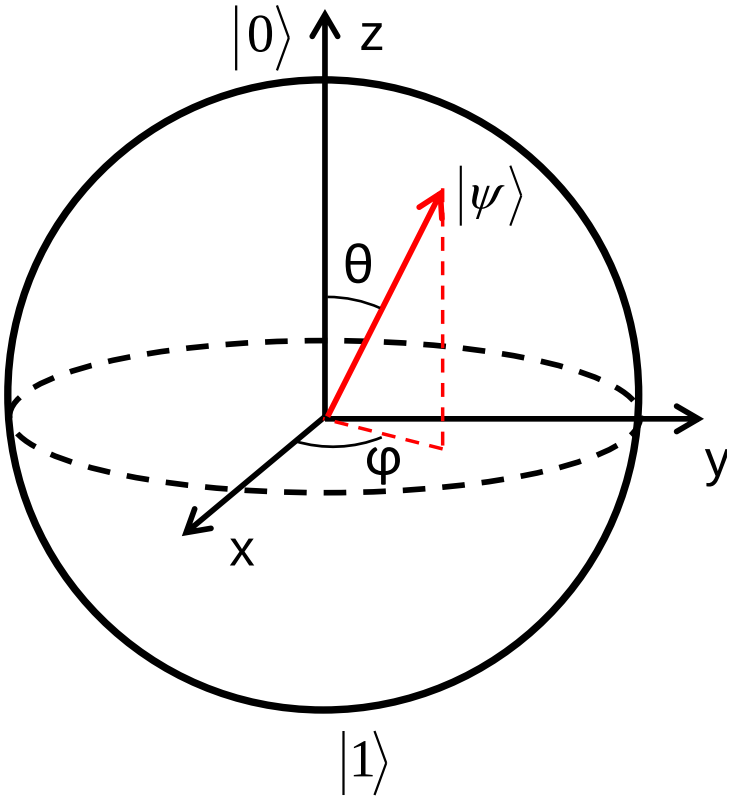

Fig. 1.1 - A vector (red), with azimuthal angle ϕ and polar angle θ, points to a location on the surface of the Bloch sphere and represents a superposition state $|\Psi\rangle = \cos(\theta/2)|0\rangle + e^{i\phi}\sin(\theta/2)$ of a qubit. If the vector points straight up, the qubit is in state $|0\rangle$, if the vector points straight down, the qubit is in state $|1\rangle$ and all other points represent superposition states.

Fig. 1.1). Systems with more than two levels can also act as effective two-level systems provided the levels can be suitably isolated from the other states of the system. For example, the ground state and first excited state of an isolated atom or ion can serve as a qubit [1.6-1.8]. The states of isolated atom-like defects in semiconductors can also serve as qubits [1.9]. Of most relevance to my thesis are manmade superconducting devices that operate at milliKelvin temperatures and also possess sharp anharmonic energy levels that can be used as qubits.

Unfortunately the state of a qubit does not last forever because qubits suffer from decoherence [1.10]. This is one of the most serious issues affecting superconducting qubits. All physical qubits have some interaction with the environment, which can ultimately cause the phase and amplitude of the superposition states to change unpredictably. Processes that cause the phase to randomize are said to produce dephasing, while relaxation causes the amplitude in the excited state to decay. Together, these processes are called decoherence and represent a loss of information. Due to relaxation and dephasing, superposition states of $|0\rangle$ and $|1\rangle$ will not last indefinitely. At the time this thesis was written, no qubit has demonstrated a coherence time of more than a few minutes [1.11]. Most superconducting qubits have much shorter lifetimes [1.12], with the best reported relaxation time being on the order of 2 ms in fluxonium qubits [1.13].

Atomic qubits tend to have much longer lifetimes than superconducting qubits. However, they typically cannot perform operations as quickly as superconducting qubits because they are naturally much more isolated from each other and from the driving fields [1.14-1.15] and thus have slower gate times. In contrast, the operating gate times of superconducting qubits can be short because they can be strongly coupled to control lines and to each other.

Although there are many physical realizations of a qubit [1.9, 1.16-1.22], it is important to understand that not all quantum systems are suitable for use in a quantum computer. David DiVincenzo developed five criteria that a physical system needed to satisfy in order to be useful for constructing a quantum computer [1.23]. First, the qubits must be scalable to large numbers. This requirement is necessary since at least thousands of qubits will likely be needed to be able to perform useful calculations. Multiple qubits

would also be needed to employ quantum error correction and limit the effects of decoherence [1.24-1.27]. Superconducting qubits appear to have good scalability, since they can be fabricated on substrates using conventional circuit lithography techniques. Second, one must be able to address and prepare each qubit in a unique initial state. This is relatively easy for atoms, since every atom of the same type is identical. In contrast the energy levels and transition frequencies of superconducting qubits have random variations due to atomic scale defects (two-level systems) and differences in the fabrication. Third, the coherence time of the qubits must be sufficiently long in order to perform the requisite number of operations for a given calculation. Fourth, to allow for calculations to be made, the system of qubits must be able to perform a set of universal quantum gate operations [1.28]. Finally, one must be able to determine the state of the qubits with good fidelity. This action is known as readout. DiVincenzo has two further criteria to allow for quantum communication and distributed computation, but these are not relevant to this thesis.

Since atoms and superconducting qubits have distinctly different advantages and disadvantages, this suggests that it might be possible to create a qubit with superior performance by combining them to form a hybrid system. This was the motivation for our Physics Frontier Center project in which we proposed to couple cold ^{87}Rb atoms to a superconducting qubit, with the atoms acting as a quantum memory and the qubit as a quantum processor. Our aim was not to construct a quantum computer, but to show that these two very different systems could be coupled together. In combining these two types of qubits, we would need to minimize the disadvantages of each in order to benefit from the individual advantages.

1.2 Description of Proposed Hybrid Quantum System

From a practical standpoint, it is challenging to construct a hybrid qubit by coupling isolated atoms to a superconducting qubit. One of the first difficulties that must be faced is the choice of the specific atom and type of superconducting qubit. For the atoms, our AMO collaborators chose neutral ^{87}Rb atoms that can be optically trapped in an evanescent field around a tapered optical fiber [1.29]. For the superconducting qubit, we chose a transmon in a 3D cavity [1.30]. At this time, transmons are the most common type of superconducting qubit and the devices have demonstrated relatively good performance and scalability.

The next difficulty that must be addressed is figuring out exactly how to couple a superconducting qubit to isolated atoms. ^{87}Rb has a magnetic moment that depends on the state of the atom [1.31] and that magnetic moment will couple to an external magnetic field. On the other hand, most transmons are designed to be insensitive to magnetic field in order to reduce dephasing from magnetic field fluctuations and flux noise [1.32]. As a result, the direct magnetic coupling between an atom and a transmon is much too weak to be useful. The transmon itself is also relatively small, of order 1 mm in extent, so the effective coupling cannot be enhanced enough by simply increasing the number of atoms. To solve this problem, we proposed to use a superconducting lumped-element microwave resonator as a coupling element between the transmon and the atoms. The electric field from the resonator's capacitor couples well to the transmon, while the magnetic field from the resonator's inductor couples to the atoms. By tuning the qubit and the resonator to the 6.834682610904 GHz hyperfine transition of ^{87}Rb [1.31], a non-negligible resonant coupling can be achieved. In addition, by choosing an inductor with a relatively large

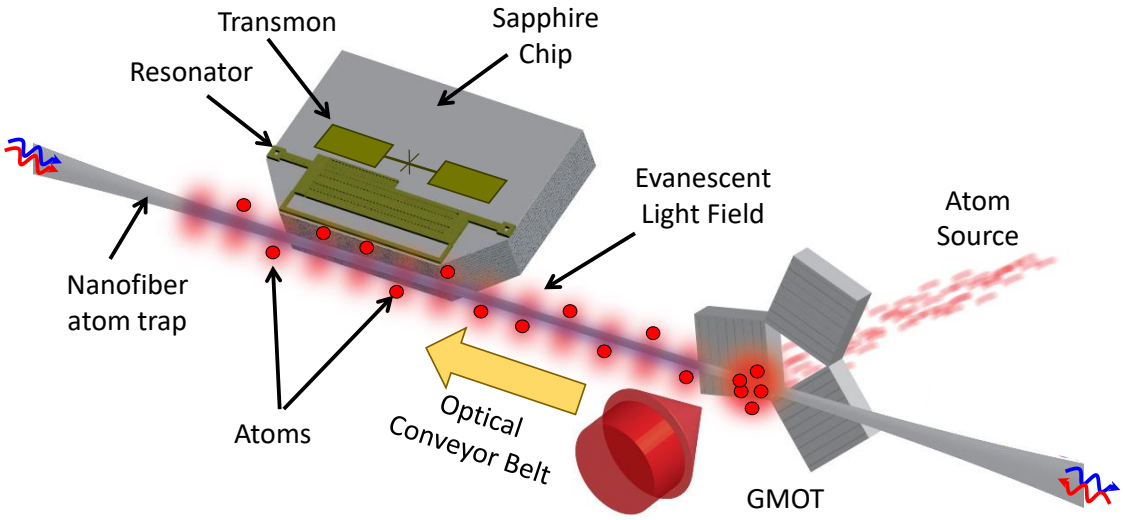

Fig. 1.2 - Physical layout for the proposed transmon-atom hybrid qubit system.

geometric size and straight-line geometry, the system can couple to multiple atoms, in an elongated one-dimensional trap. A superconducting resonator can also have a high quality factor *Q*, which minimizes noise and dephasing, and allows for better resolution of the coupling when used as the readout of the superconducting qubit [1.33].

Figure 1.2 shows an illustration of our proposed hybrid system. The superconducting resonator is coupled to a transmon qubit that is fabricated on the same substrate and both would operate at 20 mK or less. The long inductor of the resonator (green) couples to atoms trapped near the surface of a tapered optical nanofiber. The fiber will need to be placed very close to the inductor for this to work well. There are multiple methods available to cool and trap atoms, which is necessary to bring them close to the lumped-element resonator and induce an interaction in the hybrid system. An optical nanofiber trap [1.34] was chosen since it allows a relatively low level of trapping light to

be used and has an elongated one-dimensional geometry that works well along-side the straight inductor. A low level of trapping light is essential because any scattered light that is absorbed by the superconductor will lead to quasiparticle generation, which in turn will cause a reduced relaxation time T_1 of the qubit [1.35-1.37] and a reduced Q of the resonator [1.38-1.39].

An optical nanofiber traps atoms in an optical light beam that propagates along the fiber and decays exponentially in the radial direction with a length scale of $\lambda/2\pi$, where λ is the wavelength of the light. Light that is red-detuned light from the D_2 transition in ^{87}Rb can be used to create an attractive potential that increases with the intensity, which is highest near the fiber surface. To prevent the atoms from condensing onto the surface of the fiber, light that is blue-detuned from the D_2 transition is also sent down the fiber, creating a repulsive potential. Due to the shorter wavelength of the blue-detuned light compared to the red-detuned light, a potential well with a well- defined minimum ~ 100 nm outside the fiber can be created by adjusting the intensity and polarization of the red and blue detuned light [1.40-1.41].

The resulting optical trap is quite shallow, which means that the atoms must be cooled before they can be trapped on the nanofiber. Figure 1.2 shows how a grating magneto-optic trap (GMOT) [1.42] could be used for this purpose to trap and cool the atoms. The GMOT would be in the same cryogenic space but must be separated from the nanofiber and the superconducting components because of the relatively high optical power required (mW). Atoms would be shuttled from the GMOT to the resonator using an optical conveyor belt [1.43] that translates the trapping sites by changing slightly the frequency of one of the GMOT trapping beams. An atom source, such as an electron gun or a full-sized

MOT connected in a cold chamber to the dilution fridge, would provide atoms for the GMOT.

With atoms trapped on the nanofiber, the next step would be to prepare the atoms in a particular state by sending pulses of light with a frequency near the hyperfine transition in ^{87}Rb. Using pulses of suitable duration, one could perform a π-pulse, π/2-pulse, Rabi oscillation or other single-qubit gating operation. Similarly, the state of the transmon could be prepared and read out using microwave signals. By using optical control for the atom and microwave control for the transmon, the control signals would be well-isolated from cross-coupling. The coupling between the atom and transmon would then allow the atom to influence the state of the transmon, which could then be manipulated and read out using microwaves. With suitable state manipulation, the transmon-resonator system could be used to exchange information between the atoms and transmon.

As should be evident from the above description, and as discussed in detail in the next section, it will be challenging to construct a complete hybrid system with atoms coupled to a transmon. Instead, my work was focused on a first step: coupling a superconducting resonator to an optical fiber. Such a system would let us test some of the most challenging aspects of the design.

If *N* atoms were trapped on the fiber, the corresponding effective Hamiltonian for the atom and resonator system can be written as:

$$\widehat{H} = \hbar\omega\hat{a}^{\dagger}\hat{a} + \frac{1}{2}\hbar\omega_0 \sum_{i=1}^{N} \hat{\sigma}_z^{(i)} + \sum_{i=1}^{N} \hbar\lambda\left(\hat{a}\hat{\sigma}_+{}^{(i)} + \hat{a}^{\dagger}\hat{\sigma}_-{}^{(i)}\right). \tag{1.1}$$

The first term is the Hamiltonian of an isolated resonator, where ω is the resonator's angular resonance frequency, $\hat{a}$ is the annihilation operator for the resonator, and $\hat{a}^{\dagger}$ is the creation operator. The second term is the Hamiltonian of *N* isolated identical non-

interacting atoms, where ω_0 is the angular frequency of the hyperfine transition in ^{87}Rb, and $\hat{\sigma}_z^{(i)}$ is the z Pauli matrix which acts on the state of the ith atom. The final term describes the interaction between the resonator and the *N* atoms. The parameter λ is the effective coupling between the resonator and each atom, and $\hat{\sigma}_+^{(i)}$ and $\hat{\sigma}_-^{(i)}$ are the Pauli raising and lowering operators for the ith atom. The coupling is $\lambda = \vec{\mu} \cdot \vec{B}$ where μ is the atomic magnetic moment (1.4x10^{10} Hz/T). For a single photon in the lumped-element resonator, the magnetic field *B* about 5μm away from the inductor would be about 2.5 nT (according to simulations on resonator LC1 see Ch. 3). The resulting coupling $\lambda \approx 35$ Hz. This is quite small, although with subsequent resonator designs the magnetic field and coupling would be higher λ.

Tavis and Cummings [1.44, 1.45] showed that for low-lying states the Hamiltonian in Eq. (1.1) can be reduced to an approximate form, the Tavis-Cummings Hamiltonian, that gives collective excitations of *N* atoms with a single resonator mode. For these low-lying collective excitations, the final term introduces an energy that scales as $\sqrt{N}$. This enhancement in the interaction energy is essential for making this design feasible given that a single atom only contributes of order 40 Hz [1.46] to the interaction strength.

1.3 Main Challenges

There are several major challenges to building a viable atom-superconducting hybrid system. One of the first challenges that one must deal with is that optical nanofibers for optical trapsare very delicate. They comprise five regions: (1) an input section of normal un-tapered optical fiber, (2) a tapering input section where the input wave is matched to a

mode that propagates on the narrow diameter section, (3) the narrowed sub-micrometer region, (4) a tapering output region which connects the waist to the normal output fiber, and (5) the output section of un-tapered optical fiber.

For our system, the nanofibers tapered down to a diameter of about 500 nm. They were remarkably strong for their size, but still easily broken if too much tension was applied or contact was made with a sharp edge. I should also emphasize that it was essential to apply tension, since otherwise the fiber would sag, or move uncontrollably, allowing contact with the substrate or other parts of the apparatus. Increasing the tension in a fiber increases the frequency of any potential vibrational modes and decreases their amplitude. Furthermore, tension must be maintained as the system cools or warms and experiences thermal contraction or expansion.

Another problem with the optical fibers is that even the best optical fibers have some amount of intrinsic Rayleigh scattering [1.47]. Light will also leak from the tapered regions of the fiber [1.48]. In addition to Rayleigh scattering from the bulk of the fiber, irregularities formed during the nanofiber fabrication process [1.49] will result in additional scattering at the surface of the fiber. All of these can result in light incident on the superconducting devices, which causes loss and decoherence due to the generation of quasiparticles [1.35-1.37, 1.50-1.51]. Nanofibers are also sensitive to dust on their surface. When milliwatts of optical power is sent through a nanofiber that is in vacuum, the evanescent field will heat the dust particle. With no surrounding gas to dissipate the heat, the temperature can increase enough to burn through and melt the fiber.

Another challenge is figuring out how to trap atoms on a nanofiber inside of a dilution refrigerator. Before they can be trapped in the relatively shallow [1.34] evanescent

field, they must be cooled by a magneto-optic trap (MOT). It is difficult to put a MOT inside of a dilution refrigerator because a MOT requires a lot of optical power (~100 mW) compared to the cooling power of the refrigerator at the mixing chamber stage (200 μW). The MOT also uses a strong magnetic field which would create vortices in our thin-film aluminum superconductor or drive it into the normal state. Cold atoms formed in the MOT will also need to be transported onto the nanofiber trap by overlapping the MOT with a section of the nanofiber. The atoms would then need to be transported along the length of the nanofiber waist to a region next to the superconducting chip. In principle, this transport of the atoms could be achieved by using an "optical conveyor belt" [1.52] in which the frequency of the trapping light is slightly altered to move the discrete trapping sites along the length of the fiber.

To trap atoms, the optical nanofiber will need to carry of order 10 mW of optical power [1.53-1.55]. A properly tapered fiber will tightly guide the optical field, so that very little of this power is deposited into the cryogenic environment. In such a nano-scale optical waveguide, Rayleigh scattering at bulk and surface defects represents a significant loss mechanism [1.56]. Although the amount of scattered power can be quite small for a properly tapered fiber, superconducting devices are very sensitive to optical radiation because it increases loss through the production of quasiparticles (see Sec. 2.5).

Superconducting qubits and resonators are also subject to relaxation even when they are not exposed to scattered light from a nanofiber. Both transmons and LC resonators suffer from loss due to two-level systems and non-equilibrium quasiparticles. When they are not illuminated, my resonators had loss that appeared to be primarily limited by two-level systems (see Ch. 5).

Another critical issue is that the design of the resonator and the qubit requires careful thought to optimize the coupling between them. For the hybrid system, the transmon must be addressed and prepared in an initial state, allowed to interact with the atoms via the resonator, and read out, all of which takes time. This is why it is important for the transmon to have a long coherence time and the resonator to have a high *Q*. At present, the best transmons have T_1 times of ~500 μs [1.14] but these lifetimes would decrease if they were exposed to light from the nanofiber or MOT.

Another challenge is that the coupling between an atom and the resonator is relatively small, at around 40 Hz. To counteract the small coupling between a resonator and an atom, we would need to increase the number of atoms *N* to of order 1000 get an effective coupling of about $\sqrt{N}$ *40 Hz = 1.2 kHz. Achieving this level of coupling also requires that the fiber is very close to (~10 μm), and very well aligned with the inductor of the resonator. It is also important not to get the chip too close to the fiber — the evanescent field and scattering would increase rapidly as the surface of the fiber is approached to within ~1 μm. Controlling and monitoring the position of the fiber with respect to the chip is a clear challenge, especially since this must be done inside a cold dilution refrigerator without a line of sight.

1.4 Proof of Principle: an Optical Microfiber near a Superconducting Resonator

In this thesis, I describe how I addressed some of the main experimental challenges described in the previous section. In particular, I built, measured, and analyzed the behavior of superconducting resonators that were cooled to as low as 20 mK while operating in close proximity to an optical microfiber (see Fig. 1.3). Although I did not build a complete hybrid

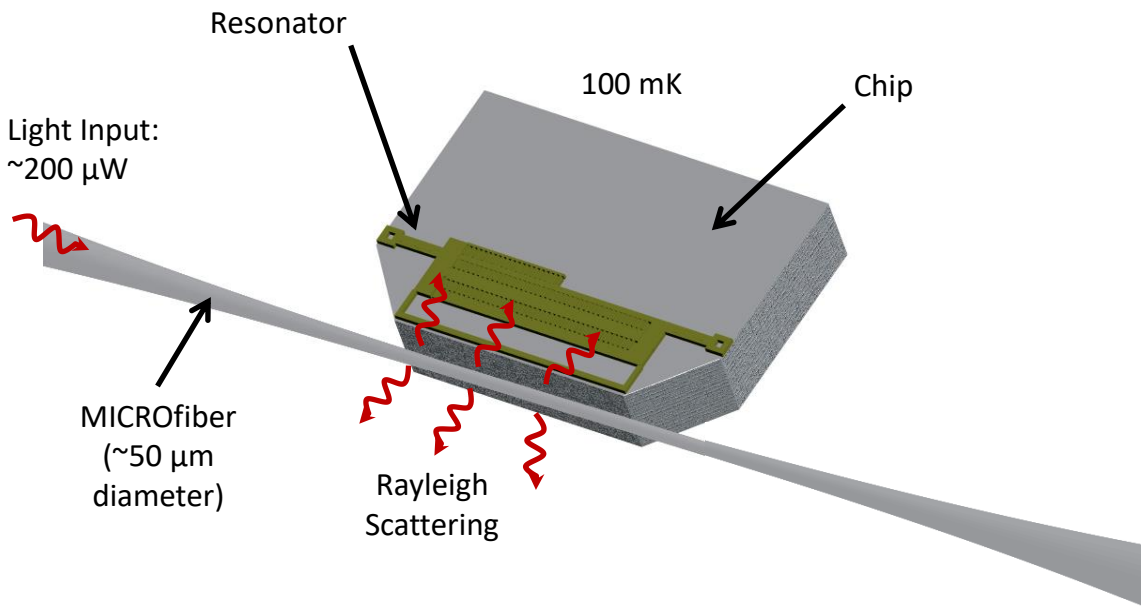

Fig. 1.3 - Schematic of microfiber-chip experiment. A microfiber passes close to a sapphire chip with a superconducting Al resonator patterned near its edge. The apparatus was operated in the 20 mK to 100 mK temperature range in a dilution refrigerator.

system, I developed several of the main components that would be needed and examined some of the most daunting issues, including how to control the relative position of the fiber with respect to the resonator at 100 mK and the resonator's sensitivity to light and the position of the fiber.

Figure 1.3 shows a schematic of a version of the microfiber-chip experiment. The nanofiber has been replaced by a microfiber, which is carrying light and produces Rayleigh scattered light. The moveable chip is placed near the fiber and supports a thin-film superconducting Al resonator. The resonator is housed inside a 3D microwave cavity (see Ch. 6), through which the microfiber passes. This arrangement allows the resonator to be driven and measured as the relative position of the fiber and chip is changed *in situ*.

The use of a microfiber rather than a nanofiber was based on practical

considerations. First, I did not intend to be trapping atoms in the proof-of-principle experiment, so it was not essential to use an optical fiber with a sub-μm diameter. Second, nanofibers are delicate, suffer from surface scattering, are sensitive to dust, and are prone to light leakage from the taper. To avoid these problems with a nanofiber, we used a microfiber with a diameter of 50 μm instead. The microfiber was physically robust, compared to a nanofiber, and could be operated so that it only has Rayleigh scattering from bulk defects near the fiber core, as opposed to a nanofiber which can have significant additional scattering from surface defects. Microfibers are also less prone to light leakage at the taper region and immune to scattering from dust because the light mode stays in the fiber core [1.57]. On the other hand, a microfiber was still useful as a stand-in for a nanofiber because there still was some light scattered from the microfiber — the Rayleigh scattered light from the core allowed me to observe effects of optical illumination as the fiber was moved near the resonator, much as would happen with a nanofiber.

The microfiber also allowed me to investigate other issues that we anticipated could cause problems with a nanofiber, including effects of thermal contraction or expansion as the apparatus cooled down or warmed up and the effect of vibrations from the refrigerator. I also examined the effect Rayleigh scattering of light from the nanofiber had on the resonator. Furthermore, the microfiber allowed me to investigate techniques for controlling and monitoring the fiber's position relative to the chip *in situ*. I note that for this purpose, the presence of Rayleigh scattered light from the fiber had utility. The amount of light absorbed in the resonator depends on the position of the resonator with respect to the fiber and this suggested this dependence could also be used to monitor the position. As I show in Chapter 7, when optical power is applied to the fiber, the resonator is very sensitive to

the position of the fiber. Essentially the intensity of light incident on the resonator depends on the position of the fiber with respect to the resonator. In addition, the resonance frequency of the resonator is perturbed by the dielectric of the fiber, providing another way to keep track of the fiber's position, independent of applied optical power.

Although I did not investigate the sensitivity of transmons to light, the response of the resonator to light allowed me investigate some effects of optically generated quasiparticles in the system. To directly resolve the expected kHz scale splitting produced by coupling atoms to a resonator, we would like to have a resonator with a Q of one million or more [1.58]. Such a high Q will tend to make the resonator very sensitive to optical illumination, which will degrade the Q.

Ultimately, we need to mitigate the resonator's sensitivity to light and the negative effects of quasiparticle production by careful design of the resonator and the arrangement of the resonator and fiber. The microfiber-resonator experiment allowed me to measure the creation and diffusion of quasiparticles within the structure of the resonator and show that the deleterious effect of scattered light could be minimized by carefully placing the fiber in the same plane as the surface of the chip and resonator.

1.5 Overview of Thesis

In the rest of this thesis, I focus on my contributions to the development of the hybrid quantum system. In Chapter 2, I provide a brief overview of lumped-element superconducting microwave resonators, including a discussion of the transmission S_{21}, quality factor Q, and resonance frequency f_0. I also briefly review how two-level system defects can couple to a resonator and cause energy relaxation.

In Chapter 3, I discuss the design, fabrication and characterization of three superconducting resonators, LC1, LC2, and LC3, which I measured. I also describe the 3D cavity that housed LC2 and LC3, and the package that LC1 was mounted in.

In Chapter 4, I present the method we used for tuning a superconducting thin-film resonator at 15 mK. I discuss why tuning is important for our hybrid system and describe the experimental setup, the tuning data, and compare my results to simulations.

In Chapter 5, I explain how I detected dipole-coupled two-level systems and capacitive two-level systems in a thin-film superconducting microwave resonator. I present our experimental setup and measurements with a comparison to theory.

In Chapter 6, I introduce the design of the microfiber-chip experiment that allowed me to integrate a tapered optical fiber with a superconducting resonator. I begin with a discussion of design constraints and then move to the design of the tapered optical fiber and the overall experimental setup. I then discuss the attocubes [1.59] that I used for translating the chip relative to the fiber. I next discuss our inductive position sensors, which allowed me to sense the movement of the chip when the apparatus was at mK temperatures, and the optical setup that I used to send light through the nanofiber. Finally, I explain how all these elements are assembled together.

In Chapter 7, I present my main results on the response of a resonator to the position of a microfiber at mK temperatures, both with and without light being sent through the microfiber. I also discuss how the cavity frequency was affected by the fiber's position. Finally, I present the resonator's response to the position of a fiber that is carrying light, and compare it to our model.

I conclude in Chapter 8 with a summary of my main results.

Chapter 2: Theory of Superconducting Resonators

2.1 Introduction

In this chapter I describe the main parts of the theory of superconducting lumped-element LC microwave resonators that was relevant for my thesis research. The basic physics of an LC resonator is the physics of a simple harmonic oscillator. In Sec. 2.2, I first describe the measurement circuit for resonator LC1, which was coupled to an on-chip transmission line. Then, I introduce S_{21}, the transmission through the circuit. I next discuss how S_{21} depends on the resonance frequency f_0, internal quality factor Q_i, the input/output quality factor Q_e, and total quality factor Q of the circuit. In Sec. 2.3, I describe the measurement circuit and the S_{21} lineshape for resonators LC2 and LC3, which were housed in a 3D cavity. In Sec. 2.4, I present the standard theory of charged dipole-coupled two-level system defects (TLS) in dielectrics. I discuss the coupling of these defects to a resonator and how they induce loss and avoided level crossings. I will refer to this as the "standard TLS-resonator electric-dipole-coupling model" in order to distinguish it from the "capacitive TLS-resonator model" that I describe in Ch. 5. In Section 2.5, I then briefly describe the physics of quasiparticles and how they induce loss in superconducting LC resonators. Finally, in Sec. 2.6, I summarize the main results that I need from LC resonator theory and discuss how these results apply to the hybrid system.

2.2 S_{21} for a Resonator Coupled to a Transmission Line

Figure 2.1(a) shows a semi-physical schematic of the circuit layout I used for measuring a microwave resonator that was capacitively coupled to an input/output transmission line via coupling capacitance C_c. The input transmission line is attached to a voltage source with a Z_0 = 50 Ω source impedance. We used an Agilent Vector Network Analyzer (VNA) as our voltage source [2.1]. There are a few cold attenuators on the input line to prevent external noise and thermal noise from reaching the cavity (see Chaps. 4 and 5 for more discussion of the set-up). For a frequency of 6 GHz, the fixed attenuators and attenuation in the coax itself give a total voltage attenuation α_{in} that produces an equivalent power attenuation of about 82 dB. The input line and output line are connected to a PCB with a tapered transmission line that is then wirebonded to the on-chip transmission line. The LCR resonator has capacitance *C*, inductance *L*, and resistance *R*, connected in parallel. The resulting bare (or uncoupled) resonance frequency is $f_0 = \omega_0/2\pi = 1/\sqrt{LC}$ where ω_0 is the angular resonance frequency. I should also note that in Fig. 2.1(a) I have not shown two circulators that were mounted in the output line at the mixing chamber. The purpose of the circulators was to prevent external noise and noise from higher temperature from reaching the cavity by going "backwards" down the output line. The voltage V_{out} in the output line is amplified by a HEMT amplifier at 4 K before going to the output transmission, which has total attenuation α_{out}.

At room temperature, I used the VNA to measure the output voltage V_2 and the input voltage V_1. The VNA then reports the complex quantity:

$$S_{21} = V_2/V_1 \tag{2.1}$$

Examining Fig. 2.1(a), it can be deduced that

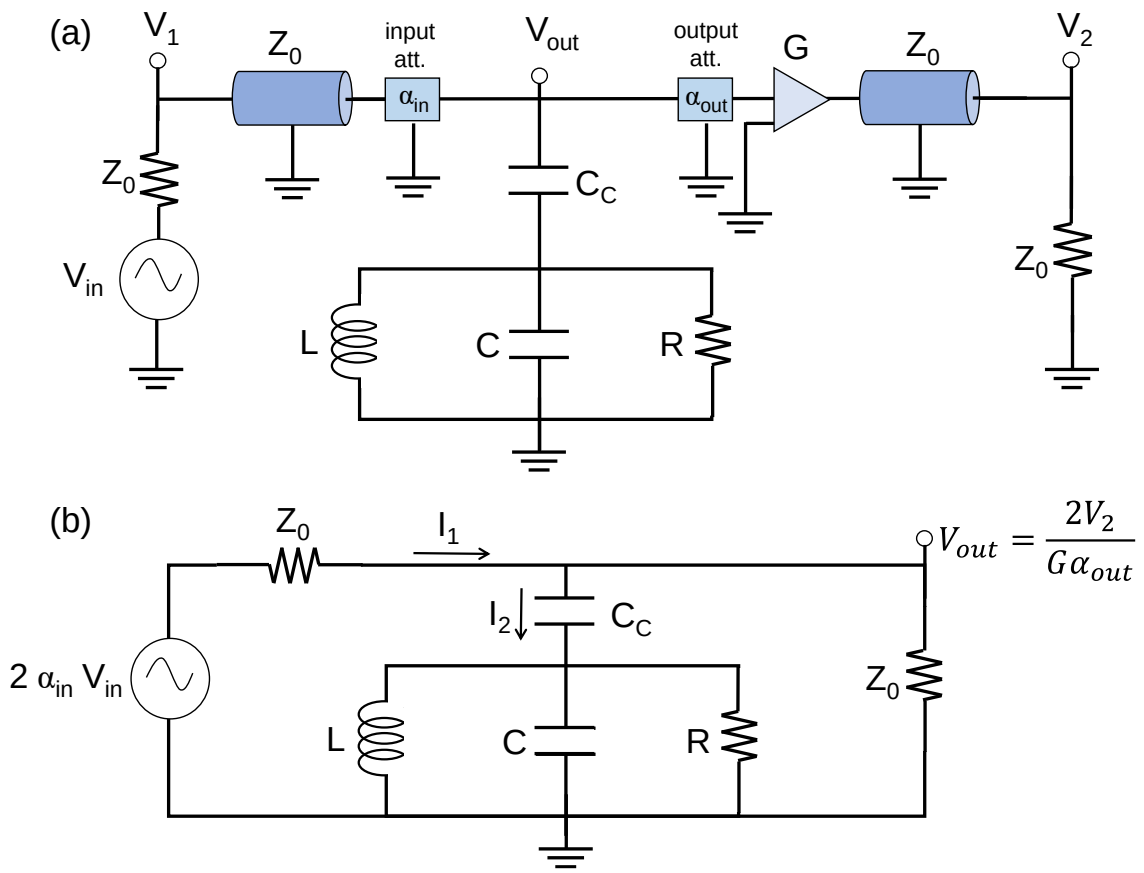

Fig. 2.1 - (a) Semi-physical circuit schematic of LCR resonator capacitively coupled to input/output transmission lines with capacitance C_c. The input line is attached to source and 82 dB attenuator. The output from resonator is amplified by a HEMT before going to the output transmission line with impedance Z_0. (b) Reduced circuit model of resonator capacitively coupled to a transmission line.

$$V_1 = V_{in}/2 \tag{2.2}$$

This is because the VNA has an output impedance of 50 Ω and drives a coaxial line with a 50 Ω impedance which in turn is attached to matched 50 Ω attenuators. From the point of view of the voltage source, this input line with its large attenuation appears as a simple 50 Ω impedance.

Figure 2.1(b) shows a reduced circuit schematic for the circuit shown in Fig. 2.1(a), viewed from the perspective of the LCR resonator. I note that the parallel resistance R in

the circuit accounts for all internal loss in the resonator, which can include loss due to TLSs and quasiparticles. Loss due to quasiparticles can be significant in our devices, especially when illuminated. Such loss is more accurately modelled physically as a small resistance in series with the inductor, but for convenience, here I will treat any such loss as an equivalent parallel resistance and include it in R. Note also that from the perspective of the LCR resonator, the voltage source and input line turn into an equivalent voltage source $2\alpha_{in} V_{in}$ with impedance Z_0, and the output line turns into a $Z_0 = 50\ \Omega$ impedance. Examining the equivalent circuit, we can show that the voltage V_2 measured by the VNA at the room-temperature output is related to the voltage V_{out} across the LCR resonator by:

$$V_2 = \frac{1}{2} G \propto_{out} V_{out} \tag{2.3}$$

where G is the voltage gain of the HEMT, α_{out} is the total voltage attenuation of the output line and the factor of 2 arises because we are assuming that the HEMT has a 50 Ω source impedance which is matched to the $Z_0 = 50\ \Omega$ line and the 50 Ω input impedance of the VNA. From Eq. (2.1), (2.2) and (2.3) we can then write

$$S_{21} = \frac{V_2}{V_1} = G \propto_{out} \left(\frac{V_{out}}{2}\right) / \left(\frac{V_{in}}{2}\right) = G \propto_{out} \left(\frac{V_{out}}{V_{in}}\right). \tag{2.4}$$

Examining Fig. 2.1(b) one can now write the following circuit equations:

$$V_{out} = (I_1 - I_2) Z_0 \tag{2.5}$$

$$2 \propto_{in} V_{in} = I_1 Z_0 + V_{out} \tag{2.6}$$

$$V_{out} = I_2 \left(Z_r + \frac{1}{i\omega C_c}\right) \tag{2.7}$$

where the currents I_1 and I_2 are shown in Fig. 2.1(b) and the impedance Z_r is defined by

$$\frac{1}{Z_r} = \frac{1}{R} + \frac{1}{i\omega L} + i\omega C. \tag{2.8}$$

Solving Eqs. (2.5), (2.6), and (2.7) for V_{out}/V_{in} gives

$$\frac{V_{out}}{V_{in}} = \frac{2\propto_{in}}{2+Z_0/(Z_r+1/i\omega C_c)}. \tag{2.9}$$

Plugging this into Eq. (2.4) and rearranging yields

$$S_{21}(\omega) = \frac{\mathrm{G}\,\alpha_{in}\,\alpha_{out}\left(1+\frac{1}{\mathrm{i}\omega \mathrm{C}_c}(1/\mathrm{Z}_r)\right)}{1+\left(\frac{1}{\mathrm{i}\omega \mathrm{C}_c}+\frac{\mathrm{Z}_0}{2}\right)(1/\mathrm{Z}_r)}, \tag{2.10}$$

which I can further rearrange to get

$$\frac{S_{21}(\omega)}{\mathrm{G}\,\alpha_{in}\,\alpha_{out}} = 1 - \frac{\left(\frac{1}{\mathrm{Z}_r}\right)\frac{Z_0}{2}(i\omega C_C)}{i\omega C_C+\left(1+i\omega C_C\frac{\mathrm{Z}_0}{2}\right)\left(\frac{1}{\mathrm{Z}_r}\right)} = 1 - \frac{N}{D}. \tag{2.11}$$

At this point it is useful to define the coupled resonance frequency as:

$$\omega_o = \frac{1}{\sqrt{L(\mathrm{C}+\mathrm{C}_c)}} \tag{2.12}$$

and consider separately the numerator *N* and denominator *D* of the second term, where

$$N = \left(\frac{1}{\mathrm{Z}_r}\right)\frac{Z_0}{2}(i\omega C_C) \tag{2.13}$$

and

$$D = i\omega C_C + \left(1 + i\omega C_C\,\frac{\mathrm{Z}_o}{2}\right)\left(\frac{1}{\mathrm{Z}_r}\right). \tag{2.14}$$

Using Eq. (2.8) and rearranging, we can then write:

$$D = \frac{1}{\mathrm{R}} - \frac{\omega \mathrm{C}_c \mathrm{Z}_o}{2}\left(\omega \mathrm{C} - \frac{1}{\omega \mathrm{L}}\right) + \mathrm{i}\frac{(\mathrm{C}+\mathrm{C}_c)}{\omega}\left[\omega^2\left(1 - \frac{Z_0}{2R}\frac{C_C}{C+C_C}\right) - \frac{1}{L(C+C_C)}\right]. \tag{2.15}$$

For my resonators, we are only interested in the limit where the effective parallel internal resistance of the resonator *R* is high relative to Z_0, i.e.

$$\mathrm{R} >> \mathrm{Z}_0 = 50\ \Omega \tag{2.16}$$

Also, the capacitance C_c between the resonator and the transmission line is much less than the capacitance *C* of the resonator's capacitor (see Ch. 3), so that

$$C_C \ll C \tag{2.17}$$

Finally, I am only concerned with frequencies ω very near to the resonance frequency ω_0,

so

$$\frac{|\omega-\omega_0|}{\omega_0} = \frac{|\Delta\omega|}{\omega_0} \ll 1 \tag{2.18}$$

where $\Delta\omega = \omega-\omega_0$. I can then write to first order in $\Delta\omega/\omega_0$,

$$\omega(\mathrm{C}+\mathrm{C}_c) - \frac{1}{\omega \mathrm{L}} \approx (\omega_0+\Delta\omega)(C+C_C) - \frac{1}{\omega_0 L}\left(1-\frac{\Delta\omega}{\omega_0}\right) \approx 2\Delta\omega(C+C_C) \tag{2.19}$$

which means that to first order in $\Delta\omega/\omega_0$

$$\omega \mathrm{C} - \frac{1}{\omega \mathrm{L}} \approx -\omega \mathrm{C}_c + 2\Delta\omega(C+C_C)\ . \tag{2.20}$$

From Eqs. (2.15) - (2.20), I then find

$$D \approx \frac{1}{\mathrm{R}} + \frac{\omega^2 \mathrm{C}_c^2 \mathrm{Z}_o}{2}\left(1 - \frac{\Delta\omega}{\omega}\frac{2(C+C_C)}{\mathrm{C_c}}\right) + \mathrm{i}(\mathrm{C}+\mathrm{C}_c)2\Delta\omega. \tag{2.21}$$

I will take $\Delta\omega/\omega << \mathrm{C}_c/\mathrm{C} << 1$ and can then write to lowest order

$$D \approx \frac{1}{\mathrm{R}} + \frac{\omega_0^2 \omega^2 \mathrm{C}_c^2 \mathrm{Z}_o}{2} + \mathrm{i}(\mathrm{C}+\mathrm{C}_c)2\Delta\omega \tag{2.22}$$

Thus I find the familiar looking denominator of a Lorentzian and I can now write from Eq. (2.22) that

$$\frac{D}{(C+C_c)\omega_0} \approx \frac{1}{\mathrm{R}(C+C_c)\omega_0} + \frac{\omega_0 \mathrm{C}_c^2 \mathrm{Z}_o}{2(C+C_c)} + \mathrm{i}\frac{2\Delta\omega}{\omega_0}. \tag{2.23}$$

The first two terms are dimensionless and do not depend on ω. The internal quality factor Q_i, the external quality factor Q_e, and the total quality factor Q can now be defined as

$$\frac{1}{Q_i} = \frac{1}{\mathrm{R}(C+C_c)\omega_0}, \tag{2.24}$$

$$\frac{1}{Q_e} = \frac{\omega_0 \mathrm{C}_c^2 \mathrm{Z}_o}{2(C+C_c)}, \tag{2.25}$$

$$\frac{1}{Q} = \frac{1}{\mathrm{Q_i}} + \frac{1}{Q_e}. \tag{2.26}$$

The total loss in the system is $1/Q$, the internal loss in the resonator is $1/Q_\mathrm{i}$, and the loss to the external environment (input and output leads) is $1/Q_\mathrm{e}$. Note that Eq. (2.25) is just what

one would expect in the Norton equivalent of the input and output circuit in the limit $1/\omega C_c >> Z_0/2$. Essentially, the resonator sees an effective resistance of $Z_e = 1/\omega_o^2 C_c^2 (Z_o/2)$ across the capacitor C [2.2] due to the input and output lines. With these definitions and approximations, I can write

$$\frac{D}{(C+C_c)\omega_0} \approx \frac{1}{Q} + i\frac{2\Delta\omega}{\omega_0}. \tag{2.27}$$

Next consider the numerator given in Eq. (2.13)

$$N = \left(\frac{1}{Z_r}\right)\frac{Z_0}{2}(i\omega C_C). \tag{2.28}$$

Using Eq. (2.8) and Eq. (2.25) I find after some algebra:

$$\frac{N}{(C+C_c)\omega_0} = \frac{1}{Q_e}\frac{\omega}{C_c\omega_0^2}\left(\frac{i}{R} + \frac{1}{\omega L} - \omega C\right). \tag{2.29}$$

Again applying the approximation from Eq. (2.19), I find

$$\frac{N}{(C+C_c)\omega_0} \approx \frac{1}{Q_e}\frac{\omega}{C_c\omega_0^2}\left(\frac{i}{R} + \omega C_c\right) \approx \frac{1}{Q_e}\frac{\omega^2}{\omega_0^2}\left(1 + \frac{i}{\omega C_c R}\right). \tag{2.30}$$

Ignoring the small imaginary piece, I find to lowest order

$$\frac{N}{(C+C_c)\omega_0} \approx \frac{1}{Q_e}. \tag{2.31}$$

Substituting Eqs. (2.27) and (2.31) into Eq. (2.12) yields

$$\frac{S_{21}(\omega)}{G\alpha_{in}\alpha_{out}} = 1 - \left(\frac{Q/Q_e}{1+2iQ\frac{\Delta\omega}{\omega_0}}\right). \tag{2.32}$$

The total quality factor Q is also given by $Q = f_0/\delta f$ where δf is the full width at half maximum (FWHM) of $|S_{21}|^2$. The time $\tau = Q/\omega_0$ that it takes for the resonator to relax or lose energy is also related to Q.

To understand the different effects that Q_i and Q_e have on the S_{21} transmission curves, in Fig. 2.2(a) I plot Eq. (2.32) for various values of Q_i, while

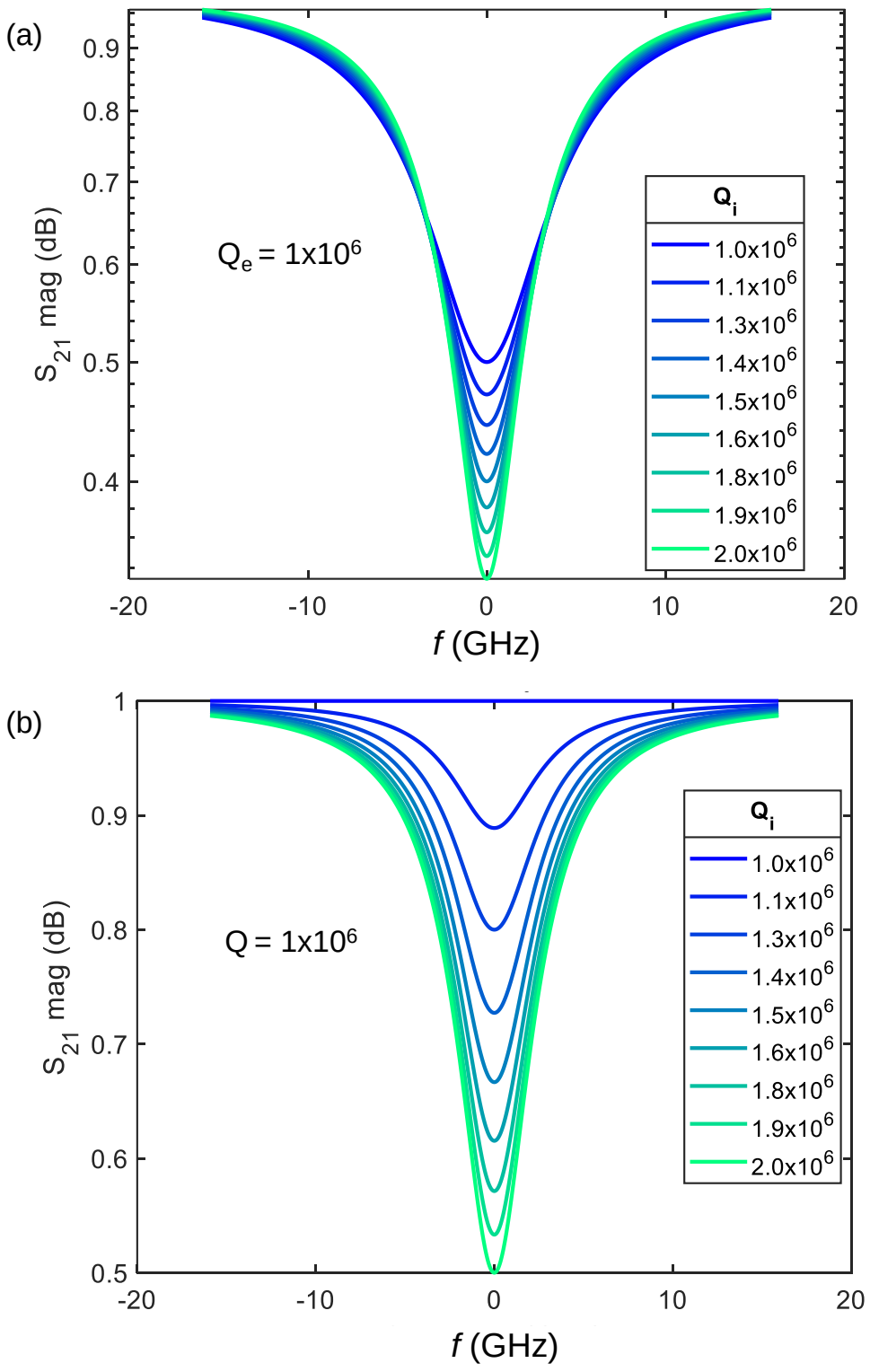

Fig. 2.2 - (a) Magnitude of S_{21} as a function of frequency, using Eq. (2.32) for various values of Q_i and with Q_e fixed at $1x10^6$. (b) The magnitude of S_{21} as a function of frequency, for Eq. (2.32) for various values of Q_i with Q fixed at $1x10^6$.

holding Q_e fixed at 10^6. Note that decreasing Q_i (increasing internal loss) decreases the total Q, increases the FWHM and decreases the depth of the resonant dip in $|S_{21}|$. In Fig. 2.2(b), I again plot Eq. (2.32) for various values of Q_i, but this time keeping Q fixed at 10^6. In this situation, Q_e will necessarily decrease as Q_i increases so as to keep Q fixed. In this case the FWHM does not change because it depends only on Q, which is constant.

I should emphasize here that the circuit shown in Fig. 2.1 is only appropriate if the input line, on-chip transmission line that couples to the LC resonator, and output line all have the same characteristic impedance Z_o. In practice, impedance matching is not perfect. This causes standing wave resonances and typically results in an asymmetric, non-Lorentzian, lines-shape for $S_{21}(f)$. Khalil et al. [2.3] examined this situation and arrived at a modified expression for S_{21} that can be written as:

$$\frac{S_{21}(\omega)}{\mathrm{G}\alpha_{in}\alpha_{out}} = Be^{i\theta}\left[1 - e^{i\phi}\left(\frac{Q/Q_e}{1+2\mathrm{i}Q\frac{\Delta\omega}{\omega_0}}\right)\right] \tag{2.33}$$

Here $Be^{\mathrm{i}\theta}$ and $e^{\mathrm{i}\phi}$ are complex numbers that depend on the impedance mismatch. Equation (2.33) is the key result from the Diameter Correction Method (DCM) of fitting a resonator response [2.3]. I note that Eq. (2.33) will typically produce a sharp feature in the transmission near ω_0, but the shape can be decidedly non-Lorentzian if ϕ is not small compared to one radian.

2.3 S_{21} for a Resonator in a 3D Cavity

In some of my experiments I measured a resonator in a resonant microwave 3D cavity. In this case, the LC resonator was capacitively coupled to microwave pins on the

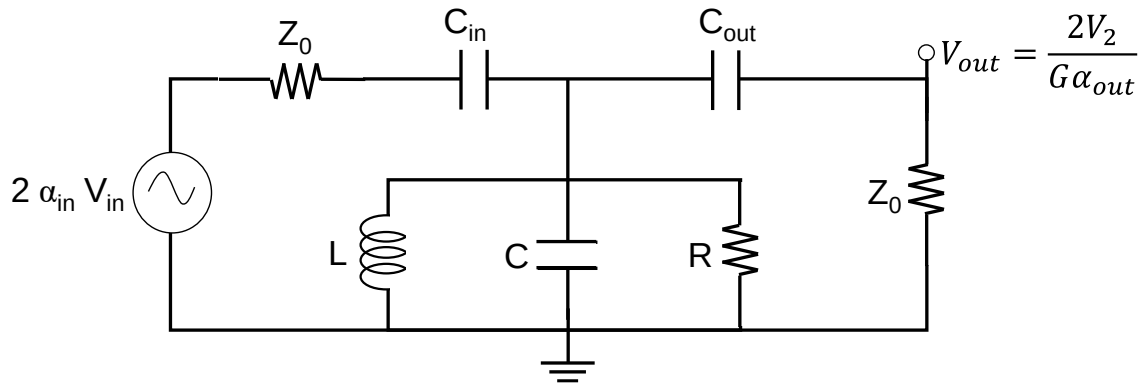

Fig. 2.3 - Circuit model of a resonator mounted in a 3D-cavity with capacitance C_{in} coupling to the input line and C_{out} coupling to the output line. The values of α_{in}, V_{in}, and V_{out} are defined as in Fig. 2.1(a).

input and output microwave leads. An equivalent lumped element circuit is shown in Fig. 2.3. This layout differs from Fig. 2.1(b) in that it couples input microwave power though the input coupling capacitor C_{in}, and couples output microwaves through a separate output coupling capacitor C_{out} to the output microwave line. With this arrangement one can couple more strongly to the output than the input, which is usually desirable for reading out weak signals.

For the circuit in Fig. 2.3, the transmission S_{21} can be written as [2.4]:

$$\frac{S_{21}(\omega)}{G\alpha_{in}\alpha_{out}} = e^{i\alpha}\frac{2/\sqrt{Q_{in}Q_{out}}}{1/Q + 2i\,\Delta\omega/\omega_0} + Ce^{i\beta} \tag{2.34}$$

C, α, and β depend on impedance mismatch while Q_{in} is the input quality factor, governed by C_{in}, and Q_{out} is the output quality factor, governed by C_{out}. In general, Q_{in} and Q_{out} are related to the total external loss $1/Q_e$ by

$$\frac{1}{Q_e} = \frac{1}{Q_{in}} + \frac{1}{Q_{out}}. \tag{2.35}$$

I should also note that for the 3D cavity I discuss in Chaps. 3, 6 and 7, the input coupling $1/Q_{in}$ was much stronger than the output coupling $1/Q_{out}$. Since we could not

measure reflection of microwaves from the resonator while it was cold, we were unable to measure Q_{in} and Q_{out} for resonators in a 3D cavity *in situ*. Nevertheless, it is possible to determine Q_e from Q and Q_i. I note also that Eq. (2.34) will produce a peak in the transmission at ω_0, instead of the dip produced by Eq. (2.33).

2.4 Standard TLS-Resonator Dipole-Coupling Theory

2.4.1 Two-Level Systems as a Source of Loss

Figure 2.4(a) shows measurements of the transmission S_{21} through a superconducting LC resonator for different source powers. Notice in particular that as the power decreases, the Q visibly decreases. This power-dependent loss is typically seen when the loss is caused by atomic-scale two-level system (TLS) defects in dielectrics, which saturate at high powers [2.5].

The importance of TLS induced loss in superconducting qubits was first reported by Martinis et al. [2.5], who also showed that the effect could be readily detected by measuring the loss in thin-film resonators that had parallel plate capacitors filled with dielectric (see Fig. 2.4(b)). They found that the loss tangent was highest at low drive power and decreased steadily with increasing drive power (V^2/Z_0). At high drive voltages, the TLSs saturate (equally likely to be in the ground state or the excited state) and an increase in drive power no longer gives a proportional increase in power absorbed by the TLSs, causing the loss tangent to decrease with increased drive voltage.

Martinis et al. also gave an approximate expression for the loss tangent due to TLS's that are in a parallel plate capacitor:

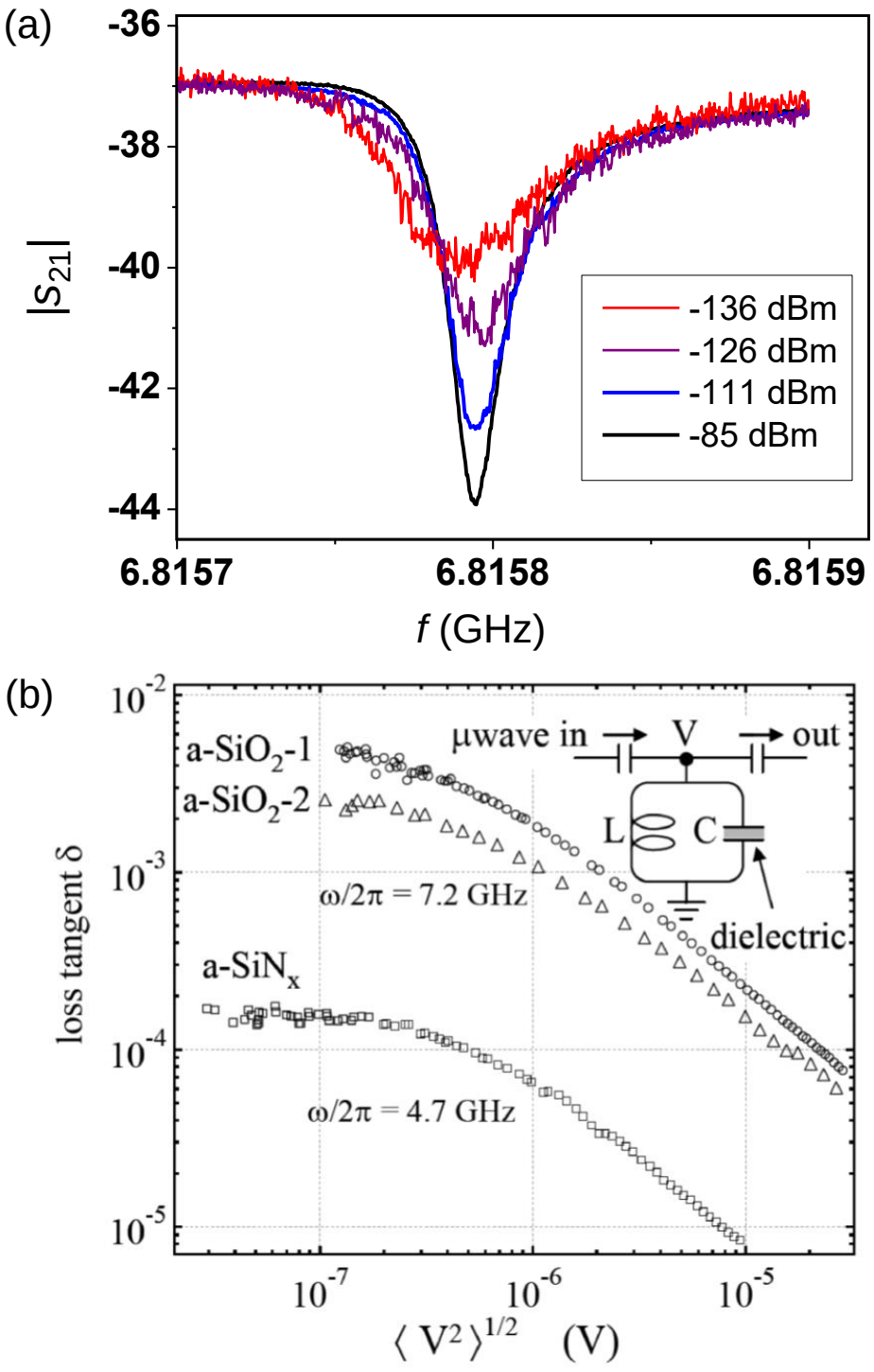

Fig. 2.4 - (a) Magnitude of S_{21} as a function of the frequency of the applied microwaves for different microwave powers for resonator LC1. (b) Plot from Martinis et al. [2.5] showing microwave loss versus rf voltage for different dielectric materials in a parallel plate capacitor of a thin-film resonator. The materials were grown using chemical vapor deposition. The circles are for SiO_2 deposited a 13 ºC, the triangles are for SiO_2 deposited at 250 °C, and the squares are for silicon nitride deposited at 100°C.

$$\tan(\delta) = \frac{\pi\rho\left(ed\right)^2}{3\varepsilon}\frac{\tanh\left(\hbar\omega/2kT\right)}{\sqrt{1+\omega_R^2 T_1 T_2}}, \tag{2.36}$$

where the plate separation is x, ρ is the density of states of the TLSs, ed is the fluctuating dipole moment of each TLS, T_1 is the relaxation time of each TLS, T_2 is the coherence time of each TLS, and $\omega_R = eVd/\hbar x$ is the Rabi frequency of a TLS [2.5] when an oscillating potential V is applied at frequency ω. This expression ignores the possible distribution of TLS dipole directions and transition energies, as well as possible distribution of T_1 and T_2. Later work by Kevin Osborn's group at LPS and others have examined the effects produced by having a distribution of TLSs [2.3, 2.6-2.7].

2.4.2 Hamiltonian of Single TLS Coupled to a Resonator

A TLS can be understood as a charged particle or defect ion that can move between two locations in a dielectric (in the substrate, surface oxide, or tunnel barrier), forming an electric dipole. I will assume an individual TLS has charge q and mass m and can hop between two points $\boldsymbol{x}_L$ and $\boldsymbol{x}_R$ (left and right) where there are local minima of the potential energy (see Fig. 2.5). For simplicity, I assume that in the absence of an external electric field, the tunneling matrix element between the left state and right state is Δ_0 and the difference in potential energy between the two locations is $\Delta = U(\boldsymbol{x}_L) - U(\boldsymbol{x}_R)$. Although the exact molecular composition of these defects is not generally known, one possibility is that they are charged OH^- bonds with one end that is free to move [2.8, 2.9].

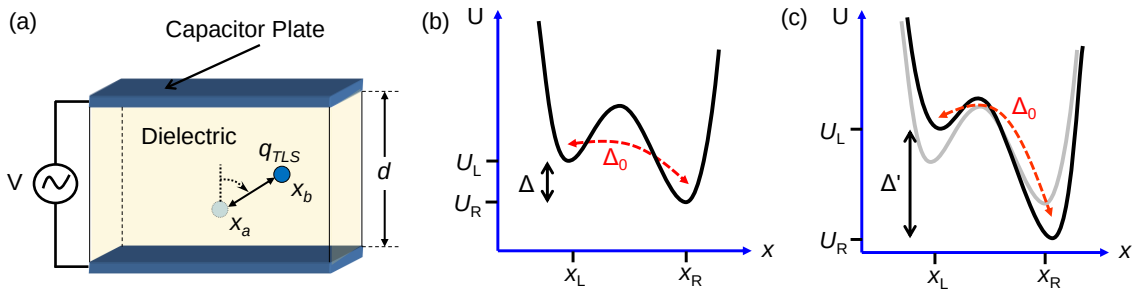

Fig. 2.5 - (a) Model of a charged tunneling TLS defect in a dielectric. The TLS has charge q and moves in an electric field produced by an applied voltage $V = V_0 cos(\omega t)$ across the plates of a capacitor. When the electric field frequency matches the resonant frequency of the TLS, it can excite the TLS and cause it to transition between positions x_L and x_R. (b) Illustration of double-well potential experienced by a TLS. The potential energy difference between the two wells is $\Delta = U(x_L) - U(x_R)$ and the tunneling energy is Δ_0. (c) When a dc voltage V_{dc} is applied, it tilts the double well potential, so that the energy difference between the left and right well becomes Δ', which changes the transition frequency of the TLS.

In general, a charged tunneling TLS may couple to a microwave resonator through one or more mechanisms. Here, I consider the situation where a charged TLS couples to the electric field $\boldsymbol{E}$ produced by the capacitor of a resonator. We can write the effective Hamiltonian of the system in the form

$$H = H_1 + H_2 + H_d, \tag{2.37}$$

where the Hamiltonian of the uncoupled resonator is

$$H_1 = hf_r\left[a^\dagger a + \frac{1}{2}\right], \tag{2.38}$$

the Hamiltonian of the uncoupled tunneling TLS is

$$H_2 = \frac{\Delta}{2}\sigma_z + \frac{\Delta_o}{2}\sigma_x, \tag{2.39}$$

and the effective dipole coupling Hamiltonian can be written as

$$H_d = hg\left(a^\dagger + a\right)\sigma_z + hg_o\left(a^\dagger + a\right)\sigma_x . \tag{2.40}$$

Here, f_r is the resonance frequency of the unperturbed LC resonator, $a^\dagger$ and a are the creation and annihilation operators for excitations in the resonator, and σ_x and σ_z are the usual x and z Pauli operators that act on the state of the TLS. The dipole coupling factors g and g_0 account for perturbations in the TLS asymmetry energy (tilting of the two-well potential as shown in Fig. 2.5) and tunneling, respectively, due to the electric field of the resonator. This picture can be extended to include coupling to the strain [2.10, 2.11]. If Δ_0 and g vanish, H reduces to the Jaynes-Cummings Hamiltonian (see Ch. 1) [2.12]. The tunneling perturbation term g_0 is often dropped from the Jaynes-Cummings Hamiltonian because, it is argued, a uniform field will not produce a significant change in the tunneling energy compared to the asymmetry energy [2.8]. Here we retain g_0 because the fields in our mesoscopic system may not necessarily be uniform on the scale of the hopping distance.

The Hamiltonians H_2 and H_d are written above in the right-left basis $|R\rangle$ and $|L\rangle$ of the TLS, with $\sigma_z|R\rangle = |R\rangle$ and $\sigma_z|L\rangle = -|L\rangle$. It is convenient to instead express them in the eigenbasis of H_2, which are the ground state and excited state of the TLS:

$$|g\rangle = \cos(\theta/2)|L\rangle - \sin(\theta/2)|R\rangle \tag{2.41}$$

$$|e\rangle = \sin(\theta/2)|L\rangle + \cos(\theta/2)|R\rangle \tag{2.42}$$

where $\theta = arctan(\Delta_0/\Delta)$. In the $|g\rangle$ and $|e\rangle$ basis, one finds

$$H_2 = \frac{\sqrt{\Delta^2 + \Delta_o^2}}{2}\sigma_z = \frac{1}{2}hf_{TLS}\sigma_z \tag{2.43}$$

$$H_{d1} = \left(a^+ + a\right)\left(hg\cos(\theta) + hg_o\sin(\theta)\right)\sigma_z = hf_r\gamma\left(a^+ + a\right)\sigma_z \tag{2.44}$$

$$H_{d2} = \left(a^{+} + a\right)\left(-hg\sin(\theta) + hg_o\cos(\theta)\right)\sigma_x = hf_r\mu\left(a^{+} + a\right)\sigma_x \tag{2.45}$$

where $f_{TLS} = \sqrt{\Delta^2 + \Delta_o^2}/h$ is the transition frequency of the bare TLS, $H_d = H_{d1} + H_{d2}$, $\gamma = \left(g\cos(\theta) + g_o\sin(\theta)\right)/\ f_r$, and $\mu = \left(-g\sin(\theta) + g_o\cos(\theta)\right)/\ f_r$. We note H_{d1} is the diagonal part of H_d in the TLS eigen-basis, while H_{d2} is the off-diagonal part. Both parts couple photon resonator states that differ by ± 1 photon.

We now write $H=H_0+H_{d2}$, where:

$$H_0 = H_1 + H_2 + H_{d1} \tag{2.46}$$

and treat H_{d2} as a small perturbation ($\mu << 1$). We note that H_0 is the Hamiltonian of a TLS coupled to a displaced harmonic oscillator [2.13]. The eigenstates of H_0 can be written as [2.14]:

$$\left|\varphi_{n,g}\right\rangle\left|g\right\rangle = \frac{1}{\sqrt{n!}}\left(a^{+} - \gamma\right)^n \exp\left(-\frac{1}{2}\gamma^2\right)\exp\left(\gamma a^{+}\right)\left|0\right\rangle\left|g\right\rangle \tag{2.47}$$

$$\left|\varphi_{n,e}\right\rangle\left|e\right\rangle = \frac{1}{\sqrt{n!}}\left(a^{+} + \gamma\right)^n \exp\left(-\frac{1}{2}\gamma^2\right)\exp\left(-\gamma a^{+}\right)\left|0\right\rangle\left|e\right\rangle \tag{2.48}$$

where n = 0, 1, 2. The corresponding energy levels of H_0 are:

$$E_{n,g} = hf_r\left(n - \gamma^2 + \frac{1}{2}\right) - \frac{1}{2}hf_{TLS} \tag{2.49}$$

and

$$E_{n,e} = E_{n,g} + hf_{TLS} \tag{2.50}$$

From Eqs. (2.49) and (2.50) we find that if we ignore the perturbation H_{d2}, then the transition frequency of the cavity does not depend on the state of the TLS. That is, if H_{d2} is ignored, the dispersive shift of the cavity $2\chi_n = \left(E_{n+1,e} - E_{n,e}\right)/h - \left(E_{n+1,g} - E_{n,g}\right)/h$ vanishes for all n, as expected.

In contrast, the off-diagonal term H_{d2} produces a TLS-dependent dispersive shift. For measurements of telegraph noise in our system (See Ch. 5), we are interested in TLSs that are in the limit $f_{TLS} << f_r$ (which allows them to be thermally excited) and that have very weak perturbations from H_{d2} ($\mu << 1$). Since H_{d2} is off-diagonal, the first order perturbation is zero. Therefore, we use second order perturbation theory to calculate the perturbed energy levels. To simplify the calculation we write the displaced harmonic oscillator states in the limit $\gamma << 1$ as $\left|\varphi_{n,g}\right\rangle\left|g\right\rangle \approx \left|n\right\rangle\left|g\right\rangle + \gamma\left(-\sqrt{n}\left|n-1\right\rangle + \sqrt{n+1}\left|n+1\right\rangle\right)\left|g\right\rangle$ and $\left|\varphi_{n,e}\right\rangle\left|e\right\rangle \approx \left|n\right\rangle\left|e\right\rangle - \gamma\left(-\sqrt{n}\left|n-1\right\rangle + \sqrt{n+1}\left|n+1\right\rangle\right)\left|e\right\rangle$. To lowest order in μ and γ, we find that the dispersive shift of the n-to-n+1 cavity transition due to H_{d2} is

$$2\chi_n = \frac{1}{h}\left(E_{n+1,e} - E_{n,e}\right) - \frac{1}{h}\left(E_{n+1,g} - E_{n,g}\right) \approx -4\mu^2 f_{TLS} \frac{f_r^{\,2}}{f_r^{\,2} - f_{TLS}^2}. \tag{2.51}$$

A key feature of Eq. (2.51) is that the dispersive shift is negative if the TLS transition frequency f_{TLS} is less than the resonator frequency f_r. This means the transition frequency of the resonator decreases when a low-lying TLS is excited. This behavior is due to the well-known phenomena of level-repulsion or anti-crossing [2.15]. Similar behavior occurs in the Jaynes-Cummings Hamiltonian [2.12] and the inclusion of additional tunneling terms here does not change this qualitative behavior. Thus, observation of a positive dispersive shift in a weakly coupled TLS-resonator system, with the TLS being thermally excited ($f_{TLS} << f_r$), would suggest that some other TLS-resonator coupling term may be present in the system Hamiltonian. The significance of this result in understanding some of our results on TLSs is discussed in Sec. 5.2.

2.4.3 Applying Voltage to a TLS and Resonator System

Having a resonator coupled to a TLS allows one to indirectly probe individual TLS properties, which may otherwise be hard to measure. Figure 2.6 shows how the transition energy $E_r = hf_r$ of a resonator varies when the resonator is coupled to two charged TLS defects whose energies are being swept by applying a dc voltage V_{dc}. In this illustration, the energy $E_{TLS-1}$of one uncoupled TLS decreases with increasing V_{dc}, while the energy E_{TLS-2} of the other TLS increases. The energy crossings in this system are forbidden and this causes a distinct splitting in the resonator's transition spectrum when the bare resonator transition frequency equals the transition frequency of the TLS. The TLS effectively tunes

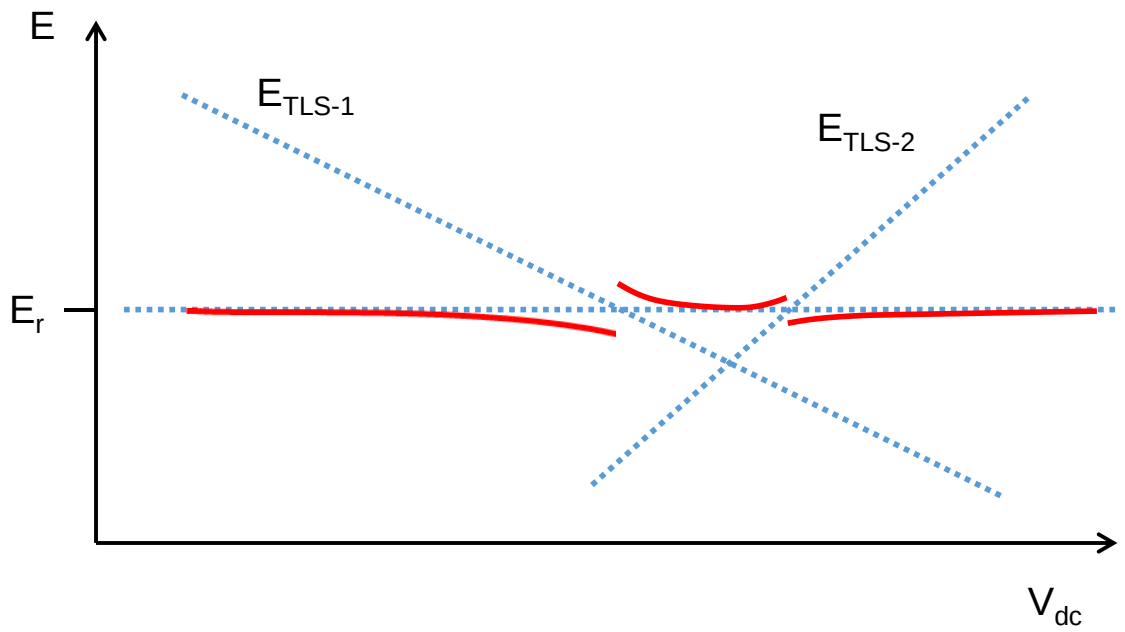

Fig. 2.6 - The interaction of individual two-level systems with the resonator can be modelled as avoided level crossings. The horizontal dotted blue line shows the transition energy $E_r = hf_r$ of the uncoupled resonator, which is a constant as a function of the applied dc voltage V_{dc}. The blue dashed lines show the transition energy of two uncoupled TLSs, which either increase or decrease with V_{dc}. The resulting transition energy of the coupled resonator is shown in red. There are avoided level crossings when the uncoupled transition frequency of a TLS equals the bare transition frequency of the resonator.

the resonator frequency higher or lower as it is swept through the resonator's bare transition frequency. As V_{dc} is swept, the presence of a TLS will show up as an avoided level crossing, with the resonance shifting lower and then higher, or vice versa. Of course if many TLSs are present, the resulting perturbations may appear as random but repeatable variations of the transition frequency as V_{dc} is swept.

2.5 Resonators, Optical Illumination, and Quasiparticles

There have been many fundamental and applied studies of the effects produced by light on superconductors [2.16-2.19]. This has continued to be an active area of research over the last decade for two reasons. First, the sensitivity of superconducting devices to light has been used to develop very sensitive optical detectors based on single nanowires [2.20, 2.21] and variations in the microwave kinetic inductance (MKIDs) [2.22-2.25]. These devices have been used for detecting single photons and for detecting optical radiation over a wide bandwidth. Second, and of particular interest for my work, it has been found that the absorption of stray incident infrared or optical radiation in superconducting resonators or qubits can be a significant or even dominant source of relaxation, limiting the relaxation time T_1 of qubits and decreasing the quality factor Q of resonators [2.26].

When light is absorbed in a superconducting resonator, the light breaks Cooper pairs and creates quasiparticles. This leads to three distinct effects. First, reducing the number of Cooper pairs causes an increase ΔL_k in the kinetic inductance. This in turn decreases the resonance frequency $f_0 = 1/2\pi\sqrt{LC}$ (see Fig. 2.7), where $L = L_0 + L_k$ is the

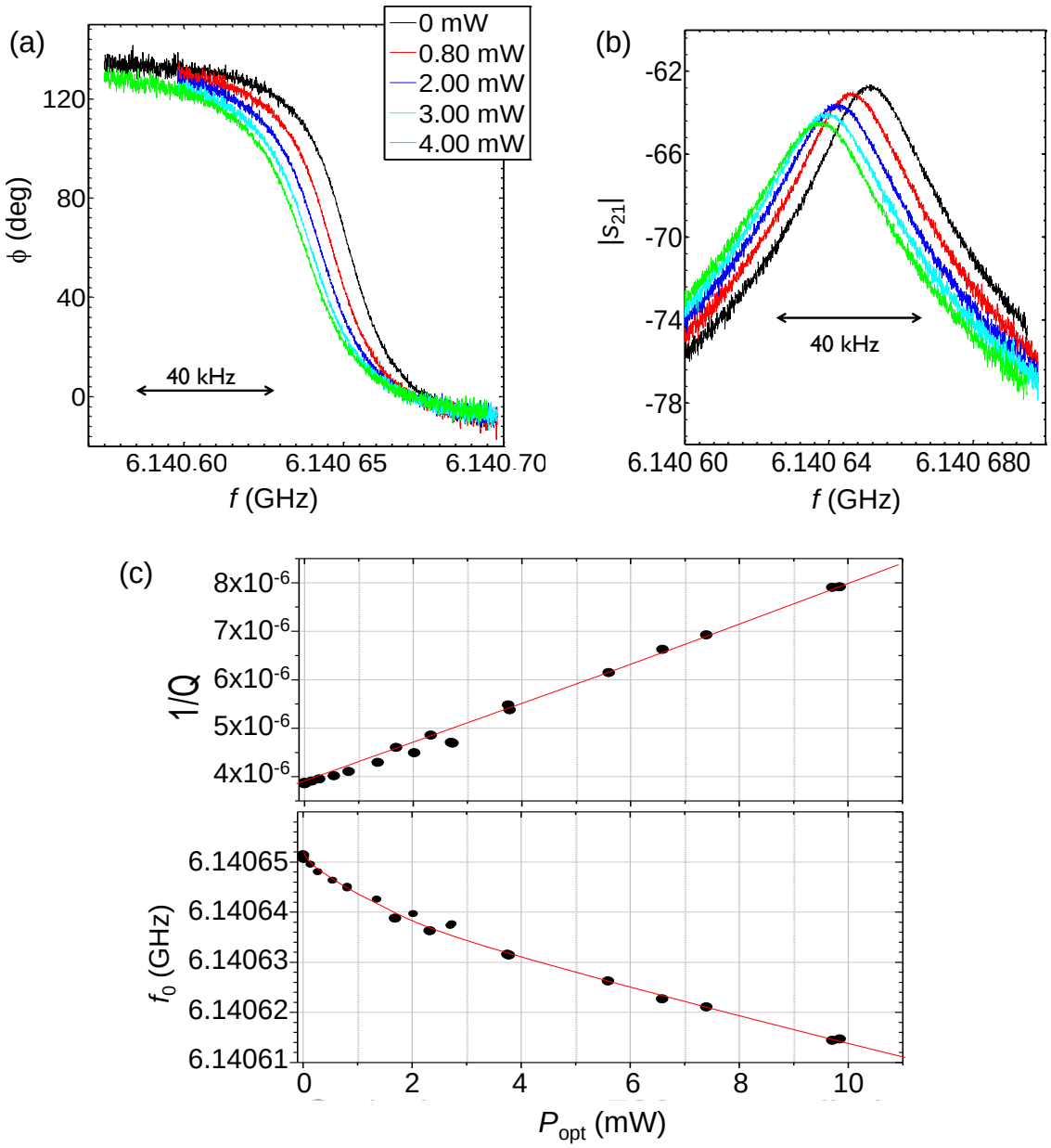

Figure 2.7 - (a) The phase ϕ of S_{21} as a function of applied microwave frequency f for different optical source powers for resonator LC2. The amount of light absorbed is approximately one part in a billion of the source power for the given position of the fiber. (b) The magnitude of S_{21} as a function of applied microwave frequency for different optical source powers. The resonance frequency f_0 shifts lower and the quality factor Q decreases as light is applied. (c) Loss $1/Q$ and resonance frequency f_0 as a function of the optical power P_{opt} applied to the fiber. Red lines are guides to the eye and are not fits to the data.

sum of the geometric (L_0) and kinetic (L_k) inductances. As we can see from a Taylor series expansion of $f_0 = 1/2\pi\sqrt{(L_0 + L_k)C}$, this shifts the resonance frequency by $\Delta f_0 = -f_0\,\Delta L_k/(4\pi L)$, where I have assumed $\Delta L_k \ll (L_k + L_0)$.

A second effect when the pairs are broken is that loss in the superconductor also increases because quasiparticles can dissipate energy. For small changes
in the quasiparticle density, we expect both the change in loss and the shift in the resonance frequency to be proportional to the density (see Ch. 7).

A third effect is that the absorption of light can cause heating of the system (dielectrics and superconductor), the creation of high-energy phonons, and other non-equilibrium thermal effects. For the experiments described in Chaps. 6 and 7, where I illuminated a resonator with Rayleigh scattered light from an optical fiber, all three of these effects were important. Here, I mainly focus on the frequency-dependent aspect.

For most of the experiments I describe in Ch. 7, there was an additional complication in that the resonator was subjected to a spatially non-uniform illumination. In general this will cause the 3D density of quasiparticles n_{qp} to be a function of position in the resonator. To understand the response of the resonator in this case, it is necessary to know the density of quasiparticles in different parts of the resonator. In practice, I am most interested in quasiparticles in the inductor because quasiparticles in this high-current region are most effective at causing loss and producing shifts in the kinetic inductance, which in turn causes changes in the Q_i and resonance frequency.

To model the 2-dimensional spatial distribution of the quasiparticles under optical illumination, I used the following diffusion equation:

$$\frac{dn_{q2}}{dt} = G_b + g_0 I_i + D_q \nabla^2 n_{q2} - R_q n_{q2}^2 - \Gamma_{tr} n_{q2} \ . \tag{2.52}$$

Here, n_{q2} is the areal density of quasiparticles (three dimensional density times the thickness of the film), G_b is the rate at which background quasiparticle areal density is generated, g_0 relates the rate of optical generation of quasiparticles per unit area to the local optical intensity I_i incident on the resonator, D_q is the diffusion constant, R_q is the 2-dimensional recombination factor characterizing the rate at which quasiparticles re-combine into Cooper pairs, and Γ_{tr} is the rate at which quasiparticles are lost due to trapping in vortices or normal regions in the film.

I note that I have chosen to use a 2-dimensional diffusion equation, rather than a 3-dimensional diffusion equation, because we expect the density of quasiparticles to be independent of depth in the film and this simplifies the resulting analysis. However, it does introduce some potential confusion in the definition of the parameters in Eq. (2.52). To convert Eq. (2.52) to a 3-dimensional diffusion equation, we can simply divide both sides of the equation by the film thickness d. For the 3-dimensional density of quasiparticles $n_{qp} = n_{q2}/d$, I then obtain:

$$\frac{dn_{qp}}{dt} = \frac{G_b}{d} + \frac{g_0}{d} I_i + D_q \nabla^2 n_{qp} - R_q d n_{qp}^2 - \Gamma_q n_{qp} \ . \tag{2.53}$$

Thus we see that G_b/d is the rate at which background 3-dimensional quasiparticle density is generated, $R_q d$ is the recombination rate factor in 3-dimensions, while D_q and Γ_q are indeed the quasiparticle 3-dimensional diffusion constant and three dimensional trapping rate, respectively.

Note that G_b is the sum of the rate G_t at which background quasiparticle density is generated thermally and the rate G_n at which quasiparticle density is generated due to the

absorption of stray background infrared or optical photons or high energy phonons. I will refer to quasiparticles that are produced by G_n as non-equilibrium background quasiparticles since they were created by a non-thermal process. For aluminum films at temperatures less than about 150 mK, which are the concern in this thesis, G_t can be ignored. In the steady state when there is no deliberate optical illumination, G_n needs to be determined. Assuming a spatially uniform mechanism that is producing non-equilibrium quasiparticles and assuming the trapping rate $\Gamma_{tr} = 0$, we can ignore diffusion. In this situation in the steady state, we find $G_n = G_b = R_q \cdot n_{b2}^2$ where n_{b2} is the 2-dimensional density of the non-equilibrium background quasiparticles.

I note also that the optical factor g_0 is not a constant for very high densities of quasiparticles, because I_i has a diminishing ability to create quasiparticles if most of the Cooper pairs have already been broken. However, for the low quasiparticle densities that I am considering in this thesis, g_0 can be taken as a constant.

I also note that the diffusion constant for quasiparticles is actually not a constant but depends on the quasiparticle energy. The expected dependence for the diffusion constant is $D_q(E) = D_n\sqrt{1-\left(\Delta/E\right)^2}$ [2.27, 2.28], where D_n is the diffusion constant of the electrons in the normal metal. To simplify the analysis, I assume that the quasiparticles will thermalize quickly to the temperature T of the system, that $k_BT << \Delta$, and that quasiparticles with energy around $E = \Delta + k_BT$ will dominate the behavior. With these assumptions, the diffusion constant becomes approximately $D_q = D_n\sqrt{2k_bT/\Delta}$, which shows that the diffusion constant decreases at low temperature. For example, at 100 mK in aluminum with $\Delta = 1.74 \times 10^{-4}$ eV, one finds $D_q = 0.304D_n$.

It is worth emphasizing here that the diffusion Eq. (2.52) is a simplified model of the quasiparticle behavior. In particular it does not take into account the energy distribution of the quasiparticles, the distribution of phonons, or effects of a radio-frequency drive. These aspects can be essential for understanding the behavior of quasiparticles that are generated at low temperatures by optical radiation and driven by microwaves. Goldie and Withington in particular have written a series of papers [2.29, 2.30] describing the complicated effects produced by radio frequency drive on both the distribution of quasiparticles and phonons in superconductors at low temperature. DeVisser et al. [2.31] has reported the observation of power-dependent response in superconducting resonators and their results appear to be in agreement with the Goldie and Withington theory. Budoyo *et al.* [2.32] extended the approach of Goldie and Withington to cover the case of quasiparticles generated by optical illumination and found good agreement with their measurements on Al resonators. Considerable detail can also be found in Budoyo's thesis [2.4]. The only reason I did not use this more sophisticated approach is that it is a great deal more complicated calculation to implement.

2.6 Conclusions

In this chapter, I first briefly reviewed the theory of the frequency dependence of the transmission S_{21} through a low-loss superconducting microwave resonator that is capacitively coupled to input and output ports. This included a discussion of the parameters that describe the resonator, including the resonance frequency, internal quality factor, external quality factor and total quality factor. I then briefly discussed effects on the resonance produced by coupling a resonator to individual two-level systems, including

avoided level crossings and loss. Finally, I discussed modelling the generation and spatial distribution of quasiparticles in superconducting resonators that are exposed to light.

Chapter 3: Chip Resonator and 3D Cavity

3.1 Introduction

In this chapter, I describe the design and fabrication of the three superconducting microwave resonators that I measured. I also describe the basic characterization of each resonator, including measurements of the resonance frequency and quality factors.

Each resonator was designed to test issues that could arise if it were used as a coupling element in an atom-transmon hybrid quantum system. In particular, each resonator used a lumped-element design, with a well-defined inductor and capacitor. This let us spatially separate the magnetic field of the inductor from the electric field of the capacitor so that atoms would be able to couple to the magnetic field of the inductor without being perturbed by the electric field.

In Table 3.1, I summarize a few characteristics of each resonator, including the name I will use in this thesis, the materials, lithographic technique, resonance frequency f_0, capacitance C, inductance L and total Q, along with the Chapters where I present detailed measurement results on each device.

In the following section, I discuss the design, fabrication, and characterization of resonator LC1. This resonator chip was wire-bonded to a printed circuit board (PCB) that was mounted in a copper sample box (see Fig. 3.1). In Sec. 3.3, I describe the 3D aluminum microwave cavity that I used in measurements on resonators LC2 and LC3. Sec. 3.4 and

Table 3.1 - Summary of a few characteristics of lumped-element microwave resonators LC1, LC2, LC3, which are all made from Al thin films on sapphire substrates. The first column gives the device name used in this thesis. The second column (Lab ID) gives the

corresponding name that I recorded in the lab notebooks during data taking. The resonance frequency is f_0, the capacitance is C, L is the inductance, and Q is the total quality factor of the device. Resonator LC2 has two values of f_0. The former corresponds to fiber-chip experiment version 1, and the latter to version 2. The last column gives chapters where detailed measurement can be found.

Resonator Name	Lab ID	Lithography	f_0 (GHz)	C (pF)	L (nH)	Q	Chapter
LC1	MW7 (2011)	Optical	6.816	0.22	2.5	1.75×10^5	4
LC2	#003 (Oct'13)	Optical	6.1406, 6.1453	0.369	1.82	1.51×10^5	6-7
LC3	CB1	SEM	6.14922	0.376	1.78	6.5×10^5	6-7

3.5 then describe the design, fabrication, and characterization of resonators LC2 and LC3, respectively. Finally, in Sec. 3.6, I conclude with a brief summary.

3.2 Resonator LC1

3.2.1 Design Considerations for Resonator LC1

Resonator LC1 (see Fig. 3.1) was designed and fabricated by Z. Kim [3.1]. It was used in the tuning experiment described in Ch. 4 and in the two-level system experiment described in Ch. 5. The resonator was made from a thin film of superconducting Al on a sapphire substrate. The lumped-element design has a meander-line inductor and an interdigitated capacitor that was capacitively coupled to an input/output transmission line (see Fig. 3.1). The geometry of the interdigitated capacitor (C = 0.22 pF) [3.2] and inductor (L = 2.5 nH) was designed to produce a resonance frequency near the 6.83 GHz hyperfine transition in ^{87}Rb. Small alignment markers were also patterned in Ti/Au to allow for optional e-beam patterning of an additional finger for "coarse" tuning [3.1] to

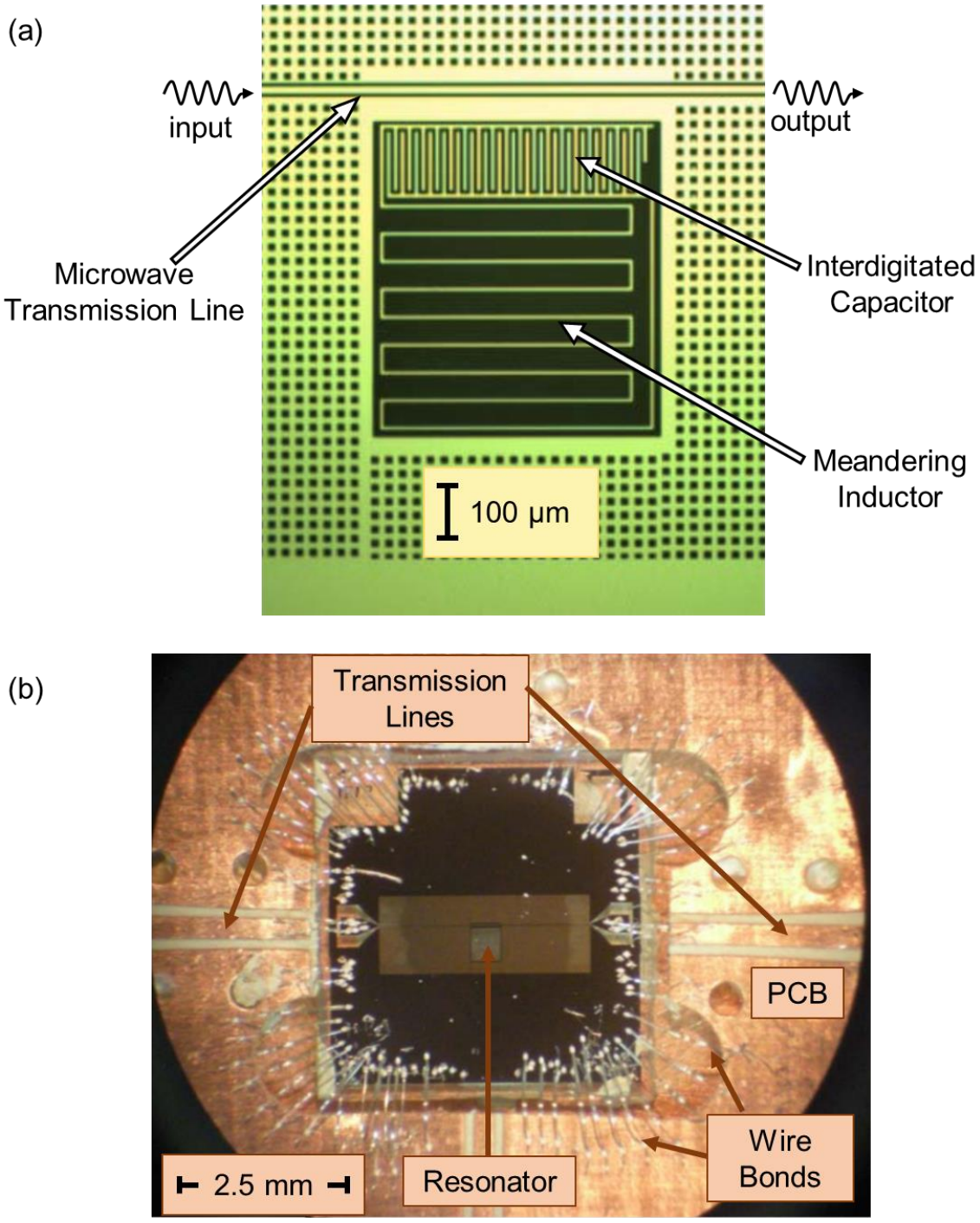

Fig. 3.1 - (a) Micrograph of lumped element resonator LC1. The sapphire appears black and the thin-film Al appears green. This resonator was used for the tuning experiments in Ch. 4 and the TLS experiments in Ch. 5. The square holes in the aluminum ground plane are for trapping magnetic vortices. (b) Micrograph of the resonator chip wire bonded to the PCB. The transmission line and the ground plane on the chip are electrically connected to the PCB with aluminum wire bonds. The resonator is visible in the middle of the image.

the transition.

We chose a lumped-element resonator, instead of a quarter-wave transmission-line resonator, so that the magnetic field was concentrated along the inductor, away from the electric field that was concentrated in the capacitor. This concentrated magnetic field would allow stronger coupling to the magnetic moment of trapped ^{87}Rb atoms, had they been incorporated into a hybrid qubit experiment. Aluminum was chosen for ease of fabrication and to achieve a high-quality factor *Q*, which would be necessary to resolve weakly coupled atoms in a hybrid qubit (see Ch. 1).

3.2.2 Fabrication of Resonator LC1

Resonator LC1 was fabricated at the Laboratory for Physical Sciences (LPS) by Zaeill Kim in May 2011. He used a c-plane oriented single-side-polished sapphire wafer substrate [3.3] with a thickness of 0.43 mm. A 230 nm Al film was deposited at a rate of 0.55 nm/s using the Sputnik thermal evaporator at LPS, which has only been used for evaporation of Al. During evaporation, the pressure reached a maximum of $2\text{x}10^{-7}$ Torr. After the aluminum deposition, the wafer was cleaned and blown dry. A layer of HMDS was applied at 2000 rpm for 60 s with a ramp down rate of 500 rpm/s. This was followed by a layer of positive photoresist, OiR 906-10, applied at 3500 rpm for 60 s with a ramp down of 1000 rpm/s. The wafer was next pre-baked at 90 ^{o}C for 1 minute. The resonator pattern was then exposed on a Karl-Suss optical contact aligner for 5 s.

After exposure, the wafer was post-baked at 120 ^{o}C for 60 s and then developed in OPD 4262 for 60 s at room temperature. This was followed by a 60 s bath in deionized (DI) water and blow drying. To etch the Al layer, aluminum etchant was first warmed on a hot plate to 55 ^{o}C and stirred with a magnetic bar at 600 rpm. The wafer was then placed in the

Al etchant for 147 s, followed by 60 s rinses in acetone, methanol, and isopropanol alcohol (IPA), and then blown dry.

In the next processing step, Dr. Kim patterned small Ti/Au alignment markers onto the surface using a negative resist. He then spun a bilayer of MMA/ZEP and baked it for 1 hour. This was followed by the deposition of an anti-charging layer of Al using the thermal evaporator. The alignment markers gave us the option to use e-beam lithography to modify the resonator after fabrication, however this was not necessary for LC1.

The wafer was then diced using diamond blades (CX-010-325-080-H from Dicing Blade Technology, Inc.) at a feed-rate of 0.75 mm/s. Since we did not need to write a qubit on the chip or use e-beam lithography, the MMA layer was lifted off and the chip was cleaned in preparation for packaging. The chip was then placed in a copper sample box and wire-bonded to a PC board (designed by Ben Palmer at LPS) that had a tapered coplanar waveguide (CPW) that transferred microwaves from the SMA connector to the transmission line on the chip. The CPW was wire bonded to the copper box for grounding (see Fig. 3.1(b)).

3.2.3 Characterization and Measured Parameters of Resonator LC1

For testing, the copper sample box containing LC1 was mounted on the mixing chamber of an Oxford Instruments cryogen-free dilution refrigerator and cooled to 15 mK. We probed the resonator by sending microwaves through the transmission line and measuring the transmitted signal V_2 and the applied drive V_1. The microwaves capacitively coupled to the resonator and we monitored the transmitted power as we swept the frequency f of the microwaves through the resonance frequency f_0. These measurements

were taken with an input power of −111 dBm (just before coupling into the sample box). Fitting the resulting $S_{21} = V_2/V_1$ versus f data using the approach of Khalil *et al.* [3.4], the resonance frequency of LC1 was found to be 6.815718 GHz, about 20 MHz less than the hyperfine transition in ^{87}Rb. The fit also gave a total quality factor $Q = 1.745\text{x}10^5$ and an internal quality factor $Q_i = 3.38\text{x}10^5$. I note that these results were from an initial cool-down in which a tuning pin (see Ch. 4) was located a few millimeters above the chip, which affected the values of Q and f_0. For additional details on the measurement apparatus, procedure and results see Ch. 4.

3.3 The 3D Cavity

3.3.1 Design Considerations for 3D Cavity

As discussed in the previous section, resonator LC1 was mounted in a copper sample box and was capacitively coupled to a thin-film transmission line that was wire-bonded to input/output microwave lines. In contrast, resonators LC2 and LC3 were mounted in a 3D superconducting aluminum cavity and no wire-bonding was involved. This approach is very similar to that used in many experiments with transmons; the transmon is mounted in a resonant 3D microwave cavity that not only isolates the device from the external environment but also allows the state of the qubit to be read out using microwave techniques [3.5]. If there was not a closed box around the transmon, relaxation would occur by radiating to free space and the transmon would also be directly exposed to infrared radiation, high-frequency microwave photons, or other external noise sources from higher temperature stages.

Similarly, for my experiments on LC2 and LC3, the 3D cavity mainly served to

isolate the resonator from external interference and couple it to the input and output microwave leads. This was a very convenient platform for mounting resonator chips since no PCB or wire bonding was required. I note that this approach was motivated by work by H. Paik, R. Schoelkopf and others at Yale [3.5], who did the first experiments on transmons mounted in 3D cavities. The rest of this section provides a description of cavity KDV1, which I used in my experiments on resonators LC2 and LC3.

Figure 3.2 shows a photograph of the outside of the 3D cavity KDV1. This cavity was made from 6063 aluminum and the internal length, width, and height were 1.40”, 0.15”, and 0.90”, respectively. The cavity was machined in the Physics Department's Machine Shop with the inside "vertical" edges of the cavity rounded because they were machined using an end mill. The cavity dimensions set the resonance frequencies of the modes. In particular, I wanted the lowest frequency mode, the TE101 mode (around 7.5 GHz), to be closer to the LC resonance frequency (typically around 6.15 GHz) than any other mode. I also wanted all of the cavity modes to be sufficiently detuned from the LC resonance frequency of the chip that they would not cause appreciable additional loss in the resonator due to the Purcell effect [3.6].

The cavity is made of two halves (see Fig. 3.3), with the lower half having a protruding lip that fits into a matching groove in the upper half. The interface between the two halves is sealed with an indium gasket and secured tightly with screws. Each LC resonator was patterned on a sapphire chip that was approximately 5 mm x 5 mm, slightly wider than the inner dimensions of the cavity. The chip was mounted into two notches made in the cavity walls (see Fig. 3.3). The notches were cut such that the chip sits parallel to the seam of the cavity and about 0.33" above the bottom of the cavity. One notch has a

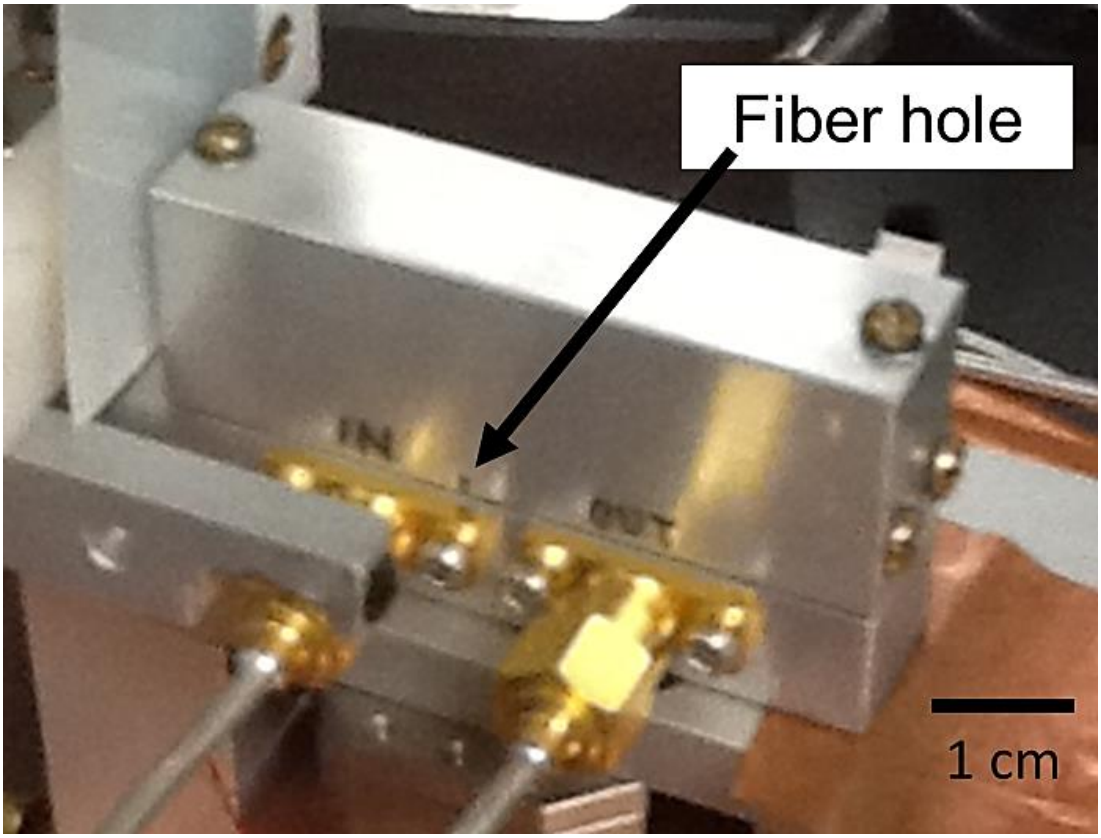

Fig 3.2 - Photograph of the 3D aluminum cavity KDV1 mounted on copper foil on top of an attocube stack. The input and output transmission lines are visible in the foreground of the image. The rectangular fiber hole is visible above and to the right of the input port.

rectangular cross section and the other notch has a dovetail shape such that the resonator is first angled into the dovetail cut and then lowered into the rectangular cut (see Fig. 3.3).

On the side with the rectangular cut, there is a threaded screw hole that accommodates a small 0-80 Ti set screw that, when tightened, secures the chip by pressing it snugly into the dovetail. Two rectangular through-holes in the cavity side walls allow an optical fiber to pass through the cavity and near the chip. I used this fiber to apply Rayleigh scattered optical power to the chip in some of my experiments, as described in Ch. 6. One edge of the chip is visible through this hole, allowing alignment of the chip and fiber during

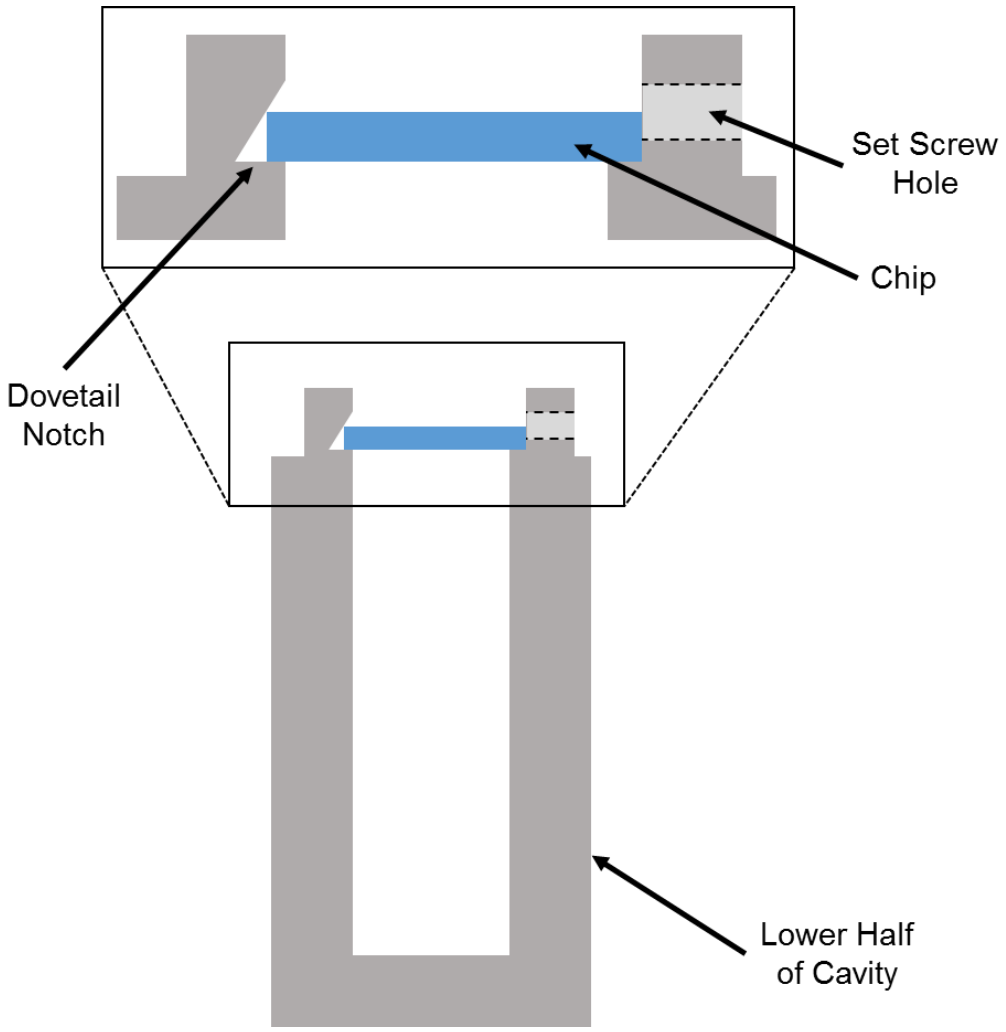

Fig. 3.3 - Cross-sectional view showing LC resonator chip (blue) mounted inside the 3D cavity KDV1 (gray). The dovetail notch to the left of the chip and the rectangular notch on the right hold the chip in place. An 0-80 set screw made from Ti pushes the chip into the dovetail notch.

set-up. Where they contacted the cavity, the edges of the chip were wrapped in a thin sheet of indium for better thermal and mechanical contact.

For the experiments I describe in Chs. 6 and 7, the cavity was mounted on top of a strip of Cu foil which was placed on a stack of attocube translation stages. These stages were mounted to a copper experimental plate that was in turn mounted to the mixing

chamber plate of a dilution refrigerator. The strip of high purity copper foil provided a thermal connection between the experimental plate and the cavity. This setup is described in detail in Ch. 6.

3.3.2 Characterization and Measured Parameters of the 3D Cavity

Input and output microwave lines were capacitively coupled to the cavity by means of short SMA launcher pins that protruded a few millimeters into the cavity. Both the input and output pins entered on the same side of the lower half of the cavity via SMA connectors (see Fig. 3.2). The cavity mode was driven by applying microwave power to the input pin and the response was measured by monitoring the transmitted power that coupled to the output pin. Since the LC resonator is relatively small and was detuned from the cavity resonance, it is relatively weakly coupled to the input and output pins. It is unknown if resonators LC2 and LC3 were mainly driven by off-resonant coupling of the input pin to the TE101 mode or by direct capacitive coupling between the resonator and the input pin.

With the cavity cooled to 15 mK on the dilution refrigerator, we drove the cavity by sending microwaves through the input coaxial line and monitored the transmitted voltage from the cavity output pin. Sweeping the frequency of the microwaves through the TE101 resonance frequency revealed a prominent transmission resonance. These measurements were typically taken with a power of -30 dBm at the source and -68 dB of attenuation in the lines (see Ch. 6 for a discussion of the input line attenuation).

Figure 3.4 shows results from a transmission $S_{21}(f)$ measurement of the cavity. The red curve shows a fit to the model of M. Khalil *et al.* [3.4], modified to fit peaks rather than dips (See Appendix A). For the plot in Fig. 3.4, the resonance frequency was 7.5083 GHz,

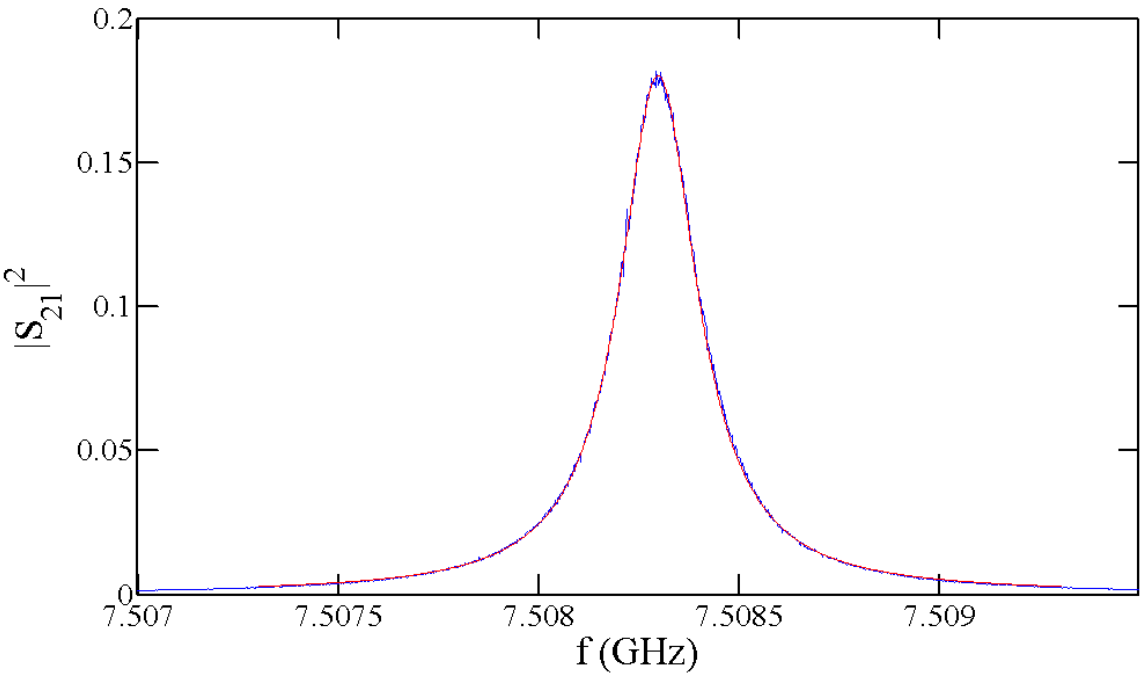

Fig. 3.4 - Plot of microwave power transmission $|S_{21}|^2 = (V_{out}/V_{in})^2$ through cavity KDV1 as a function of the frequency f of the input microwaves. The blue curve is data and the red curve is a modified Lorentzian fit. These data points were collected at 11 mK with resonator LC2 mounted in the 3D cavity.

the total quality factor was $Q = 3.20\text{x}10^4$ and the internal quality factor was $Q_i = 5.78\text{x}10^4$. The input and output Q of the cavity were very sensitive to the length and position of the pins and could only be determined accurately at room temperature. Typical values were $Q_{in} = 7.07\text{x}10^4$ and $Q_{out} = 2.88\text{x}10^5$.

Table 3.2 summarizes the measured resonance frequency, Q, Q_i, Q_{in}, Q_{out} at room temperature and 15 mK for different runs of cavity KDV1. I note that the resonance frequency of the cavity varied slightly in the different runs, either because different resonator chips were placed in the cavity for different runs or because the same chip was in a slightly different location. The different chip size or location caused different perturbations of the empty cavity resonance frequency.

Table 3.2 - Parameters for 3D aluminum microwave cavity KDV1 when it contained microwave resonator chips LC2 or LC3.

Cavity KDV1 contents	**Run Date**	f_o **(GHz)**	Q	Q_i	Q_{in}	Q_{out}
LC2 (11 mK)	1/05/14	7.508299	3.20×10^4	5.78×10^4	-	-
LC2 (300 K)	1/20/15	7.475964	1.72×10^3	1.72×10^3	7.07×10^4	2.88×10^5
LC3 (300 K)	1/7/16	7.493694	1.16×10^3	1.16×10^3	-	-
LC3 (13 mK)	2/8/16	7.534753	8.45×10^3	9.24×10^3	-	-

3.4 Resonator LC2

3.4.1 Design Considerations for Resonator LC2

Jared Hertzberg and I designed resonator LC2 by starting with the design for LC1 and modifying it so that it was better suited to our hybrid proof-of-principle experiment. One of the biggest modifications was to change from a meandering inductor to a single-line inductor. This reduced the inductance, increased the effective magnetic field coupling to atoms and also concentrated the field into a linear region. We also increased the length of the inductor to about 1 mm to allow coupling to ~1000 atoms trapped on a corresponding 1 mm long section of optical fiber. Since some light would be emitted from the fiber when it was positioned close to the inductor, we moved the capacitor further away from the inductor to reduce the amount of Rayleigh scattered light it would absorb from the fiber. Decreasing the absorbed light decreases the density of optically generated quasiparticles, which reduces the microwave loss. Finally, we added 0.5 mm long antenna pads to each

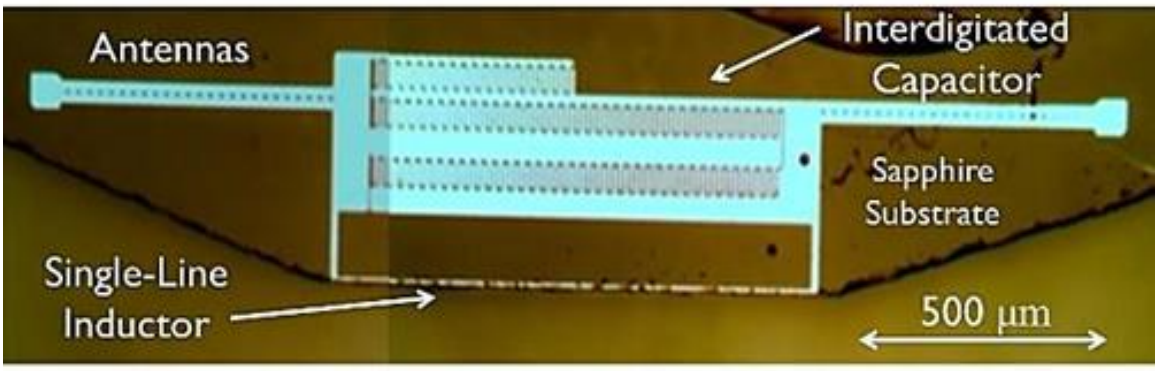

Fig. 3.5. Photograph showing superconducting microwave resonator LC2 (light blue) on polished and shaped sapphire substrate. The dark blotches on the single-line inductor are dirt left from the polishing and not breaks in the line. Note that the inductor is only about 2 μm from the polished edge of the chip. The small holes in the antenna lines act as traps for magnetic flux.

end of the capacitor (see Fig. 3.5) to increase the resonator's coupling to the electric field inside the 3D cavity. The resulting structure was ~ 2 mm long, which we expected to give coupling to the cavity about double that of a 1 mm transmon in a 3D cavity.

The use of a straight 1 mm long inductor line caused the inductance of the resonator to decrease by about 50% from the 2.5 nH inductance in resonator LC1 (see Table 3.1). To keep the resonance frequency in the 6-7 GHz range, we increased the capacitance to about C = 0.369 pF [3.2]. Note that the impedance *Z* of the resonator decreased with the increase in capacitance *C* and decrease in inductance *L*. For the same amount of energy stored in the resonator, the decreased impedance results in a higher current and a stronger B field coupling to atoms.

3.4.2 Fabrication of Resonator LC2

Resonator LC2 was fabricated by Dr. Jared Hertzberg. Jared began with a 3"

diameter sapphire wafer which was 0.43 mm thick. It was polished on just one side. The first step in the processing involved cleaning the wafer in a 90 °C piranha bath for 15 minutes. It was then rinsed in a deionized water (DI) bath and spun dry.

To ensure the surface remained clean, the wafer was loaded into a sputter system at the Center for Nanophysics and Advanced Materials (CNAM) within 20 minutes after cleaning. An Al film was deposited using an Ar gas pressure of 1.3×10^{-3} Torr, an RF power of 400 W, and a deposition time of 17 minutes. The deposition rate varied from 0.2 to 0.8 nm/s, resulting in a final film thickness of 480 nm. The pressure before deposition was 2×10^{-8} Torr and the pressure after deposition was 3×10^{-7} Torr. Upon inspection under an optical microscope, the aluminum film appeared to have grains on the order of 1 μm in size, and this relatively large size may indicate good film growth.

The film was then baked on a hotplate in the Kim Nanofab Lab at 120 ^{o}C for 10 minutes. Next, Shipley 1813 photoresist (S1813) was spun on at 3000 RPM for 60 s. This was followed by a soft bake at 90 ^{o}C for 5 minutes. Approximately 3 hours after spinning the resist, the wafer was exposed in the EV620 contact aligner with an exposure of 2.8 s using mask "JQI AOS 10-13 DEVICE". After exposure, the wafer was developed in Shipley 352 for 50 s, followed by two rinses in DI water.

Inspection under an optical microscope revealed a good, clean, pattern with the exception of some blistering under the aluminum in some of the patterns (although not resonator LC2). Blistering is usually an indication of poor adhesion due to surface contamination. It is also possible this blistering occurred during the bake at 120 ^{o}C, but a visual inspection was not performed at that time. The wafer was then etched in Al Etch Type A [3.7] for 9 minutes while constantly agitating. This was followed by a rinse in DI

water. The wafer was then etched for an additional 1.5 minutes and rinsed again in DI water. Inspection under an optical microscope revealed a clean pattern with a possible slight slope on the sidewall. The resist was stripped in Resist Remover PG [3.8] at room temperature for 10 minutes. It was then rinsed with IPA and then with DI water.

Inspection of the completed wafer under an optical microscope revealed well-formed patterns, a possible sidewall slant on the capacitor fingers, capacitor fingers approximately 4 μm in width and capacitor gaps of approximately 6 μm. Using a Tencor Alpha Step 200 Profilometer, the thickness of the film was measured at several test points on the chip, yielding thicknesses of 410, 400, 440, and 420 nm. The resistivity of the film was 5.7×10^{-8} Ωm which is more than twice the resistivity of pure aluminum at room temperature (2.82×10^{-8} Ωm). This is consistent with the incorporation of impurities into the films during the relatively slow deposition or possibly contact resistance in the measurements. The residual resistivity ratio (RRR) was not measured, but the high value of the room-temperature resistivity suggests that the film is fairly dirty and this would give a low value for the RRR and a relatively short electron mean-free path. From the room temperature resistivity, I can get an estimate for mean-free path at low temperatures. I note that the mean-free path of pure bulk aluminum is approximately 19 nm at room temperature. This is mainly due to scattering from thermal phonons. Since our films at room temperature had double the resistivity of pure samples, this means that the mean free path in the films was about 1/2 as long, or 9.5 nm. This is consistent with a 19 nm mean free path due to impurity scattering combining with the 19 nm mean free path from room-temperature phonons. In the normal state of Al at millikelvin temperatures, the contribution from phonons would disappear while the impurity scattering would remain. Thus at low

temperatures I get that the electron mean free path was approximately 19 nm (see Sec. 7.9).

In preparation for dicing, a tape backing was applied to the wafer. A protective resist layer (S1813) was then spun on and the wafer was baked at 95 ºC for 5 minutes. The wafer was next diced using a diamond saw with a feed-rate of 0.5 mm/s. During dicing it was noticed that some of the chips came loose from the tape - the chip hosting Resonator LC2 was unharmed. The chip was then sent to Neocera, where the edge of the substrate near the inductor of the resonator was removed, bringing the inductive line to within about 2 μm of the edge of the chip (see Fig. 3.5).

To remove grit on the surface of the inductor that was left over from polishing, the chip containing Resonator LC2 was cleaned in acetone at room temperature for 10 hours. It was next sprayed with IPA for one minute, with acetone for one minute, and then again with IPA for one minute. It was then soaked in acetone for 22 hours and finally rinsed again in acetone, IPA and DI water. These cleaning steps had no visible effect on the grit left on the inductor, which may have contributed to a slightly lower *Q* but had no effect otherwise.

3.4.3 Characterization and Measured Parameters of Resonator LC2

For more details on the measurement apparatus and procedure used to test resonator LC2, see Ch. 6. Briefly, LC2 was mounted into the 3D aluminum cavity KDV1 at 100 mK (see Fig. 3.6) as described in Sec 3.3.1.

Figure 3.7 shows the measurement set-up. Microwaves were generated by a vector network analyzer (VNA) and sent down a coax through attenuators with a total of 50 dB of attenuation at 6 GHz and an additional loss in the coax lines of 18 dB. The attenuators were thermally anchored at successive temperature stages in the refrigerator to reduce

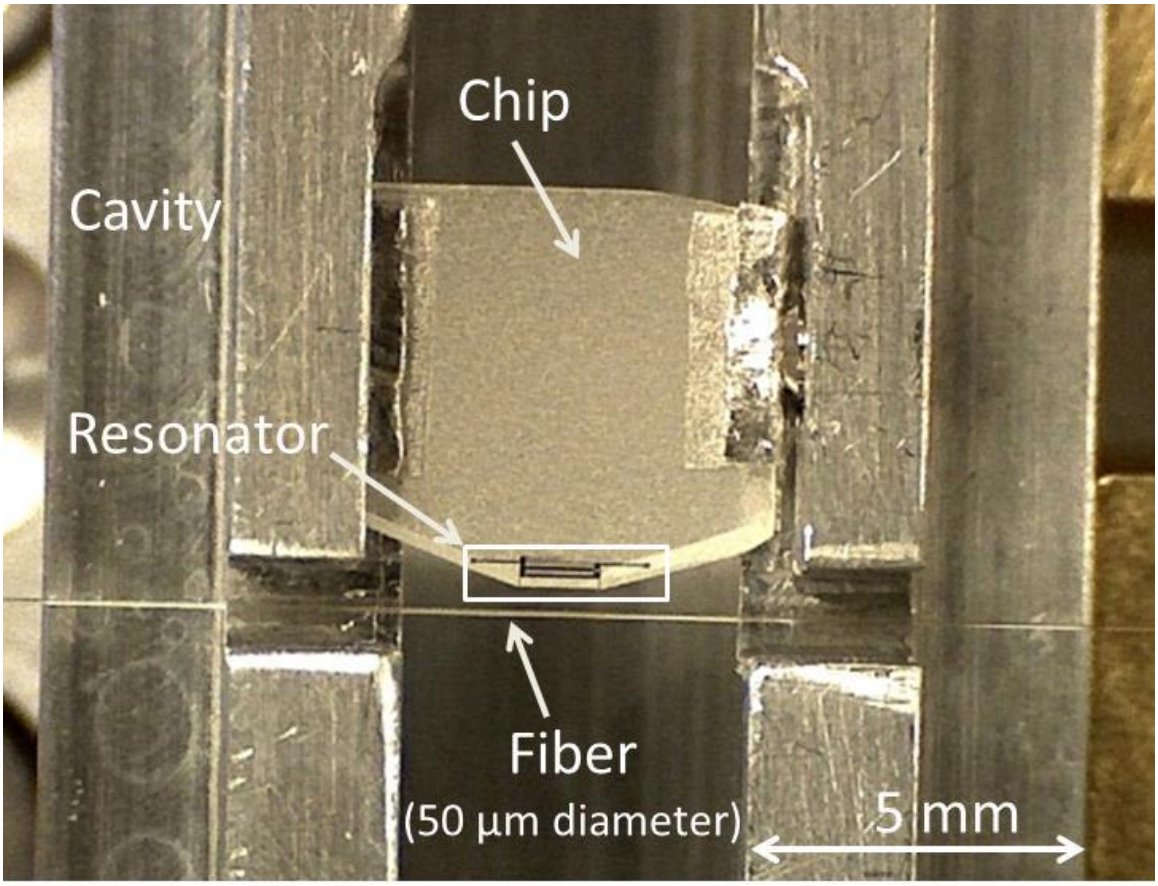

Fig. 3.6 - Photograph showing superconducting microwave resonator LC2 mounted in the bottom half of the 3D aluminum cavity KDV1. Note optical microfiber passing through the slots in the cavity wall.

Johnson-Nyquist noise from room temperature and the higher temperature stages. The microwaves were coupled into the cavity and the output from the cavity was amplified by a low-noise amplifier mounted on the 1 K stage before being fed back into the input of the VNA. There were a pair of cold isolators in the cavity output line to prevent noise from higher stages and reflections at the amplifiers from entering back into the cavity via the output line.

The measurements were taken with a power of -30 dBm at the output of the VNA. We fit the resulting $S_{21}(f)$ data (see Fig. 3.8) using an approach based on that of Khalil *et*

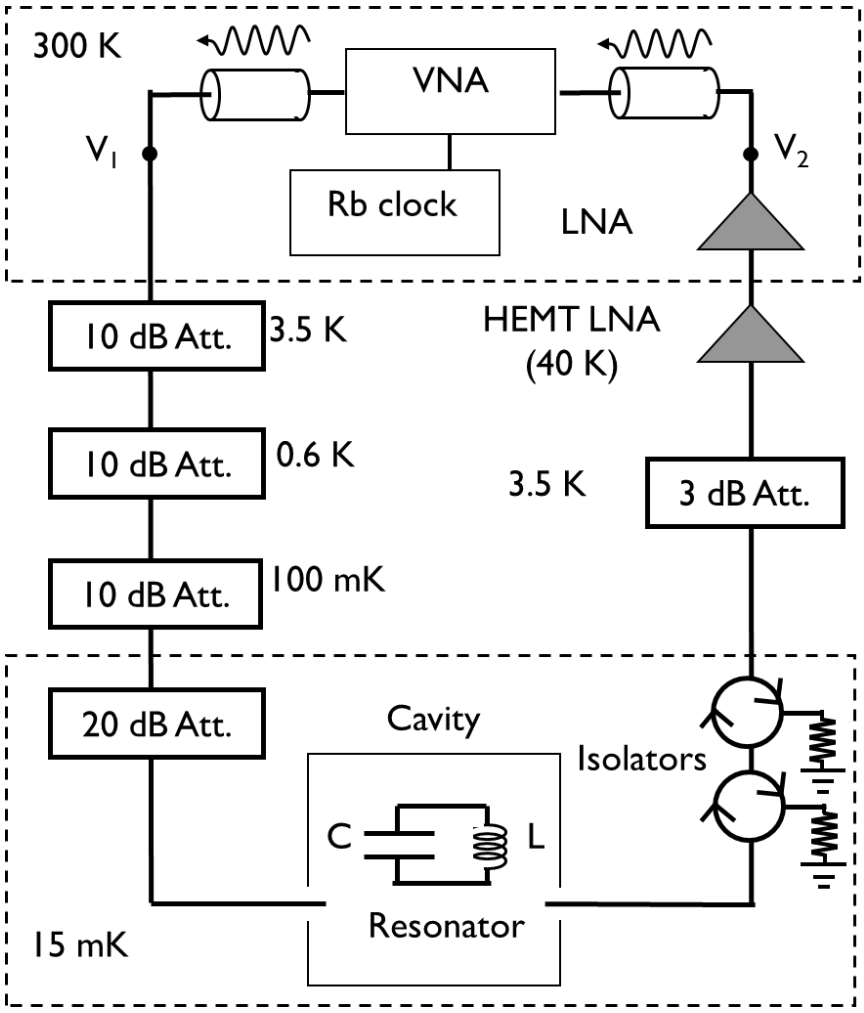

Fig. 3.7 - Experiment layout for measuring the LC resonator.

al. [3.4], but modified to fit a peak rather than dip (see Appendix A). Our system produces a peak on resonance because microwaves only couple strongly from the input pin to the output pin if they are near the resonance frequency of the chip or cavity. In contrast, a dip is produced when the input and output terminals in a system are connected by a through transmission line, as in the setup used to measure resonator LC1. The resonance frequency of LC2 was found to be 6.140654 GHz. The total quality factor was $Q = 1.51 \times 10^5$ and the internal quality factor Q_i was equal to Q, because the external coupling was very low. I

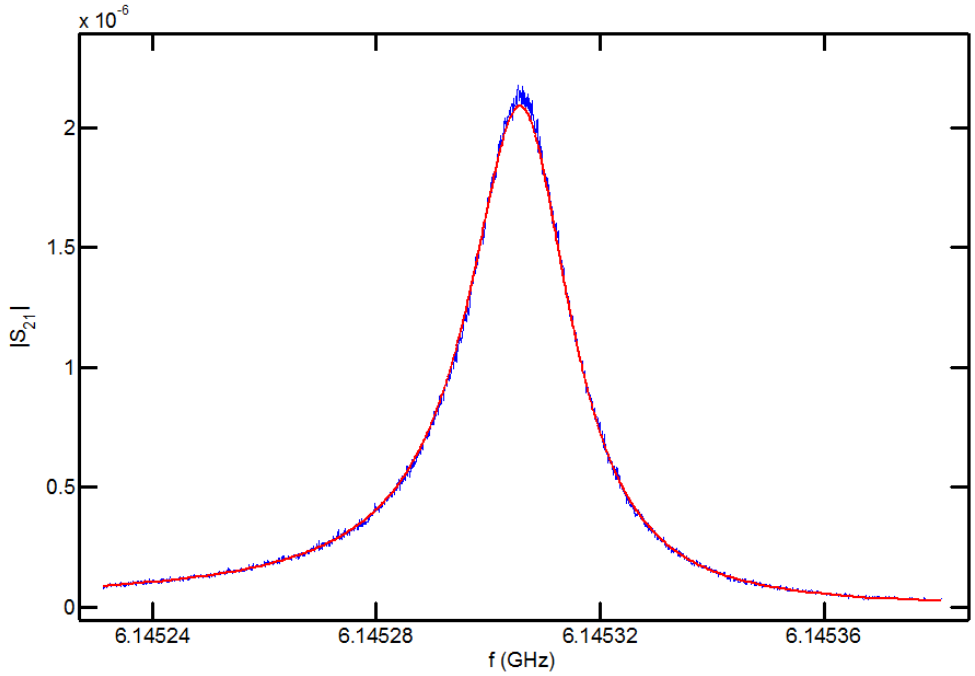

Fig. 3.8 - Resonance curve of resonator LC2 showing $|S_{21}| = |V_{out}/V_{in}|$ as a function of the frequency for a input power of -98 dBm. The blue curve is data, and the red curve is a modified Lorentzian fit.

note that these results are from an initial cool-down in which a microfiber (see Ch. 6) was about 1 mm away from the resonator, which is relatively far.

3.5 Resonator LC3

3.5.1 Design Considerations for Resonator LC3

As can be seen by comparing Fig. 3.9 to Fig. 3.5, the overall design of LC3 was very similar to the design of LC2. The most significant difference was the placement of the antenna pads, which are closer to the single-line inductor in LC3. This was done to allow increased diffusion of quasiparticles out of the inductor and into the antenna, where they will contribute less internal loss in the resonator. The other significant change was the addition of two more capacitive fingers in the top row of the IDC of LC3, which nominally

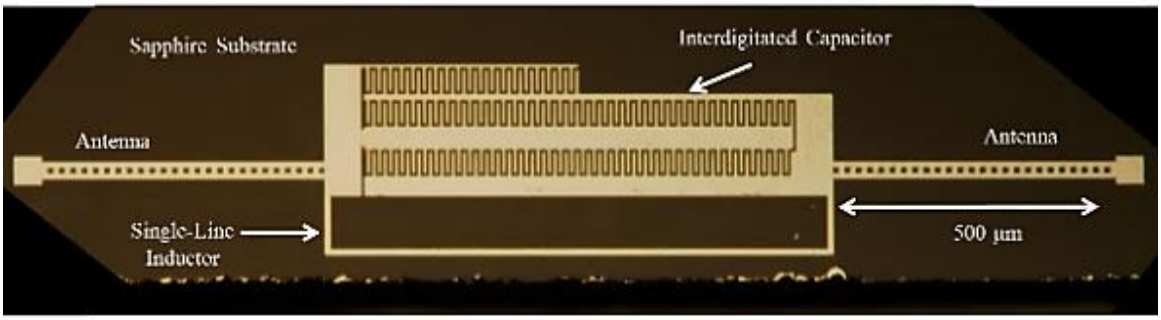

Fig. 3.9 - Superconducting thin-film aluminum microwave resonator LC3 on un-shaped sapphire substrate. The diagonal borders to the left and right in this image are not the edges of the sapphire chip but are just the edges of the microphotograph, which has been rotated by here. Note that the single line inductor is about 40 μm from the bottom edge of the chip.

increased the capacitance by ~2%.

3.5.2 Fabrication of Resonator LC3

Resonator LC3 was fabricated by Cody Ballard. He started with a sapphire chip that was coated with the following layers in ascending order from the surface of the sapphire wafer: LOR 10A resist, PMMA resist, aluminum anti-charging layer, and 1813 photoresist. Starting from an individual coated chip, he performed the following steps:

Step 1 - Remove the 1813 protective layer by soaking the chip in acetone for 3-5 minutes.

Step 2 - Spin on a layer of Aquasave as an additional anti-charging layer. Ramp the spin peed up from 0 to 4000 RPM and then spin for about 1 minute.

Step 3 - Write the pattern on the chip using the Raith eLine electron beam lithography tool.

Step 4 - Remove Aquasave layer by rinsing the chip in water.

Step 5 - Remove aluminum anti-charging layer by placing the chip in MF CD-26

developer for 3 minutes and then rinse with water.

Step 6 - Develop PMMA layer in MIBK: IPA 1:3 solution for 80 s and then rinse in IPA.

Step 7 - Remove exposed LOR10A resist by placing the chip in MF CD-26 developer for 30-40 s and then rinsing with water.

Step 8 - Thermally evaporate approximately 200 nm of aluminum (100 nm according to the crystal monitor, which later calibration has shown to have a tooling factor of 2).

Step 9 - Lift off the resist and aluminum that is on top of resist, leaving behind the resonator.

3.5.3 Characterization and Measured Parameters of Resonator LC3

The measurement setup for characterizing resonator LC3 was the same as discussed briefly in Sec. 3.4.3 and is discussed in detail in Ch. 6. With a input power of -98 dBm at the cavity input, the LC3 resonance frequency was measured to be 6.14922 GHz. Using the same fitting technique as in Sec. 3.4.3., the total quality factor was found to be $Q = 6.5\text{x}10^5$. As in the case of resonator LC2, the external quality factor Q_e is very large compared to the total Q, and thus the internal quality factor Q_i is very nearly equal to Q. I note that these results were from an initial cool-down in which a microfiber (see Ch. 6) was approximately 1 mm away from the resonator.

3.6 Conclusions

In this chapter, I discussed three resonators that I used for the proof-of-principle

experiments that are described later in this thesis. For each resonator, I described the design and fabrication process, and presented some of the key device parameters obtained from initial measurements. For use in an atom-transmon hybrid system, one wants a resonator with $Q > 10^6$ to be able to directly resolve coupling to about 1000 ^{87}Rb atoms. Resonator LC3 with a Q of 6.5×10^5 was near to this level and comparable to large Q's obtained in thin-film aluminum resonators by other groups [3.9].

As I noted above, the meandering geometry of resonator LC1 was not well optimized for use in a hybrid system. In contrast, resonators LC2 and LC3 were designed to have a higher B field in a well-defined linear region where it could be used to couple to atoms trapped on a fiber. Re-designing the resonator with a single line inductor separated 100 μm from the capacitor was also intended to reduce the absorption of Rayleigh scattered photons in the capacitor, which makes up by far the largest surface area of the resonator. To further reduce loss in the resonator caused by the absorption of Rayleigh scattered light, careful placement of the fiber and further re-design of the chip could be considered, as I discuss in later chapters. Also, I will show that it was possible to position the resonator within 5-10 μm of the edge of the chip, by either polishing back the sapphire substrate, or by directly patterning it using an SEM. This allowed the fiber to be positioned in-line with the inductor and the plane of the chip, significantly reducing the absorption of scattered light in the resonator.

Finally, I note that for the hybrid system we would like the resonance frequency to be within one linewidth Δf of the ^{87}Rb ground-state hyperfine splitting $f_{\mathrm{Rb}} = 6.834682$ GHz. For a resonator with a Q of 1×10^6, the linewidth is $\Delta f = 6$ kHz. Fabrication of LC1 gave a resonance that was only within 20 MHz of f_{Rb} [3.1], which was many linewidths away. In

the following chapter, I discuss how we demonstrated that we could tune resonator LC1 to within one linewidth Δf of f_{Rb}.

Chapter 4: Tuning a Superconducting Resonator at 15 mK

4.1 Introduction and Motivation

In this chapter I discuss our work on the compact frequency-tunable microwave resonator LC1. I show that we were able to precisely tune the resonator's frequency to the hyperfine splitting frequency of ^{87}Rb atoms, or detune it, and verify an effect due to a resonant interaction. We used two methods of tuning the resonator. First, after measuring the resonance frequency, we did a 'coarse' tuning by patterning additional capacitor fingers onto the resonator. Second, we 'fine' tuned the resonator inside the dilution refrigerator by moving a superconducting aluminum pin into the magnetic field produced by the inductor of the LC resonator.

In the next section, I discuss the physics of tuning in the LC resonator, including HFSS simulations of the magnetic field from the resonator, which were used to better understand the tuning. In Sec. 4.3, I then discuss how we tuned thin-film superconducting resonator LC1 and describe the experimental setup that I used for measurements. I next describe the tuning data and the main results, including the maximum tuning range. Finally, I conclude with a discussion of the applicability of this technique to the hybrid experiment.

4.2 Physics of Tuning

An essential idea behind our proposed atom-transmon hybrid quantum system is coupling the magnetic moment μ_{Rb} of about one thousand optically trapped ^{87}Rb atoms to the magnetic field $\vec{B}$ from the inductor in an LC resonator that is tuned to the 6.83 GHz

hyperfine transition. The effective coupling depends on the geometry of the inductor and location of the atoms, but is roughly $\tilde{\lambda} \sim \sqrt{N} * 40$ Hz in resonator LC1, where N is the number of atoms [4.1]. To directly observe an avoided level crossing from coupling the LC resonator to the ^{87}Rb atoms, the resonator would need to have its resonance frequency tuned through the 6.83 GHz hyperfine transition, with the splitting being largest when the resonator is within $\pm\tilde{\lambda}$ (~3 kHz for LC1) of the hyperfine transition. Note that this frequency scale set by $\tilde{\lambda}$ is also comparable to the FWHM of a 6 GHz resonator with a *Q* of 10^6, which suggests that the splitting may be directly observable in the microwave transmission spectrum of the resonator.

To understand how the atoms can be measured using the LC resonator, it is helpful to examine some previous experiments that used tunable resonators to detect individual two-level system (TLS) defects (see Ch. 2). In particular, B Sarabi *et al.* found that a relatively long-lived two-level systems (TLS) produces a sharp additional dip or feature in the resonator's transmission curve when the TLS is tuned within the bandwidth of the resonator's resonance [4.2-4.5]. The sharpness of the additional dip due to the TLS is determined by the Q of the TLS and its frequency stability.

A ^{87}Rb atom has a very long lifetime and therefore a high *Q*. In practice however, the trapping lifetime of a tapered optical fiber appears to be only on the order of milliseconds [4.6], which would broaden the linewidth of the ^{87}Rb hyperfine transition to a few hundred Hz. This is still an order of magnitude sharper than the effective coupling strength of a few kilohertz from coupling to 1000 atoms, which suggests that an avoided level crossing should still be observable. A high- *Q* LC resonator is desirable as it aids in detecting the small perturbation of the resonance frequency due to the coupling. Ideally for

spectroscopic measurements, a *Q* of several million would be desirable, as it would allow clean separation of the transitions in the avoided crossing. However, Sarabi found [4.2-4.4] that this is not essential, as long-lived weakly coupled systems can be observed as sharp features within a broader resonance peak in the spectrum (or dip for a notch resonator configuration). Thus, to observe a small perturbation of the resonance, it helps to have a high *Q*, but we must be able to tune the sharp atomic feature through the broader peak of the resonator, or vice versa.

In addition to fine tuning, we also may need to "coarse" tune the resonator by tens of MHz. Our design and fabrication process has limited ability to achieve a precise pre-determined resonance frequency f_r. In practice, our group has found that the as-built measured resonance frequency can typically vary by ~100 MHz from the designed simulated frequency. Considering that our resonators have interdigitated capacitors with spacing of about 5 μm between the teeth (see Fig. 4.1), a 0.1 μm increase (2%) in this spacing would cause a 1% increase in the resonance frequency, or about a 60 MHz shift. Since the spacing between the teeth is determined by the lithography and etching, which is hard to control to 0.1 μm, we expect that even resonators fabricated with identical designs made on the same wafer at the same time will have resonance frequencies that vary by tens of MHz.

As discussed in the next section, Kim *et al*. [4.7] was able to "coarse" tune an LC resonator by 36 MHz by using e-beam lithography to add a partial tooth to the resonator's interdigitated capacitor. This increased the capacitance, which in turn decreased the resonance frequency because $f_r = 2\pi/\sqrt{LC}$. This coarse tuning technique can only add to the capacitance, so it is only able to decrease f_r, and it is a not something that can be changed

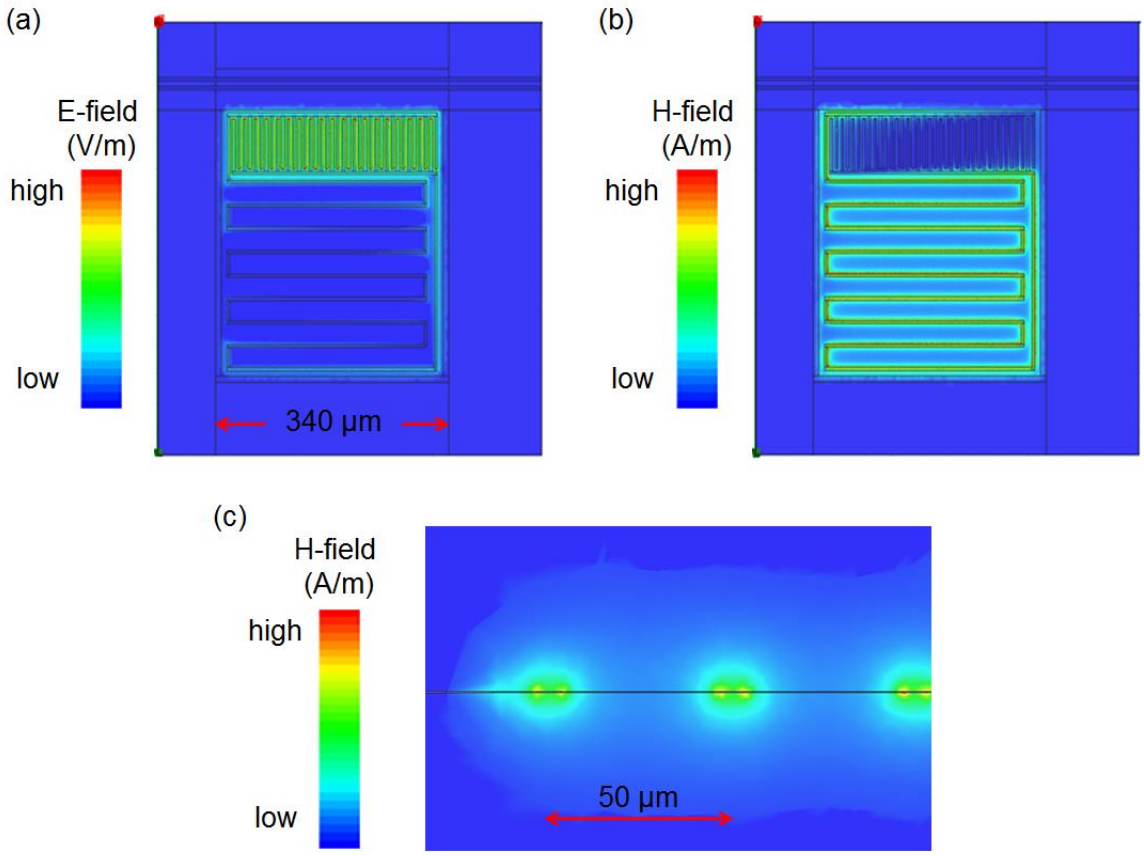

Fig. 4.1 - Simulations of LC resonator's electromagnetic fields using HFSS software [4.9]. (a) False color image showing simulated electric field strength from resonator while driven on resonance. The electric field is predominately in the interdigitated capacitor. Color bar shows relative E-field intensity. (b) False color image of simulated relative magnetic field strength from the resonator while driven on resonance. The magnetic field is concentrated predominately near the inductor. (c) Side view of a line-cut bisecting the resonator in figure (b). Only three of the turns in the meandering inductor are shown. These concentrated areas of magnetic field are regions that the trapped atoms would interact with most strongly.

in situ.

Regardless of our ability to fabricate and 'coarse' tune devices to a fixed frequency, ultimately we want to be able to tune the LC resonance to the ^{87}Rb transition while it is in the dilution refrigerator. We achieved *in situ* "fine" tuning by varying the inductance of the thin-film LC resonator using a superconducting tuning pin that was positioned by an

attocube piezoelectric translation stage [4.8]. The pin perturbs the magnetic field of the inductor (see Fig. 4.1), with the largest perturbation occurring when the field is placed in a region of high field. An image current in the pin is created, which generates a screening field that opposes the original field from the inductor. With a smaller total magnetic field, less energy is stored in the inductor, and the effective inductance of the resonator is decreased, which in turn increases the resonance frequency. In this case, the self-inductance L of the resonator can be written as [4.10]

$$L \simeq L_0 \left(1 - \frac{M^2}{L_0^2} \right) \tag{4.1}$$

where L_0 is the bare self-inductance of the resonator and M is the mutual inductance between the meandering inductor and the image current that is produced in the pin. The mutual inductance will increase as the pin approaches the meander. In principle, bringing any piece of metal close to an inductor will cause the same effect. We use a superconducting pin rather than normal metal because we need to maintain a high Q resonance, and normal metal would produce additional loss. We found that loss can also occur when microwave power is radiated out through the pin. Ideally the pin is very well-grounded and the image current presents a pure inductive impedance to the resonator. In Sec. 4.3, we discuss our implementation of an improved pin with ‘wings’ that touch the chip on either side of the resonator. The purpose of the wings is to improve grounding of the pin and thereby prevent power from being radiated by the pin.

4.3 Experimental Arrangements

From the above discussion we can see that we need to be able to bring a superconducting pin very close to a small thin-film LC resonator. Figure 4.2(a) shows thin-film Al superconducting lumped-element resonator LC1 (described in detail in Sec. 3.2). It consists of an interdigitated capacitor and meandering inductor printed on a sapphire substrate. The resonator is capacitively coupled to an on-chip transmission line for measurements of the transmission $S_{21}(f)$. The holes in the ground plane are to trap magnetic flux vortices, preventing them from causing loss. The chip that the resonator is printed on is wire-bonded to a PCB, as shown in Fig. 4.2(b).

Figure 4.3 shows the experimental setup used to measure the resonator inside the dilution refrigerator. The frequency of the resonator was adjusted by using an attocube to move the aluminum pin and tune the inductance of the meander. The Agilent vector network analyzer (VNA) [4.11] sent microwaves into the dilution refrigerator via coaxial input lines. To reduce Johnson-Nyquist noise, the input lines had 50 dB of total attenuation from commercial attenuators mounted at 3.6 K, 0.6 K, 0.1 K and the mixing chamber [4.12-4.13]. The input lines added an additional 32 dB attenuation. The input microwave power is transmitted down the input transmission line and capacitively couples to the LC resonator. The microwave power inside the resonator then capacitively couples back out to the transmission line. Half the power goes to the output end of the transmission line and then passes through two isolators, which block microwaves from going down the output line and reaching the resonator. A cold low-noise amplifier (LNA) [4.14] is mounted on the 3.6 K stage. A 3 dB attenuator was placed at the input of the amplifier, preventing resonant oscillations that can occur in the amplifier if it sees an impedance mismatch.

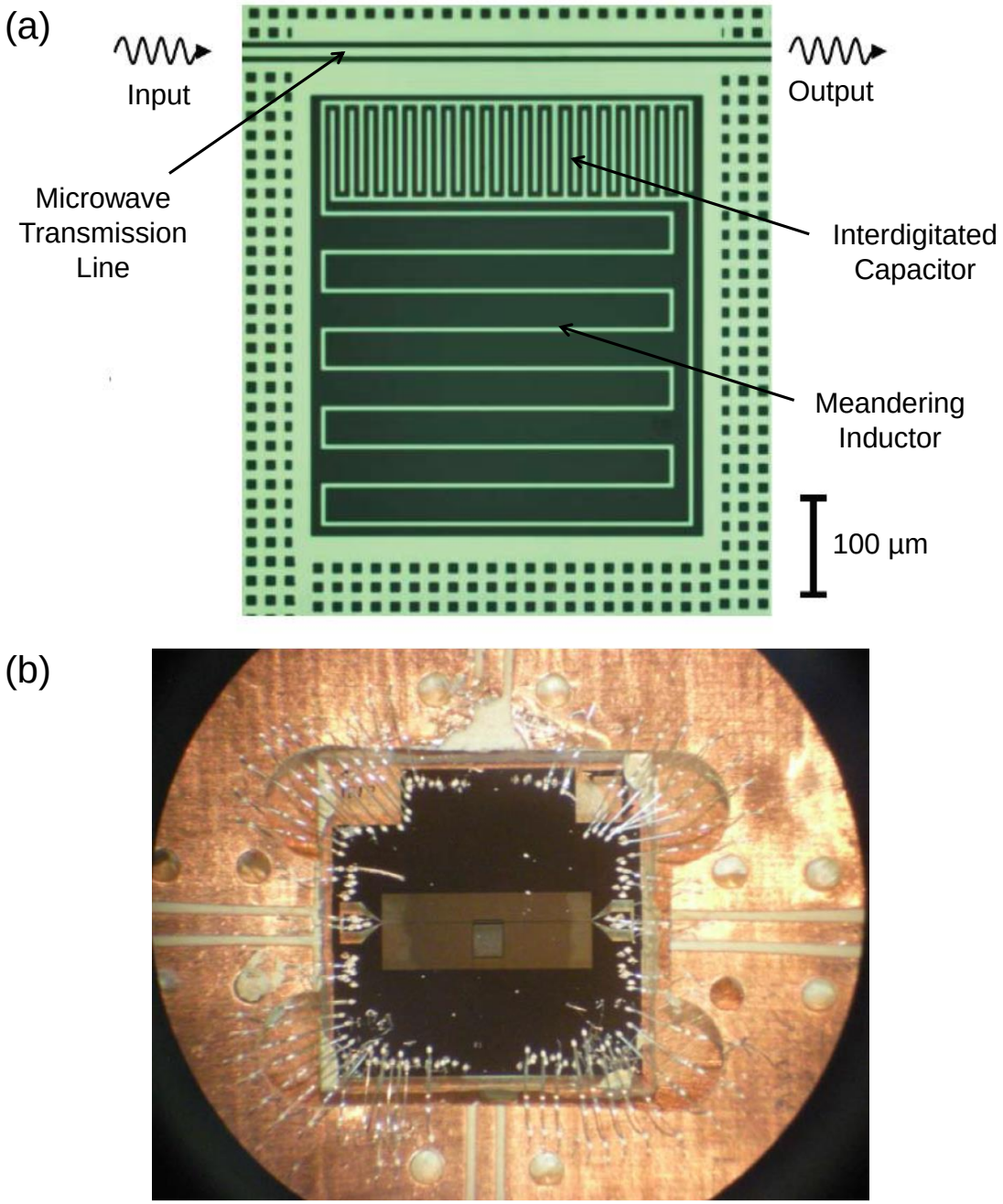

Fig 4.2 - (a) Micrograph of lumped element resonator LC1, made from thin film Al. The sapphire appears black on the image and the Al appears green. The square holes in the aluminum ground plane are for trapping magnetic flux vortices. (b) Micrograph of chip LC1 wire bonded to the PCB. The transmission line and the ground plane of the chip are electrically connected to the PCB with wire bonds. The resonator is visible in the middle of the image.

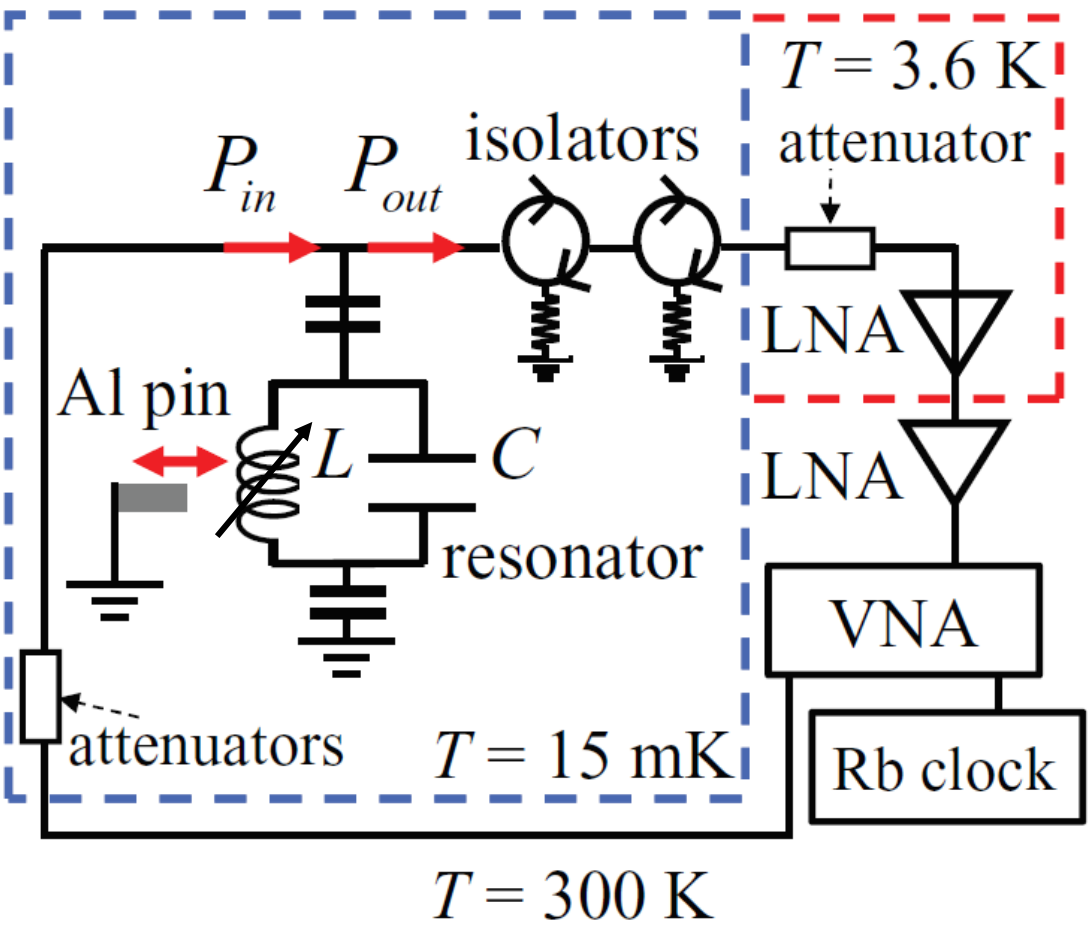

Fig. 4.3 - Setup for measuring the tuned LC resonator. The moveable aluminum pin turns the on-chip inductor L into a variable inductor.

The output microwave signal from the LNA was then sent to a room-temperature LNA and back to the measurement port of the VNA. The VNA reports S_{21}, which is the transmitted output voltage V_2 divided by the input voltage V_1. The VNA is referenced to a rubidium clock [4.15] so that it can supply an accurate and precise swept frequency.

The chip and PCB were mounted in a Cu sample box. A small hole in the top cover plate, positioned directly above the resonator, allowed a superconducting Al tuning pin to penetrate the sample box close to the Al resonator (see Fig. 4.4). Cu fabric was fixed around

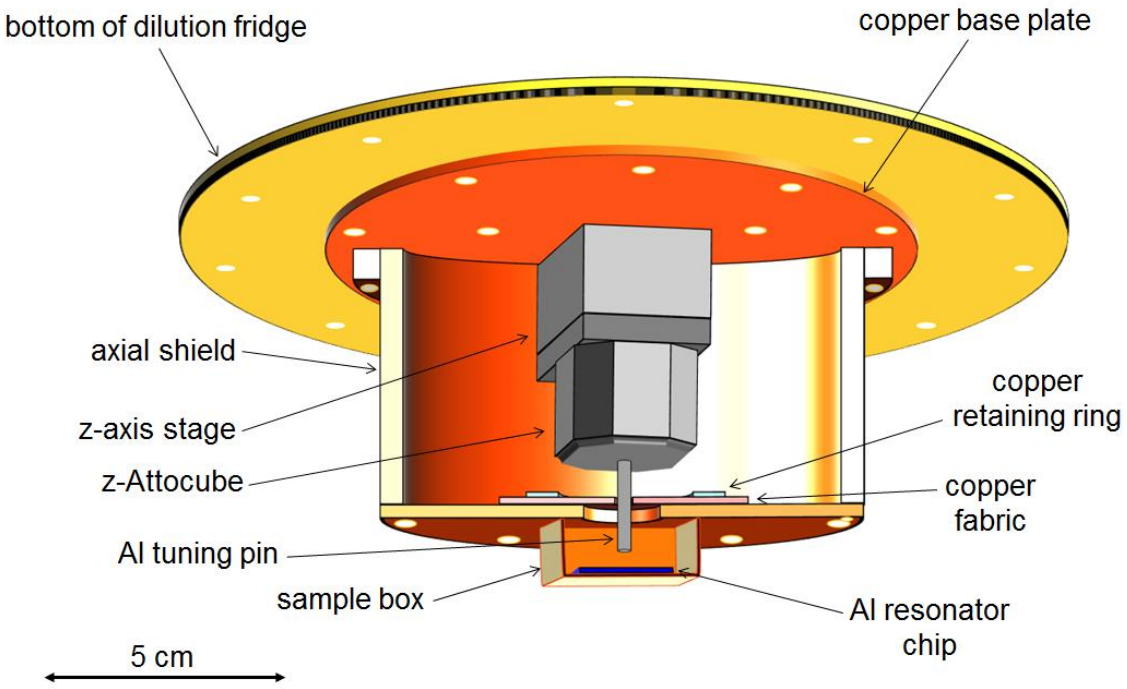

Fig. 4.4 - CAD drawing of the tuning pin system mounted on the mixing chamber plate of the dilution refrigerator.

the hole to make contact with the pin. The purpose of this fabric was to ground the pin, shield the resonator from external noise, and prevent power from the resonator form being radiated out of the sample box via coupling to the pin. The tuning pin was mounted to an attocube translation stage [4.8] that moves it in the z direction (along the pin axis). The attocube stage was attached to a Cu baseplate that was mounted to the dilution refrigerator (see Fig. 4.4). An axial shield was mounted to the Cu baseplate to shield the resonator from the high voltages used in the attocube.

Figure 4.5(a) shows a photograph of the 'winged' tuning pin. This pin was an improvement on the original cylindrical tuning pin, which was used in preliminary experiments described in ref. [4.7]. When positioned close to the chip, the wings contact

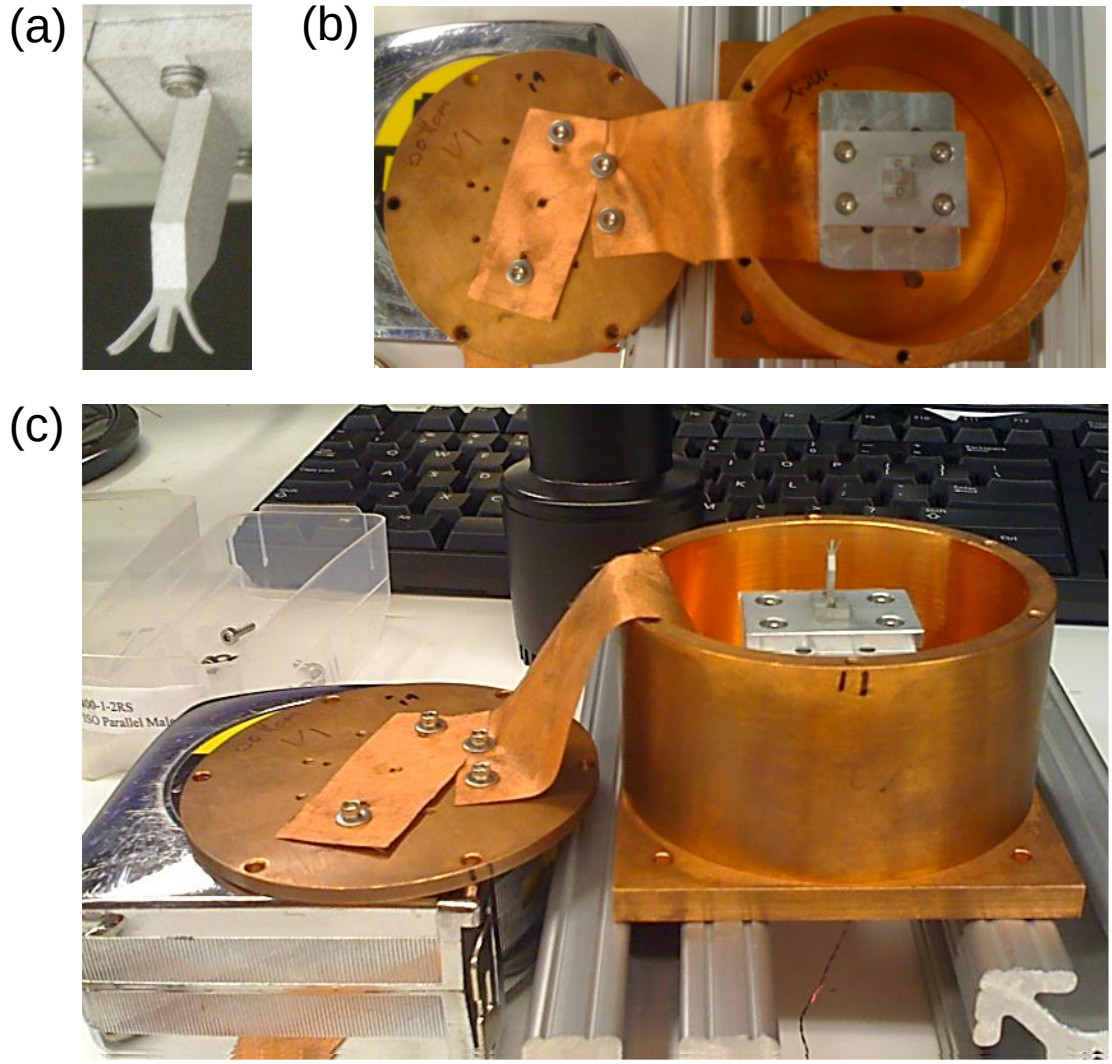

Fig. 4.5 - (a) Photograph of aluminum tuning pin with grounding wings, mounted to adapter plate. (b) Bottom view of pin mounted inside axial shield (on right) with copper fabric connecting bottom of the axial shield (on left). (c) Side view of pin mounted inside axial shield.

the aluminum ground plane on the sapphire substrate, grounding and mechanically stabilizing the pin.

Figure 4.5(b) shows a photograph of the copper axial shield, attocube, and pin, all inverted, before they were attached to the refrigerator. The bottom copper lid of the axial

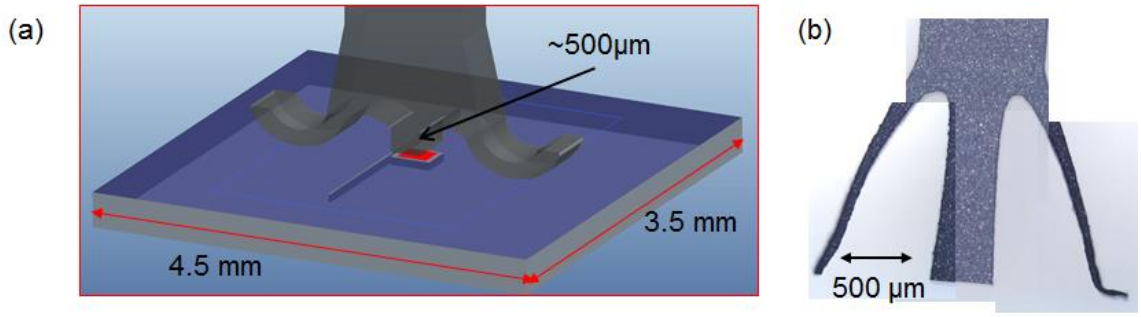

Fig. 4.6 - (a) CAD drawing of tuning pin with grounding wings in contact with sapphire chip (purple). The tuning pin head is just above the 500 x 500 μm resonator (red). (b) Composite photo stitched together from four microscope photos to show tuning pin.

shield (left side of photo) is mechanically, thermally, and electrically connected via copper fabric to the Cu baseplate. Also visible is the hole in the Cu fabric and base plate through which the tuning pin passes, contacting and grounding the pin. Fig. 4.5(c) shows a side view of this set-up.

Figure 4.6(a) shows a close-up 3D CAD drawing of the tuning pin. The end of the pin has a 500 μm x 500 μm flat face in the center that is large enough to cover the resonator chip area, which is slightly smaller than this. The illustration also shows the two thin grounding wings, which were designed to extend further than the central flat face of the pin, so that when they make contact with the aluminum ground plane on the sapphire chip, they bend slightly as the central pin gets closer to the resonator. Figure 4.6(b) shows a composite microscope photo of the tuning pin, which was fabricated using wire EDM, and Fig. 4.7 shows another photograph of the tip and wings.

In our initial resonator measurements using this pin, we found evidence of TLSs on the surface of the pin that were strongly coupling to the resonator. Figure 4.8(a) shows an image of the flat face of the tuning pin which shows obvious roughness (on the scale of 4.6 μm height differences) due to the wire-EDM fabrication process. The electric field lines

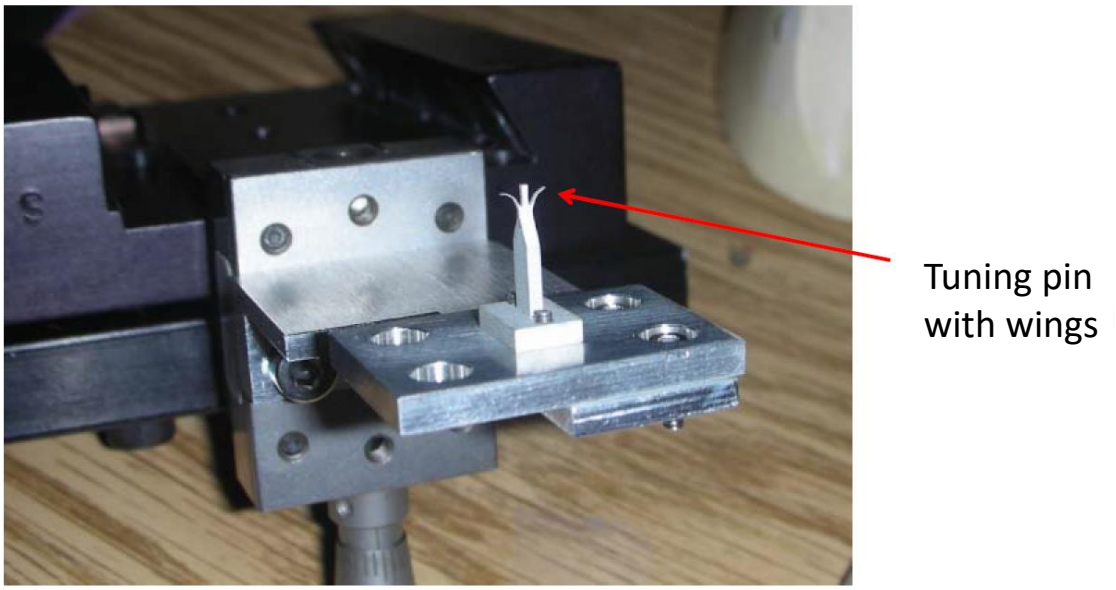

Fig. 4.7. - Photograph of tip and wings of the tuning pin (red arrow) on the polishing mount.

from the resonator would tend to be highly concentrated at the many small sharp points on the surface of the pin. This could allow strong coupling to individual TLSs that naturally occur in the aluminum oxide surface of the pin (discussed in Sec. 4.4). To combat this effect, we polished the pin with fine-grit diamond sandpaper. To keep the surface of the pin flat, we mounted the pin on a polishing mount (see Fig. 4.7). We gently bent back the wings so they did not make contact with the sandpaper, and then carefully repositioned them after the polishing. Figure 4.8(b) shows the surface roughness was reduced to about 0.7 μm. We found that this seemed to reduce the coupling of TLSs to the LC resonator, as discussed in Sec. 4.4.

(a)

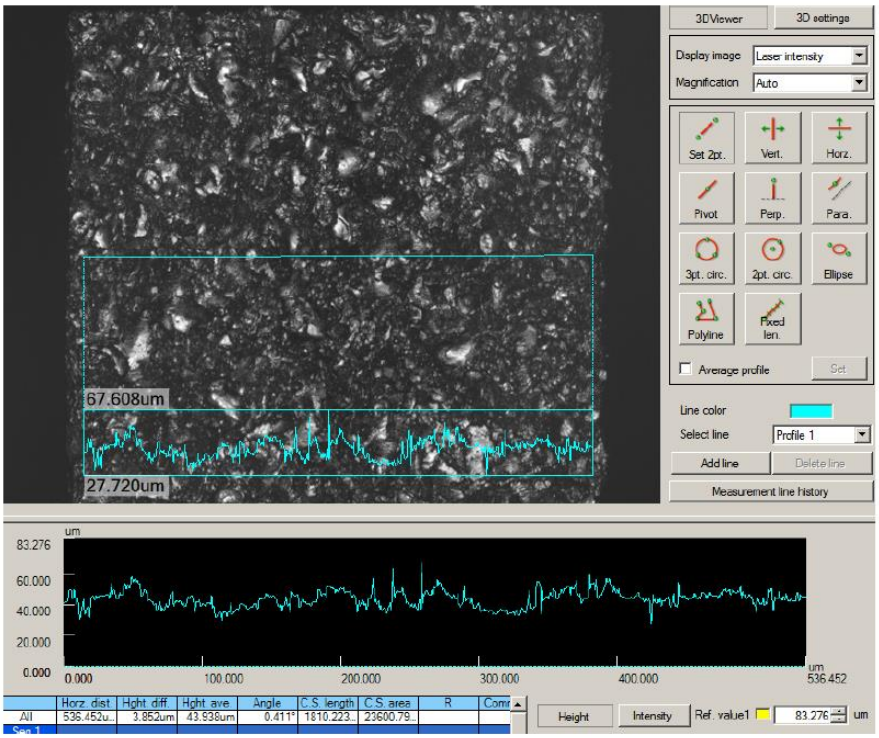

(b)

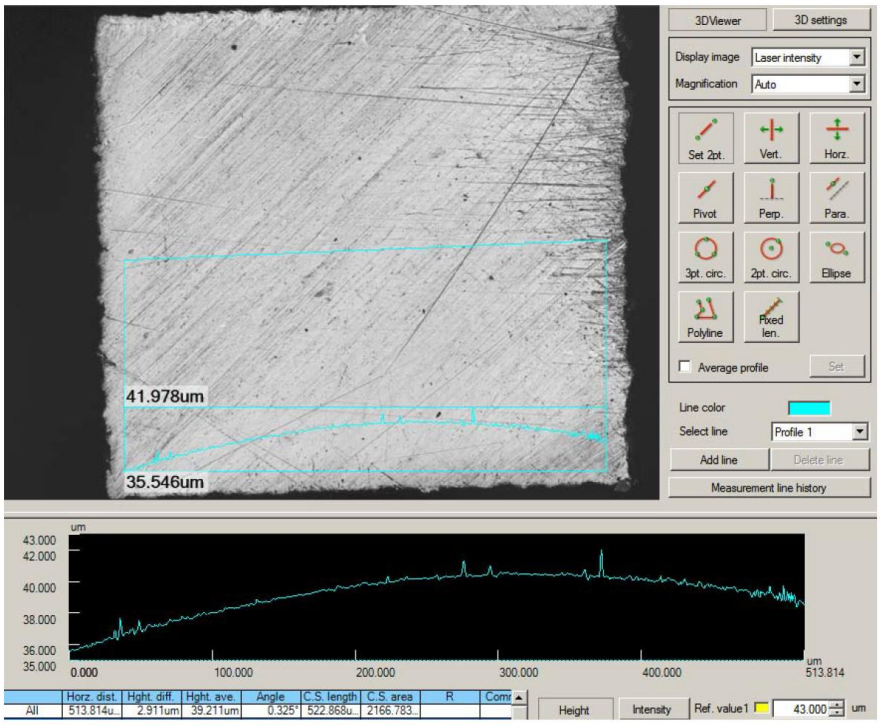

Fig. 4.8 - (a) Confocal microscope image of the bottom of the center flat face of the tuning pin (wings not shown). Blue traces show measured cross section profile has roughness of 4.6 µm. (b) Image of the same pin after polishing. Roughness of selected cross section profile is 0.7 µm.

4.4 Measurements of Resonator S_{21} and Tuning

At a temperature of 15 mK, we measured $S_{21}(f)$ near the 6.8 GHz resonance of LC1 and used the attocubes to vary the separation z between the tuning pin and resonator. For each value of z, Dr. Kim and I used a fitting code developed by Khalil *et al*. [4.16] to extract the resonance frequency f_r, internal quality factor Q_i and external quality factor Q_e from our $S_{21}(f)$ data.

Figure 4.9 shows a plot of the measured resonance frequency f_r for increasing pin-resonator distance *z*. The origin for the pin-resonator distance scale was estimated by comparing our data to an HFSS simulation of the pin and resonator (not shown here). In between each measurement the pin was moved by the piezoelectric attocube, which heats up the surrounding copper and the resonator, we leave time (about 40 min) for it to cool down again before measuring the resonator. Examination of the plot shows that the measured f_r increased as the pin approached the resonator, as expected from screening of the resonator's inductor by the pin. We were able to tune the simple lumped element over an impressive range of 137 MHz, and actually tuned right through the ^{87}Rb hyperfine transition frequency at 6.83468 GHz (indicate by red horizontal dashed line in Fig. 4.9). From the plot, we can see that the tuning becomes much more sensitive as *z* approaches 0, when the pin is close to the surface. The minimum step size of the attocubes is about 60 nm if we use 36 V drive pulses. Smaller drive voltages can yield smaller steps, but the motion is less repeatable. This step size yields a resonance frequency change of about 150 Hz for *z* values around 600 μm, while for small pin-to-resonator distances, the resonance frequency can change by more than 16 kHz per step, which is comparable to the resonators FWHM.

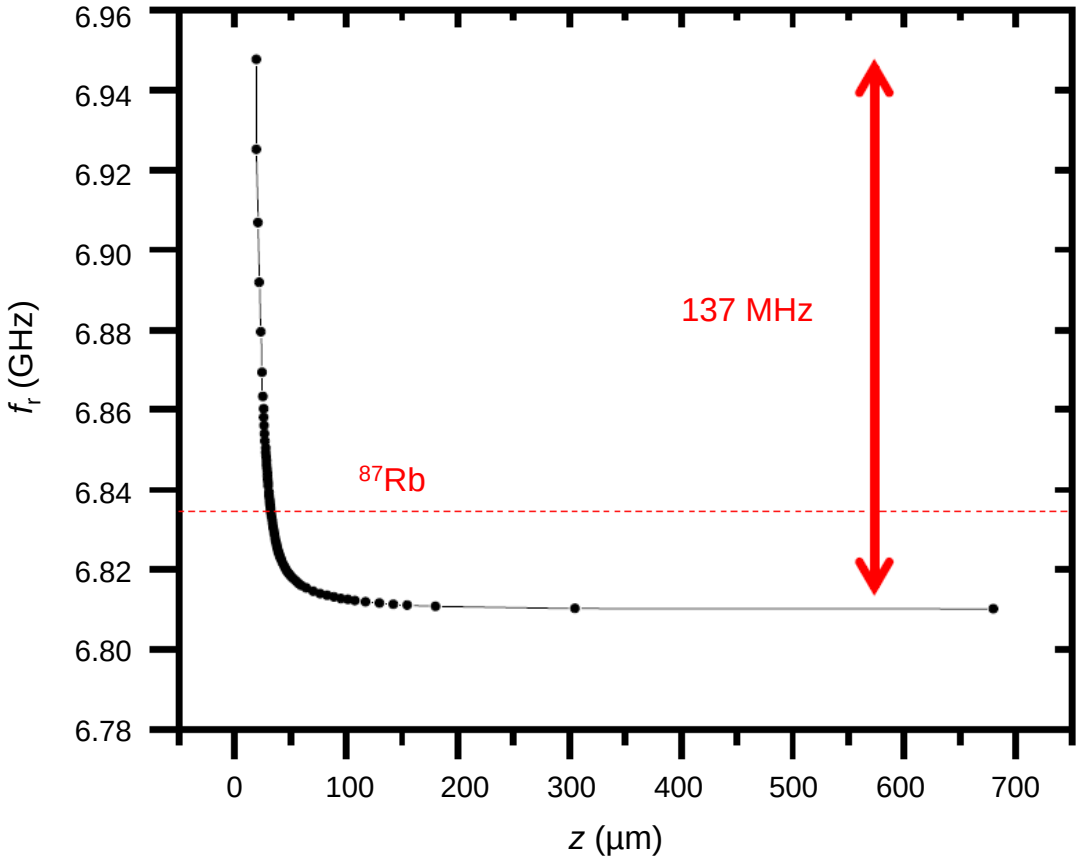

Fig. 4.9 - Resonance frequency extracted from fits to measured S_{21}(f), plotted as a function of nominal distance z between Al pin and resonator.

While Fig. 4.9 demonstrates our ability to tune the resonator's frequency through the ^{87}Rb transition, we are also concerned about maintaining a high Q in the resonator. In general, the tuning pin can act as an antenna, carrying away power from the resonator. In Figure 4.10(a), I plot the internal quality factor Q_i of the resonator as a function of z for several different RF powers. As is typical for dielectric loss from a distribution of two-level system defects [4.17-4.18], Q_i increases with increasing RF power. However, for each RF power, we see the same trend: starting from z = 700 μm and moving the pin closer, Q_i decreases. This decrease appears to be due to the resonator's coupling energy to the pin,

which then transmits it out of the system. The best evidence for this mechanism is the sudden jump at z = 70 μm where Q_i increased by about a factor of 4. This is where we expect the pin's wings made contact with the chip. This decreases vibrations of the pin and also reduces the ability of the pin to act as an antenna because it is now better grounded to the chip's ground plane. Further decreases in z cause Q_i to again decrease steadily as the pin continues to approach the resonator with the wings still in contact. Considering the loss, the best choice for z is where the wings first make contact with the chip, where Q_i is highest. However, this is a secondary consideration compared to the main purpose of the pin, which is for tuning.

Figure 4.10(b) shows a plot of the measured external quality Q_e as a function of z. Q_e measures coupling of the resonator to the input/output transmission line so one expects Q_e to be fixed by the configuration of the on-chip transmission line and the LC resonator. However, the pin not only screens the magnetic field of the LC resonator, but from this plot it also appears that there is significant coupling between the pin and the transmission line. Depending on the position and grounding of the pin, this can affect the impedance mismatch between the transmission line and the resonator, which would affect Q_e. In Fig. 4.10(b), we see that Q_e gets bigger as z gets smaller. However, in separate cooldowns, we saw the opposite effect (Q_e got smaller as z decreased), probably because the pin was aligned in a slightly different configuration or grounded differently. We also note that there is a jump in Q_e at z = 70 μm, when the wings make contact, although it is much less prominent than the jump in Q_i.

Although we only have a limited tuning range, it is important to understand that the pin was only meant to give fine tuning. Because lithography techniques can only be

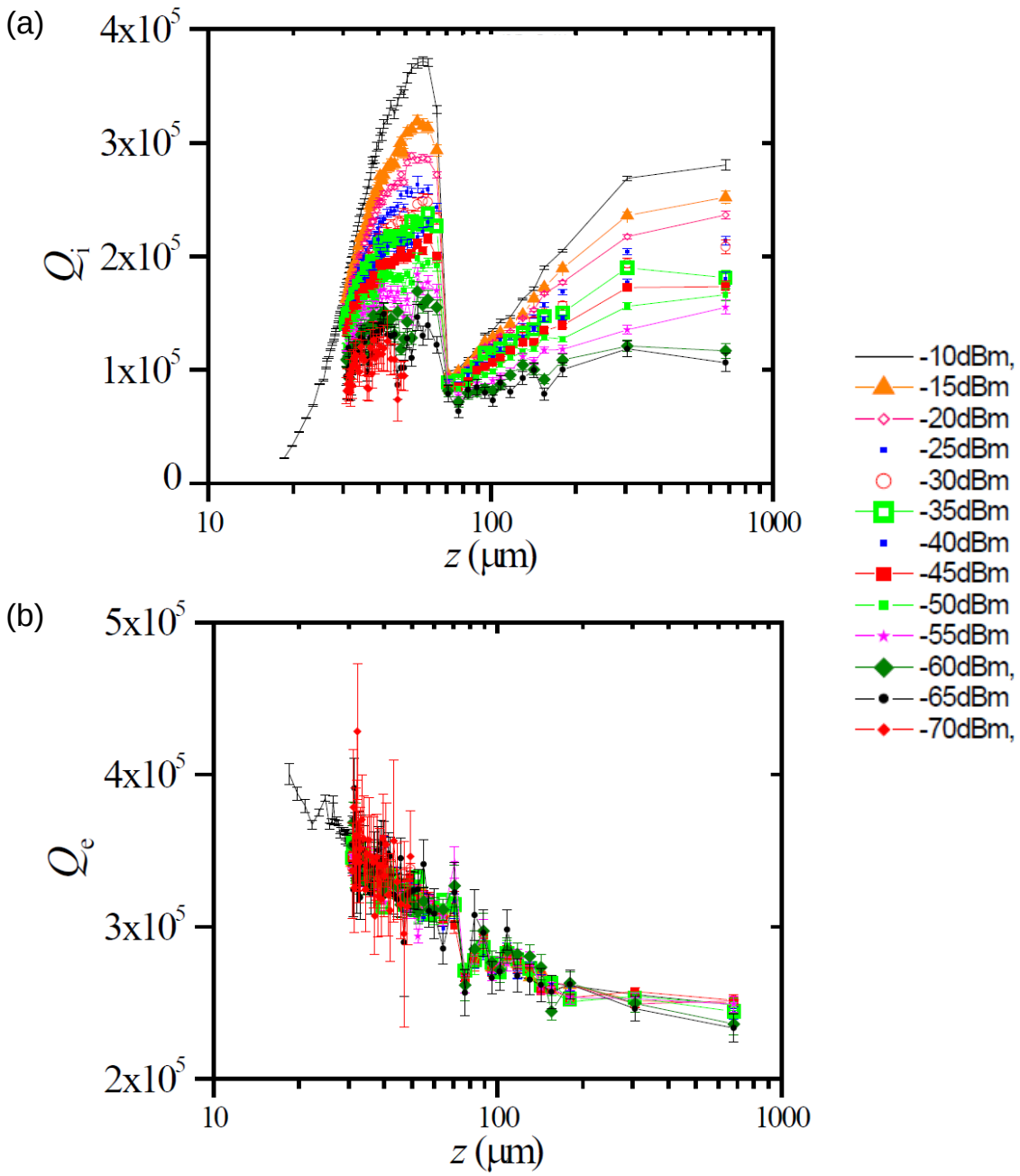

Fig. 4.10 - (a) Measured internal quality factor Q_i versus z, for multiple source microwave powers. Sudden change in Q_i at around z = 70 μm is due to contact of the tuning pin wings. (b) Measured external quality factor Q_e vs. z.

so precise, our nominally identical resonators typically had resonant frequencies f_r that differed by about 1%. To get around this problem, Kim *et al*. showed that the resonance frequency of a lumped-element LC resonator can be decreased in a controlled fashion by using e-beam lithography to add a partial capacitor finger to the IDC. Figure 4.11(a) shows an example where a partial aluminum finger has been added to a niobium resonator [4.7]. This increased the capacitance and decreased the resonance frequency by 36 MHz (about 0.5%). I emphasize here that that this is not the resonator LC1 described elsewhere in this chapter, but just an example of what can be done. Our simulations using Microwave Office software [4.19] show that adding a full 100 μm finger will decrease the resonance frequency by 80 MHz (see Fig. 4.11 (b)). With coarse tuning, one could try to set $f_r = f_{rb}$ near the pin position where Q_i is optimized (when the wings first make contact) or at a location where fine-tuning has a pre-determined sensitivity.

The data discussed above on resonator LC1 was all taken after the surface of the pin was polished. We also collected tuning data before the pin was polished (see Fig. 4.8 (a)) which showed some interesting features. For the unpolished winged tuning pin, we measured the resonator's internal loss $1/Q_i$ at various RF source powers P for many pin positions. As the pin moved, the resonance frequency varied. In Fig. 4.12, for each RF source power, we plot the relative loss, which is the measured $1/Q_i$ at the given power minus $1/Q_i$ measured at -5 dBm source power (with -82 dB attenuation in the input lines) as a function of f_r. For this data set, the tuning wings did not make contact with the ground plane of the chip. For the lowest source power of -60 dBm (green diamonds in the plot), the relative loss is consistently higher and there are several sharp peaks. For increasing RF source power the peaks become smaller and broader. This is clear evidence of TLSs (see

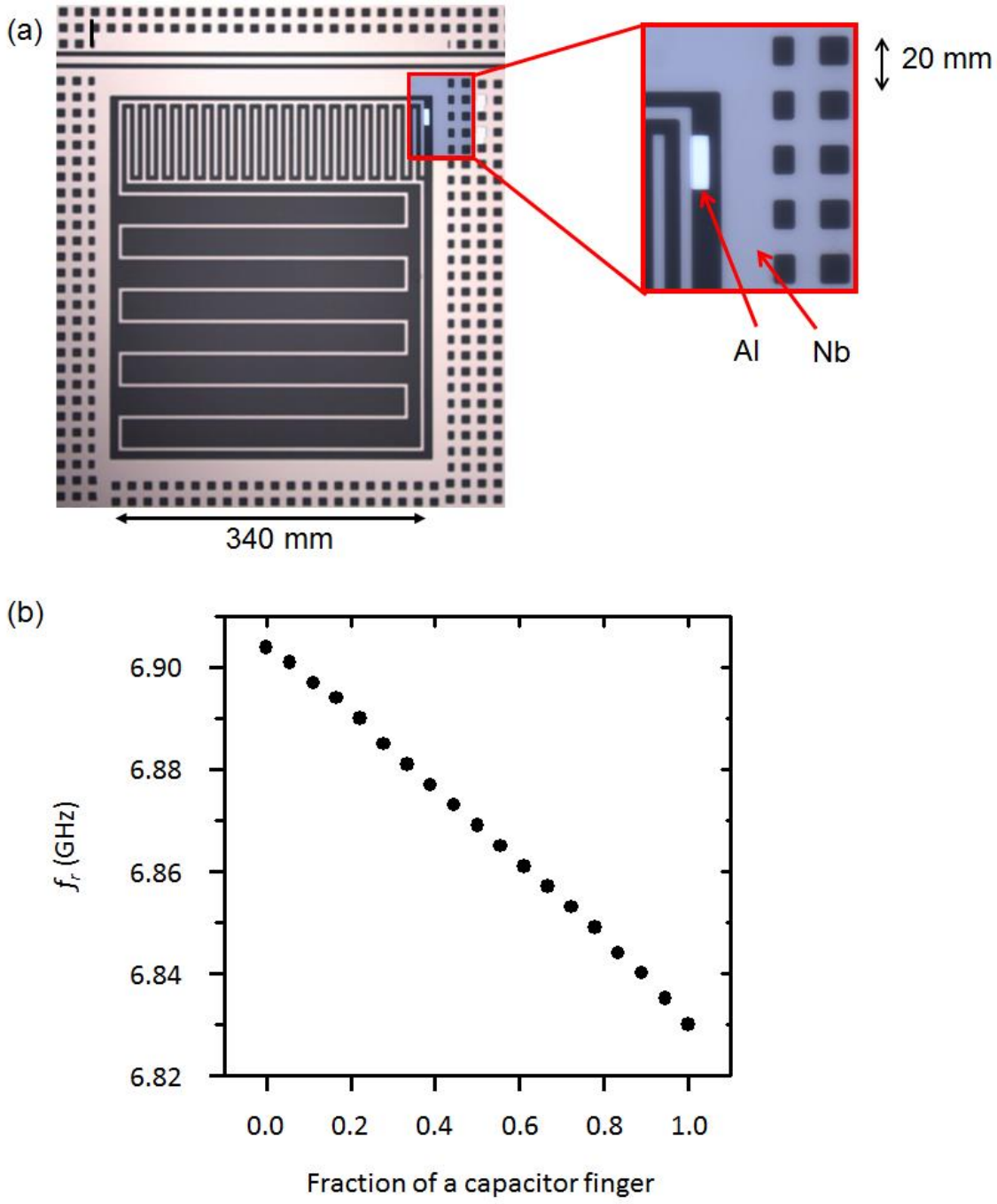

Fig. 4.11 - (a) Photograph of Nb lumped-element LC resonator from ref. [4.7] - note that this is not resonator LC1. Inset shows addition of partial Al tooth to the last tooth in the interdigitated capacitor (IDC). (b) Simulation of the resonance frequency versus the fractional length of an added finger on the IDC. Adding a full finger gives a 80 MHz decrease in the resonance frequency of the 6.8 GHz resonator.

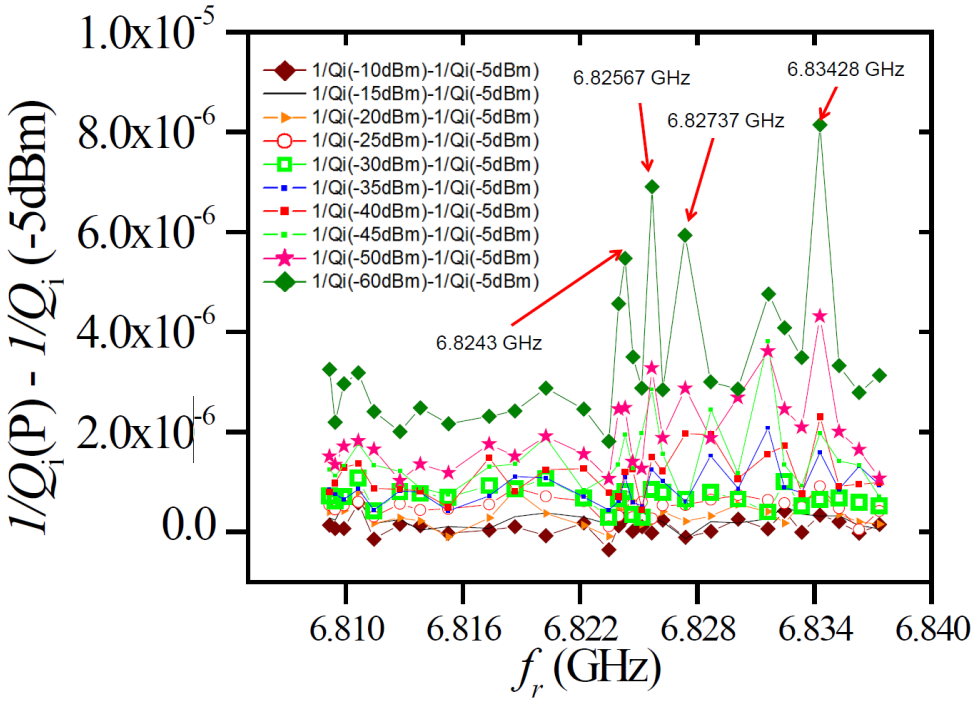

Fig. 4.12 - Plot of residual loss $1/Q_i(P)-1/Q_i$ (P_o) versus resonance f_r frequency for different powers P, where P_o = -5 dBm of source power at the VNA. The power-dependent peaks are due to absorption from individual TLS resonances on the surface of the Al pin. Saturation of the peaks occurs at higher powers, as expected for TLSs. The peaks are more obvious at higher resonator frequencies, where the pin was closer to the resonator and gives stronger coupling between the resonator and TLSs on the surface of the pin.

Ch. 2), which saturate at high power and undergo power-broadening. With this interpretation, each peak in the internal loss corresponds to an individual TLS that couples to the resonator as the resonator's f_r is tuned through the transition frequency of that TLS. Tuning the resonator to a TLS transition allows the TLS to absorb some of the resonator's energy, causing the resonator's internal loss $1/Q_i$ to increase.

The fact that we see more peaks at high resonance frequency, when the pin is close, is consistent with the TLSs being on the surface of the pin. Two-level systems outside of the resonator are not technically "internal", but in our model of S_{21} the external loss is only due to coupling to the transmission line - all other loss is incorporated into the internal loss.

The rough surface of the unpolished pin (see Fig. 4.8) had many sharp points where the electric field lines from the resonator would have converged. Individual TLSs that were near a sharp point would be more strongly coupled to the resonator (see Ch. 2). This expected behavior was consistent with our observations, which showed far less pronounced peaks in the internal loss after the experiment was repeated with a pin that had its surface polished (see Sec. 4.2 and Fig. 4.10).

4.5 Conclusions

In this chapter I explained why we needed a microwave resonator that can be tuned close to the hyperfine transition frequency of ^{87}Rb. Our tuning technique involves placing a moveable superconducting aluminum pin close to a thin-film superconducting LC resonator so that it screens the inductance. I described the experimental setup inside the dilution refrigerator, which had the pin attached to an attocube translation stage that held the pin closely above the LC resonator. Our data showed that we could tune the resonator over a range of 137 MHz with a precision of 0.150 to 16 kHz/step depending on the resonator-pin distance. In particular, this suggests that with proper positioning of the pin, the resonance frequency could be tuned to within 150 Hz of the ^{87}Rb hyperfine position. This is just a few times larger than the $\lambda \sim 40$ Hz coupling of the resonator to a single ^{87}Rb atom. To increase the tuning precision, we simply need to increase the pin distance. We could design or carefully bend the tuning wings to be slightly longer so that they make contact with the chip, and increase Q_i for larger pin distances where tuning sensitivity is highest. In order for the resonator to work better in an atom-transmon hybrid system, it would help to increase the Q of the resonator to greater than 10^6, as discussed in Sec. 4.2.

This is possible and has been demonstrated by other groups [4.20], although not in a tunable system.

Using an unpolished pin, we measured Q_i as a function of pin distance for various RF powers. One remarkable result from this experiment was that we were able to see resonances from TLSs and determine that they were on the end of the pin because the resonances went away when the pin was moved far from the resonator. This suggests that this approach could be used to probe TLSs in other materials, with the surface of the pin serving as a sample stage. Other materials that would be interesting to measure include sapphire and Si substrates, which are used for qubits, low-loss dielectric thin-films such SiN, and low-loss superconductors such as TiN.

Chapter 5: Detecting Capacitive and Dipole-Coupled Two-Level Systems in a Thin-Film Superconducting Microwave Resonator

5.1 Introduction

In glassy dielectric insulators at low temperatures, physical properties such as the heat capacity, microwave dielectric loss, and ultrasonic attenuation can be dominated by the behavior of two-level system defects [5.1-5.6]. Over the last decade, such two-level systems (TLS) have also been found to produce undesirable effects in superconducting qubits, including unexpected avoided level crossings (ALC) in the transition spectrum, energy relaxation, dephasing, loss of readout fidelity, loss of gate fidelity, and random telegraph noise or drift in system parameters [5.7-5.11]. TLS related effects have also been observed in low-loss thin-film superconducting resonators [5.12, 5.13], which are now commonly being used for circuit-QED based qubit readouts [5.14] and microwave kinetic inductance detectors [5.15-5.17]. Resonators are sensitive to TLS induced loss [5.6, 5.7, 5.18] and this has made them useful for detecting TLSs and studying their behavior [5.6, 5.7, 5.19-5.21]. The two-level systems of interest are generally understood to be atomic scale ionic defects, such as OH^-, which occur in dielectric thin films from which the devices are constructed. These defects can tunnel between two locations, and couple to the electric field or strain field [5.19, 5.22-5.24]. Recent work has largely confirmed this model, which was first proposed by Phillips [5.1], and extended it to include quantum coherent behavior and the single-photon regime.

In this chapter, I report observations of random-telegraph noise [5.25, 5.26] in the resonance frequency of a thin-film superconducting resonator and argue that it is due to coupling to individual two-level-systems (TLS). In particular, I find that the fluctuations are not consistent with the "standard" electric-dipole coupling model considered by Phillips and others (see Ch. 2). Instead they are consistent with the presence of an additional coupling term in the resonator-TLS Hamiltonian that changes the capacitance of the resonator depending on the TLS state. For clarity, I will call a TLS with such coupling a capacitive TLS or cTLS. Standard TLS coupling can be distinguished by the effect it has on the resonator spectrum. For example, TLSs can produce avoided level crossings when they are dipole-coupled to a tunable resonator or qubit, and the presence of avoided level crossings has been one of the main approaches used to identify the presence of TLSs [5.8, 5.27-5.29]. In contrast, a cTLS need not produce a conventional avoided level crossing and thus need not show up in a spectroscopic search for avoided level crossings.

Here I only consider dipole-coupled TLSs and cTLSs, while ignoring other well-known types that have behavior that appears to be inconsistent with our observations. For example, I can exclude hopping magnetic vortices [5.30-5.33] from further consideration because we observe TLS behavior that is sensitive to static electric field, which is difficult to reconcile with vortices, which are neutral. Similarly, I can exclude critical current fluctuators [5.34-5.37] because our measurements are on resonators that did not contain Josephson junctions. On the other hand, an inductance fluctuation in an LC resonator would produce effects that would be very similar to those produced by a capacitance fluctuation. Moreover, ferromagnetic-paramagnetic fluctuations in coupled spins [5.38-5.40] have been identified as the underlying cause of a ubiquitous low-temperature 1/f magnetic flux

noise in superconducting devices [5.41]. Here we exclude this mechanism because this 1/f flux noise is not known to depend on static electric field and typically does not display distinct random telegraph noise due to the switching of individual TLSs.

In the next section, I introduce the theory for the transition spectrum of a resonator that is capacitively coupled to a charged tunneling cTLS. I identify interesting features of the spectrum, including one that can be used as a signature of a cTLS. In Sec. 5.3, I expand this theory to look at the transition spectrum of a resonator coupled to two non-interacting cTLSs. Section 5.4 then describes our thin-film Al resonator and the measurement apparatus. In Sec. 5.5, I present our observations of the resonance frequency and quality factor of a resonator as a function of applied dc electric field and discuss evidence for the presence of TLSs. I then discuss my procedure for identifying voltage biases where random telegraph noise appears in the resonator transition frequency. In Sec. 5.6, I discuss my analysis of the fluctuations and, based on this analysis, I argue that the observed frequency shifts are inconsistent with standard dipole coupling but compatible with a cTLS. Finally, in Sec. 5.7 I conclude with a discussion of some of the implications of these findings.

5.2 Theory of a cTLS Coupled to a Resonator

A cTLS couples differently to a resonator than a standard electric-dipole coupled TLS (see Sec. 2.4) and has a different effect on the resonator. To model a cTLS, I again consider a TLS with charge q and mass m , but we now assume it is moving in a double-harmonic potential [5.42] (see Fig. 5.1). When the charge is in the left well it experiences a quasi-harmonic potential with harmonic frequency ω_L and spring constant $k_L = m\omega_L^2$. In

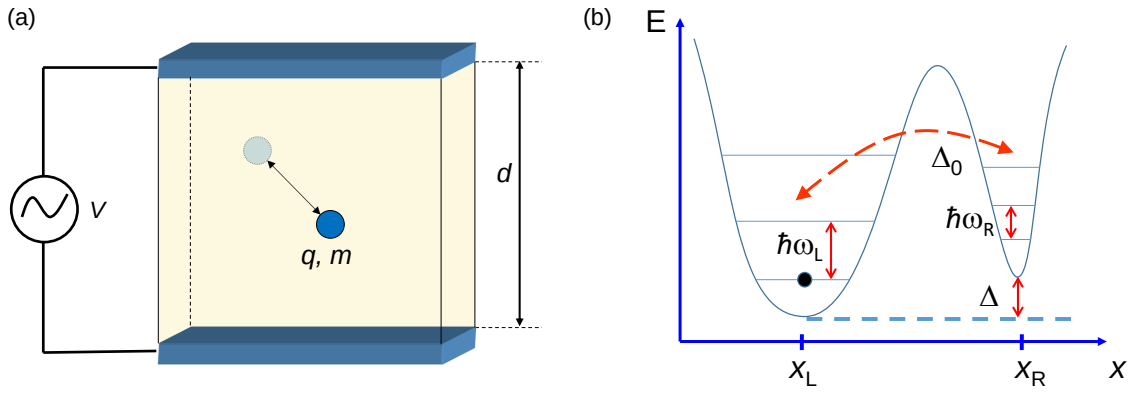

Fig. 5.1 - (a) Two-level system modelled as a charge hopping between two locations in an electric field between two capacitor plates. (b) Double-well potential as a function of position as seen by the charged particle. Left well has energy levels separated by $\hbar\omega_L$ and right well has energy levels separated by $\hbar\omega_R$. Potential energy difference between minima of the two wells is Δ and tunneling energy between the wells is Δ_0.

the right well it has a harmonic frequency ω_R and spring constant $k_R = m\omega_R^2$. If such a TLS is placed between the plates of a capacitor and a small voltage of amplitude V_0 is applied across the plates, an electric field $\vec{E}_0$ will be created at the location of the TLS. If V_0 is sufficiently small, and the TLS stays in the left well for example, the charge will be displaced from equilibrium by

$$\delta\bar{x} = q\bar{E}_0 / m\omega_L^2 \,. \tag{5.1}$$

Using Green's reciprocation theorem [5.43], the displacement of the charge q can be shown to induce a small charge δq on the capacitor plate given by [5.44]:

$$\delta q = \frac{q\bar{E}_0 \bullet \delta\bar{x}}{V_0} \quad . \tag{5.2}$$

If the TLS is in the left well, this induced charge leads to a contribution C_L to the effective capacitance of the capacitor given by $C_L = \delta q/V_0$. Inserting Eq. (5.1) and (5.2) into this expression gives

$$C_L = \frac{q^2}{m\omega_L^2}\frac{\left|\bar{E}_o\right|^2}{V_o^2} \approx \frac{q^2}{md^2\omega_L^2}\ , \tag{5.3}$$

where in the last step we have assumed a parallel plate capacitor with distance *d* between the plates.

When the TLS is in the right well, we find a similar expression, but with ω_L replaced by ω_R. If the TLS is in a capacitor, with total capacitance *C*, in a resonator with resonance frequency f_r, which is much less than $\omega_L/2\pi$ or $\omega_R/2\pi$, the resonance frequency will shift by $\delta f_r / f_r \approx -\delta C/2C$ for small $\delta C << C$. Therefore, the change in the resonance frequency is

$$\delta f_r \approx -\frac{f_r q^2}{2md^2C}\left(\frac{1}{\omega_L^2}-\frac{1}{\omega_R^2}\right) \tag{5.4}$$

when the TLS moves from the right well to the left well. From Eq. (5.4), we see that δf_r may be positive or negative, depending on whether the right well or left well has a higher frequency. Note that if ω_L and ω_R are nearly equal, or if ω_L and ω_R are sufficiently large, then a cTLS will have little effect on the resonance frequency. In general, a charged TLS could have a standard electric-dipole-coupling term as well as a piece that causes a shift in the capacitance, and in principle either could be dominant.

The above discussion has been semi-classical. To understand the effect on the transition spectrum, we need to examine the system Hamiltonian. The effective Hamiltonian for a resonator coupled to a double-harmonic potential TLS can be written as:

$$H = H_0 + H_{d2} + H_c \tag{5.5}$$

where H_{d2} and H_0 are given by Eqs. (2.39) and (2.46), respectively, and in the right-left TLS basis the capacitive coupling term H_c between a cTLS and the resonator can be written

as simply:

$$H_c = \frac{h\delta \mathrm{f}_r}{2}\left\{n+\frac{1}{2}\right\}\otimes\sigma_z \ . \tag{5.6}$$

Here, n is the number of excitations in the LC resonator and we ignore any anharmonicity of higher levels associated with the left and right well. The effect of H_c is very simple, it just shifts the resonance frequency by $\delta \mathrm{f}_r$, depending on whether the TLS is in the right or the left well.

To find the transition spectrum, I treat H_c as a weak perturbation on H_0 and consider the weak-dipole-coupling limit, as I did in Sec. 2.4, where $|\gamma| << 1$ and $|\mu| << 1$. To lowest order in $|\gamma|$ and $|\mu|$, first order perturbation theory gives a shift in the energy levels of:

$$\begin{aligned} E'_{n,e} - E_{n,e} = -\left(E'_{n,g} - E_{n,g}\right) &= -\frac{h\delta \mathrm{f}_r}{2}\left(\left\langle \varphi_{n,g}\middle| n \middle|\varphi_{n,g}\right\rangle + \frac{1}{2}\right)\left\langle g\middle|\sigma_z\middle|g\right\rangle \\ &= h\left(n+\frac{1}{2}\right)\frac{\delta \mathrm{f}_r}{2}\frac{\Delta}{\sqrt{\Delta^2+\Delta_o^2}} \end{aligned} \tag{5.7}$$

The dispersive shift of the n-to-n+1 transition of the resonator is then:

$$2\chi_n = \frac{1}{h}\left(E'_{n+1,e} - E'_{n,e}\right) - \frac{1}{h}\left(E'_{n+1,g} - E'_{n,g}\right) \approx \delta \mathrm{f}_r \frac{\Delta}{\sqrt{\Delta^2+\Delta_o^2}} \tag{5.8}$$

Since δf_r may be positive or negative, depending on which of the two TLS potential wells is more compliant, Eq. (5.8) thus gives the unsurprising result that the dispersive shift may be positive or negative. Thus a cTLS in its excited state may cause the resonator to have a higher resonance frequency than when the cTLS is in its ground state. This is a key result because, in contrast, exciting a standard dipole-coupled TLS only decreases the resonator's transition frequency if $f_{\mathrm{TLS}} < f_r$.

Provided H_c is not too small compared to H_{d2}, numerical simulations of the

Hamiltonian confirm that the dispersive shift can be of either sign for a wide range of coupling strengths. Although the discussion above is only valid for resonator resonance frequencies f_r much less than $\omega_L/2\pi$ and $\omega_R/2\pi$, we note that this does not imply that f_{TLS} must be less than f_r. However, we are particularly interested in cTLSs with $f_{TLS} \sim k_B T << f_r$. Such cTLSs can be thermally activated and could cause random telegraph noise, as discussed below.

Note also that $2\chi_n$ in Eq. (5.8) is independent of n for the approximations we have made. This is the dispersive shift that we would measure experimentally if the cTLS was thermally excited from its lowest energy state $|g\rangle$ to its highest energy state $|e\rangle$. From Eq. (5.8) we also see that in the limit that $\Delta \ll \Delta_0$, the dispersive shift vanishes. In this case the minima of the double well potential would be nearly equal and the particle would tunnel rapidly between the left and right wells for both the ground and excited wave functions. This would give same the capacitance for the ground and excited state. The opposite limit, where $\Delta \gg \Delta_0$, gives $2\chi_n \sim \delta f_r$. So in this limit, Eq. (5.4) determines the maximum shift in the resonance frequency, while increasing Δ_0/Δ results in a steady decrease in $2\chi_n$.

To get some feel for the expected size of the dispersive shift, Table 5.1 shows results from evaluating Eq. (5.4) and (5.8) for a tunneling electron and an OH^- rotor in the limit where $\Delta \gg \Delta_0$ and $2\chi_n \sim \delta f_r$. Here I have assumed f_r = 6.8 GHz, C = 220 pF, $\omega_L = 2\pi$*15 GHz and $\omega_R = 2\pi$*50 GHz for both the tunneling electron and for the rotor. There is nothing intrinsic about these values and they have been selected merely to illustrate the magnitude of the effect. For a tunneling electron, I have taken d = 5 μm, which is characteristic for the spacing between the fingers in the thin-film interdigitated

Table 5.1 - Example of potential values of cTLS parameters that would result in a dispersive shift $2\chi_n$ of 1 to 2 kHz in the $\Delta \gg \Delta_0$ limit in a 6.8 GHz LC resonator. Final column calculated using Eq. (5.4).

TLS type	**q (C)**	**C (fF)**	**$\omega_L/2\pi$ (GHz)**	**$\omega_R/2\pi$ (GHz)**	**m (kg)**	**d (μm)**	**δC (zF)**	**$2\chi_n \sim \delta f_r$ (kHz)**
Tunneling e^-	1.60×10^{-19}	220	15	50	9.11×10^{-31}	5	115	-1.78
OH^- rotor	1.60×10^{-19}	220	15	50	1.67×10^{-27}	0.1	157	-2.43

capacitors of our superconducting resonators. This gives a capacitance change $\delta C = C_L - C_R \sim 100$ zF and a resonance frequency shift of $\delta f_r \sim -1$ kHz when the TLS moves from the excited state to the ground state. For a dangling OH^- bond that acts as a rotor, we assume that it could be located at the edge of a sharp feature at the edge of the thin film, where the electric field would be enhanced due to fringing effects. In this case, I chose $d = 0.1$ μm as the distance across which the voltage drops, in order to get a δf_r of roughly 2 kHz.

Note that these choices yield a roughly 0.5 ppm change in the resonance frequency, which is the approximate size of the effect we observed, as I discuss in Sec. 5.6. I also note that these estimated capacitance changes are much smaller than those found by studies done by the Ashoori group [5.45-5.49] who used a single-electron transistor to observe charging and discharging of individual defects in SiO_2. However, such a charging-discharging capacitance is due to the charge tunneling between the two wells as an external potential is swept, with the tunneling occurring when the wells are nearly degenerate. The resulting physics is that of Sec. 2.4 rather than the cTLS behavior discussed here.

Another implication of Eq. 5.8 is that the magnitude of the dispersive shift would not change if the cTLS were tuned through the resonator's transition frequency f_r. We also

note that since the energy level shifts in Eq. 5.7 arise from a first order perturbation from H_c, it does not involve level repulsion and does not result in an avoided level crossing in the spectrum. Thus, unless H_{d2} is also present and sufficiently large, a spectroscopic search for avoided level crossings may miss the presence of a cTLS.

5.3 Theory of Two cTLSs Coupled to a Resonator

In reality, there can be many TLSs coupled to the same resonator, with different types and strengths of coupling. Here, I consider two cTLSs coupled to a resonator, but not coupled directly to each other. In Fig. 5.2(a), both cTLS 1 and cTLS 2 are represented by a double well potential. For both cTLSs, I have chosen the left wells to have a higher resonance frequency ($\omega_L > \omega_R$) and to be at a higher potential. However, I could have modeled a cTLS with $\omega_R > \omega_L$ or a cTLS with the right well at higher potential.

In this example, I assume both cTLSs are coupled to a resonator. I also assume that the transition frequencies f_{TLS1} and f_{TLS2} of the TLSs are much less than the resonance frequency f_r of the resonator and small enough that the TLS can be thermally excited, i.e. hf_{TLS1} and hf_{TLS2} are comparable to k_BT. I also assume that the tunneling energies are $\Delta_{0(1)} << \Delta_1$ and $\Delta_{0(2)} << \Delta_2$, and that in the state $|g\rangle$, each cTLS is most likely to be in the right well, while in the state $|e\rangle$, each cTLS is most likely to be in the left well. Figure 5.2(b) shows the four possible configurations of the two cTLS. When TLS 1 is in the right well, it adds more capacitance to the resonator than when in the left well because $\omega_R < \omega_L$. This is true for TLS 2 as well. In the $|gg\rangle$ state (red), the resonator would have the largest possible added capacitance and therefore yield the lowest resonator resonance frequency of the four possible states. In the $|ee\rangle$ state (magenta) the resonator would have the highest

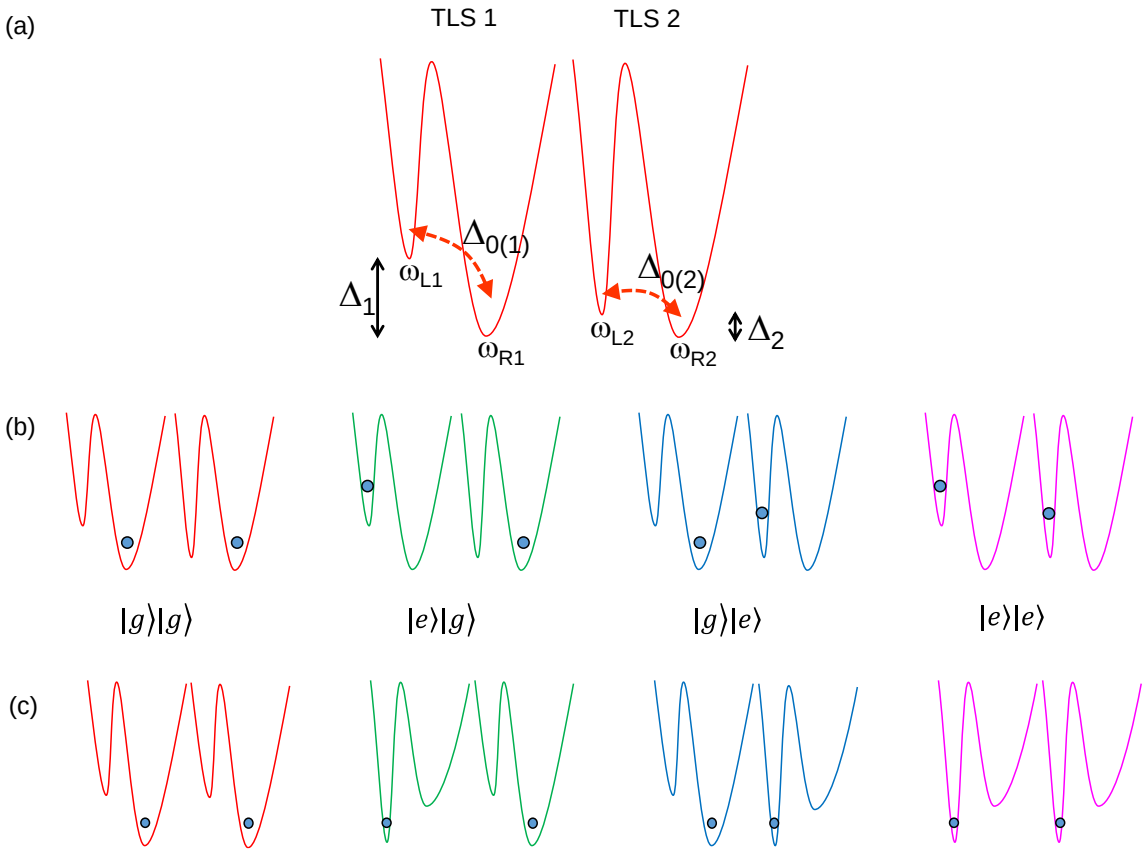

Fig. 5.2 - (a) Two non-interacting cTLSs. Each cTLS moves in a double well potential and has an associated frequency for its left (ω_{L1}, ω_{L2}) and right (ω_{R1}, ω_{R2}) wells. As with a standard dipole-coupled TLS, each double well potential has an asymmetry energy (Δ_1, Δ_2) and a tunneling energy ($\Delta_{0,1}$ and $\Delta_{0,2}$). (b) The four possible states of the two-cTLS system. (c) Comparing the potential energy diagrams to those in (b) shows how each cTLS's asymmetry energy would have to be tuned by applied dc voltage, so that the states occupied in (b) become the ground state and the energy difference to the excited state becomes larger. This which would suppress thermal fluctuations. Thus, for example, the left well of the left TLS must be lowered and the left well of the right TLS must be raised for $|e\rangle|g\rangle$ to become the ground state (green) with suppressed thermal occupancy of the higher energy states.

resonance frequency.

If a dc voltage is applied across the capacitor, it will shift the asymmetry energy of a given cTLS by an amount that depends on the strength of the local dc electric field, the shape of the cTLS double-well potential, and the orientation of the cTLS potential wells

relative to the direction of the dc electric field. Figure 5.2(c) shows how each cTLS's asymmetry energy must change in order for the corresponding state in (b) to become the ground state with reduced thermal occupancy of the higher energy. The main point here is that, unlike a "standard" dipole-coupled TLS, if the asymmetry energy Δ is tuned such that the TLS gets stuck in one well or the other, it still contributes to the resonator's capacitance, with the contribution depending on the curvature of the well that the TLS is in, rather than how detuned the resonator is from the TLS transition. This is very different behavior than found when one tunes through an avoided level crossing.

5.4 Experimental Set-up

The experimental setup is shown in Fig. 5.3 and a photo of the high-Q superconducting resonator is shown in Fig. 5.4. The superconducting resonator was mounted in a copper sample box that was attached to the mixing chamber stage of an Oxford Instruments Triton 200 dilution refrigerator with a base temperature of 12 mK. The microwave lines and all components were impedance matched to 50 Ω. An input microwave signal V_1 was applied by an Agilent E5071C vector network analyzer (VNA) [5.50] which was locked to a Stanford Research Systems FS725 frequency standard [5.51].

The input line has several attenuators at the refrigerator's different temperature stages to decrease Johnson-Nyquist noise and prevent external noise from the room-temperature environment from reaching the resonator. At the mixing chamber stage, an Anritsu 0.1 to 60 GHz bias tee [5.52] allowed us to apply a voltage bias to the center of the transmission line. This dc voltage V_{dc} produces an electric field at the resonator that

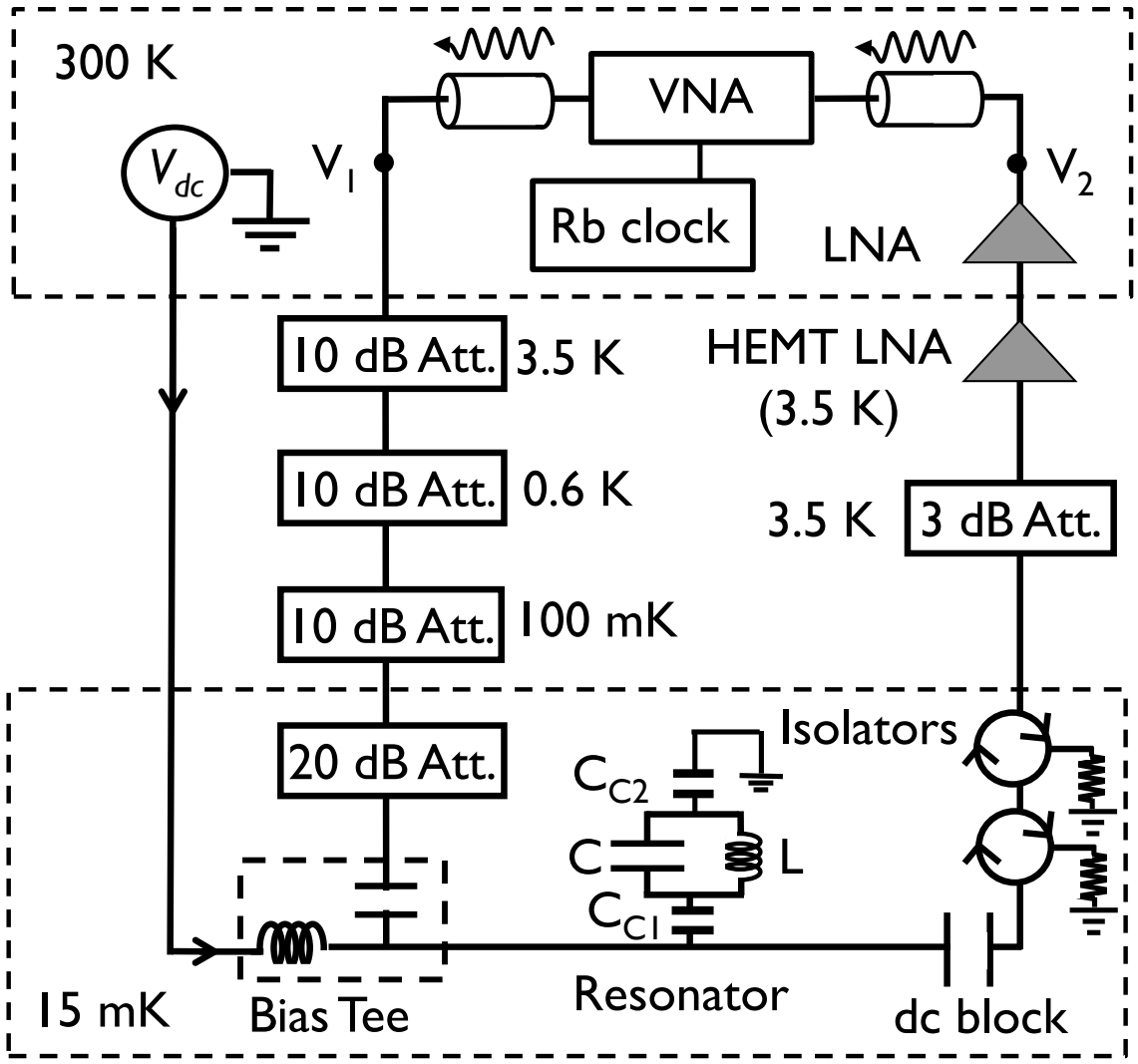

Fig. 5.3 - Experimental setup showing input and output microwave lines going to a thin-film microwave resonator that is mounted in a copper sample-box in the dilution refrigerator. The setup allows a static electric field to be applied to the resonator while the microwave transmission is measured.

controllably tilts the potential wells seen by TLSs in the chip. The resonator is capacitively coupled to the transmission line through C_{C1} and capacitively coupled to ground through C_{C2}. The output signal travels through a dc block to filter out V_{dc}, then through a pair of circulators to prevent reflections from reaching the resonator. The signal is amplified by a HEMT low-noise amplifier at 3.5 K. A 3 dB attenuator is placed on the input of the HEMT

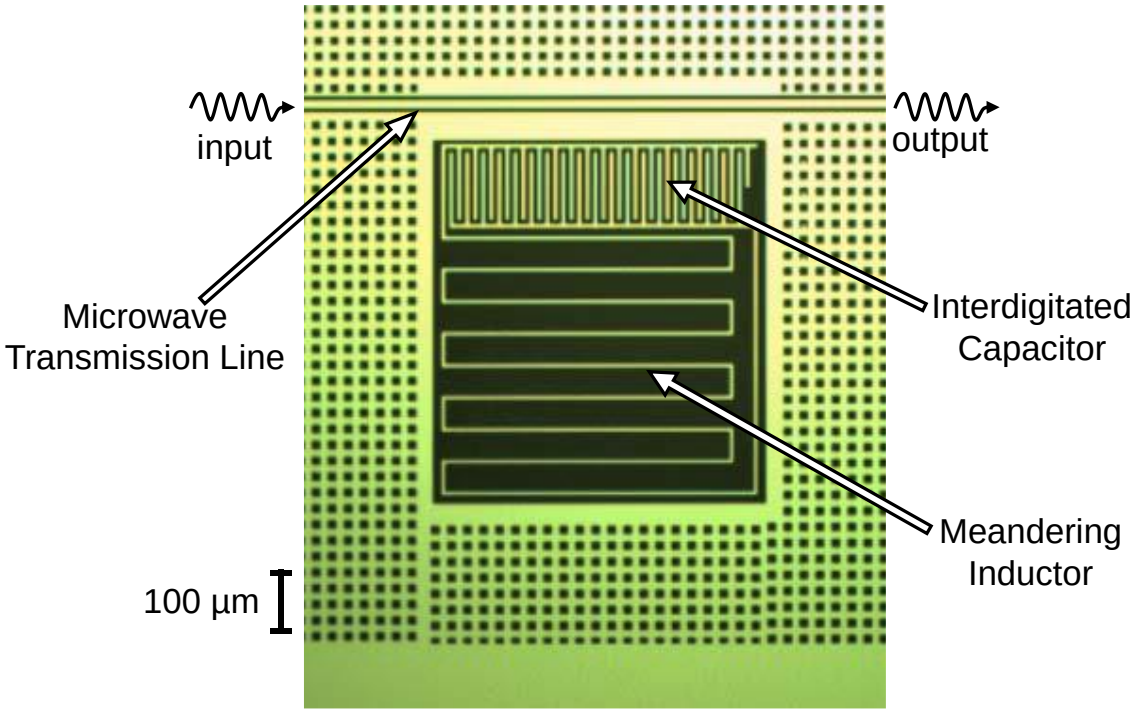

Fig. 5.4 - Optical image of thin-film microwave resonator LC1. Dark regions are sapphire substrate and light green regions are thin-film Al. The interdigitated capacitor and meandering inductor are surrounded by the ground plane, which has holes in it to prevent flux trapping. The device had a resonance frequency of about 6.8157 GHz.

amplifier to provide a well-defined 50 Ω input impedance. At room temperature, the signal is further amplified by a low noise amplifier (Miteq LNA) [5.53]. The VNA monitors the output signal V_2 and the input drive signal V_1 and records the magnitude and phase of the transmission $S_{21} = V_2/V_1$ as a function of the swept input frequency.

The high-*Q* superconducting resonator LC1 (see Fig. 5.4) was fabricated using photolithography, as described in detail in Sec. 3.2. A 200-nm film of aluminum was deposited by a thermal evaporator on a low-loss sapphire substrate. The chip consists of a meandering inductor and an IDC which are capacitively coupled to the transmission line. The resulting device is about 800 µm x 800 µm in overall size. The interdigitated capacitor

(IDC) has an estimated capacitance of 0.22 pF and the meandering inductor has an estimated inductance of 98 nH. The transmission line width is 5 μm, as is the gap between the IDC teeth. The transmission line and the ground plane of the chip are electrically connected to a printed circuit board (PCB) with wire bonds. The sample was mounted inside a copper sample-box using silver paint for thermal conduction.

5.5 Measurements of TLSs Dipole Coupled to a Resonator

After cooling the chip to 12 mK, we measured the transmission $S_{21}(f)$ near the resonance frequency f_r while applying static voltage V_{dc} to the center of the transmission line. This creates a non-uniform dc electric field at the resonator.

Figure 5.5(a) shows a false color plot of the magnitude of $|S_{21}|$ vs f and V_{dc}. This data was taken using a power of -111 dBm at the input to the chip's transmission line, corresponding to an average of about 4000 photons in the resonator when driven on resonance. Due to the relatively large spacing (5 μm) between the IDC teeth, this corresponds to a microwave electric field strength of about 60 V/m between the IDC teeth. This is about an order of magnitude larger than the expected critical electric field at which TLS saturation effects become significant in Al-oxide deposited via atomic layer deposition [5.22] or SiN [5.20, 5.21, 5.54]. At this power, only some TLSs are saturated. $|S_{21}(f)|$ shows a somewhat asymmetric Lorentzian dip at the resonance frequency f_r with distinct variations in the resonance as V_{dc} varies. These variations are expected due to TLSs that are dipole-coupled to the resonator and are randomly distributed in space and energy. The TLSs cause level repulsion (see Sec. 2.4) and effectively shift the resonator's resonance frequency. Depending on V_{dc}, many TLSs are tuned into or out of resonance

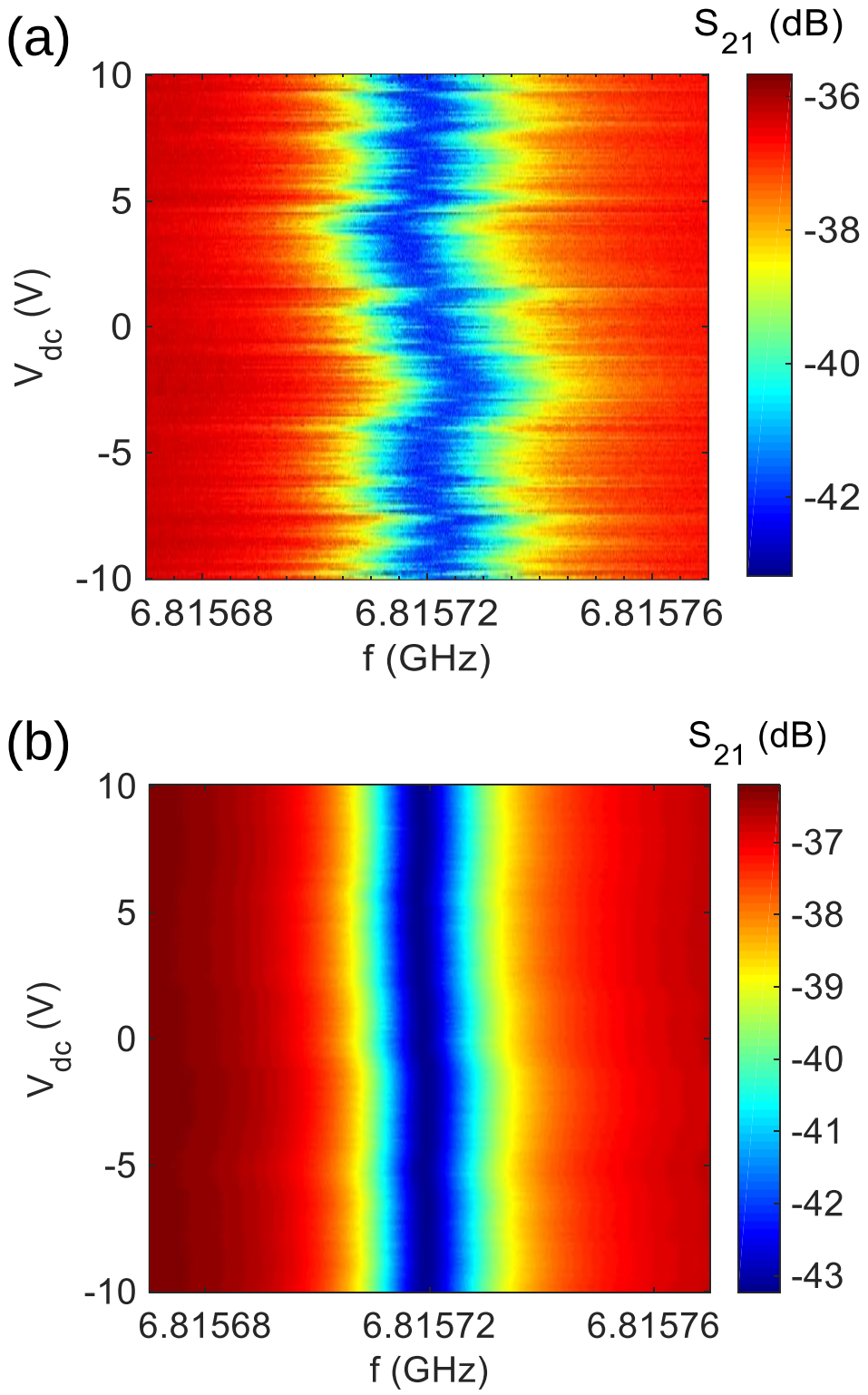

Fig. 5.5. (a) False color image showing magnitude of transmission $|S_{21}|$ as a function of input microwave frequency f and static applied voltage V_{dc} for low applied power at the transmission line (-111 dBm). The shifts in resonance frequency are pronounced. (b) Corresponding false color image at higher power measured at the on-chip transmission line (-91 dBm). The shifts in frequency are much smaller.

with the resonator, with the most strongly coupled and least-detuned determining how much the resonance frequency shifts.

For comparison, Fig. 5.5(b) shows a similar plot for a power of -91 dBm at the input to the chip's transmission line. At this higher power, $|S_{21}|$ shows much less variation with voltage. This is what one expects for power that is high enough to saturate the TLSs.

To verify that the features in Fig. 5.5(a) were not randomly varying in time, I repeatedly measured $S_{21}(f)$ as a function of V_{dc}, acquiring ~16,000 spectra over 86 hours with V_{dc} repeatedly scanning over ± 10 V with a 0.1 V step size.

To analyze the data, for each measurement time t and voltage V_{dc}, I fit the measured values of $S_{21}(f)$ to [5.55]

$$S_{21}(f) = K(f) S_0 e^{i\theta_0} \left[1 - e^{i\phi} \frac{Q/Q_e}{1 + 2iQ\dfrac{f - f_r}{f_r}} \right]. \tag{5.9}$$

I note this is functionally the same as Eq. (2.33). Here $K(f)S_0e^{i\theta_o}$ accounts for the frequency dependence of the input and output lines (see Appendix B), ϕ is a phase offset that accounts for asymmetry in the line shape, Q is the total quality factor, and Q_e is the external quality factor. I simultaneously fit the real and imaginary part of S_{21}(f) by minimizing χ^2 with respect to S_o, θ_o, ϕ, Q, Q_e, and f_r.

Figure 5.6 shows a gray-scale plot of the shift δf_0 in the resonance frequency f_0, relative to $f_0(V_{dc} = 0\ V)$, as a function of time t and applied voltage V_{dc}. The maximum variations in δf_0 are only ± 10 kHz, which is about 2 ppm of the resonance frequency. Examining the figure, we can see there are some horizontal bands or streaks that can persist for hours. This indicates that the frequency shifts are fairly repeatable in applied voltage. I

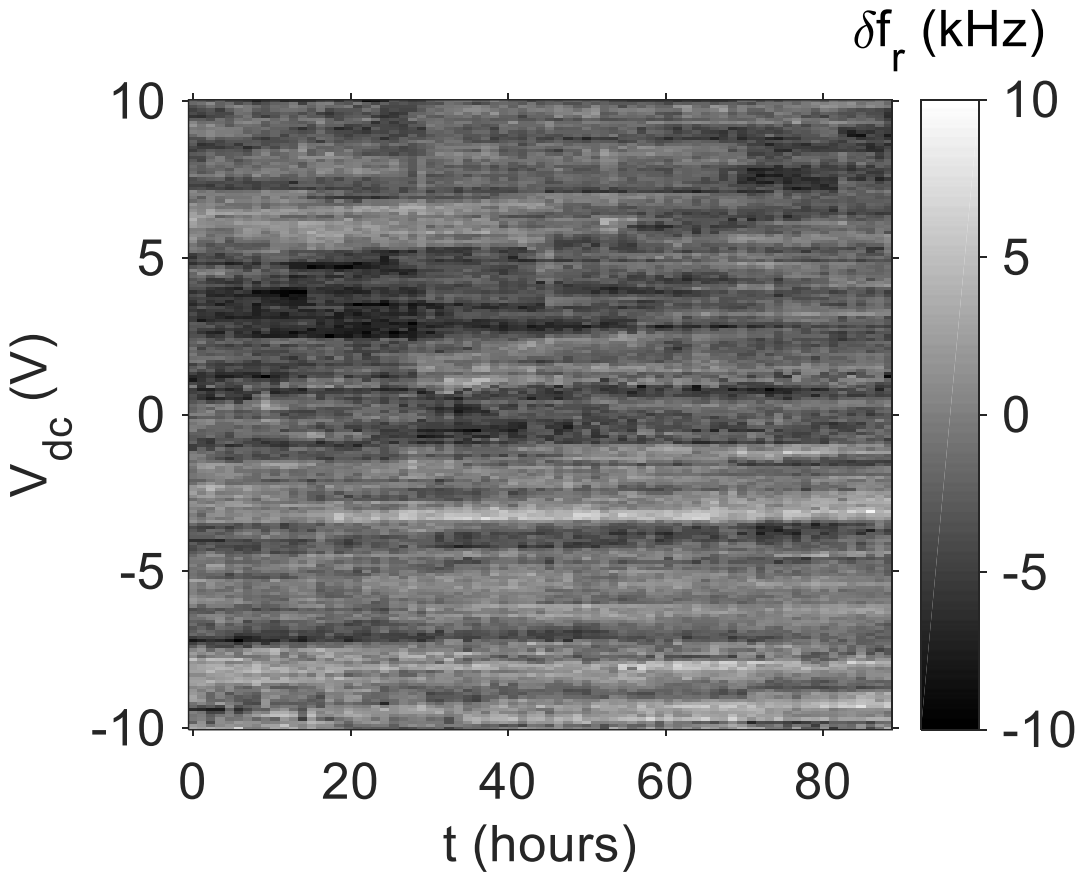

Fig. 5.6 - Gray-scale plot of the extracted shift in resonance frequency δf_r as a function of applied dc voltage V_{dc} and time t. Horizontal bands or streaks are evidence of repeatable frequency shifts that may persist for hours.

also note that at -3.5 V there is a single prominent dark horizontal band that is next to a light horizontal band. This is what one expects for an avoided-level crossing due to a standard dipole-coupled TLS as it is tuned through the resonance frequency by the applied voltage.

There are also repeatable features in other properties of the resonator. For example, Fig. 5.7 shows the corresponding gray-scale plot of Q_i as a function of t and V_{dc}. Note in particular the large repeatable variation in Q_i at around 1 V after t = 40 hours. The features in this plot were more stable in time and did not necessarily correspond to features in f_r.

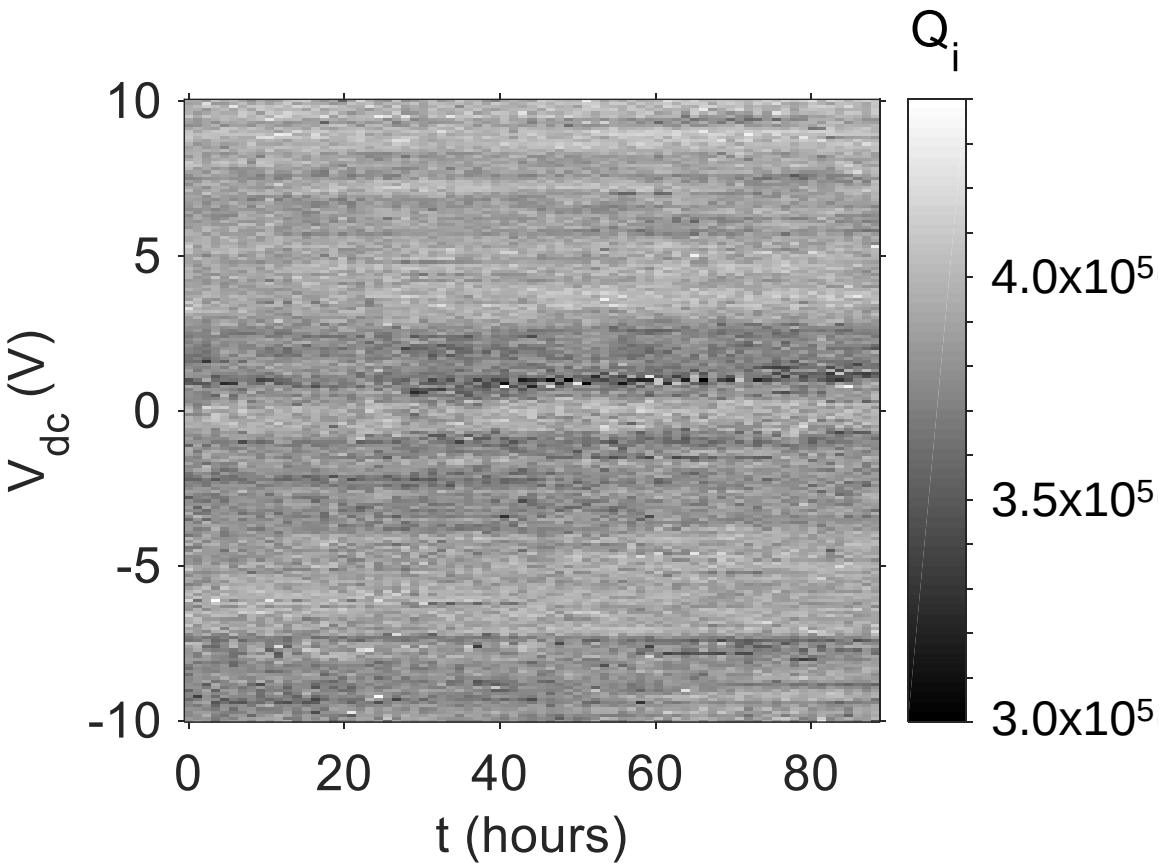

Fig. 5.7 - Gray scale plot of Q_i as a function of applied dc voltage V_{dc} and time t. There are fewer horizontal features than in the resonance frequency shift δf_r (Fig. 5.6), but a large repeatable variation in Q_i is seen around 1 V, especially after t = 40 hours.

See Appendix B for other examples of the behavior of the fitting parameters.

A natural question that one should always ask about values that are extracted from fitting is whether the fits were good. Figure 5.8 shows a gray scale plot of the resulting χ^2 as a function of dc bias voltage V_0 and time t. Each value of χ^2 was obtained from a sum with 3202 quadratic terms found from both the real and imaginary parts of S_{21} at 1601 frequencies. With 6 fitting parameters, this gives 3196 degrees of freedom. Assuming that we have done a good job of characterizing the uncertainty, good agreement between data and theory corresponds to $3050 > \chi^2 > 3150$. Examination of the plot shows that there are

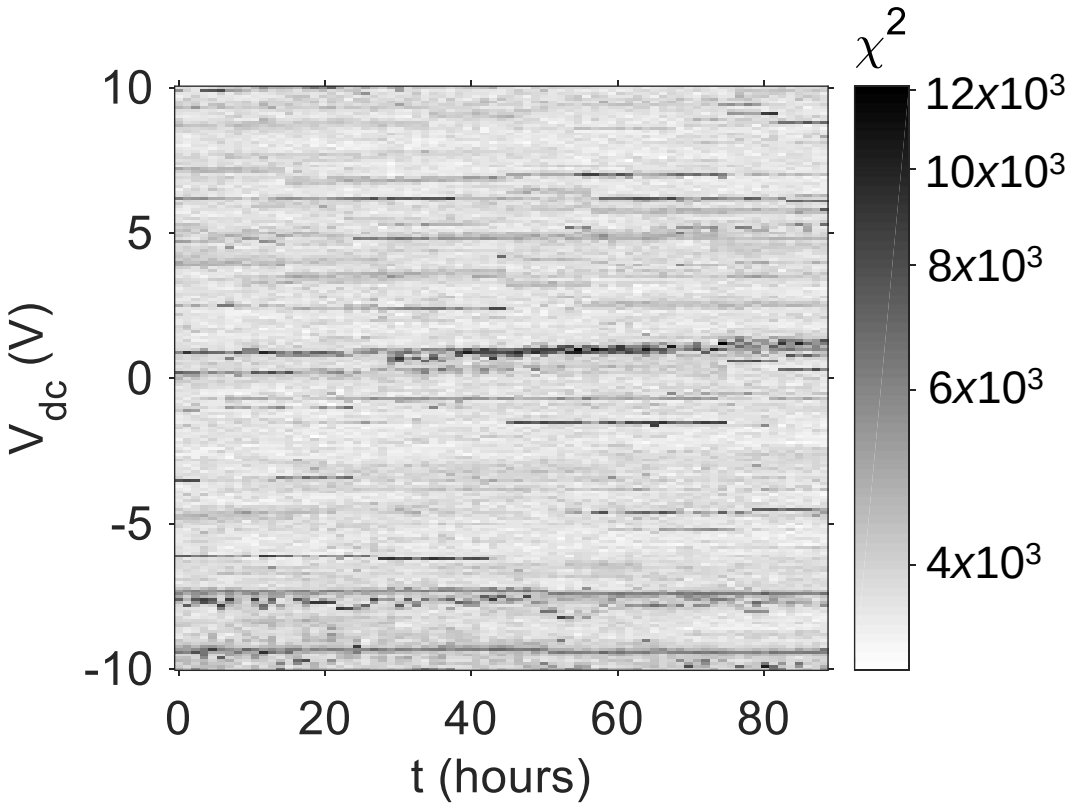

Fig. 5.8 - Gray-scale image showing χ^2 values as a function of applied dc voltage V_{dc} and time t. Dark regions indicate high χ^2 values where the fit was bad. In some cases this was because the resonance frequency was undergoing random telegraph noise as S_{21} was being acquired.

regions where χ^2 reaches a minimum value of around 3600. For 3196 degrees of freedom this indicates a poor fit, but I note that there is uncertainty in our estimate of the uncertainty of S_{21}, and this easily accounts for the discrepancy. Thus I argue that the regions where χ^2 reaches a minimum value are representative of acceptable fits. However, there are also many sharp horizontal dark streaks or bands that indicate much larger values of χ^2. These are clearly regions where the fits were very bad.

Inspecting the data in some of the poor fit regions revealed S_{21} curves that appeared

to be switching back and forth between Lorentzian line-shapes that had different resonance frequencies, as I discuss in the next section. Such behavior is inconsistent with Eq. (5.9), which assumes there is a single resonance frequency, and explains why these regions yielded very poor fits.

5.6 Measurements of Two cTLSs Coupled to a Resonator

Inspecting Fig. 5.8, we see that there is something going on at V_{dc} = 1.0 V that is causing large χ^2 values. The fits to these 77 resonance curves also showed relatively large variations in f_r, Q, Q_e, and Q_i from run to run. However, it is important to note that since the fits were bad, these parameter values cannot be trusted. Examining the 77 S_{21} curves at V_{dc} = 1.0 V revealed that many of the $S_{21}(f)$ curves seemed to be switching during the frequency sweep, going back and forth between curves with different resonance frequencies.

Interestingly, not all of the S_{21} curves at V_{dc} = 1.0 V gave bad fits. Figure 5.9 shows four examples of the $S_{21}(f)$ curves acquired at V_{dc} = 1.0 V where the fits appeared to be acceptable. We picked these specific curves out of the 77 taken at V_{dc}=1.0 V, because each had a slightly different resonance frequency, but did not appear to show any obvious random telegraph noise (see Fig. 5.9). The four curves of Fig. 5.9 were taken at t = 73.1, 20.9, 26.7, and 34 hours, and are shown in red, green, blue and magenta, respectively. Each gave a visually acceptable fit to Eq. 5.9, but the fits gave significantly different values for the resonance frequency and internal quality factor Q_i (see Table 5.2). The 4 different values for the resonance frequency suggests that we are finding the system in a different microscopic configuration each time we return to a bias of 1.0 V. The green and blue curve are quite close to each other, but never the less, we note that four curves are consistent with

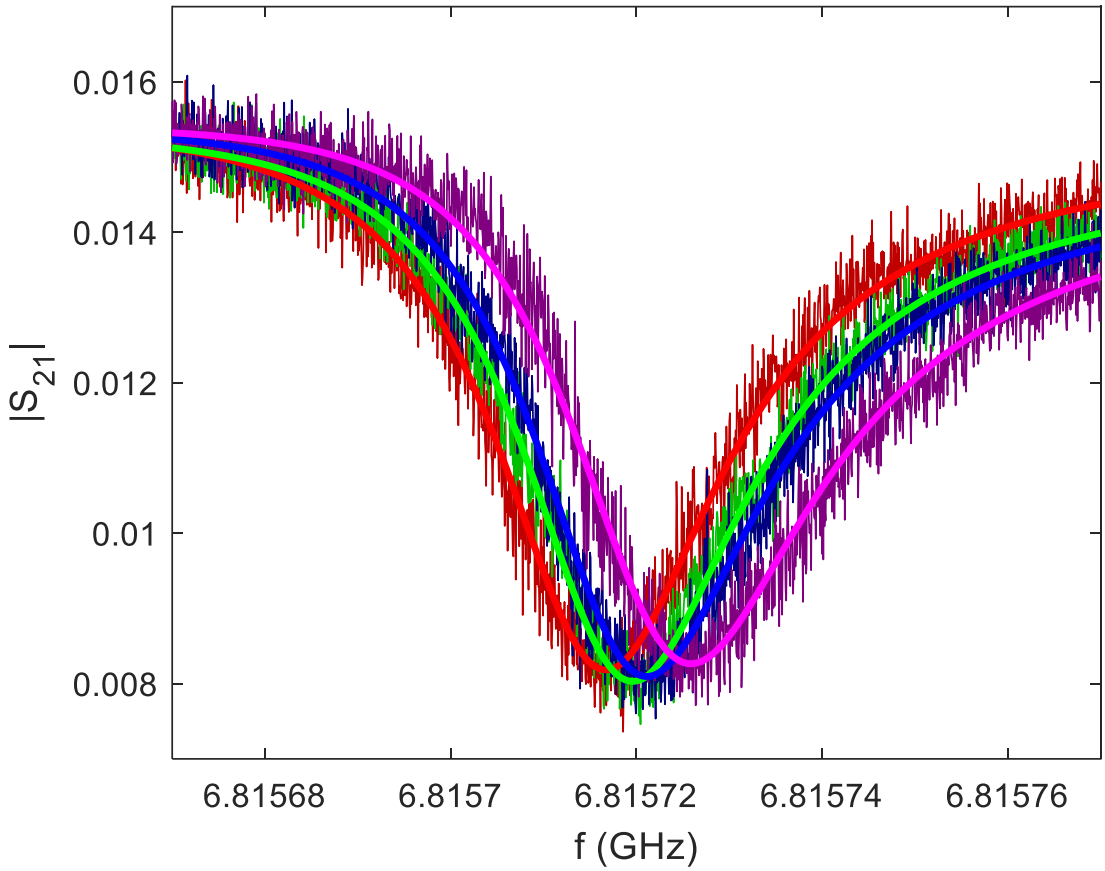

Fig. 5.9 - Resonance transmission curves S_{21} versus frequency f and fits, for resonator LC1 data-runs #63 (red), #18 (green), #23 (blue), and #30 (magenta), taken at t = 73.1, 20.9, 26.7, and 34 hours respectively. For all curves, V_{dc} = 1.0 V.

the four possible states $|g\rangle|g\rangle$, $|e\rangle|g\rangle$, $|g\rangle|e\rangle$, and $|e\rangle|e\rangle$ of two TLSs. I also note that it is possible that the asymmetry energy for a charged TLS can change each time we sweep the voltage due to other nearby charges rearranging during the sweep, which would change the local electric field.

As I noted above, the data sets in Fig. 5.9 gave acceptable fits. However, I was mainly interested in what was happening when there were bad fits at the 1.0 V bias point. Figure 5.10 shows an example of the magnitude and phase of the S_{21}(f) curve for run #48,

which was taken at V_{dc} = 1.0 V at around t = 56 hours. Throughout the 1.5 s scan, which swept the frequency from low frequency to high frequency, we see S_{21} appears to switch between resonance curves. It is not surprising that this gave a very bad fit. Overlaid on the amplitude and phase plots are the four fits to the S_{21}(f) curves shown in Fig. 5.9, which were also taken at 1.0 V, but at other times. The gray shading in each panel helps identify

Table 5.2 - Best fit parameters obtained by fitting Eq. (5.9) to the four resonance curves (red, green, blue, magenta) shown in Fig. 5.9. The resonance frequency is f_r, δf_r is the change in the resonance frequency relative to the 'red' state, Q_e is the external quality factor, Q_i is the internal quality factor, ϕ is the phase shift factor, and $\Delta\phi$ is the change in the phase factor from that of the red curve. See Appendix B for additional results from the analysis.

	Red	Green	Blue	Magenta
Run #	63	18	23	30
f_r (GHz)	6.8157143	6.8157164	6.8157172	6.8157210
δf_r (kHz)	0	2.08	2.92	6.72
δC (zF)	0	130	190	430
Q	1.93×10^5	1.92×10^5	1.91×10^5	1.82×10^5
Q_e	4.08×10^5	3.99×10^5	3.97×10^5	3.84×10^5
Q_i	3.66×10^5	3.70×10^5	3.68×10^5	3.45×10^5
ϕ	12.1^o	15.6^o	18.9^o	22.4^o
$\Delta\phi$	0^o	3.6^o	6.8^o	10.3^o

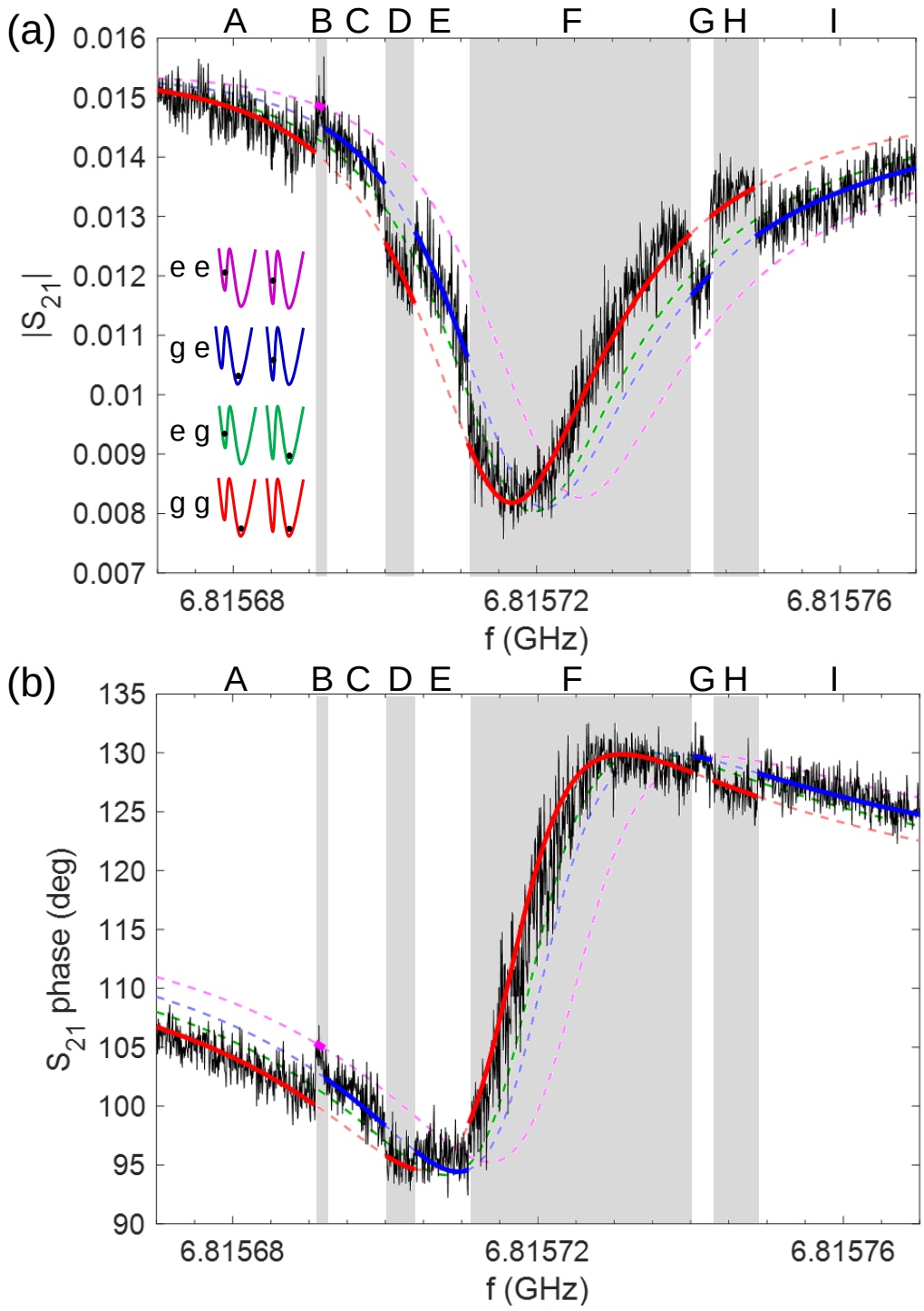

Fig. 5.10 - (a) Black trace shows $|S_{21}|$ as a function of frequency f from run #48 with V_{dc} = 1.0 V at around t = 55.7 hrs. Dashed curves are fits to $S_{21}(f)$ from runs #63 (red), #18 (green), #23 (blue), and #30 (magenta) as in Fig. 5.9. Bold colored sections highlight regions where measured S_{21} appears to follow corresponding colored dashed curve. Inset shows corresponding 4 possible occupations of two double-well potentials of two cTLSs. (b) Corresponding plot showing phase ϕ of S_{21} vs f from run #48 in black.

regions where S_{21} switches.

In region A, it appears that the system is in the ‘red’ state. Then, it briefly switches to the ‘magenta’ state in region B, before switching to the ‘blue’ state in region C. In region D, it switches back to the ‘red’ state. In region E, it switches to the ‘blue’ state, although it is difficult to distinguish it from the ‘green’ state due to the noise. In region F, it returns to the ‘red’ state for a relatively long period of time. In G, it briefly switches to the ‘blue’ state before returning to the ‘red’ in region H. In region I, it appears to switch to the blue state, but it is again difficult to distinguish the ‘blue’ from the ‘green’ state. It is quite notable that the switching in the amplitude plot appears to be consistent with that seen in the phase plot, and this gives some confidence that the state assignments are reasonable.

Further examination of Fig. 5.10 reveals that the resonator spent about 60% of the time following the red curve, 39% of the time on the blue curve and about 1.4% of the time on the magenta curve. Each time it is in the red state, it spends an average time of about 230 ms before it switches. Switching out of the blue curve takes about 150 ms and the average time to switch out of the magenta state is about 22 ms. The average times for red and blue were calculated including sections at the beginning and end of the sweep, which were cut short, so the true average time spent in those two states was likely greater.

I also found that the standard deviation of the times spent in the red state is about 160 ms, which is close to the average time spent in the red state. This behavior is also true for the blue state, which gives a standard deviation of 110 ms. This behavior is consistent with the time spent in each state being drawn randomly from an exponential distribution. Given the small number of red-blue switching events during this sweep, the probability of following the red curve is not significantly different from the probability of following the

blue curve. Nevertheless, the probability of following the magenta curve is significantly smaller than the probability of following either the red or blue curves.

I note that these switching times are quite long compared to the coherence times of superconducting qubits and also quite long compared to many previously reported characteristic lifetimes [5.11, 5.23, 5.27, 5.29] of two-level systems in superconducting devices. However, much longer switching times have also been observed [5.11], well in excess of 1 minute, so that these times cannot be regarded as remarkable.

The random nature of the switching is consistent with two TLSs with small enough g-to-e energy difference at the 1.0 V bias that they are being randomly thermally excited. In this case, if the system had a significantly higher energy in the magenta state than the red or blue states, it would be significantly less likely to be found in the magenta state than in the red or blue states. In this interpretation, the green state is not seen here because it also has a significantly higher energy than the red or blue states. Note however that this implies that the resonator has a higher frequency when at least one of the TLSs is excited (magenta curve), than when it is not excited (red or blue curve), i.e. the dispersive shift produced by the TLS is positive. As discussed in Sec. 2.4 and Sec. 5.2, a positive dispersive shift is inconsistent with standard dipole coupling of a low-lying TLS to a resonator, but it is consistent with coupling to a low-lying cTLS that has a less compliant excited state.

The inset to Fig. 5.10(a) shows a model for the double-well potentials for two cTLSs that is consistent with this picture (see Sec. 5.3). Based on the occupancy probabilities, we can identify $|g\rangle|g\rangle$ with the red state, $|e\rangle|g\rangle$ with the green state, $|g\rangle|e\rangle$ with the blue state and $|e\rangle|e\rangle$ with the magenta state. To produce the observed dispersive shifts, we assign the first TLS to have a double-well potential such that the lower well has

the larger spring constant. The second TLS also has a two-well potential such that the lower well has a larger spring constant. With this assignment of well asymmetries and spring constants we reproduce the observed qualitative behavior.

Our conclusion that the observed behavior is inconsistent with standard dipole coupling to a TLS is not sensitive to the details of our fits. We could have instead argued that some sections of the data follow the green curve, for example. In any such interpretation the system still spends relatively little time with the resonator at its highest resonance frequency (magenta), which is inconsistent with standard dipole coupling to a low-lying TLS that can be thermally excited, but consistent with a low-lying cTLS that can be thermally excited.

Given this interpretation, it is interesting to consider again the non-switching behavior shown in Fig. 5.9. In particular, we see that at V_{dc} = 1.0 V, it can happen that any of the four curves is preferred. This behavior is consistent with two TLSs that have small asymmetry energy at this bias, with small random variations in the applied bias or changes in the local field determining which well is lowest. A very low asymmetry energy and low tunneling energy is also necessary for the fluctuations to be driven by thermal activation at a 12 mK operating temperature. In our model of a cTLS, we note that such small changes in asymmetry energy would only change the thermal occupancy of the states but not the effective capacitance or dispersive shift of each state. In contrast, for standard dipole coupling to a TLS, random tilting of the well not only changes the occupancy, but also detunes the TLS from the resonator frequency, and this would lead to random changes in both the occupancy and the dispersive shift.

Figure 5.11 shows a false-color plot of the same frequency shift data that I

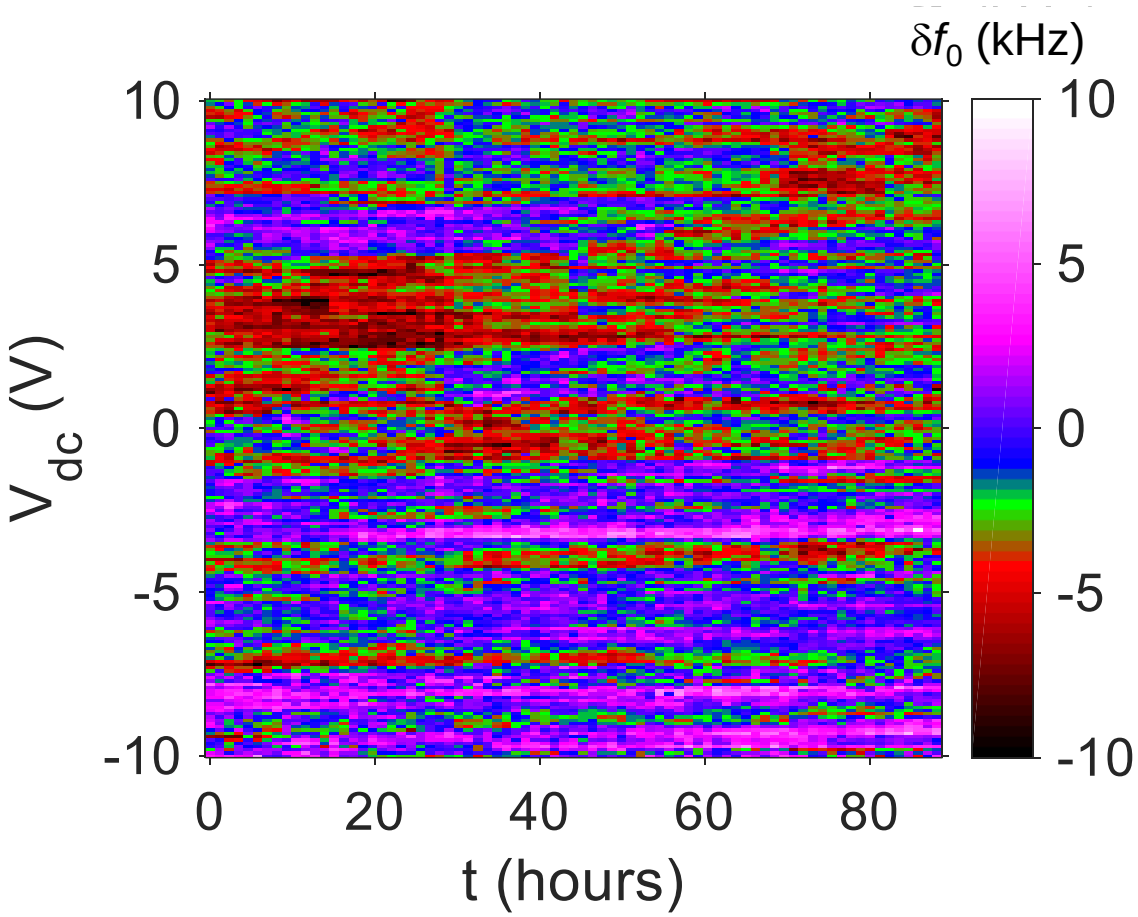

Fig. 5.11 - Replot of Fig. 5.6 with a false color scale that reflects the resonance frequencies of 'red' gg, 'green' eg, 'blue' ge, and 'magenta' ee states. For V_{dc} > 1.0V, there is more 'red', consistent with both cTLSs being biased such that they are more often in their more compliant well, shifting f_0 lower. For V_{dc}<1.0V there is more of the 'magenta' state, consistent with both cTLSs being in their less-compliant well, shifting f_0 higher on average.

presented in gray-scale in Fig. 5.6. Here the color-scale has been chosen to reflect resonance frequencies of the 'red' |gg⟩, 'green' |eg⟩, 'blue' |ge⟩, and 'magenta' |ee⟩ states. This does not mean that all frequencies in this plot are determined by just the two cTLSs, but such a plot may reveal additional insights into the tuning of the TLSs. For example, for V_{dc} > 1.0 V, the plot tends to be redder, consistent with both cTLSs being biased into their

more-compliant well, which tends to shift f_0 lower. This corresponds to the 'red' state in Fig. 5.2(c). Similarly, For $V_{dc} < 1.0$ V, the plot looks more magenta, consistent with both cTLS being tilted into their less-compliant well, which tends to shift f_0 higher on average. This corresponds to the 'magenta' state in Fig. 5.2 (c).

There are some other noteworthy features of the data. In Figs. 5.6 and 5.7, we see that once the dc bias is removed (return to 0 V), the resonance frequency and loss tend to recover, indicating non-glassy behavior. This is consistent with TLSs that are non-interacting or weakly interacting. Relatively large fluctuations have also been reported in the lifetime of the longest lived transmons. If these are also due to charged two level systems, our results suggest that application of a relatively small static bias voltage may allow a TLS to be tuned out of the operating range.

5.7 Conclusions

In this chapter I discussed measurements on a voltage biased superconducting resonator that showed effects from coupling to two-level systems. I introduced a model of a cTLS coupled to a resonator and contrasted this with the standard theory of a resonator coupled to a TLS via an electric-dipole. Next, I described the experimental setup, which included a superconducting thin-film LC microwave resonator mounted in a dilution refrigerator. I was able to apply a variable dc voltage to the transmission line while measuring the transmission S_{21}(f). I then discussed measurements of resonator LC1 as a function of applied dc voltage bias and time.

Most of my measurement results can be explained by standard dipole-coupled near-resonant TLSs. I then discussed a subset of the measurements at a particular dc bias that sometimes showed telegraph noise. Examination of the data revealed that some of the

fluctuations corresponded to an increase in the resonator's resonance frequency when a TLS appeared to be in its excited state. Such a dispersive shift is consistent with thermal activation of a low-energy TLS that modulates the resonator's capacitance by ~100 zF but inconsistent with coupling to a low-lying TLS via standard electric dipole terms. It should be emphasized here that other explanations of the behavior may be possible. In particular, it appears that interacting TLSs with standard dipole coupling can yield similar behavior [5.56]. Although we have argued that our TLSs do not appear to be interacting with each other, because we see non-glassy behavior, there may be a range of interaction strengths and densities that permit non-glassy behavior.

We also note that the observed frequency fluctuations were quite small (ppm) and only occurred at a few specific voltages. These voltages evidently correspond to biases for which the well-asymmetry was so small that the TLS could be randomly thermally excited. Given the relatively large size of the resonator's capacitance, such fluctuations would only be discernible in resonators such as ours which have a sufficiently high *Q*. If the phenomena really is due to cTLSs, then it seems quite likely that such cTLSs may also occur in superconducting qubits. Our results also demonstrate that the application of a small dc voltage may allow a particularly detrimental TLS to be tuned out of the operating range. For both dipole-coupled TLSs and cTLSs, we see that once the dc bias is removed, the resonance frequency and loss are recovered, indicating non-glassy behavior.

Chapter 6: Integrating a Tapered Optical Fiber with a Superconducting Microwave Resonator

6.1 Introduction

Constructing a hybrid quantum system with optically trapped atoms coupled to a superconducting quantum device presents many experimental challenges (see Chapter 1). I approached this complicated problem by starting with a simpler, proof-of-principle experiment: coupling a tapered optical microfiber to a superconducting resonator inside of a dilution refrigerator. Hereafter I will refer to this as the microfiber-chip experiment. Although this was a far easier problem than building a complete hybrid system, it was far from being a simple task. Nevertheless, this allowed me to approach the development of a full hybrid system by working on a few relatively independent and manageable pieces, which I could tackle through a series of experiments. In this Chapter, I describe these experiments and how the system evolved over time as I incorporated new results. The main purpose of each experiment was to investigate issues that were expected to arise in the hybrid system and test techniques to mitigate problems.

One key issue was to find out how much light was absorbed in the superconducting resonator and how this light affected the behavior of the resonator. Since I would not be trapping atoms for this work, I did not need to use a delicate dust-sensitive nanofiber. Instead, I used an optical microfiber with a diameter of about 56 μm. The microfiber was much more robust than a nanofiber and, because it confined light to the core of the fiber, it was insensitive to dust. For a realistic test of light absorption in the resonator, I also needed

a setup that would allow me to controllably position the microfiber close to the inductor in the superconducting resonator. Closely connected to the positioning issue was the need to investigate techniques for determining the relative position of the fiber and resonator. This positioning problem was one of the main challenges of the hybrid system, not just because we needed μm-scale control, but also because the positioning would need to be done *in situ* at millikelvin temperatures when the fiber and chip would not be directly visible inside the dilution refrigerator.

The overall layout for the microfiber-chip experiment is shown in Fig. 6.1. A superconducting 3D microwave cavity houses a sapphire chip with a thin-film superconducting resonator. Two small holes (about 1 mm x 1 mm) in opposite walls of the cavity allow an optical fiber to pass through the cavity and close to the chip, which is mounted near the center of the cavity. The fiber is held rigidly under tension by two arms of a fiber holder bracket (only one arm is visible in Fig. 6.1). The cavity sits on top of two translation stages that can move the cavity relative to the fiber in the x and z-directions. Two SMA connectors, which are attached to the cavity, attach to pins that extend partially into the cavity. The pins allow the thin-film resonator to be measured by coupling microwave signals into and out of the cavity. The entire setup is thermally anchored to the mixing chamber stage of an Oxford Instruments Triton 200 dilution refrigerator which can be cooled to 10-20 mK.

Although I used an optical microfiber for this experiment, it is worth emphasizing here that the same apparatus could have been used to test an optical nanofiber. This would have been an interesting next step, but it would have required that we maintain a clean-room environment when preparing the set-up and while evacuating the vacuum space

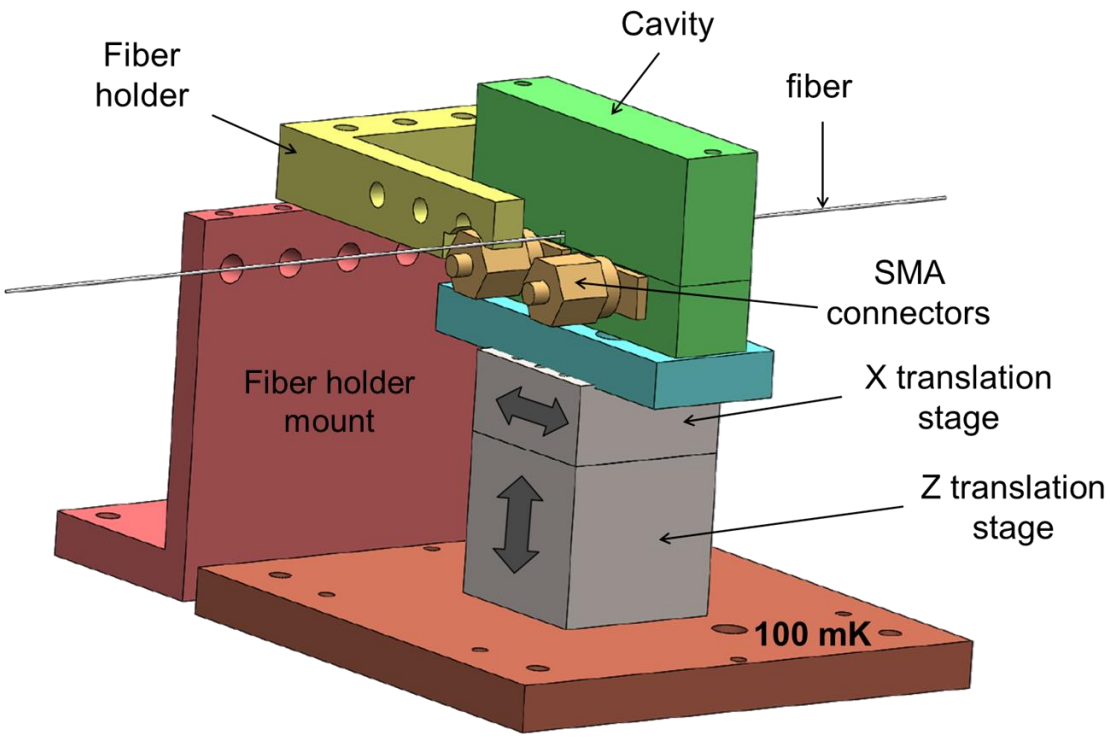

Fig. 6.1 - Overall layout of the millikelvin microfiber-chip experiment. The superconducting 3D microwave cavity (green) is mounted on an x-z translation stage and houses a sapphire chip (not shown) that has a thin-film superconducting microwave resonator. The setup allows the resonator to be positioned close to the optical microfiber, which passes through the cavity.

around the set-up before cool-down.

Dr. Jared Hertzberg and I developed four versions of this experiment (see Table 6.1). Using the first version, we were able to measure the microwave resonance of the LC resonator and observe an optical response from the resonator. However, we soon realized that the response did not vary reproducibly with the fiber position. Eventually we found that this was due to the fiber detaching from the holder bracket due to failure of the epoxy (see Sec. 6.4). The third version also did not produce useful data; the thin-film inductor in the resonator broke sometime during setup or cooldown. For these reasons, I describe in detail only the experimental set-ups for the second and fourth versions, which

did produce useful results. The main results from these experiments are presented in Chapter 7.

Although it was far simpler than a full hybrid system, the microfiber-chip set-up still had many design constraints. These are described in Section 6.2. In Section 6.3, I provide details on the optical fiber, including a discussion of light propagation in tapered fibers, atom trapping, the resulting design specifications, and fabrication. In Section 6.4, I describe the design of the fiber holder and how the fibers were tensioned and attached to the holder. In Section 6.5, I describe the Attocube translation stages, which I used to move the fiber relative to the cavity and resonator. In Section 6.6, I describe the inductive position sensors I used for measuring changes in the position of the cavity. Section 6.7 describes the fiber's light source and Section 6.8 describes how the chip-fiber-cavity

Table 6.1 - Summary of four versions of the microfiber-chip experiment, which involved positioning an optical microfiber near to a thin-film superconducting resonator at millikelvin temperatures. Chapter 3 has a detailed description of resonators LC2 and LC3.

Version #	**Date**	**Resonator**	**Resonator Description**	**Comments**
1	12/24/13 - 04/21/14	LC2	Al, lumped element, antenna, polished chip edge	epoxy failed, fiber disconnected, little useable data
2	07/24/14 - 09/22/14	LC2	Al, lumped element, antenna, polished chip edge	resonator optical response with fiber near inductor
3	05/25/15 - 06/10/15	LC2	Al, lumped element, antenna, polished chip edge	resonator inductive line broken, no useable data
4	01/11/16 - 09/20/16	LC3	Al, lumped element, similar to LC2 except for antenna placement	resonator optical response, mainly with fiber above chip

system was assembled. Finally, in Section 6.9 I describe operation and control of the apparatus during an experiment.

6.2 Design Constraints

For a proof-of-principle experiment to be meaningful, I needed to make sure that the design of the apparatus was compatible with a complete hybrid experiment. Perhaps the most important design choice was that the complete hybrid system would use a tapered optical nanofiber [6.1-6.2] to trap atoms. One advantage of this approach is that it can yield a convenient, tightly packed, linear array of atoms that can be coupled to a small linear inductive element. Other advantages of this approach are that the amount of light scattered from the fiber can be minimized by suitable preparation of the tapered sections of the fiber and it eliminates the need for large magnetic fields, which can interfere with the operation of superconducting devices.

Jared Hertzberg designed thin-film superconducting microwave resonators LC2 and LC3 to maximize coupling of the resonator's inductor to a linear array of atoms. These devices were fabricated on sapphire substrates and are described in detail in Ch. 3. In both resonators, the inductance is dominated by a single straight-line section of thin-film wire that is about 1 mm long and located close to the edge of the chip. The inductive line is connected to a thin-film interdigitated capacitor (IDC) to form an LC resonator. To reduce light absorption in the relatively large area of the capacitor, it is placed about 80 μm away from the edge of the chip and the inductive line. In the microfiber-chip experiment, I measured the response of the LC resonator, with and without light applied to the fiber, as the position of the fiber was changed relative to the resonator.

As discussed in Ch. 1, the optimum placement of the atoms in the hybrid system is about 5 to 10 μm from the inductor. This is close enough that the coupling between atoms and the magnetic field produced by the resonator's inductor is relatively strong. It is also far enough that the intensity of the evanescent optical field at the surface of the chip should be weak enough to not degrade the performance of the superconducting LC resonator. Note in particular that the evanescent field strength decays exponentially on a length scale of $\lambda/2\pi \sim 160$ nm, which means it is reduced by a factor of $e^{-10/0.16} \sim 10^{-27}$ at a distance of 10 μm from the fiber.

As I noted above, in thin-film superconducting resonators LC2 and LC3 the inductor was a straight-line section near the edge of the chip. The optimum geometry for the setup was to have the fiber aligned parallel to the inductor and the edge of the chip, with the fiber positioned just to the side of the chip and at the same height as the top surface of the chip. With such an arrangement, the fiber would primarily illuminate the resonator from the side, exposing only the small 400 nm thick Al cross-section of the inductor line, rather than the top surface of the inductor and IDC. With careful alignment, this would greatly reduce the amount of light absorbed by the resonator. Since the alignment and position of the fiber relative to the resonator would be affected by differential thermal contraction, we had to be able to position the fiber relative to the resonator when the system was at cryogenic temperatures and not directly viewable. Furthermore, we needed both translational and rotational adjustments to achieve alignment. I address these design considerations in Sec. 6.5.

A weak constraint on the experiment is the limited cooling power of the dilution refrigerator. For our Oxford refrigerator, 200 μW of heat at the mixing chamber plate will

drive this stage to 100 mK, at which point one would expect a superconducting qubit to suffer from significant dephasing due to thermally generated occupancy of the resonator [6.3-6.4]. This puts a very rough upper bound on the maximum power that can be dissipated at the cold stage. Of particular concern is that in a complete hybrid system, a relatively high optical power (~10 mW) would need to be delivered to the fiber to allow the trapping of atoms. Fortunately, a well-constructed high-transmission nanofiber would only scatter a very small fraction of the applied light, an amount that should be insignificant compared to the cooling power of the refrigerator, and the un-scattered light would be transmitted back to room temperature via a return fiber rather than being absorbed at the cold-stage.

A more problematic issue is that a Magneto Optical Trap (MOT) will be required to trap and cool atoms before they could be moved onto a fiber. MOTs use multiple beams with relatively high power trapping light [6.5] compared to a fiber trap. A MOT also requires an atom source, which can be a source of blackbody radiation, and requires significant applied current to produce magnetic fields. Minimizing these potential sources of heat will likely require placing the MOT outside of the mK stage and carefully designing the optics, shielding, and thermal grounding. In our proof-of-principle experiments, we did not use a MOT or trapped atoms and this let me avoid these atom-trapping related issues.

A tighter constraint on the maximum allowable amount of scattered light is set by the effect that light has on the quality factor Q of a thin-film superconducting aluminum resonator. In particular, absorption of light in the resonator's inductor will generate quasiparticles that can decrease the internal Q of the resonator [6.6-6.8]. This is a non-equilibrium process, rather than a simple heating effect. Ultimately, we need to maintain a

sufficiently large Q to resolve coupling to atoms that are weakly coupled to the resonator. In a complete hybrid system, with a transmon coupled to a resonator that is in turn coupled to ~1000 atoms, the maximum allowable amount of scattered light may be even smaller since the qubit's lifetime is also very sensitive to quasiparticles [6.8-6.11].

Although a tapered nanofiber will be required for a complete hybrid system, we only needed to use an optical micro-fiber to understand the impact of scattered light. Tapered nanofibers do not have perfect transmission and the majority of the loss typically occurs at the tapered regions, which would typically be outside of the cavity and centimeters away from the resonator. With careful design and implementation of the pulling algorithm, the transmission through a nanofiber can be as high as 99.95% [6.12] and it is possible to improve this number by perfecting the geometry of the taper region to be strictly adiabatic. Even if the fiber had perfectly tapered input and output sections, the fused silica that makes up the fiber inherently contains impurities that cause Rayleigh scattering. For un-tapered fiber, the loss is reported to be < 5 dB/km [6.13]. If I assume that the loss is due purely to Rayleigh scattering and that none is absorbed (good enough for order of magnitude estimates), this gives a scattering rate of about $1.2\text{x}10^{-6}$ of the input optical power per mm. For an input power of order 10 mW (the power needed to trap atoms), this would imply that a 1 mm section of fiber would scatter about P_s = 12 nW. Of course, most of the scattered light would not be incident on the aluminum film in the LC resonator and most of the light that was incident on the aluminum in the resonator would be reflected. To get a rough estimate for the light absorbed by the LC resonator, I assumed:

1) The fiber is in line with the plane of the chip and parallel to the inductor so that resonator is only illuminated from the side

2) The fiber and inductor are r = 10 μm away from each other and are each L = 1 mm long

3) The aluminum film has a thickness of h = 400 nm

4) The P_s = 12 nW of Rayleigh scattered light from the fiber is isotropic

5) Only α = 10% of the light incident on the aluminum is absorbed.

With these assumptions, the total power absorbed in the resonator is:

$$P_a = \alpha P_s \frac{hL}{2\pi rL} \approx 8\,pW \tag{6.1}$$

I note that this estimate does not include light that is reflected from the substrate or 3D cavity that can be incident on the surface of the thin-film resonator.

Another potential issue with the optical fiber is that fused silica has a very low thermal conductivity at low temperatures, typically ~1 W/Km [6.14]. An open question is how hot the fiber gets when it is carrying power and whether or not it heats up so much that it emits enough thermal radiation to affect the resonator. At a wavelength of 780 nm, the loss due to absorption is of the order 0.5 dB/km [6.15]. For trapping atoms we would use 7.5 mW at 730 nm and 4.5 mW at 1064 nm in a standing wave configuration. For an input power of 12 mW (where we assume the lost due to absorption is the same for these wavelengths as for 780 nm), the absorbed power in a L = 1 mm section of nanofiber with radius a = 250 nm would then be approximately 1.4 nW, or about 10% of the power from the Rayleigh scattered light. Since the thermal conductivity of fused silica is very poor, we can safely assume that very little of this power will be removed by conduction down the fiber. Instead, I consider the limit where the fiber heats up until the absorbed power is equal to the power emitted by black-body radiation. One then finds that the fiber will reach a temperature of

$$T = \left(\frac{P}{\sigma 2\pi a L \varepsilon}\right)^{1/4} = 63\ K \tag{6.2}$$

where I have taken the emissivity of the fiber as ε =1. From Wien's displacement law, the wavelength at which the maximum intensity is radiated is

$$\lambda_{max} = b/T = 46\ \mu m \tag{6.3}$$

where b = 2.89×10^{-3} Km. The energy of the average black-body photon is approximately 27 meV. This energy is well above the superconducting gap for aluminum (2Δ = 340 μeV) and therefore it is sufficiently high to break pairs and generate non-equilibrium quasiparticles. I note that if this effect is significant, turning off the optical power would cause the fiber to slowly cool, and one would see a corresponding slow increase in the *Q* of the resonator. If the fiber were not cooled completely prior to heating via optical power, the temperature may be slightly higher but would likely not significantly change the amount of power capable of breaking quasiparticles inside the resonator.

I note that the above temperature estimate is only approximate and an accurate calculation is difficult because the length scale of the emitter, i.e. theradius of the fiber, is smaller than the wavelength of the radiation [6.16]. Nevertheless, we expect the radiated power estimate is still quite good since, whatever temperature is eventually reached, the radiated power will come into steady state equilibrium with the absorbed power.

In addition to the above general constraints, there are many practical constraints on the design. For example, we must be able to mount the fiber on the fiber holder without damaging it or producing additional scattered light. We will also need to align the chip and fiber, and ensure that differential thermal contraction does not cause the chip and fiber to come into contact during cooling. We also must make sure that, at all temperatures, the fiber is under sufficient tension that it does not sag. On the other hand, we must ensure that

the fiber does not become over-tensioned and break when cooled due to differential thermal contraction between the fiber holder and the fiber. When the fiber is cold, we must make sure it does not vibrate excessively. In addition, optical nanofibers are extremely sensitive to dust particles on their surface, as the evanescent mode will scatter at imperfections. Although I avoided this dust problem by using a microfiber, it was still important to prevent dust from contaminating the fiber and chip, as this could have led to additional heating from Rayleigh scattered light or produce contact with the chip. In Sec. 6.4, I discuss how I dealt with some of these issues associated with mounting the fiber.

6.3 Tapered Optical Fiber

6.3.1 Tapered Optical Fiber and Nanofiber Theory

Our optical fiber was made from fused silica, also known as fused quartz, which is a nearly pure form of silicon dioxide. The optical fiber carries light through a core that is doped to have an index of refraction that is slightly higher than the cladding layer that surrounds it (see Fig. 6.2(a)). If the wavelength of the light is much smaller than the diameter of the cladding, geometric optics applies. A light ray that enters the core at a sufficiently shallow angle (see Fig. 6.2(b)) will undergo total internal reflection at the core-cladding interface with very little loss and continue through the fiber.

For our fibers, the wavelength of the applied light is comparable to the diameter of the core and geometric optics does not apply. Instead one can solve Maxwell's equations and find the intensity profiles of the allowed modes. Figure 6.3(a) shows a simulation of the transverse intensity profile for the unmodified fiber (not tapered) [6.17] for 780 nm light. One finds that the intensity profile for the unmodified fiber is well-confined to the

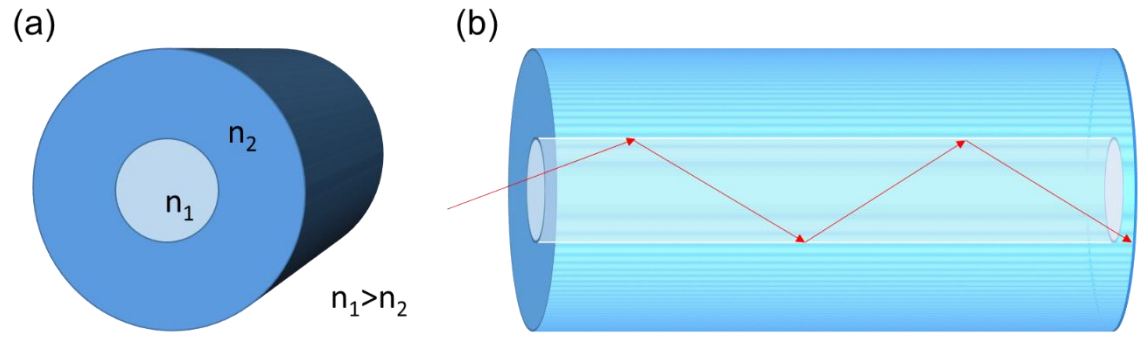

Fig. 6.2 - (a) Illustration of core and cladding in an optical fiber. The core has an index of refraction n_1 and the cladding has a slightly lower index of refraction n_2. (b) Light with a sufficiently short wavelength is confined to the core by total internal reflection.

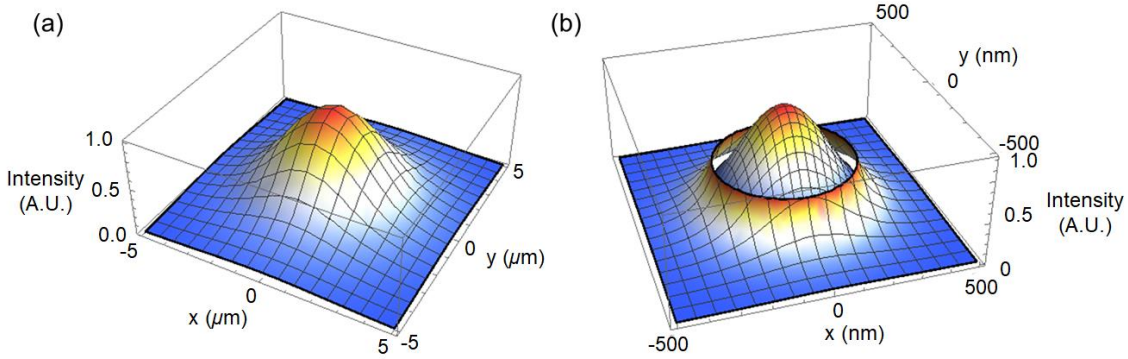

Fig. 6.3 - (a) Simulated transverse intensity profile of 780 nm light in our unmodified fiber as a function of distance *x* and *y* from the center of the fiber. The radius of the core is 2.5 µm and the outer radius of the cladding radius is 62.5 µm. The mode is well-contained in the core. (b) Intensity profile of 780 nm light in a nanofiber with a 250 nm radius. The discontinuity in intensity occurs at the radius of the fiber, with an evanescent wave present outside of the fiber.

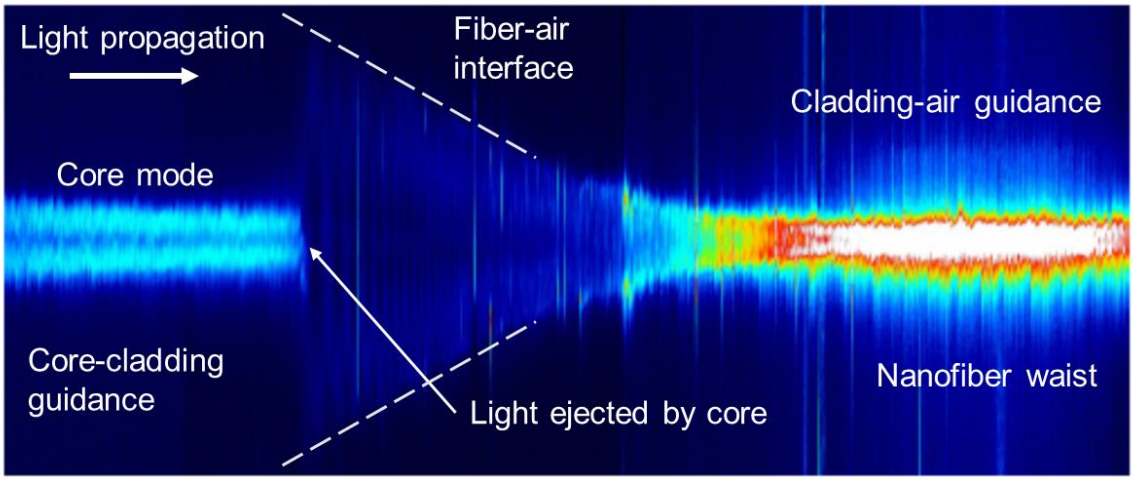

Fig. 6.4 - Rayleigh scattering in tapered optical fiber showing mode transfer from core-cladding guidance to cladding–air guidance. Incident light travels along the fiber, from left to right. Horizontal light blue stripe on left shows where incident light in the core has been Rayleigh scattered. Triangular feature to the right of this shows where core becomes too small to confine the mode and the light transfers to the cladding. Next, light travels into the narrow waist region where scattering is most intense, due to scattering from roughness or contaminants on the surface of the waist introduced during the pulling process. Figure with permission from [6.18].

2.5 μm diameter core and there is negligible intensity at the 62.5 μm outer radius of the cladding. Figure 6.3(b) shows the corresponding intensity profile of a nanofiber that has been drawn down from an outer radius of 62.5 μm to a 250 nm radius. For such a small diameter fiber, part of the mode appears as an evanescent wave that resides in the vacuum, outside of the core and cladding. Examining Fig. 6.3(b), one sees a clear discontinuity in the intensity that occurs at the radius of the nanofiber.

When tapering a standard-diameter fiber to produce a nanofiber with a sub-micrometer radius, the allowed modes change significantly. As the radius decreases along the tapered region, one first reaches a critical point where the mode cannot be contained within the core and leaks into the cladding (see Fig. 6.4) [6.18]. If the taper is sufficiently gradual, the light will remain in the cladding and be guided by the fiber. As the radius

decreases further and approaches a few microns, the mode starts to leak into the vacuum, with the cladding acting as the core and the air or vacuum acting as the cladding. This is the nanofiber limit, where part of the mode propagates outside of the cladding as a tightly confined evanescent wave (Fig. 6.3(b)) that can be used for trapping atoms. With a proper taper geometry, the evanescent wave can be matched to the main mode in the fiber, with very little reflection or loss of light to vacuum.

6.3.2 Trapping Atoms on a Nanofiber: Theory

An optical nanofiber trap confines atoms in the evanescent optical field near its surface. To trap ^{87}Rb atoms [6.18], x-polarized 1064 nm light (red-detuned from the 780 nm transition in Rb) is applied to both ends of the fiber and blue-detuned (760 nm) y-polarized light is applied to one end of the fiber (see Fig. 6.5). The interference of the counter-propagating red-detuned beams creates a standing wave. Since Rb atoms will be attracted to locations where red-detuned light has the highest intensity, each antinode in the standing wave becomes an atom trapping site (see Fig. 6.5 (b)) [6.19]. On the other hand, Rb atoms will be repelled from locations where blue-detuned light has a high intensity. Blue-detuned light is used to prevent atoms from approaching too closely to the fiber, where they would be pulled in by van-der-Waals forces and end up getting stuck to the surface of the fiber. Figures 6.5(c) and (d) show intensity cross-sections of the nanofiber waist for the red-detuned and blue-detuned light, respectively.

By properly choosing the powers of the red-and blue-detuned beams, and properly accounting for the van der Waals potential that attracts atoms close to the nanofiber surface, one can create a trapping potential with a stable minimum at a few hundred nanometers

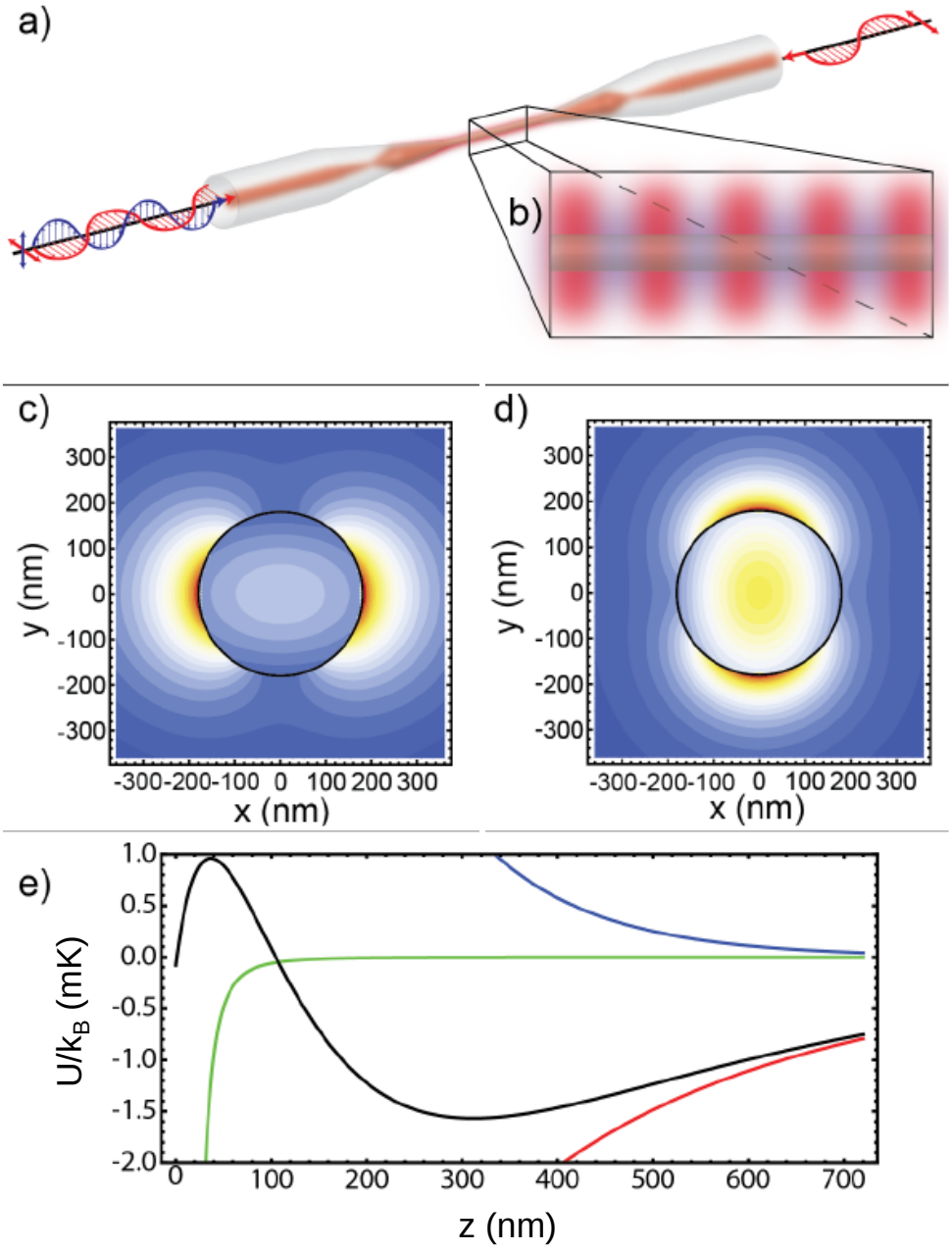

Fig. 6.5 – (a) X-polarized red-detuned light enters both ends of a non-tapered section of fiber, which connects to a tapered section, and then a nanofiber. Y-polarized blue detuned light enters the left end. (b) Detailed view showing blue- and red-detuned evanescent field surrounding the optical nanofiber waist. (c) Intensity of horizontally-polarized light field at an anti-node of the 1064 nm standing wave on the nanofiber waist. High intensity is red, low intensity is blue. (d) Intensity of vertically-polarized light field at a point on the nanofiber waist for 730 nm laser. (e) Trapping potentials *U* as a function of distance *z* from nanofiber waist surface. Green shows van-der-Waals potential, red is attractive potential from red-detuned light (1064 nm), blue is repulsive potential from blue-detuned light (730 nm), and black is the total potential.

from the nanofiber surface (see Fig. 6.5(e)). For the simulation shown in Fig. 6.5(e), the power of the 1064 nm beam was 4.5 mW in a standing wave configuration, the power of the 730 nm beam was 7.5 mW and the resulting potential had a maximum depth of 1.5 mK at about distance of z = 300 nm from the fiber surface.

6.3.3 Tapered Optical Fiber Fabrication

We fabricated tapered optical fibers (TOFs) using a heat and pull method [6.20]. Conceptually, this process involves sweeping a hydrogen-oxygen flame along a fiber while pulling on the ends of the fiber. The flame causes the fiber to melt locally and the pulling causes this melted region to stretch out and reduce its diameter. If the flame is held stationary while the ends are pulled steadily, the taper diameter will decrease exponentially with the pull distance, while the length of the uniform waist region is set by the size of the flame (see Fig. 6.6 (a)). Typically, this yields a rapid change in fiber radius as the pull proceeds and results in a significant amount of light loss due to poor matching of the main fiber mode to the evanescent mode in the nanofiber waist. Instead, by sweeping the flame along the fiber in a precise oscillatory manner as the fiber is pulled, a gentle taper and a waist with a chosen length and diameter can be produced. If the angle of the taper is small enough, up to 99.95% of the light will remain contained in the fiber [6.12]. Nanofibers (with waist diameter below 1 μm) and microfibers (with waist diameter between about

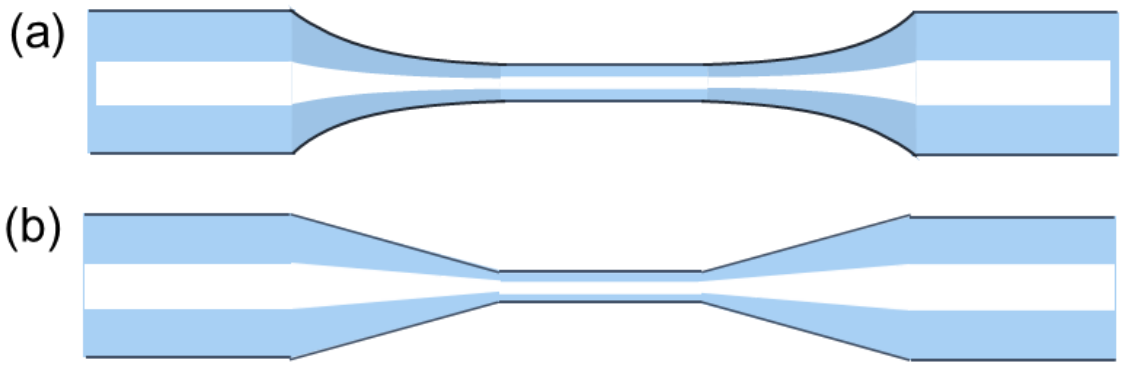

Fig. 6.6 - Taper profiles for optical nanofibers. (a) Without sweeping the flame nozzle, the diameter of the fiber in the tapered region decreases exponentially, resulting in light loss at the sharp angle where the taper begins. (b) Sweeping the flame nozzle while pulling can be used to produce a gentler taper profile that allows adiabatic transfer of light into and out of the waist with minimal light loss.

100 μm and 1 μm) are fabricated in similar ways but with different pulling parameters.

The tapered optical fibers (TOF) I used were fabricated by Jonathan Hoffman. Hoffman's thesis [6.18] contains a detailed description of the apparatus and the procedure, and the following is a brief summary. The flame was made using two parts H_2 and one part O_2, so that the resulting byproduct was water. The gas mixture was delivered to a nozzle that was made of a relatively long stainless-steel cylinder with many small holes drilled closely together parallel to the axis so that the flame was laminar. This was important for achieving a precise fiber geometry and preventing the fiber from breaking during the pulling process [6.18]. The flame was ignited by an electric heater made from a platinum wire catalyst to minimize the generation of contaminants that could degrade the fiber's surface.

The pulling apparatus (see Fig. 6.7) was located under a nominally class-100 clean room to prevent dust from reaching the fiber surface, which can cause the fiber to break

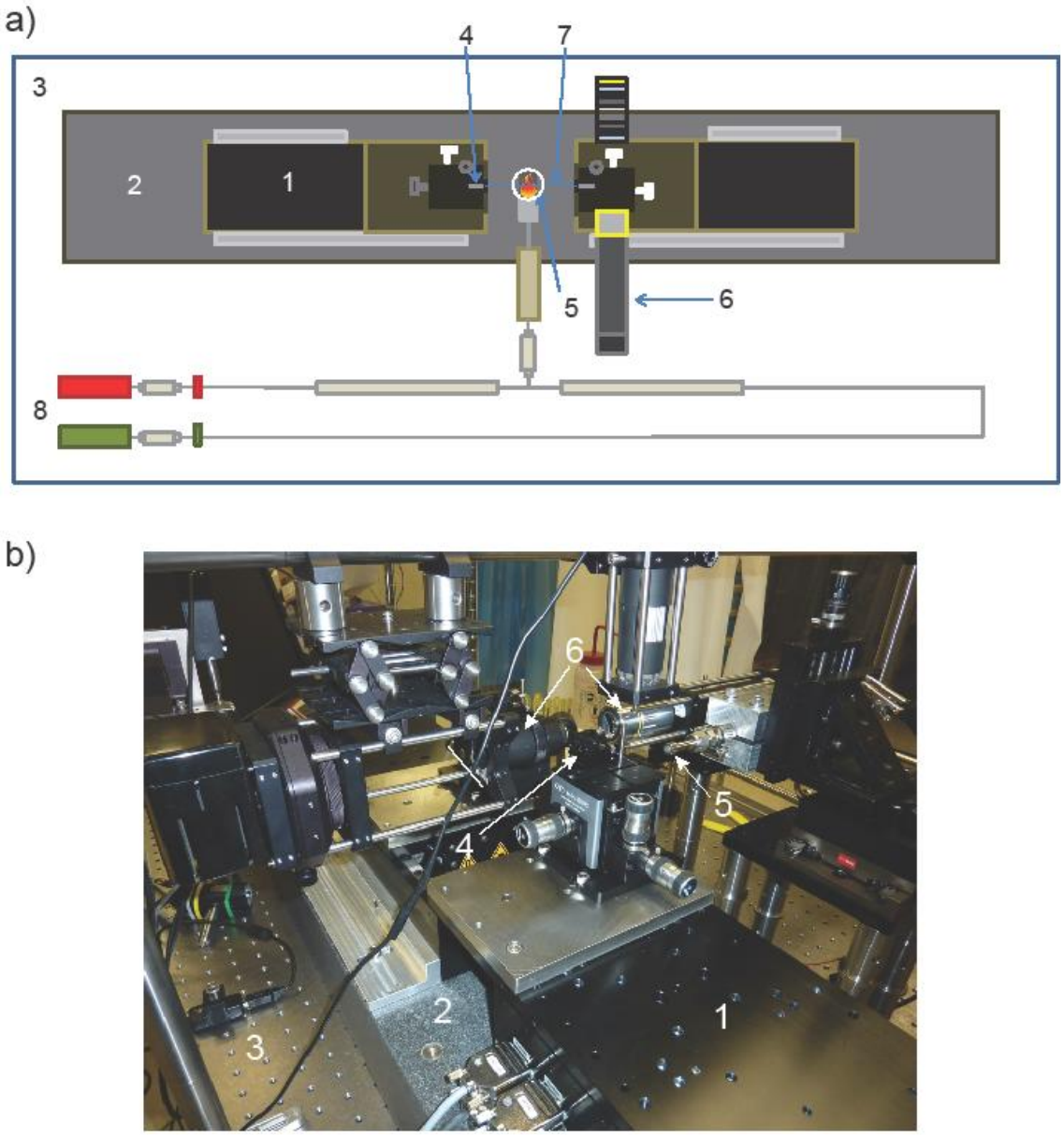

Fig. 6.7 - (a) Diagram of optical fiber pulling apparatus. (b) Photograph of fiber puller showing: 1) x-translation stage, 2) granite slab, 3) optical table work bench, 4) fiber clamps, 5) flame nozzle, 6) alignment camera, 7) fiber being pulled, and 8) gas lines for H_2 and O_2.

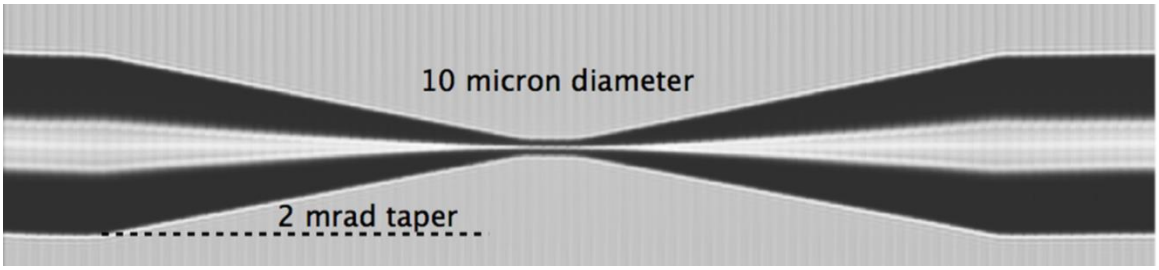

Fig. 6.8 - Image of a tapered optical fiber made of 96 individual photos that were stitched together. The vertical bands are artifacts from the stitching process and the dark and light horizontal regions of the fiber on the left and right are lensing artifacts. The image has been compressed laterally and stretched vertically by about a factor of 100 to 1, such that the actual taper angle of 2 mrad (or 0.115^{o}) appears to be $\sim 10^{o}$ in the image. The diameter of thinnest section is 10 μm.

during the pulling process or reduce the final transmission through the fiber. The apparatus has two motorized x-translation stages (Newport XML 210) sitting on top of a large slab of granite. The mass and stiffness of the granite reduces shaking of the apparatus as the stages move.

To begin the pulling process, an unmodified SM800 fiber was stripped of its protective plastic buffer and cleaned thoroughly with acetone and methanol. Hoffman *et al.* found that the cleaning process was important to achieving high transmission [6.12]. After cleaning, the fiber was clamped in place on either side of the stripped region and imaged to verify that it was clean. Next, the flame was lit and the automated translation stage moved the flame into the fiber and then began to scan the fiber back and forth in front of the flame, while pulling the ends of the fiber apart. The motion followed an algorithm to optimize the final geometry of the tapered section and set the length and diameter of the waist [6.18] (see Fig. 6.8). We monitored the light transmission of a laser through the fiber before, during, and after the pull. The characteristic transmission of a completed TOF was

obtained by dividing the time averaged transmission (over several seconds) at the end of the pull by that just before the beginning. At the conclusion of the pull, the flame was pulled away from the TOF, which was then carefully transferred to a fiber holder, where it was epoxied in place or temporarily held with adhesive tape to be epoxied later.

6.4 Microfiber and Fiber Holder Specifications

For the microfiber-chip experiment, we used Fibercore SM750 optical fiber and pulled to achieve input and output taper angles of 5 mrad (see Fig. 6.9) and a 20 mm long waist with a nominal diameter of 50-56 μm. With this geometry, 780 nm light should be completely contained within the core. The transmission of all the microfibers was measured to be above 99%.

Table 6.2 gives the characteristics of the four different fibers I used for the four versions of the microfiber-chip experiment. The first three fibers were designed to have a 50 μm waist diameter, while the fourth was designed to have a 56 μm waist. Note that the waist diameter of the fiber used in version 3 varied between 49 and 54 μm over the 20 mm long waist. This was caused by a mechanical problem with the fiber puller. Although this was a significant variation, it was relatively gentle on a 1 mm length scale (the size of the chip), and did not affect the light scattering or transmission in the fiber. I also note that in version 4, I used a microfiber with a 56 μm diameter because issues in the pulling system at that time caused transmission rates under 99% in the 50 μm diameter microfibers; a loss of 1% was unacceptable for our low-temperature application.

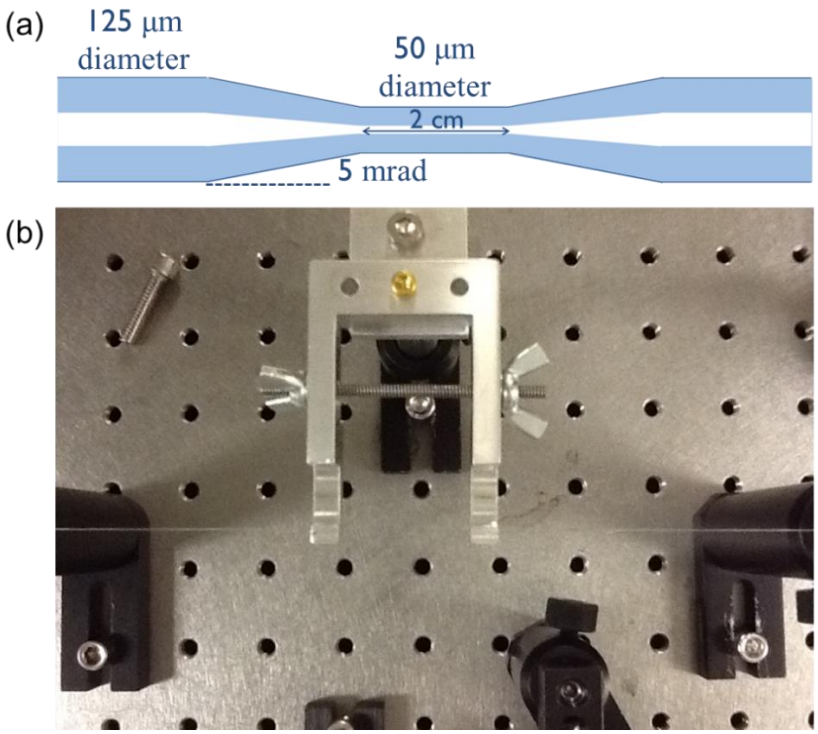

Fig. 6.9 - (a) Diagram showing nominal dimensions of microfibers used in versions 1 to 3 of the microfiber chip experiment. (b) Photograph of a microfiber above the aluminum microfiber holder prior to being epoxied. Note threaded rod and wing nuts.

Table 6.2 - Summary of characteristics of the four microfibers used in the microfiber-chip experiment. Here, d is the diameter of the waist, ℓ is the length of the waist, θ is the taper angle, T_r is the optical transmission through the fiber, m_T is the mass used to apply tension to the fiber, L_T is the distance the fiber mount was compressed during tensioning. The diameter of the waist of fiber #3 varied along the fiber's length due to issues with the pulling apparatus. Fibers #2 and #3 had transmission that was comparable to that of fibers #1 and #4, but precise values were not recorded. For fiber #1, we did not carefully measure the pre-tensioning prior to epoxying and the combination of UV epoxy and 5 minute epoxy failed during the cool-down.

Fiber #	d (μm)	ℓ(mm)	θ (mrad)	T_r	m_T (g)	L_T (μm)	Epoxy Type
1	50	20	5	~99.8 ± 0.1 %	-	200	UV epoxy and 5 min epoxy
2	50	20	5	-	16	150	Black Stycast 2850FT
3	49-54	20	5	-	16	150	Black Stycast 2850FT
4	56	20	5	99.5 ± 0.2 %	20	150	Black Stycast 2850FT

To mount a microfiber without damaging or destroying it, we epoxied the fiber to the arms of a fork-like fiber holder (see Figs. 6.9(b) and 6.10). This procedure was developed after some trial and error. When mounted, a fiber needed to be under tension to prevent sagging and minimize vibrational motion. Vibrations of the fiber would add uncertainty to the distance between the fiber and resonator, produce time-dependent variations in the resonance frequency and Q, or allow the fiber to contact the chip. Although the Triton dilution refrigerator has vibration isolation that minimizes shaking from the pulse tube stage and external mechanical noise, some vibration-exciting impulses do occur [6.21]. Since the fiber would potentially be within a few μm of the chip, even quite small vibrations were undesirable. In addition, when the Al fiber holder cools, it contracts more than the glass fiber, causing the fiber tension to decrease.

To prevent these issues, we pre-tensioned the fiber at room temperature (see Fig. 6.9(b) and Table 6.2). With sufficient pretension we could ensure that the cold fiber would not sag. By keeping the fiber under tension, we also raised the frequency of the lowest string mode so that the fiber responded less to low-frequency mechanical noise.

After a fiber was pulled, we tensioned it by holding one of the untapered ends in a clamp and draping the other untapered ends over a horizontal rod. We then hung a mass m_T from the free end, to apply a known tension. We next compressed together the arms of the fiber holder by placing a threaded rod through both tensioning-holes (see Figs. 6.9(b) and 6.10), securing both sides with wing nuts and tightening by a predetermined distance L_T. We found that the incidence of fiber breakage was less when we used this compress-and-tension technique as opposed to only tensioning the fiber with a relatively large mass. We determined good values for L_T and m_T which we could reliably apply, by making several

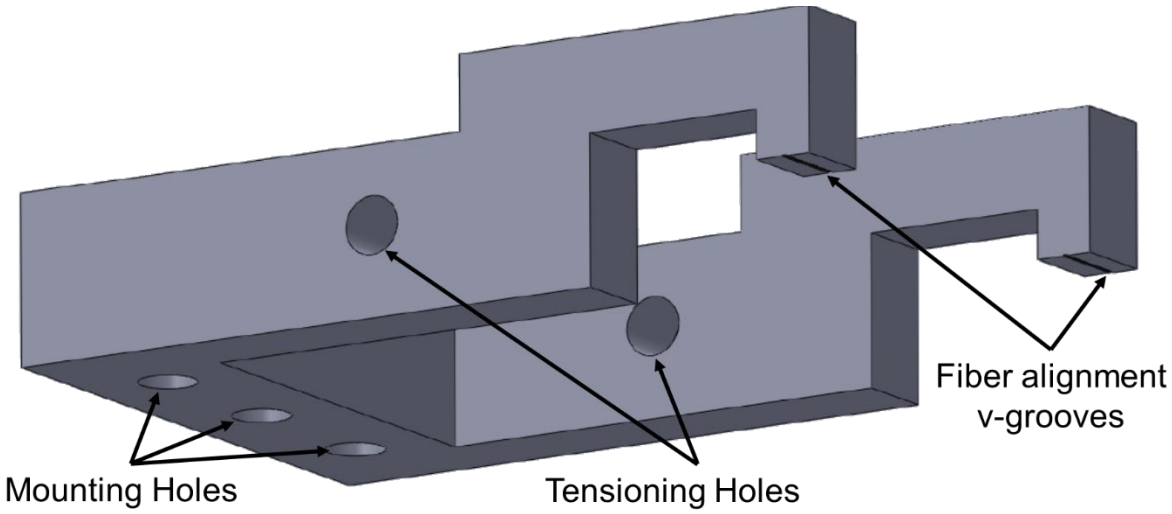

Fig. 6.10 - CAD drawing of the Al fiber holder used to mount fiber #4. The three mounting holes were used to attach the fiber holder to the fiber block (see Fig. 6.1). This version had more clearance for the SMA connectors than the version shown in Fig. 6.1, which was used for Fibers # 1-3. The fiber was epoxied next to the fiber alignment v-grooves, which provided a reference. The two tensioning holes accepted a threaded rod for compressing together the arms of the fiber holder while the epoxy cures, as seen in Fig. 6.9(b).

test fibers and epoxying them with different amounts of tension applied. Table 6.2 reports the values used for fibers #2-4.

With the fiber pre-tensioned and the fiber holder compressed, we mounted the fiber holder to an x- and z-translation stage on the setup breadboard. The two fiber clamps holding the fiber straddled the fiber holder, such that the fiber was held in place while the fiber holder was translated close to the fiber. We placed the fiber parallel to, but not in, the fiber alignment v-grooves (see Fig. 6.10). We then moved the fiber holder until the fiber was positioned within about 1 mm of the surface of the fiber holder pads, but not touching them, and applied black Stycast 2850FT. To prevent the fiber from being too close to the sharp edge of the fiber holder, which could cause it to break when we released the

compression in the fiber holder, we tried to apply the Stycast so that it completely surrounded the fiber. The Stycast was then cured for 24 hours. After curing, if the fiber was still intact, we gradually released the pressure on the tensioning rod, allowing the fiber holder to expand and further tension the fiber. If the fiber survived tensioning, we proceeded to the next stage of assembly.

For fiber #1, we used UV epoxy because it was found to not mechanically damage the fiber. However, thermal cycling tests revealed that the UV epoxy would sometimes disconnect from the aluminum holder during cool-down or warm-up. In an attempt to prevent this, we applied 5-minute epoxy on top of the cured UV epoxy. The 5-minute epoxy did not directly contact the fiber, but instead covered the UV epoxy and held it in contact with the aluminum holder. This method seemed to work during thermal cycling tests in liquid nitrogen. However, during version 1 of the micro-fiber experiment, both epoxies failed on one side of the Al fiber holder during the cooldown, leaving the fiber intact but not held in a fixed position.

After failing to secure fiber #1 with Stycast, we did some more testing and found that using black Stycast 2850FT did not damage the fiber as it cured and that the fibers seemed to survive thermal cycling. For the rest of the fibers, we used this low-temperature epoxy and had no further issues with epoxy failure. Starting with fiber #2, we also used pre-tensioning of the fiber with a hanging mass, as described above. This allowed us to set the tension in the fiber before it was epoxied. In fiber #1, the magnitude of the pre-tension force was not well-known because we placed the fiber in the clamps by hand.

6.5 Attocubes

In order for our proof-of-principle experiment to accurately simulate the operation of a hybrid system, we needed to be able to position the fiber very precisely, on the μm scale, with respect to the inductor in the superconducting resonator (see Fig. 6.11). Ideally the fiber should be parallel to the thin-film aluminum line that forms the inductor in the LC resonator; I will call this direction the y axis. In Fig. 6.11 this corresponds to $\theta = 90°$ and $\varphi = 0°$. While it is important to align the chip and fiber at room temperature, differential thermal contraction may change both their relative position and alignment during cooling. To allow *in situ* positioning of the chip relative to the fiber, we used attocube translation stages [6.22]. The main advantage of an attocube is that it can make sub-μm steps at millikelvin temperatures.

Figure 6.12 illustrates the operating principle of an attocube, which involves a piezoelectric driven stick-and-slip motion. A voltage is applied to the piezo relatively slowly, allowing the piezo to extend and move the guide rod, clamped table, and flexible membrane as static friction holds them together. The voltage is then turned off suddenly, quickly retracting the piezo and letting the guide rod slip through the jaws holding it to the clamped table. This leaves the clamped table in a new position and the guide rod and flexible membrane at their starting position. This process can be repeated by applying a sawtooth voltage to move the table a chosen distance, up to 5 mm for our attocubes. The amplitude and frequency of this voltage is controlled by the ANC300 attocube controller.

In order to position the resonator with respect to the fiber in the x and z directions, I stacked an x-attocube on a z-attocube stage. To allow rotational alignment of the resonator and fiber, I would need to add attocubes for the θ and ϕ directions, but this was left for

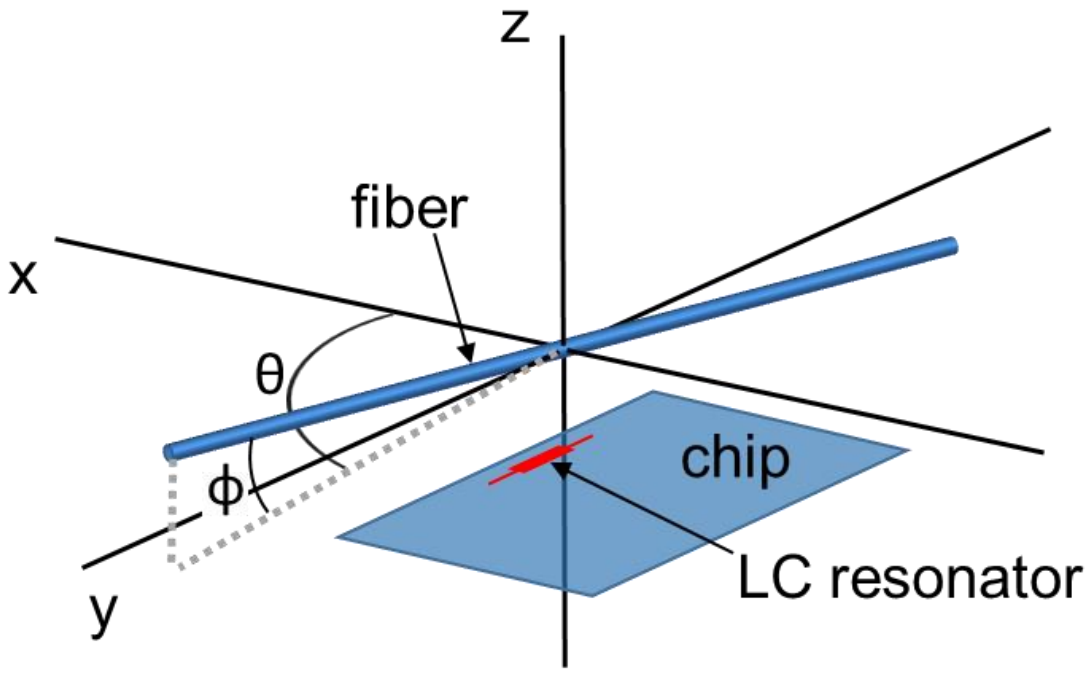

6.11 - Coordinate system for the microfiber and chip in the microfiber-chip experiment.

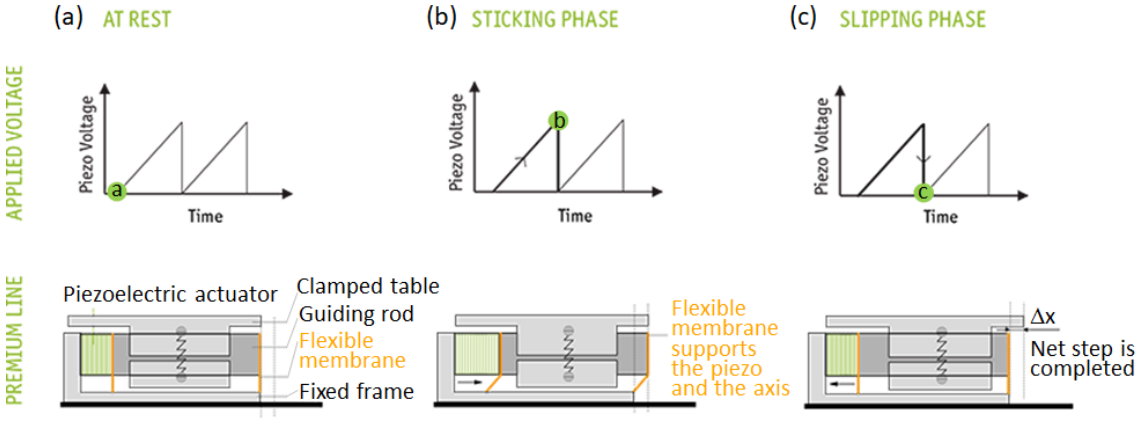

Fig. 6.12 - Figure from ref. [6.22]. (a) With no voltage applied to the piezo-electric actuator, the table is clamped in place. (b) In the sticking phase, the voltage on the piezo is slowly increased, and the guiding rod, flexible membrane, and table move as static friction holds them together. (c) In the slip phase, the voltage is suddenly reduced and the piezo and the guiding rod move, while the table stays in place. Each period in the sawtooth voltage corresponds to a step in the attocube motion. Repeated steps allow the stage to be translated by up to 5 mm.

future versions. Instead all rotational alignment was done manually at room-temperature during assembly. For the attocubes to move reliably, I also needed to make sure that the weight on each attocube did not exceed the maximum weight limit [6.22]. For example, the z-attocube had to carry the x-attocube, a spacer block, and the cavity, with a combined mass of 60 g, which was less than the 100 g limit.

Figure 6.13 shows a wiring diagram and some other details for the experimental setup. Microwaves were generated by a vector network analyzer (VNA) and sent down a coax through attenuators with a total of 50 dB of attenuation. The input coax had an additional attenuation of 18 dB at 6.8 GHz. The attenuators were thermally anchored at successive temperature stages in the refrigerator to reduce Johnson-Nyquist noise from room temperature and the higher temperature stages. The microwaves were coupled into the cavity and the output from the cavity was amplified by a low-noise amplifier mounted on the 1 K stage and by a Miteq amplifier at room temperature before being fed back into the input of the VNA. There were also a pair of isolators (not shown) at the output of the cavity to prevent noise from higher stages and reflections at the amplifiers from entering back

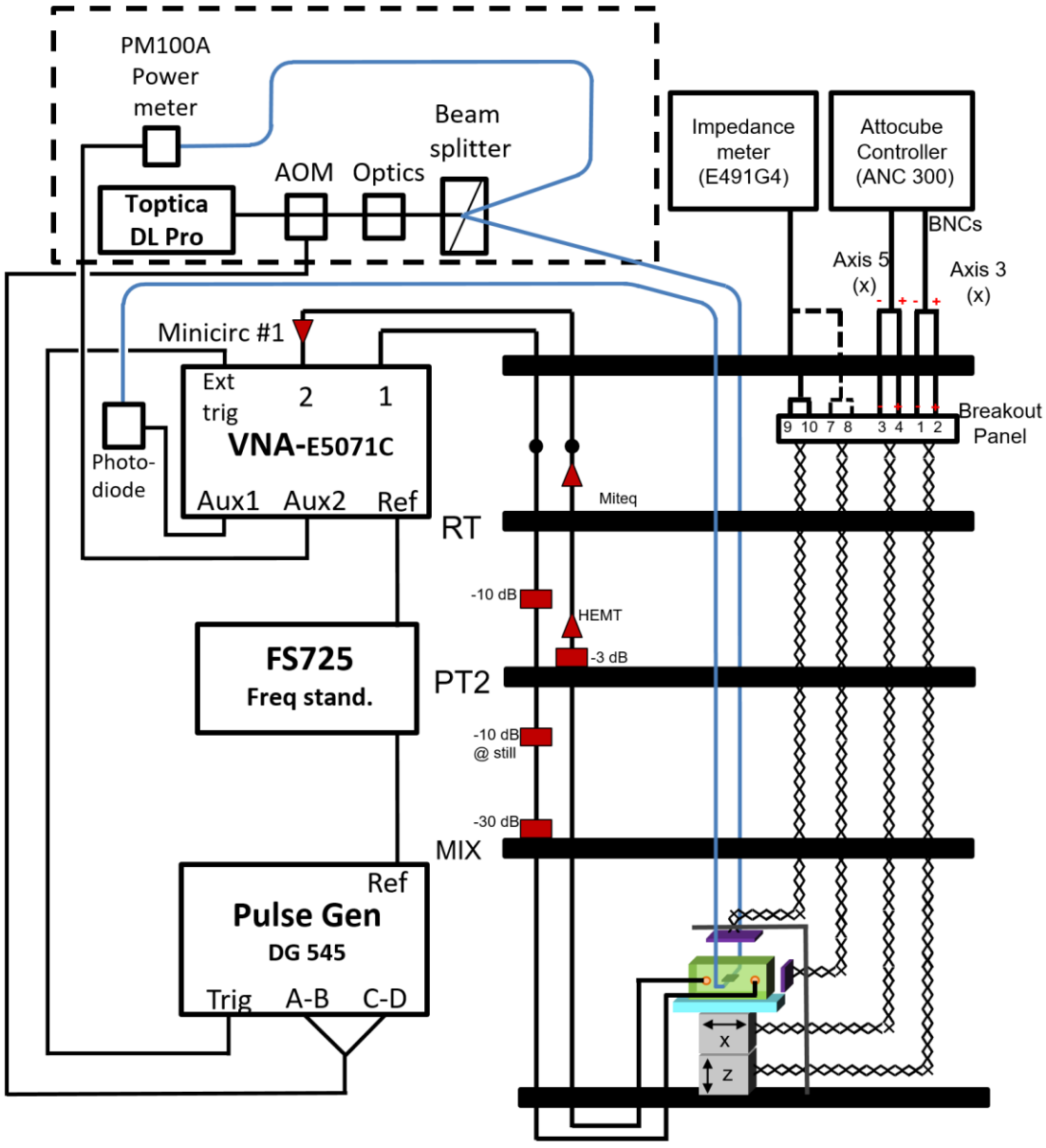

6.13 - Wiring and measurement layout for version 3 of the microfiber-chip experiment. Blue lines show optical fiber. Green box is Al cavity mounted, which is mounted on x and z attocubes.

into the cavity via the output line.

The attocubes are mounted on the mixing chamber and connect to the room-temperature electronics through a low-impedance loom supplied by Oxford. The loom

wires were thermally anchored to each stage and connected to a short section of twisted pair wires in a breakout box at the mixing-chamber stage. At room temperature, the loom wiring connected to a breakout panel and homemade cable with multiple twisted-pair wires. Upon exiting the refrigerator, the wires went to a breakout box that split the wires into separate BNC connections on the wall of the screen room. Each attocube had two BNC connections (one for power and one for ground) and we used a BNC expander at the shielded room wall to connect each BNC power/ground pair into a single coaxial cable, which was then connected to the attocube controller (ANC300).

Operation of the attocubes was imperfect. At low temperatures, we found that the attocubes movement was not entirely consistent or repeatable. In particular, the motion did not occur for every voltage step. The most reliable motion we could obtain was by operating using a sawtooth voltage of 70 V and a frequency of 1 kHz. Also, the movement of the attocubes caused significant heating at mK temperatures, and we had to take care to thermally anchor them. To cool the lower section of the z-attocube, it was directly bolted to the Cu experimental plate. To cool the top of the z-attocube and the bottom of the x-attocube, one end of a strip of high-purity Cu was thermally anchored to the Cu experimental plate and the other end was connected between the z- and x-attocube. To cool the top of the x-attocube and the cavity, another Cu strip was attached between the cavity and adapter/spacer plate, and anchored to the experiment plate (see Fig. 6.14).

Typically, we moved the attocube several hundred steps at a time. With the

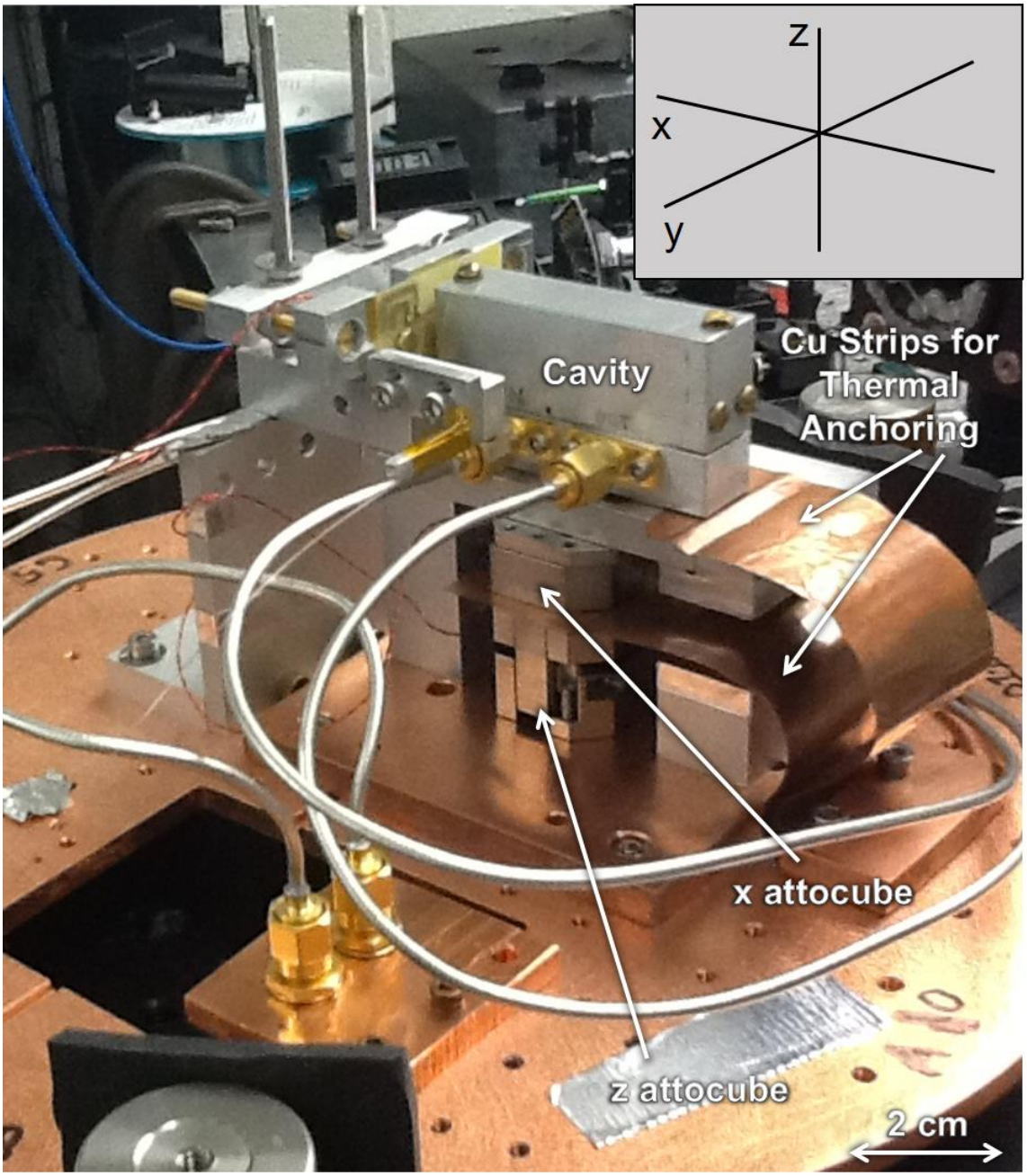

Figure 6.14 - Photograph of version 4 of the microfiber-chip experiment, with coordinate system shown in inset in upper right. The curving silver-colored tubes are long flexible sections of coaxial cables for the input and output microwave lines that maintain the microwave connection with the cavity as it is moved.

refrigerator at an initial temperature of about 12 mK, the temperature of the mixing chamber would climb to several hundred mK within the first few seconds of moving an attocube. It would then take about 45 minutes for the temperature to return back to 15 mK and another 45 minutes to reach base temperature. For this reason, we typically ran the experiment at 100 mK, a temperature at which the resonator still had high *Q* but the recovery time after attocube heating was only 10 to 15 minutes.

Although the specifications for the attocube list a step size, we found that the actual step size varied and occasionally no motion occurred during a step. Also, the load on the attocube affected the step size. Since the load on the attocubes was slightly different from one version to the next, and thermal cycling seemed to affect their performance, I checked the motion of each attocube at room temperature before every cool down. To do this, I repeatedly extended and retracted the attocubes and used an optical imaging system to measure the distance they traveled after applying a known number of steps.

In Table 6.3, I list the measured room temperature extend and retract step sizes Δx_{ext}, Δx_{rtr}, Δz_{ext} and Δz_{rtr} for the x- and z-attocubes, respectively, for the four versions of the Microfiber-Chip experiment. These step sizes let me convert the number of steps in the

Table 6.3 - Room temperature calibration of the extend (ext) and retract (rtr) single step sizes Δx_{ext}, Δx_{rtr}, Δz_{ext} and Δz_{rtr} for the x and z attocube stages for all four versions of the Microfiber-Chip experiment. V_s is the voltage amplitude used to drive the attocube. The uncertainty in each step size is approximately 0.05 μm.

Version	Date	V_s (V)	Δx_{ext} (μm)	Δx_{rtr} (μm)	Δz_{ext} (μm)	Δz_{rtr} (μm)
1	12/17/13	30	1.5	1.4	2	1.6
2	6/30/14	70	2.19	1.95	1.48	1.85
3	3/12/15	70	2.06	2.22	1.52	1.75
4	12/16/15	70	2.06	2.22	1.47	1.71

sawtooth voltage into an approximate distance that the chip moved with respect to the fiber. For example, in the first version, one step forward by the x-stage gave Δx_{ext} = 1.5 μm while one step backwards gave Δx_{ext} = 1.4 μm. After version 1, I decided to calibrate the attocubes at 70 V, which was the same voltage I used at mK temperatures.

Once the attocubes were cold, the step size was smaller than it was at room temperature. We determined the cold step size in a test run in which we removed the inner heat shields of the dilution refrigerator, allowing us to directly observe the motion through a viewing port while the system was cold. Table 6.4 shows the resulting measured step sizes for temperatures down to 200 mK. We found that the step size at low temperatures was a factor D = 3.5-4.7 times smaller than at room temperature. While we only reached 200 mK with the shields removed, I do not expect the step size to change significantly for temperatures below a few Kelvin.

Table 6.4 - Extend (ext) and retract (rtr) step sizes for the x and z attocubes as a function of temperature. The factor $D(T)$ is the ratio of the step size at room temperature to the step size at temperature T. For example, at room-temperature the x-attocube extends by a factor $D_{xext}(9\text{ K}) = \Delta x_{ext}(300\text{ K})/\Delta x_{ext}(9\text{ K}) = 3.4$ more than it does at 9 K. All numbers are for a 70 V drive voltage.

T (K)	Δx_{ext} (μm)	D_{xext}	Δx_{rtr} (μm)	D_{xrtr}	Δz_{ext} (μm)	D_{zext}	Δz_{rtr} (μm)	D_{zrtr}
300	1.61	1.0	1.77	1.0	1.66	1.0	1.82	1.0
70	0.76	2.1	0.80	2.2	0.78	2.1	0.96	1.9
9	0.47	3.4	0.45	3.9	0.38	4.4	0.45	4.0
0.2-0.26	0.47	3.4	0.44	4.0	0.37	4.5	0.39	4.7

6.6 Inductive Position Sensors

The attocubes did not have position monitoring and feedback. Of course, we could estimate changes in the position by keeping track of the number of extend and retract steps and then using the calibration of the step size. This estimated position turned out to be too unreliable because the attocubes did not always move when they were pulsed or the step size would sometimes change unpredictably. For this reason, we added x and z position sensors to monitor the stage motion *in situ*.

We first implemented position sensors in the second version of the experiment. These sensors were designed by Jared Hertzberg and Liam Fowl and used two 4.7 μH air core inductors connected in series. Each inductor consisted of a small coil of wire, about 1 mm in diameter and 1 mm long. The coils were mounted at fixed positions near the moveable cavity, with one coil facing and normal to the external x-face of the cavity, and the other coil facing and normal to the external z-face of the cavity. When the coil was close to the cavity wall, its inductance was reduced by screening currents, producing a measurable position dependent signal (this is the same principle used in tuning the LC resonator that I discussed in Ch. 4).

Testing version 2 in the refrigerator revealed that the sensors did not provide enough position sensitivity over the required range. The sensitivity was limited by the fact that the coil diameter and length were comparable to the typical separation from the cavity wall, which could change by about 1 mm, and this produced only relatively small changes in the inductive signal over much of the motion range.

For versions 3 and 4 of the experiment, I designed generations 2 and 3 of the sensors, respectively, with assistance from Alessandro Restelli. Figure 6.15 shows

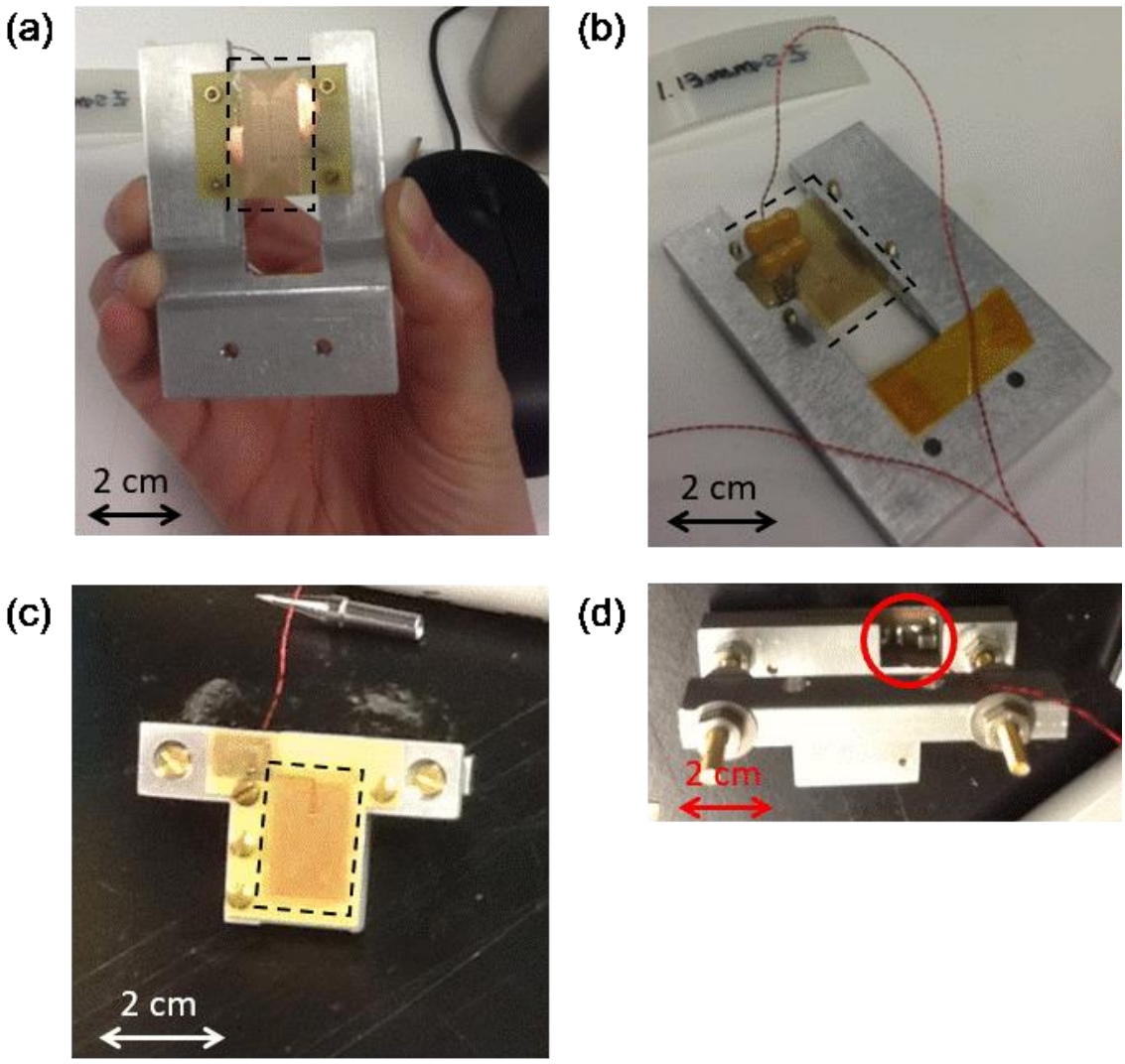

Fig. 6.15 - (a) Photograph of z spiral inductor (in black dashed box) mounted to aluminum sensor holder. (b) Back side of the z spiral inductor. Two capacitors are also visible, soldered to the sensor. (c) Photograph showing x spiral inductor mounted to the sensor holder. (d) Back side of the x-sensor. The surface mount capacitor can be seen inside the red circle, soldered to the x-sensor.

photographs of this setup, in which the inductor was formed from a rectangular spiral coil that was placed close to an external face of the 3D cavity. This geometry produced a magnetic field that extended out from the plane of the spiral where it could be strongly perturbed by screening currents in the 3D cavity wall.

Each coil was mounted on an aluminum holder and connected to the loom wiring using about a foot of homemade twisted pair wires. This allowed me to measure the impedance of the coil as a function of frequency. The impedance showed multiple resonances. One of these resonances was the LC resonance of the coil and the cable capacitance, while the rest were due to standing wave resonances in the measurement wiring, which was not impedance matched at either end. The lowest resonance was below 5 MHz and, as expected, the resonance frequencies were sensitive to changes in the wiring and the distance of the coil from the cavity.

In generation 2, I added two 750 pF silver-mica capacitors in parallel to the input of the spiral inductor to reduce sensitivity to changes in the connecting wires (see Fig. 6.15(b)). Since the added capacitance was much larger than the capacitance presented by the cables, it lowered the LC resonance frequency significantly and made the LC resonance relatively insensitive to the cable impedance. For generation 3, I again modified the z-sensor and x-sensor, this time by using a 1250 pF surface-mounted capacitor in parallel (see Figs. 6.15(c) and (d)). This was more mechanically stable.

I calibrated each sensor at room temperature by mounting it to a translation stage and recording its impedance as a function of the distance from a flat solid metal object (see Fig. 6.16). Although the resonance frequency and resonance curve changed upon cooling down, I assumed that the fractional change in frequency, which was proportional to the fractional change in inductance, would be the same as at room temperature. The sensors could readily detect cavity movements of order 10 μm with the senor separated from the cavity at a working distance of about 1 mm (see Fig. 6.16(b)).

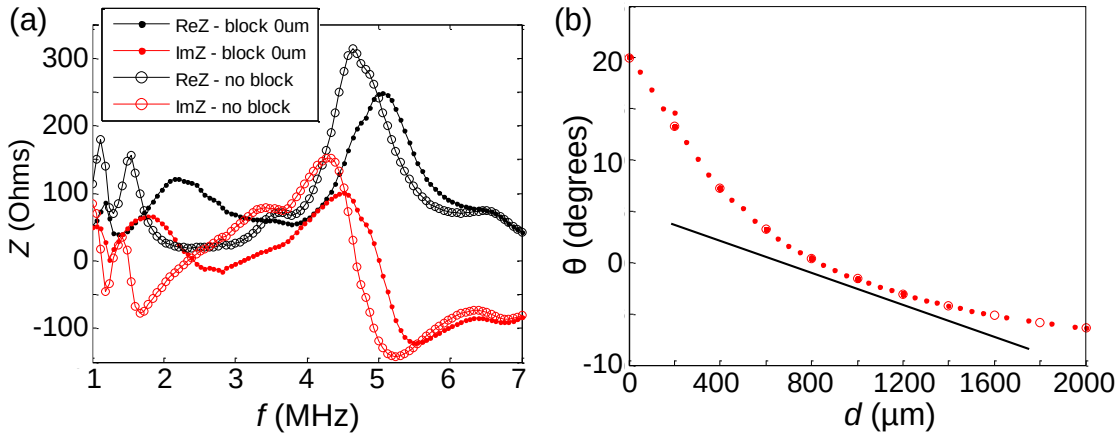

Fig. 6.16 - (a) Room temperature calibration for version 3 of the position sensors showing real part (black) and imaginary part (red) of the impedance *Z* of the z-position sensor as a function of frequency *f*. Open circles are for unperturbed sensor and solid dots are for sensor directly adjacent to metal block. Resonance near 5 MHz increases in frequency as block is introduced. (b) Phase θ of impedance, measured near the unperturbed resonance frequency at 4.82 MHz, as a function of distance d from the block. Black line shows tangent line at the approximate 1 mm working distance of the sensor from the cavity.

6.7 Optical Setup

Figure 6.13 shows a schematic of the experimental set-up for version 3 of the microfiber-chip experiment, including the optical layout. Since much of the experiment involved measuring the optical response of LC resonators, the optical setup was a critical part of the apparatus. Here I provide a brief discussion of the optical system; for a full discussion, see Hoffman's thesis [6.18] and Grover's thesis [6.23].

I used a 780 nm Toptica TA Pro diode laser [6.23] for supplying light to the fiber. The output beam was modulated using an acousto-optic modulator (AOM) that was driven by pulses supplied by a Stanford Research System DG235 pulse generator (see section 7.2). The light then traveled through an optical fiber and an in-fiber beam splitter. One leg of the beam splitter output was measured by a power meter, and the output signal from this

meter was sent to the Auxiliary 2 input of the VNA where it was recorded. The other leg of the fiber beam splitter output was fed through a Teflon ferrule at the top plate of the refrigerator and then spliced to the refrigerators input optical fiber just above the PT2 plate. The input fiber next wrapped 30 times around a 1" diameter stainless steel mandrel mounted to the PT2 stage of the dilution refrigerator. The purpose of the mandrel-wrap was to remove any light that might be propagating in cladding modes of the fiber before it got to the low-temperature stages of the refrigerator. The refrigerator also has an output fiber that travels from the low-temperature stages of the refrigerator, connects to an output 30-turn mandrel wrap at the PT2 stage and exits the refrigerator through the same Teflon ferrule at the top plate, which has two feed-through holes for the fiber in it. The output fiber goes to a photodetector that measures the output power; the signal from the photodetector is recorded by the VNA's Auxiliary 1 channel. From independent measurements of the splitting ratio of the two legs, we were able to use the VNA channel 2 to accurately measure the power being sent into the refrigerator, while the channel 1 signal allowed us to monitor the power coming out. The channel 1 signal was particularly useful for verifying that the fiber was still intact.

6.8 Assembly of Microfiber-Chip Experiment

In this section, I provide a step-by-step description of how I assembled the different parts of the setup for the Microfiber-chip experiment. The assembly was non-trivial and required considerable attention to detail to prevent destruction of the fiber and ensure successful operation at low temperatures. In the following detailed description, I have broken the assembly procedure into seven main steps: (1) inserting the chip into the 3D

cavity, (2) assembling the Attocubes and support infrastructure on the fiber plate, (3) gluing the tensioned fiber to the fiber holder fork, (4) transferring the fiber to the fiber plate, (5) attaching the inductive sensors, and (6) attaching the setup to the refrigerator.

Assembly Step I. Insert Chip into Cavity

1. Flatten out indium wire with a rolling pin.
2. Carefully cut two 3.5 μm x 1.5 μm rectangles from the flattened wire using a razor.
3. Wrap each rectangle around an edge of the resonator chip, covering slightly less than half of rectangle, apply pressure in center of chip with tweezer, and fold indium over sides with another tweezer.
4. Clean vacuum tweezers
5. Pick up chip, place in cavity (be sure to angle it into the dovetail notch in the side of the cavity lip), release vacuum, gently press chip in rest of way with tweezers.
6. Check position of chip under microscope (see Fig. 6.17) and then gently tighten 0-80 set screw while applying pressure to center of chip so it is secured in place.
7. Close the cavity to protect chip.

Assembly Step II. Assemble Attocubes and Fiber Plate

1. Assemble x attocube on top of z-attocube, with flexible Cu strap between z and x attocubes. Put the fiber-plate on the optical work-bench and attach three vertical optics posts around the plate. Place sorbothane between the optics posts and the fiber plate to hold and cushion the fiber plate while it is being worked on.

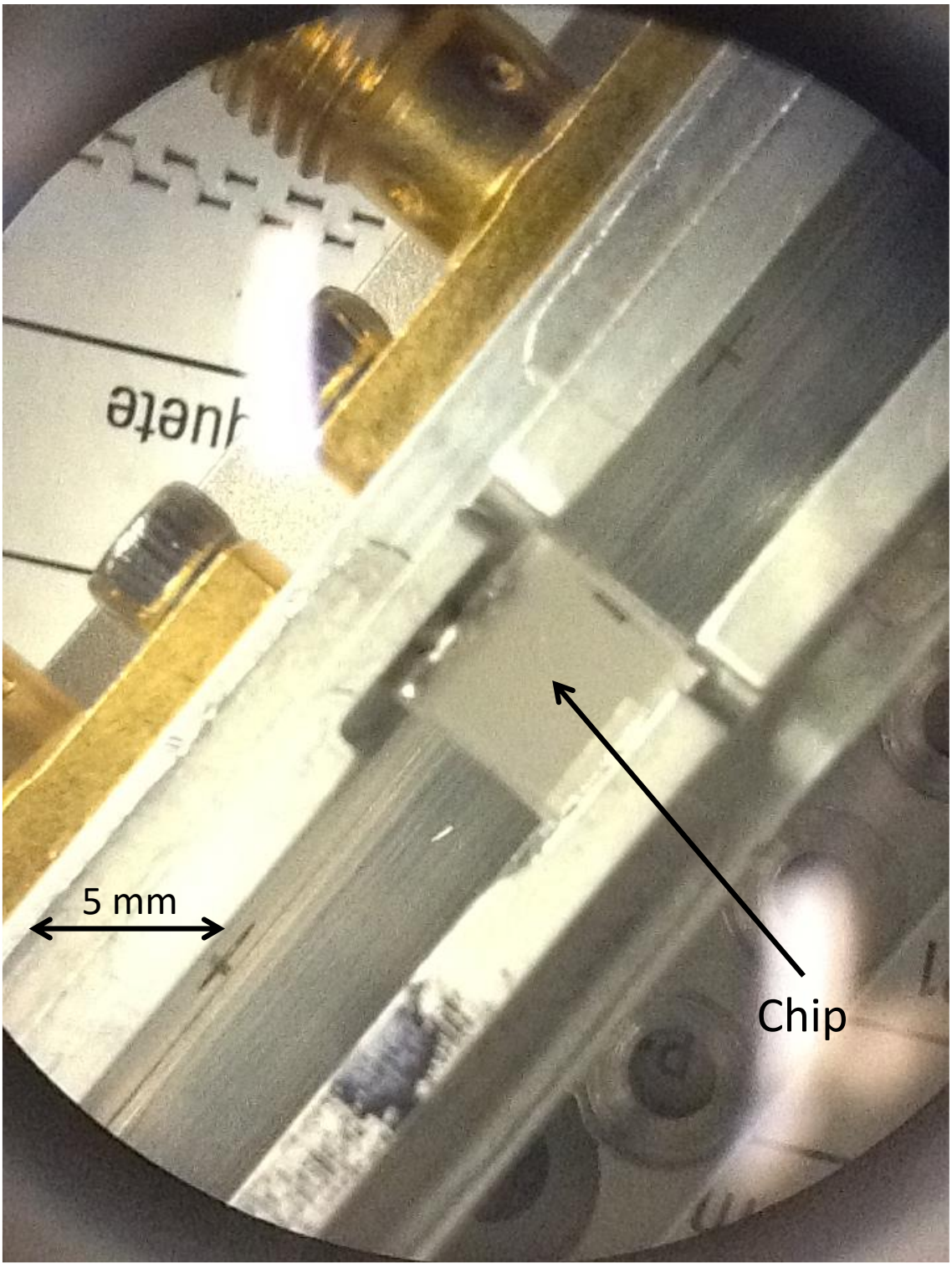

Figure 6.17 - Photograph of the chip secured in the cavity.

2. Attach Cu shim between adaptor plate and cavity, attach one end of a second flexible Cu strip to fiber plate, then attach the other end of the Cu strip to the cavity.
3. Attach SMA cable to cavity. Make sure filed-away portion of SMA connector is facing up and verify that it is not hitting fiber holder.
4. Start with z attocube fully retracted, insert support block, raise z attocube, attach adapter plate to attocubes. The support block prevents the z-attocube from moving.
5. With support block still in place, carefully remove the top of cavity to view chip.

Assembly Step III. Glue and Tension Fiber to Fiber Holder Fork

1. Assemble the fiber-holder-fork measurement setup on the optical breadboard (see Fig. 6.18). Using threaded rod and wing nuts, compress the fiber fork by 150 μm (this assumes a fiber with a 50 μm waist is being used).
2. Screw on fiber-protecting wings to guard against fiber breakage due to excessive bending of the fiber at the glue point (see Fig. 6.19).
3. Assemble the fiber gluing setup on the optical bread board (see Fig. 6.20). Mount fiber holder to x and z translation stage stack and align using a test fiber.
4. Clean and pull the fiber, being sure to leave 4 m of fiber on either end of the tapered section. Secure ends in a loop with Kapton tape. Straddle pulling-rig clamps with a large transfer fiber holder (length ~ 10 cm) and secure fiber to transfer holder with Kapton tape.

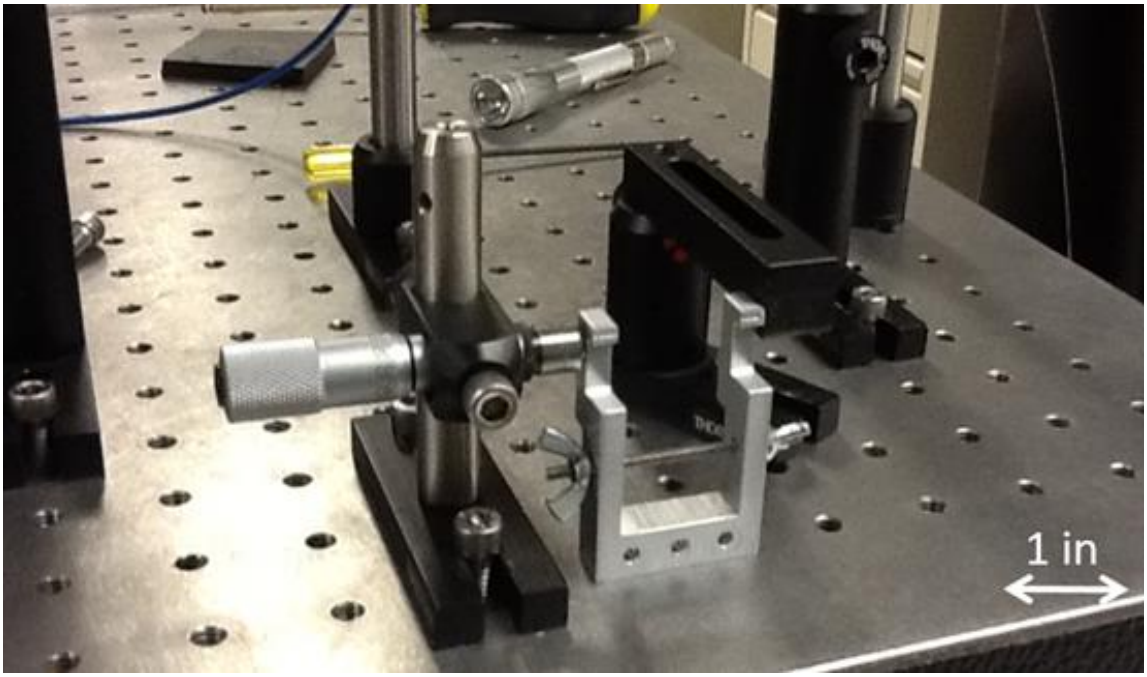

Figure 6.18 - Photograph of fiber-holder fork measurement setup used to measure distance between the outer edges of the fiber holder arms. This measurement was made before and after compression was applied with the threaded rod and wing nuts.

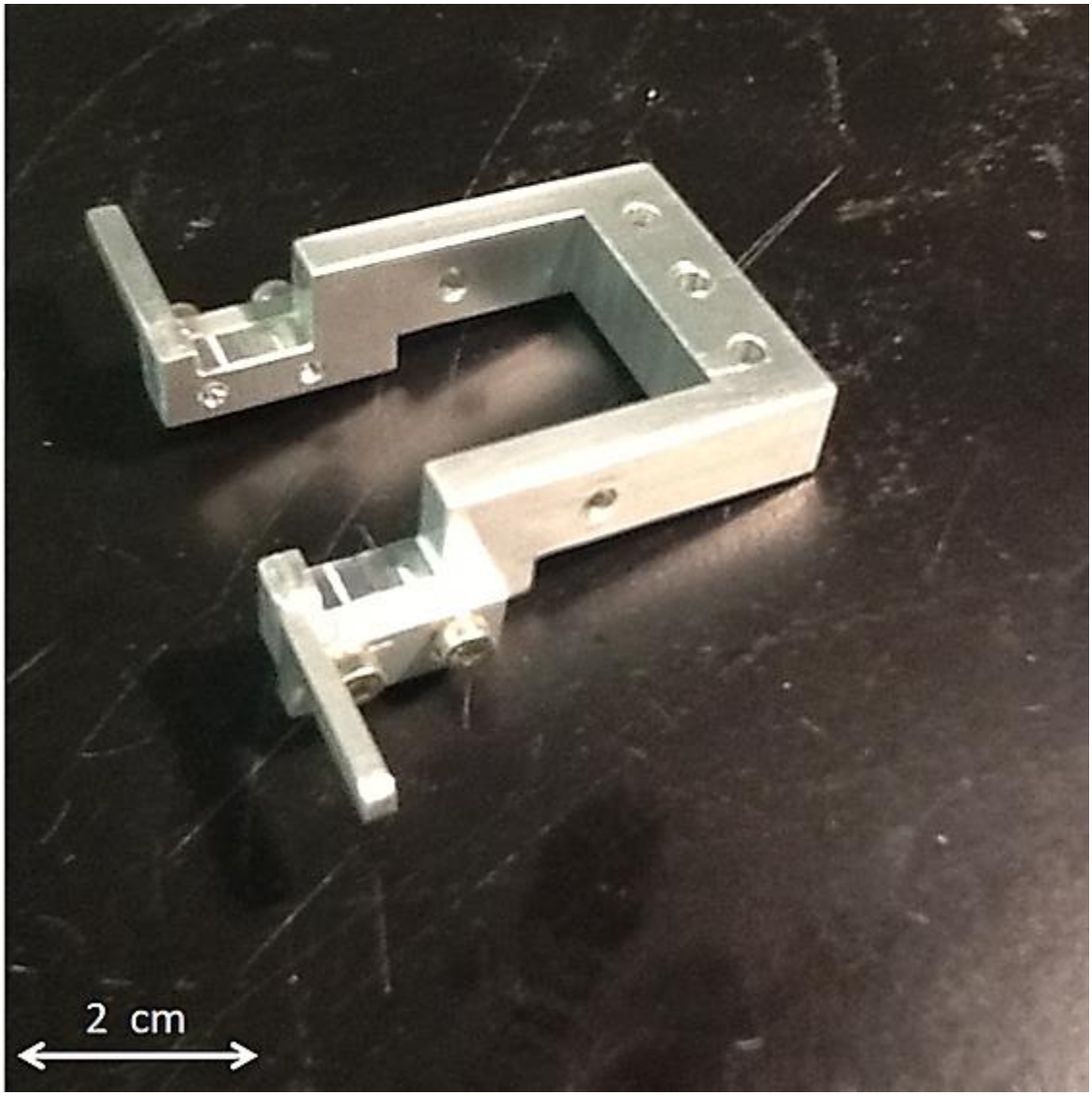

Figure 6.19 - Photograph of fiber holder with the fiber protecting wings secured.

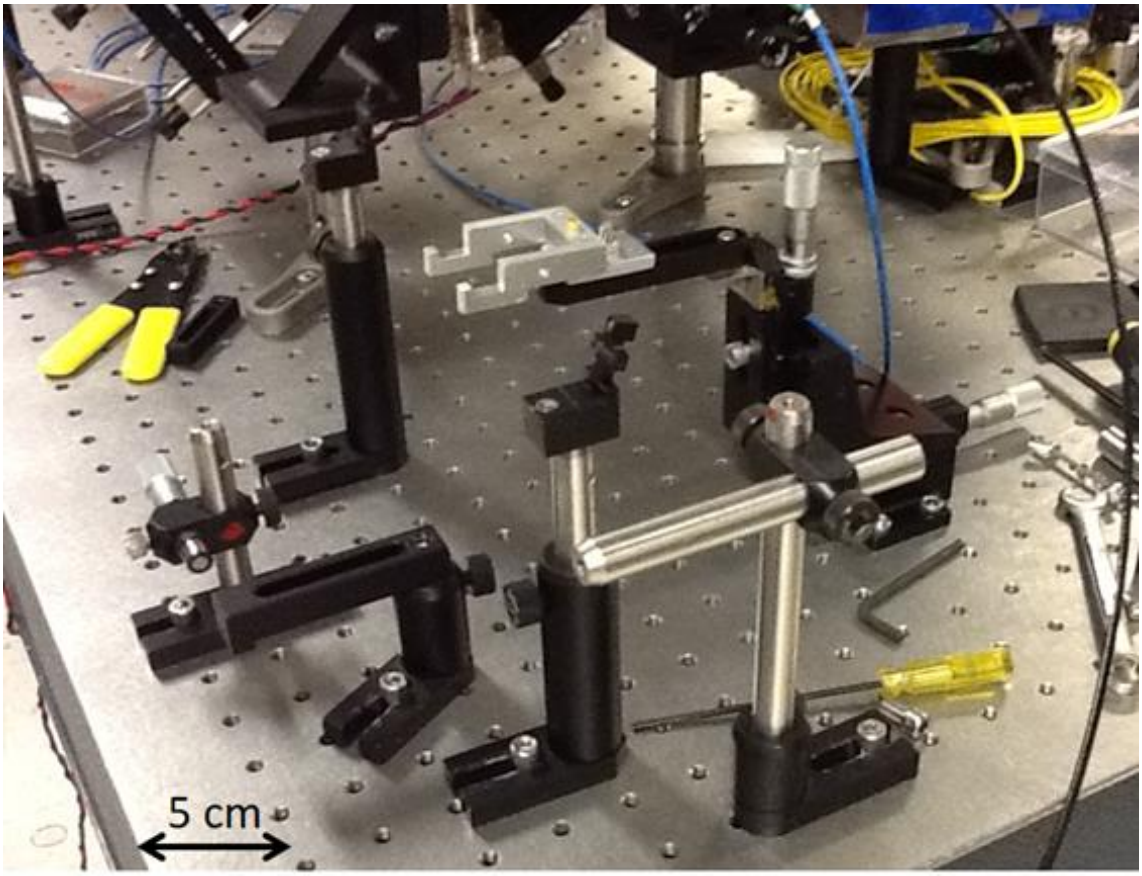

Figure 6.20 - Photograph of fiber gluing setup.

5. Transfer the tapered fiber to the fiber gluing setup (see Fig. 6.21). Adjust the fiber's position and alignment so that the striped portion of the fiber straddles the fiber fork symmetrically and it is less than 1 mm above groves on fiber fork, but not touching the groove.
6. Hang a 16 g weight (assuming 50 μm waist) from the end of the fiber to pre-tension the fiber. Open the fiber clamp to allow the tension from the hanging weight to propagate to the waist portion. Then, reclose clamp, glue with Stycast epoxy, cure for 24 hours (see Fig. 6.22).

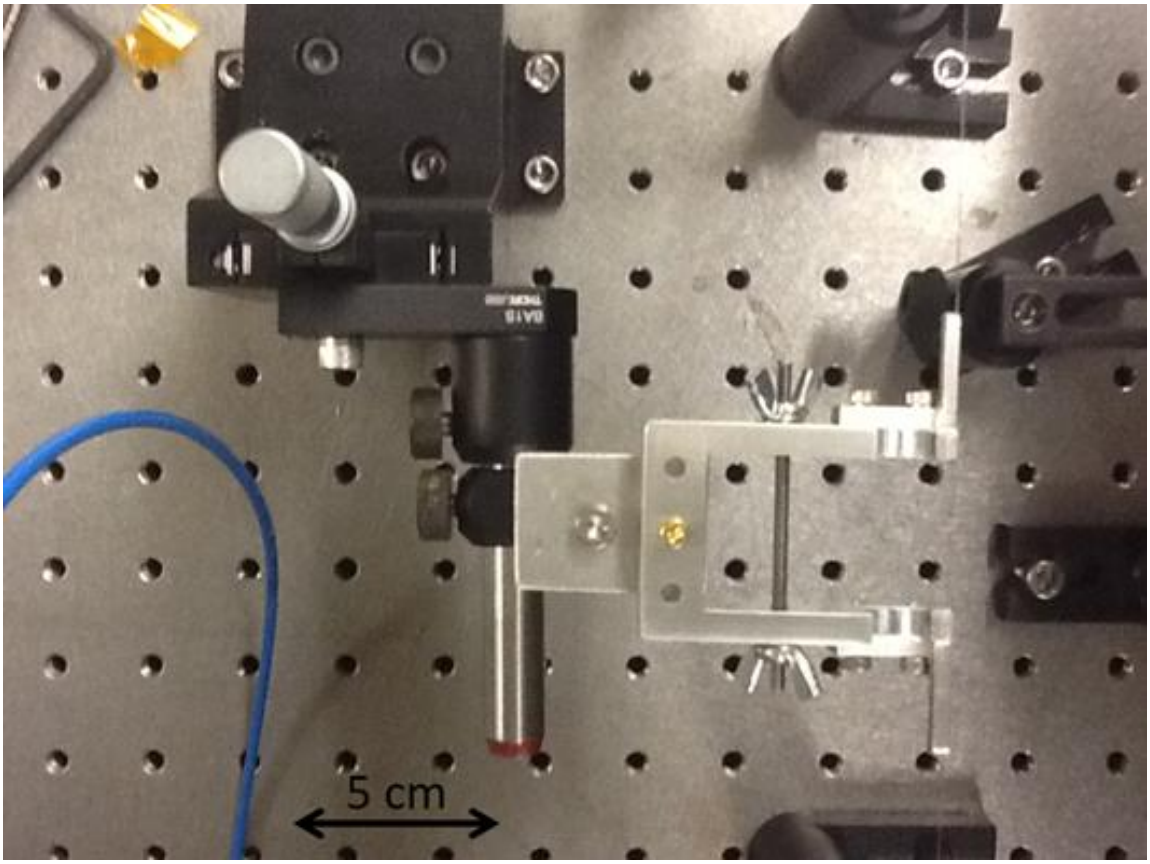

Figure 6.21 - Photograph of fiber holder secured to fiber gluing setup. Note tensioning rod is compressing the forks of the fiber holder.

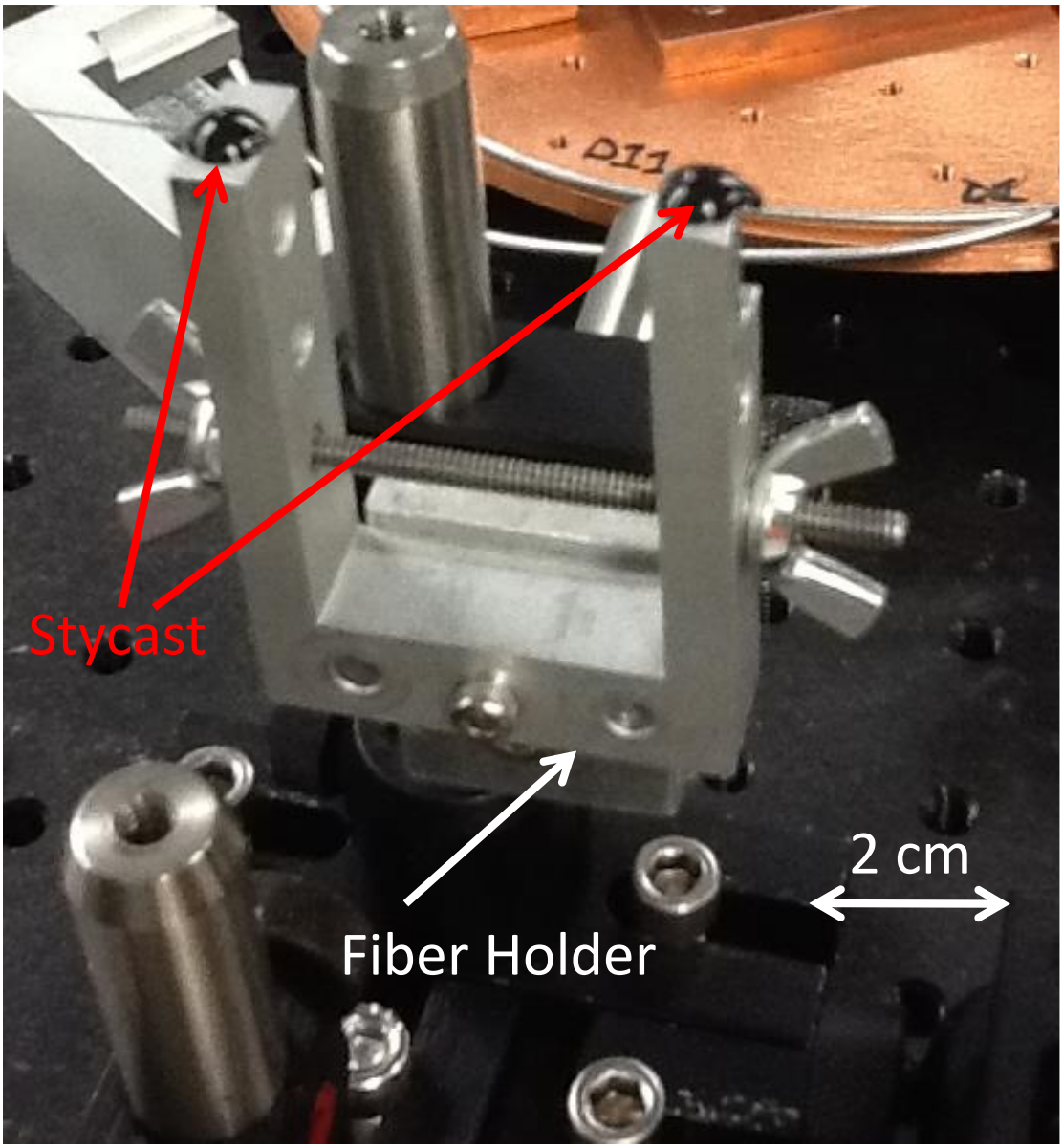

Figure 6.22 - Photograph showing tensioned fiber holder and black Stycast applied to the fiber holder and fiber.

7. Carefully unscrew the wingnuts to release the compression of the fiber holder fork and tension the fiber. Then carefully tape the ends of the fiber to the "fiber-protecting wings".

Assembly Step IV. Transfer Fiber to Fiber Plate

1. Verify that the thermal straps are attached to the cavity and attocubes, the coax cables are attached to the input and output SMA connectors on the cavity, indium has been applied to the cavity seal on the bottom half of the cavity, and the bottom half of the cavity has been secured to the transfer plate and attocube stack using long screws. The fiber plate should be mounted on sorbothane and secured from the sides using sorbothane lined optical posts. Sorbothane should also be placed on the bottom of table legs to prevent the table from shaking when moved.
2. Remove the support block. Retract the z attocube fully and attach the fiber holder to the fiber plate assembly (see Fig. 6.23). Tape the excess length of input and output fiber to the fiber plate and check that fiber is intact by sending light through.
3. Set up two cameras to image the fiber during alignment, one overhead along z-direction and one looking along x-direction (see Fig. 6.24). Turn off room lights and leave only camera lights on to reduce glare. I used "microcapure" software for one camera and "IMAQ" software for the other. The microcapure software needed to open first or it would freeze, while the IMAQ software was accessible by going to Measurement and Automation from National Instruments → select cam2: Digital Microscope → click "grab".

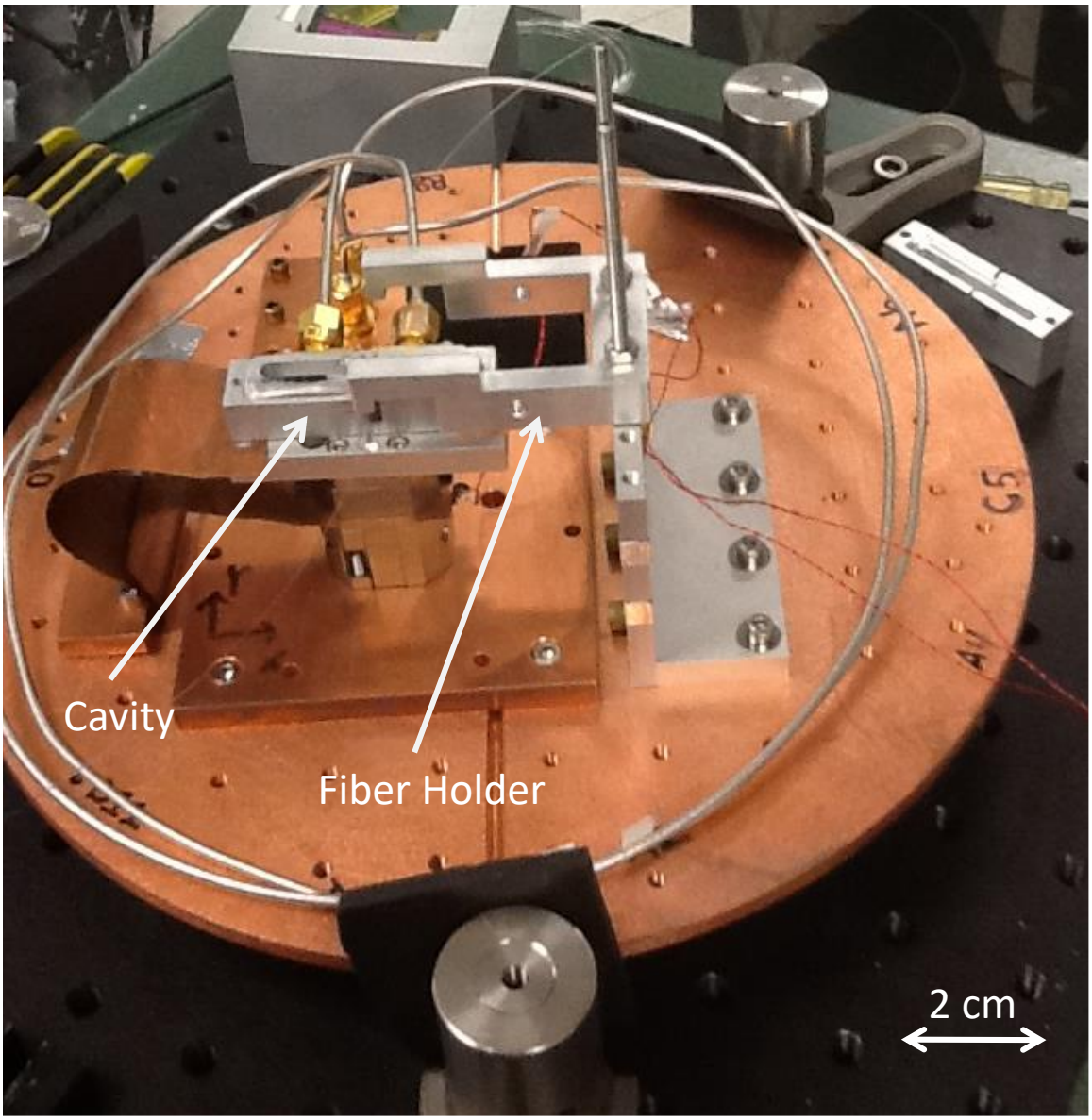

Figure 6.23 - Photograph of the assembly after fiber holder has been attached. Note that the cavity is still open.

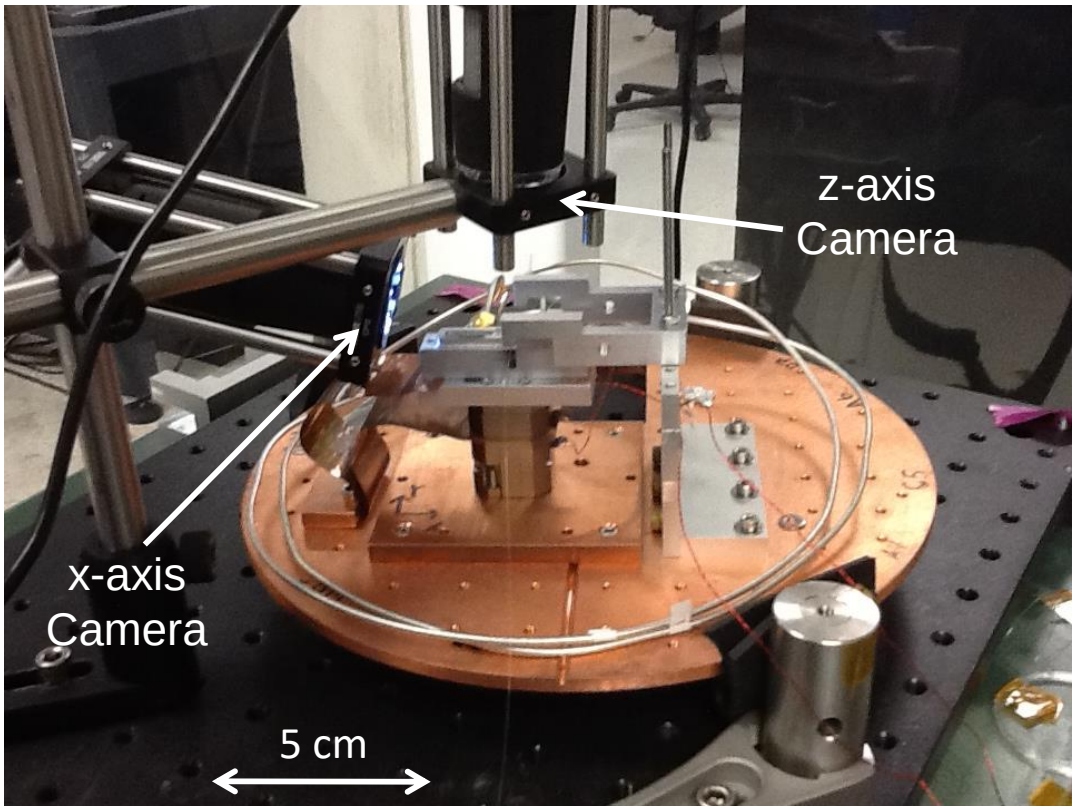

Figure 6.24 - Camera placement for the x- and z- axes while aligning the fiber and chip.

4. Take image along x-axis camera, looking slightly down into the cavity. Use ruler against computer screen to estimate angle of fiber and angle of cavity wall, adjust for tilt by using kapton/metal tape as a shim. It may be necessary to extend the z-attocube so that the chip is nearer to fiber and within the depth of field of the camera.
5. Take image along z-axis. Use ruler against computer screen to measure angle that fiber makes with edge of the resonator chip. Adjust the angle by loosening nuts and rotating fiber holder by hand until the fiber is parallel to the chip edge. Save images for later analysis.

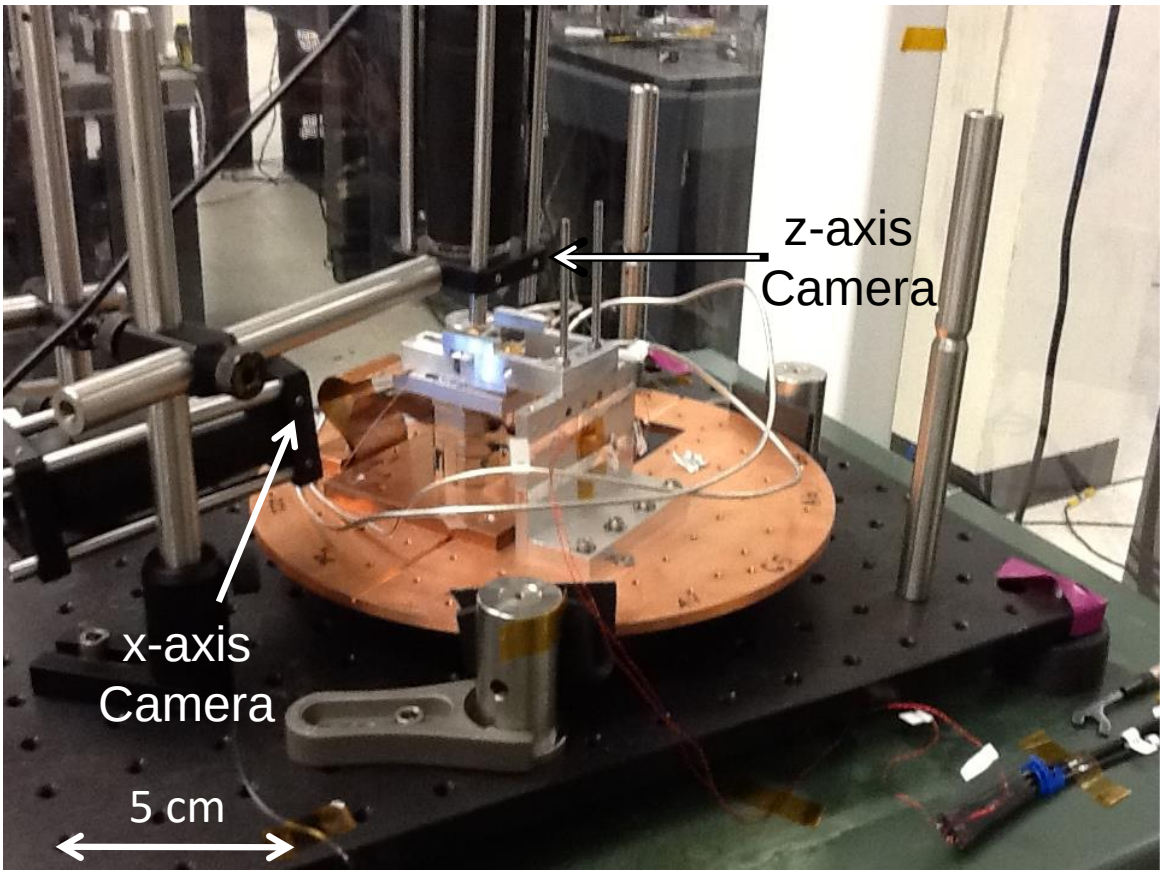

Figure 6.25 - Photograph of the placement of the cameras relative to the experimental setup with the cameras placed along the y- and z-axes.

6. Move x-camera to look along y-axis (see Fig. 6.25). Make sure fiber holder does not block view of “mouse hole” in cavity wall and leave room for support block to be inserted later.
7. Roughly calibrate attocube step sizes in x then z by using the ruler printed on cavity to measure advance and retreat position changes for a known number of steps.
8. Using the z-camera image, carefully position the fiber laterally so that it is running through the center of the mouse-holes in the cavity wall. Then use the other camera to deduce the z position of the fiber. Looking along y axis, use the z-attocube to bring the fiber level with the top of cavity and start recording position of fiber.

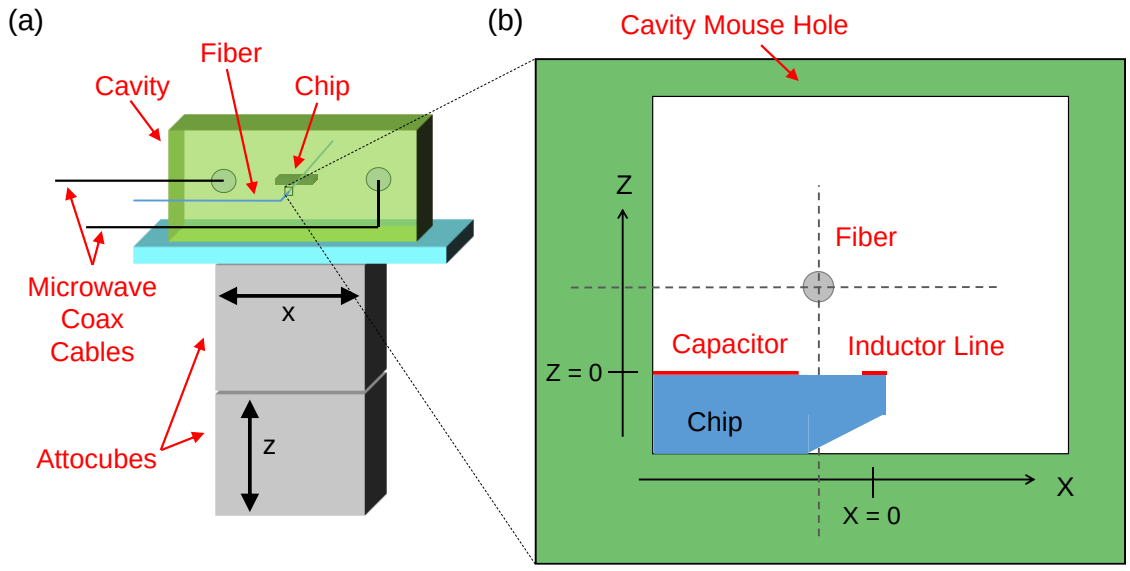

Figure 6.26. (a) Arrangement of the fiber and chip showing chip position inside cavity relative to attocubes and fiber. (b) Zoom-in view of cavity mouse hole. Side view of polished chip used in version 2 of the microfiber-chip experiment. The coordinate system originates at the inductor line. The size of the mouse hole is roughly 1 mm x 1 mm.

9. Extend the cavity so there is room for the support block. Then slide the support block underneath the adapter plate. Retract the cavity while recording all attocube movements. Remove the z camera.
10. Using brass screws, carefully secure the cavity top to the bottom while taking a video of the operation. Watch the live feed to make sure that cavity does not move. After the cavity has been closed up, check that the fiber is intact by sending light through. Make sure that the support block is still in place (see Figs. 6.26-6.28).
11. Make mandrel wraps: leave just over 1 m of fiber between epoxy point and mandrel, then ~30 wraps leaving ~2' of fiber at end. After every 10 wraps, secure wraps with kapton tape.

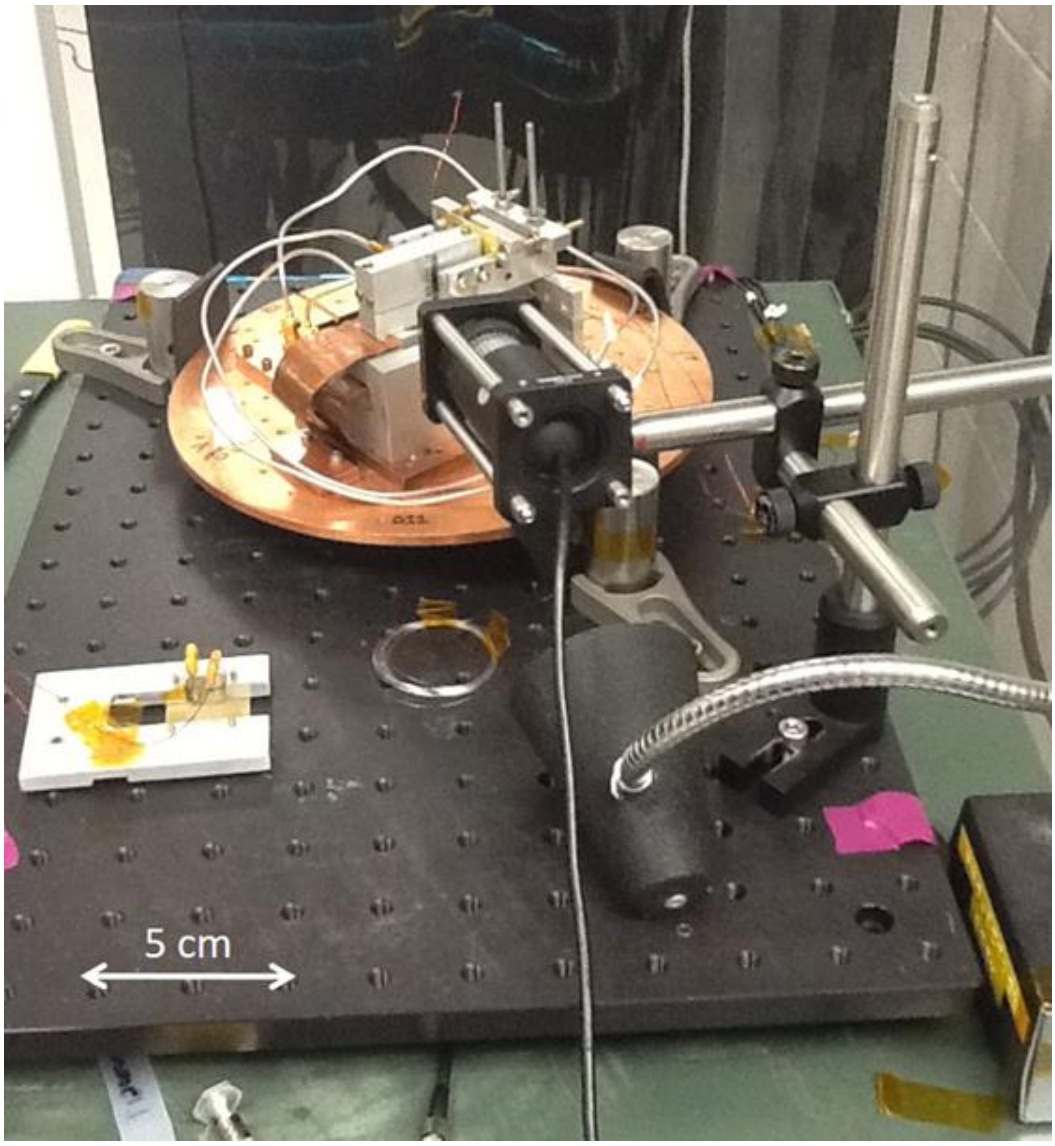

Figure 6.27 - Photograph of setup showing cavity top secured and the microfiber running through it. Note coiled fiber on optical table and camera pointing along y-axis, both in foreground. The x-sensor is attached, but the z-sensor is not.

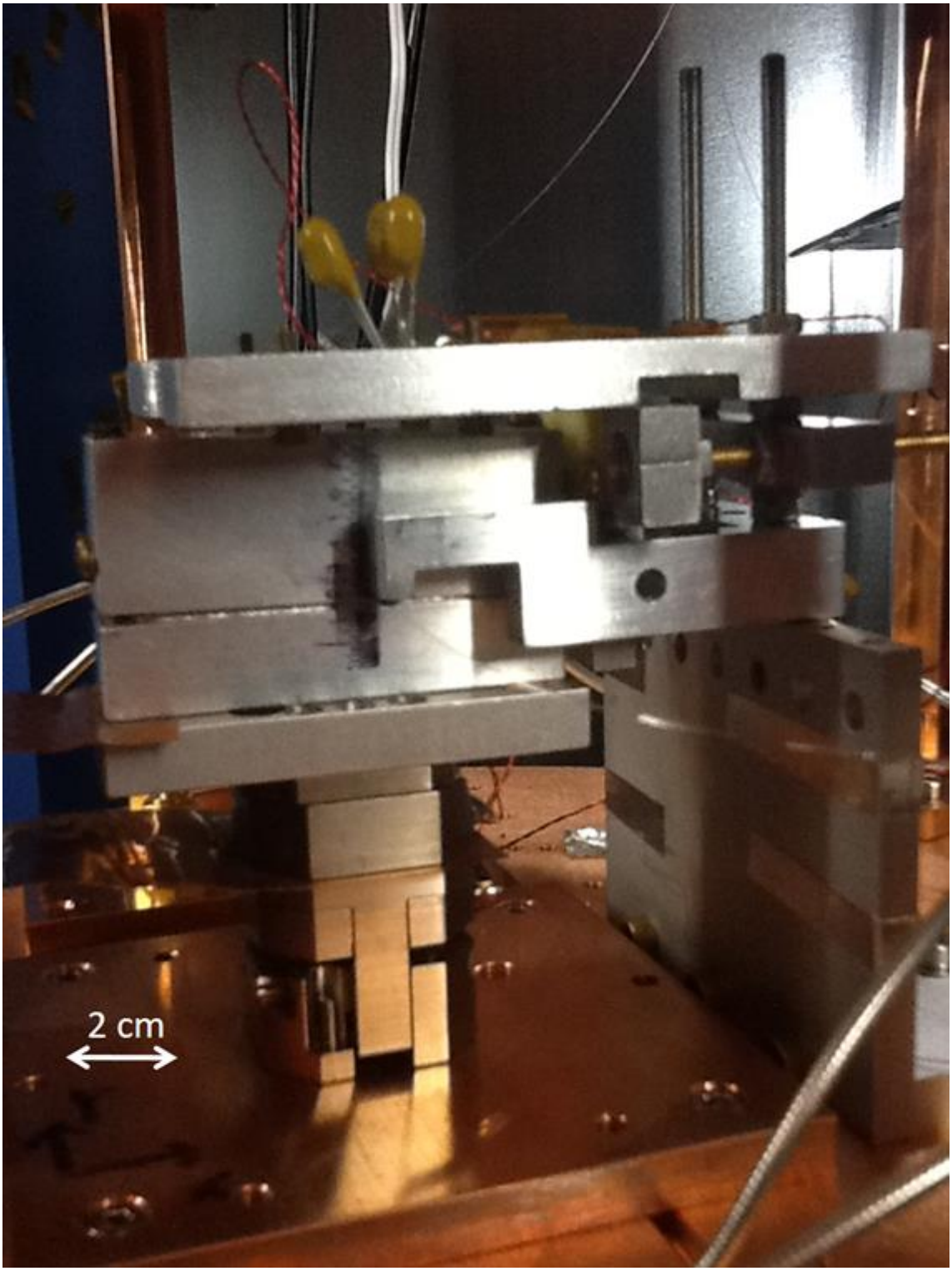

Figure 6.28 - Photograph of attocubes, cavity and position sensor setup used in version 3. Both the x- and z-sensors are attached.

Assembly Step V. Attach Inductive Sensors

1. Verify that the support block is in place.
2. Given the position of the fiber, determine the best location for the x and z position sensors so that they will not block cavity movement but still be close enough (~1 mm) to sensitively detect motion of the cavity. Create an x-shim equal to the distance between the x-sensor and the cavity. I used nylon strips that were 0.5 mm thick combined with layers of tape of known thickness. Create a z-shim equal to the distance between the z-sensor and the cavity.
3. Carefully attach the x-sensor to the fiber plate assembly, being sure to not bend/move the fiber holder. Adjust the distance to the cavity so that x-shim barely slides in. Attach z-position sensor to the fiber plate and adjust its height by stacking washers on threaded rod until the z-shim barely slides in between the cavity and coil. Secure in place.
4. Use the z-attocube to raise the cavity. Remove the support block and then return cavity to previous position.
5. Position the fiber to be in the center of the cavity mouse hole at 550 μm to the right and 600 μm above the lower left corner of the mouse hole, where the chip is on the left side and the origin is located at lower left corner (see Fig. 6.26).
6. Attach the Cu support rods to the fiber holder plate (see Fig. 6.29). At this point, the rods should just be finger tight. Leave the camera in position if possible (use holes on experiment plate labeled: A2, C5, A6, B8, D11).

Assembly Step VI. Attach Fiber Plate Assembly to Refrigerator

1. Move the entire table holding the optical table and assembled fiber plate underneath the mixing chamber stage of the dilution refrigerator (see Fig. 6.29).
2. Connect the x and z position sensors to the refrigerator wiring. Check the resonance curves.
3. Plug in attocube wires, making *certain* that the polarity is aligned properly. Check that both attocubes are functioning properly by moving a small amounts in x and z. Use camera to check the step size and verify that the position sensors are operating. Use ruler marks on cavity as a reference.
4. Remove excess tape holding input and output fiber. Remove posts and sorbothane securing fiber-plate. Slightly loosen copper support rods so they can be rotated on the fiber plate but do not slide around on their own.
5. With a couple of people assisting, carefully lift the fiber plate assembly and attach it to the mixing-chamber stage (See Fig. 6.30).
6. Use the fusion splicer to connect the input and output fibers to the refrigerator fiber.
7. The system is now ready for the dilution refrigerator shields and vacuum cans to be put in place. The rest of the steps involved in checking the setup, preparing the refrigerator and cooling down are standard.

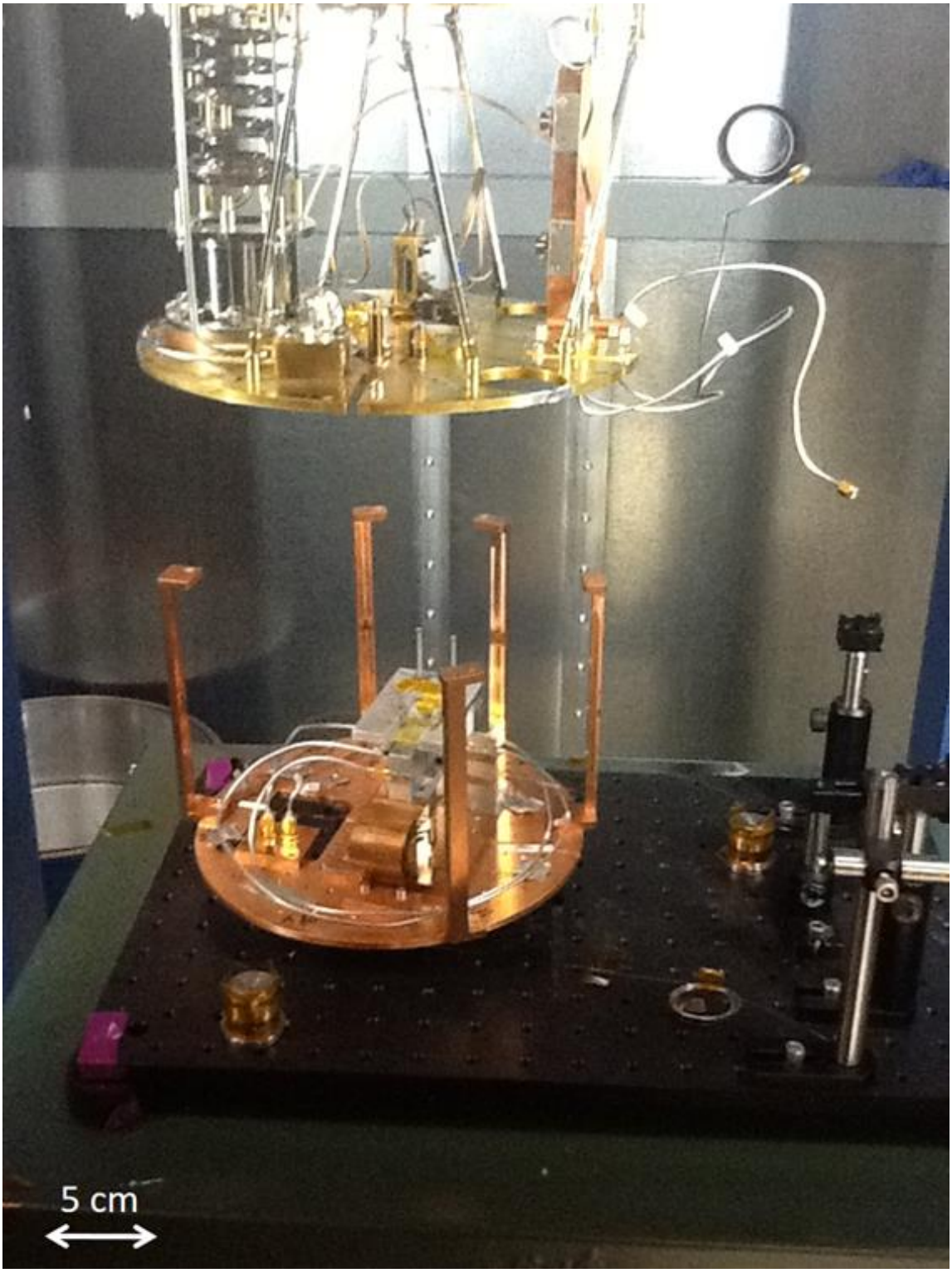

Fig. 6.29 - Assembled fiber plate just before attaching to the mixing chamber stage.

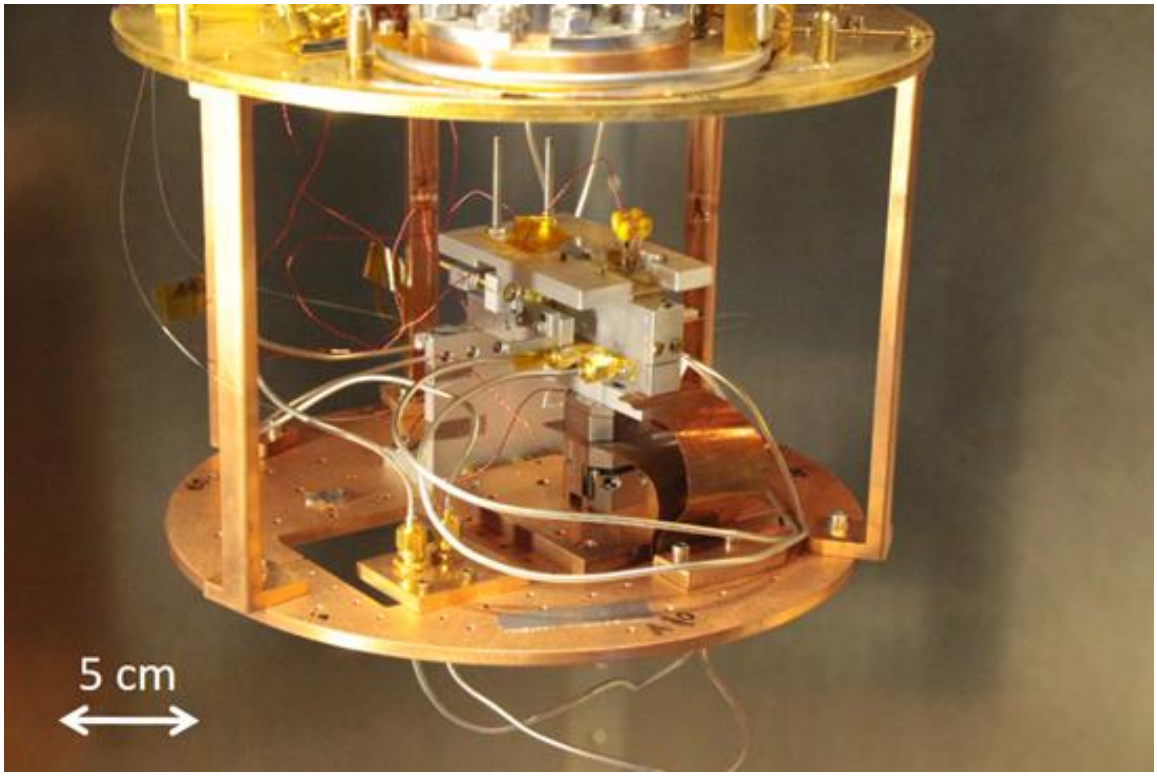

Fig. 6.30 - Completed fiber-plate assembly attached to the mixing chamber stage.

6.9 Conclusions

In this chapter, I described the design and assembly of key components in the proof-of-principle microfiber-chip experiment. I first described the constraints for the microfiber-chip experiment and how they were addressed in the design of my apparatus. I then briefly reviewed the basic physics of microfibers and nanofibers, described the fabrication process and detailed the microfiber parameters I used in the four different versions of the experiment. I next described how I positioned the fiber relative to the chip at millikelvin temperatures using attocube x and z translation stages. I also described the inductive sensors I used to monitor the position of the cavity. Finally, I provided a detailed procedure of how I assembled the experimental setup.

Chapter 7 Response of Superconducting Thin-Film Resonators

7.1 Introduction

In this chapter I discuss the optical and dielectric response of thin-film superconducting Al lumped-element microwave resonators to the position of an optical microfiber. In these experiments, I translated a thin-film LC resonator with respect to an optical microfiber and measured the frequency shift and quality factor Q of the resonator for different levels of optical power. Details of the experimental setup are described in Ch. 6.

For these measurements, we cooled the thin-film superconducting resonator to the 10-100 mK range, with the majority of the data being taken at 100 mK. When 780 nm light was sent through the fiber, Rayleigh scattering in the fiber caused a non-uniform illumination of the resonator, exciting quasiparticles in the superconducting film and thereby affecting the resonance frequency f_0 and quality factor Q. The response was dependent on the position of the resonator with respect to the fiber. I report on the response of the resonator to both the applied optical power and the fiber's dielectric, as the thin-film resonator is moved with respect to the fiber.

In Section 7.2, I describe how I estimated the relative position of the fiber with respect to the chip by using a combination of nominal movements of the attocube translation stages (see Sec. 6.5), measurements of the inductive sensors (see Sec. 6.6), and post-processing. Additional discussion of the many issues associated with determining the

position can be found in Appendix C. In Section 7.3, I present measurements of the resonator response as a function of fiber position without any input optical power. The fiber is made of a dielectric material (glass) that effectively raises the capacitance of the thin-film resonator's interdigitated capacitor when placed in its electric field, thus decreasing the LC resonance frequency. This allows the fiber to act as a probe of the resonator's electric field. The LC resonator chip was mounted in a superconducting Al cavity, and in Section 7.4, I discuss the cavity's response to the fiber position, which is much smaller than the response of the thin-film resonator. I present data on how the LC resonator responds to varying optical power through the fiber in Section 7.5. In Section 7.6, I present data on how the resonator responds to varying the position of the fiber with fixed optical power. In Section 7.7, I then discuss a model of the optical response of the resonator that considers the resonator-fiber geometry, as well as effects produced by the optical generation, diffusion, and recombination of quasiparticles. In Section 7.8, I compare this model to the data and in the final section I conclude with a summary of the main results.

7.2 Estimating the Relative Position of the Fiber with Respect to the Chip

As I discussed in Sec. 6.5, the x and z attocubes did not move a consistent repeatable distance upon repeated application of identical voltage pulses. Also, the average length of an extend step typically did not equal the average length of a retract step. Furthermore, the ratio between the length of extend steps and retract steps seemed to drift over time. As I discussed in Chapter 6, I estimated the average step size by taking the step size measured at room-temperature (see Table 6.3) and reducing it by a factor of D = 4.6 at 100 mK that was obtained from separate cryogenic measurements (see Table 6.4). A summary of the

resulting nominal step sizes at 100 mK is shown in the first two lines of Table 7.1. Data was collected in "sweeps", in which one attocube was extended or retracted a certain number of steps, the system was given time to cool back down to 100 mK, the resonator response was measured, and the procedure repeated for each subsequent data point in the sweep. I assumed that the attocube step size did not change much within a given sweep. We soon found that repeated sweeps were not repeatable if plotted using the nominal step size. We concluded that the attocube step sizes ($\Delta_{x,ext}$, $\Delta_{x,rtr}$, $\Delta_{z,ext}$, $\Delta_{z,rtr}$) changed over time by a significant amount and that counting step sizes and using dead-reckoning led to significant errors in the position. This behavior was not surprising because the attocubes employ a stick-and-slip motion that relies on friction and is affected by loading and thermal contraction.

I was able to estimate the position of the fiber (x_f, z_f) for version 2 by making manual corrections to the attocube step size using two different methods. In both correction methods, I assumed that the *z* attocube moved independently of the *x* attocube and vice versa. For consistency in method 1, I assumed that the retract size for each attocube was fixed and the extend size drifted in an uncontrolled manner. I also assumed that the step size did not change during a sweep, but that it could change between sweeps.

Table 7.1 - Nominal estimates for attocube step sizes for version 2 and version 4 of the fiber-chip experiment and best estimates for version 4 of the fiber-chip experiment.

Version	Δx_{ext} (μm/step)	Δx_{rtr} (μm/step)	Δz_{ext} (μm/step)	Δz_{rtr} μm/step)
2 (nominal)	0.48	0.42	0.32	0.40
4 (nominal)	0.45	0.48	0.32	0.37
4 (best estimate)	0.45	0.37	0.32	0.315

In the first correction method for the z attocube, I compared data from two or more *z* sweeps taken at a constant *x* position. I then simply adjusted the *z* offset extend size to roughly align the two data sweeps. This same procedure could be used for the x-attocube for x-sweeps taken at fixed z. In the second method, I relied on the characteristic "dip" in the optical response $|\delta f_0|$ (magnitude of the change in the resonance frequency when light is turned on), which appears when the fiber is in line with the plane of the chip (see Fig. 7.1). I collected two or more sweeps and then adjusted both the *z* extend and retract sizes to align the dip at $z_f = 0$. Figure 7.1(a) shows $|\delta f_0|$, for several sweeps, as a function of the nominal position $z_{f,nom}$ for different $x_{f,nom}$ values. The effect of cumulative errors in *z* is clear. Figure 7.1(b) shows $|\delta f_0|$ as a function of the adjusted position z_f, using the second method. Additional details on exactly how step sizes were adjusted can be found in Appendix C.

To determine the position for version 4 of the fiber-chip experiment, I was able to make use of some of the data from the inductive position sensors (see Sec. 6.6). However, I was only able to measure one sensor at a time. Additionally, there were some sensor measurements that were inconsistent due to intermittent wiring issues. To estimate the position of the attocubes in version 4, I used a hybrid method of determining the position, using the sensor data when available and using dead reckoning from the nominal steps taken when sensor data was not available. The nominal measurements for the attocube step sizes for version 4 (see second line of Table 7.1) did not yield extend and retract sweep data that was aligned. To try to correct for this, I took extend step sizes to be fixed and used method 1 to determine the initial retract step sizes for first sweeps. For example, an x retract step size of $\Delta_{x,rtr} = 0.37$ μm aligned sweeps 17 and 18, while a z retract step size of

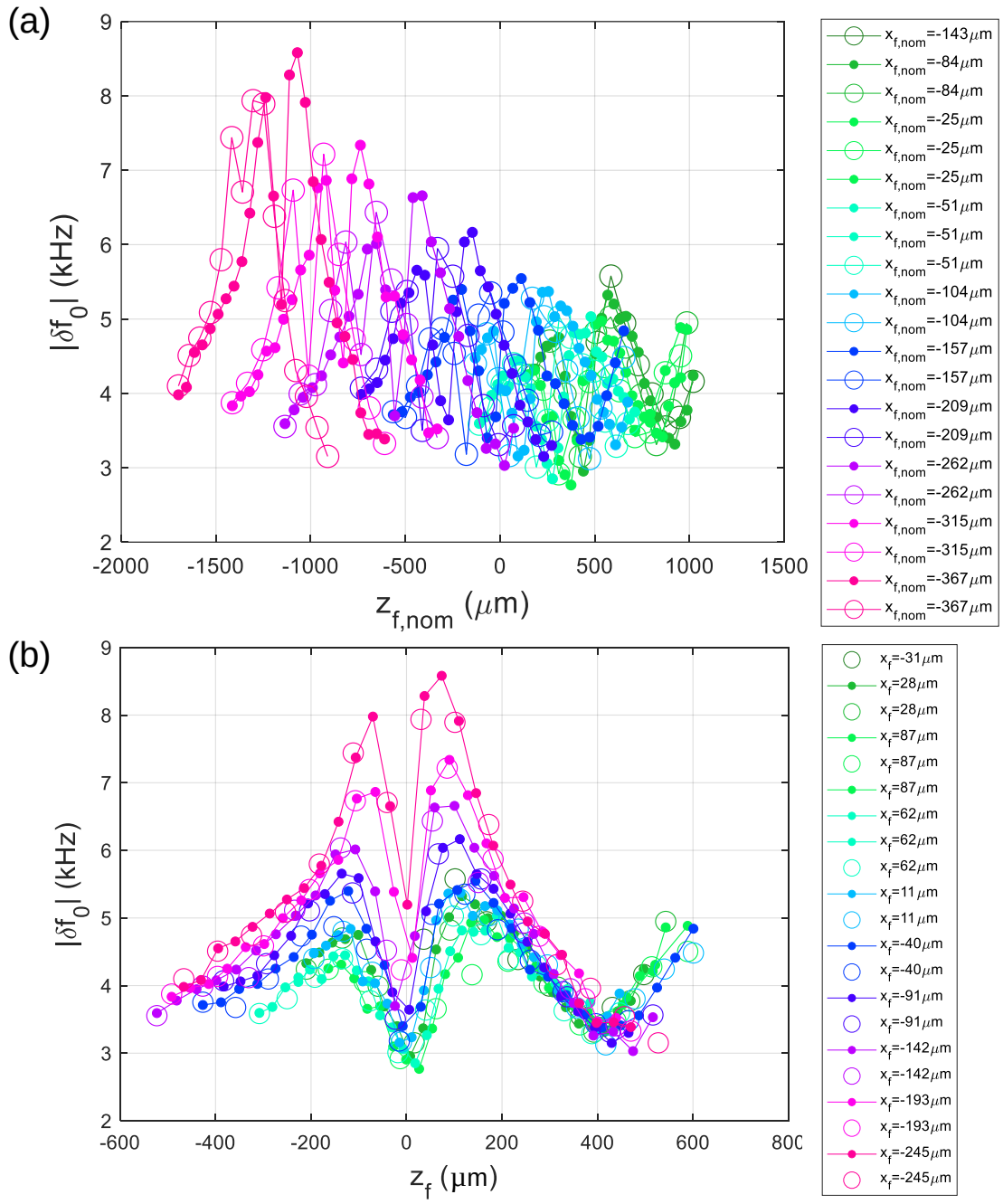

Fig. 7.1 - (a) Plot of the optical response $|\delta f_0|$ of LC2 (in version 2) as a function of $z_{f,nom}$ before making adjustments to z-attocube step size. Solid points were measured when the z-attocube was extended and open points were measured when the attocube was retracted. Each sweep has a "dip" that should occur at $z_f = 0$. The error in the attocube step size is cumulative and shifts each subsequent sweep to falsely lower z_f values. (b) Plot of $|\delta f_0|$ as a function of the best estimate z position z_f, after using method 2 to adjust the z attocube extend step size. The dip in each scan now occurs near $z_f = 0$.

$\Delta_{z,rtr}$ = 0.315 μm aligned sweeps 64 and 65. The 'best estimate' starting value of step sizes used in version 4 are shown in the third line of Table 7.1.

I also flagged inconsistent position sensor values and instead used the nominal positions to estimate distance between those points. I calibrated the resonance frequency f_{xf} and f_{zf} of the x and z sensors using the earliest sweeps, as subsequent sweeps were subject to drift in the attocube step size. For these initial sweeps, I fit both f_{xf} vs $x_{f,nom}$ and f_{zf} vs $z_{f,nom}$ to quadratic functions and used these functions in later sweeps to extract x_f and z_f from f_{xf} and f_{zf}.

To determine the 'adjusted' position (x_f, z_f) of the fiber in version 4, I examined the optical response $|\delta f_0|$ and the dielectric response f_0 from repeated x scans over the capacitor and repeated z-scans past the inductor. For the x-scans, I set (x_{f0}, z_{f0}) = (-365 μm, 222 μm) to correspond to the dip in f_0 being roughly over the capacitor for the first 100 x-sweeps because it is expected that the electric field is concentrated here. This also aligns the maximum in $|\delta f_0|$ (for the first 100 x-sweeps) over the capacitor and a local maximum in $|\delta f_0|$ near the inductor (see Fig. 7.13). We expect a local maximum in $|\delta f_0|$ over the inductor for sweeps close to the chip. For z sweeps 143 through 159, I set z_{f0} such that the minimum in f_0 was at z_f = 0 μm. This also aligns the dip in$|\delta f_0|$ near z_f = 0 μm. I chose these sweeps because they displayed a clear dip in $|\delta f_0|$ and f_0. From this starting point, I cumulatively added changes from f_{xf} and f_{zf} that were measured and viable, and I added the estimated change in x_{nom} and z_{nom}, respectively if they were not viable. See Appendix C for additional discussion of the position calibration issues.

Despite the uncertainty in the fiber-chip positioning, the calibration schemes provided qualitative and quantitative corrections to the relative fiber-chip position. Future

hybrid system experiments would benefit from using upgraded translation stages with integrated position tracking or improved sensors, which should greatly reduce the fiber-chip positioning uncertainty. While some of the position data has hard-to-quantify systemic uncertainty, particularly in versions 1-3, it still provides important qualitative information.

7.3 Resonator Response vs. Position - Without Optical Power

If we moved the microfiber closer to the resonator, the dielectric material of the fiber perturbed the fringing electric field of the resonator's interdigitated capacitor in the vacuum space above the chip. This increased the effective capacitance C of the resonator. Since $f_0 = 1/\sqrt{LC}$, this in turn lowers the resonance frequency. This dielectric perturbation should depend strongly on the fiber's position with respect to the resonator and should progressively lower f_0 as the microfiber moves towards a region of greater electric field intensity. The dielectric constant of the fiber [7.1] is expected to be $\varepsilon = 2.10*\varepsilon_0$ where ε_0 is permittivity of free space. The fractional change in capacitance $\Delta C/C$ will be proportional to $\mathcal{E}_{fiber}/\mathcal{E}_{tot}$ where the electric field energy $\mathcal{E}_{tot}$ is found by integrating the square of the electric field from the resonator over all space and the energy $\mathcal{E}_{fiber}$ is determined by integrating the square of the electric field over the volume of the fiber for a given location of the fiber. Consequently, the fractional change in resonance frequency $\Delta f_0/f_0 = \Delta C/2C = \mathcal{E}_{fiber}/2\mathcal{E}_{tot}$. The fiber should also perturb the Q of the resonator as the fiber is glass and should have many TLSs.

Ideally the microfiber should be aligned perfectly parallel to the inductor. Although the alignment is not going to be perfect in the actual setup, every effort was made to carefully align the system at room temperature. Measuring f_0 and Q of the resonator as a

function of the fiber's position, should thus give a detailed map of the effective electric field strength of the resonator integrated over the fiber. This information, used in conjunction with positioning information from the inductive sensors (described in Sec. 6.6 and Sec. 7.2), was important because there was no optical access to the fridge and thus no direct way of determining the precise relative position of the fiber with respect to the resonator.

In addition, the frequency perturbation caused by the fiber's dielectric is important because the resonance frequency of the hyperfine splitting of ^{87}Rb is very precise [7.2] and ideally we would like the resonator's frequency to match it to within about the linewidth of the resonator, which would be in the range of 1 kHz. When trapped on a nanofiber, the exact linewidth of ^{87}Rb is not known. Therefore, it is important to examine how the fiber affects the LC resonance frequency so that this effect can be counteracted by tuning. Since a hybrid system with trapped atoms would use a nanofiber, rather than a microfiber, this perturbing effect will scale as the fiber radius squared and increase with decreasing distance between the fiber and the LC resonator's inductor. We expect this to be a small but readily measurable effect.

The data collection method was the same for all versions of the microfiber-chip experiment. With the microfiber in a fixed position and no optical power injected, we measured $S_{21}(f)$ for chip LC2 as a function of the input microwave frequency at 20 mK. The power at the input of the cavity was -68 dBm for version 2. For version 4 the input power depended on whether we were measuring the LC3 resonator (-88 dBm) or the 3D cavity (-98 dBm). However, the coupling to LC2 in version 2 was different than the coupling to LC3 in version 4, and the photon occupation of the resonator cannot be

determined solely from the input power. We repeated this measurement for multiple positions of the fiber. I then extracted f_0 and Q at each location by fitting S_{21} to a modified Lorentzian curve, as described in Sec. 2.2.

Figure 7.2(a) shows a side view of the setup during the version 2 measurements. Looking through the hole in the 3D cavity, we see chip LC2 with the edge and bottom of the chip nearest the inductor polished away to allow the fiber to occupy the area nearby. The origin of the coordinate system for the position of the fiber is through the center of the inductor line.

In Fig. 7.2(b), I show a false color plot of a subset of the data showing f_0 as a function of the relative position of the fiber from version 2 with resonator LC2. I note that here I have omitted values of f_0 that gave bad fits. In version 2 of the fiber-chip experiment, we found that when the fiber was at $x_f \leq$ -180 μm, the resonance line shape was distorted. As the fiber was moved back to $x_f \geq$ -180 μm, the line shape recovered. Initially, we suspected this could be due to vibrations of the fiber as it entered the relatively higher field of the capacitor, but in version 4 we did not see sudden distortion in the line-shape. It could have been due to the fiber touching something or a wiring issue (a cable, connector, or some sensor pulling loose or making electrical contact) as we extended the x attocube past a certain point, but then recovering as we brought it back. Therefore, we mostly measured values to the right of the inductor (see Fig. 7.2 (b)). Note that when the 50 μm diameter microfiber was in the plane of the LC2 chip and the center of the fiber was estimated to be just 71 μm to the right of the inductor, we found that f_0 was 80 kHz lower than at positions measured farthest from the inductor (~500 μm).

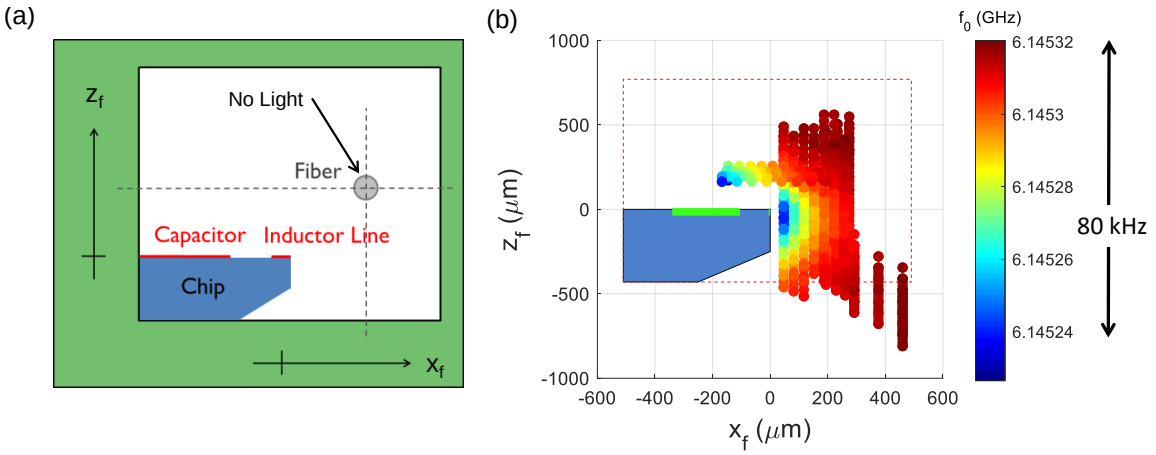

Fig. 7.2 - (a) Schematic side-view through hole in the 3D cavity (green) for version 2 of microfiber-chip experiment showing the edge of the chip (blue) with the capacitor and inductor line (red). The fiber (gray) is stationary and the chip can be translated horizontally and vertically. The fiber's estimated position is denoted by x_f and z_f. (b) False color plot of a resonance frequency f_0 of resonator LC2 as a function of fiber position with no light is going through the fiber. Note that due to uncertainty in the z-position some points fall outside the boundary of the 3D cavity hole, indicated by red dotted line.

Figure 7.3 shows line-cuts along z_f through the LC2 data in Fig. 7.2(b). The dip in f_0 near $z_f = 0$ is clear and can be used to check the alignment of the scans. The sweep in z_f that is closest to the chip occurs at $x_f = 71$ µm and the furthest sweep occurs at $x_f = 460$ µm. At $x_f = 257$ µm, we see the dip in f_0 is about 12 kHz. When we move the fiber 186 µm closer in x_f to the chip and repeat the scan in z_f, the size of the dip increased by nearly a factor of 7, to 80 kHz. With no light through the fiber, the dip provides a reference point for z_f and also lets us verify that the maximum value of f_0 at fixed values of x_f did not change for repeated scans, which implies that the x attocube did not drift as the z attocube moved.

In version 4 of the microfiber chip experiment, we positioned chip LC3 to stick out further into the hole of the 3D cavity to ensure that the fiber could be swept above the

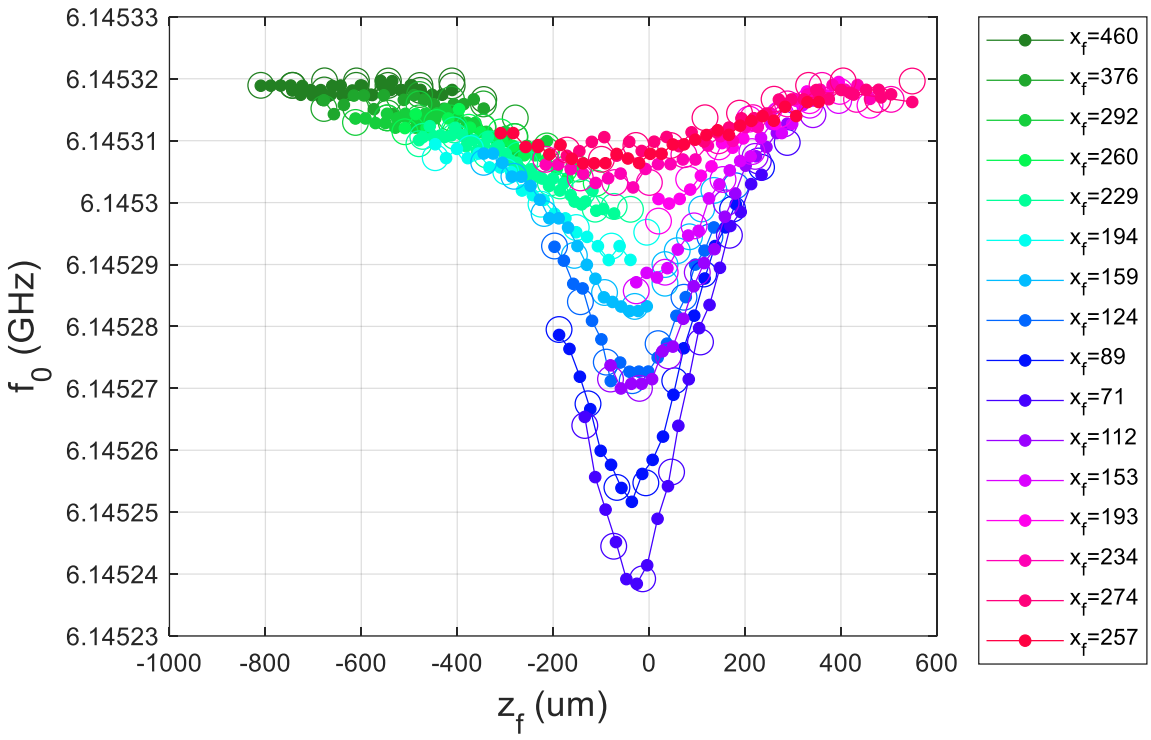

Fig. 7.3 - Resonance frequency f_0 of thin-film resonator LC2, as a function of z_f measured at different fixed x_f, for microfiber-chip experiment version 2 at 100 mK. The legend indicates the position x_f in μm of the fiber. The list is in chronological order, first decreasing in x_f and then increasing, as this was the order that the data was taken. Solid points indicate that the z attocube was extending between data points and open data points indicate that it was retracting.

capacitor without hitting the cavity wall. Figure 7.4 shows a side view of the version 4 arrangement of the chip and cavity. Compared to the version 2 arrangement shown in Fig. 7.2, the chip in version 4 was further to the right in the hole. Figure 7.4 also shows a false-color plot of f_0 as a function of fiber position (x_f, z_f) above the capacitor, again with no optical power applied to the fiber. The change in f_0 is largest within 100 μm of the surface of the capacitor. This is consistent with what we would expect from fringing electric fields from the capacitor. The interdigitated capacitor has 5 μm wide teeth spaced

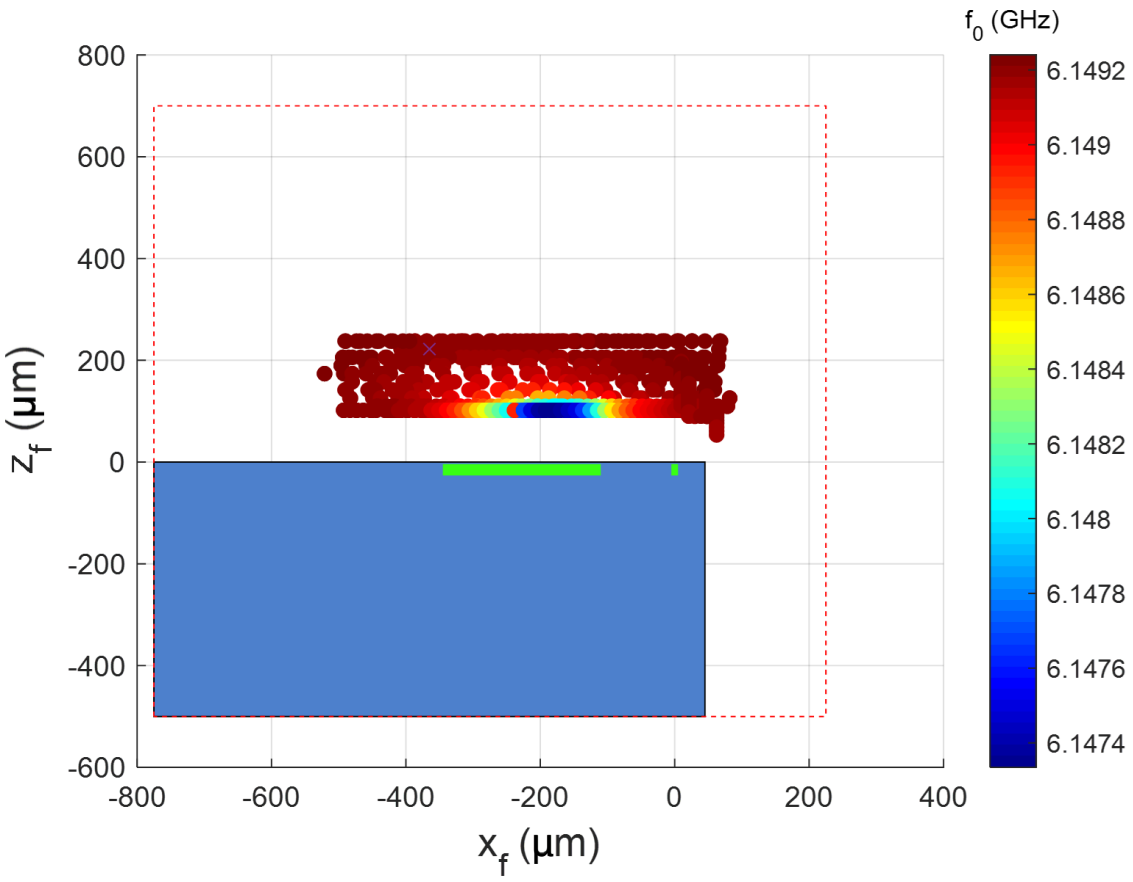

Fig. 7.4- False color map of f_0 of resonator LC3 versus estimated position (x_f, z_f) of the optical microfiber, in version 4 of the microfiber-chip experiment. Note that chip LC3 has a different cross section and is mounted differently than LC2 was in version 2 (see Fig. 7.2 (a)). No optical power was applied during these measurements, *i.e.* this is the frequency response of the LC resonator due to the dielectric of the fiber. The estimated boundary of the 3D cavity hole is indicated by the red dotted box.

by 5 μm arranged in three banks (see Fig. 3.9). These distances determine characteristic length scales over which the electric field falls off rapidly.

To more clearly see the behavior of f_0 during the x-sweeps over the capacitor in version 4, Fig. 7.5 shows line-cut plots of f_0 as a function of x_f. Comparing the x-sweep furthest from the chip at z_f = 238 μm to the x-sweep at z_f = 102 μm, we see the dip increases

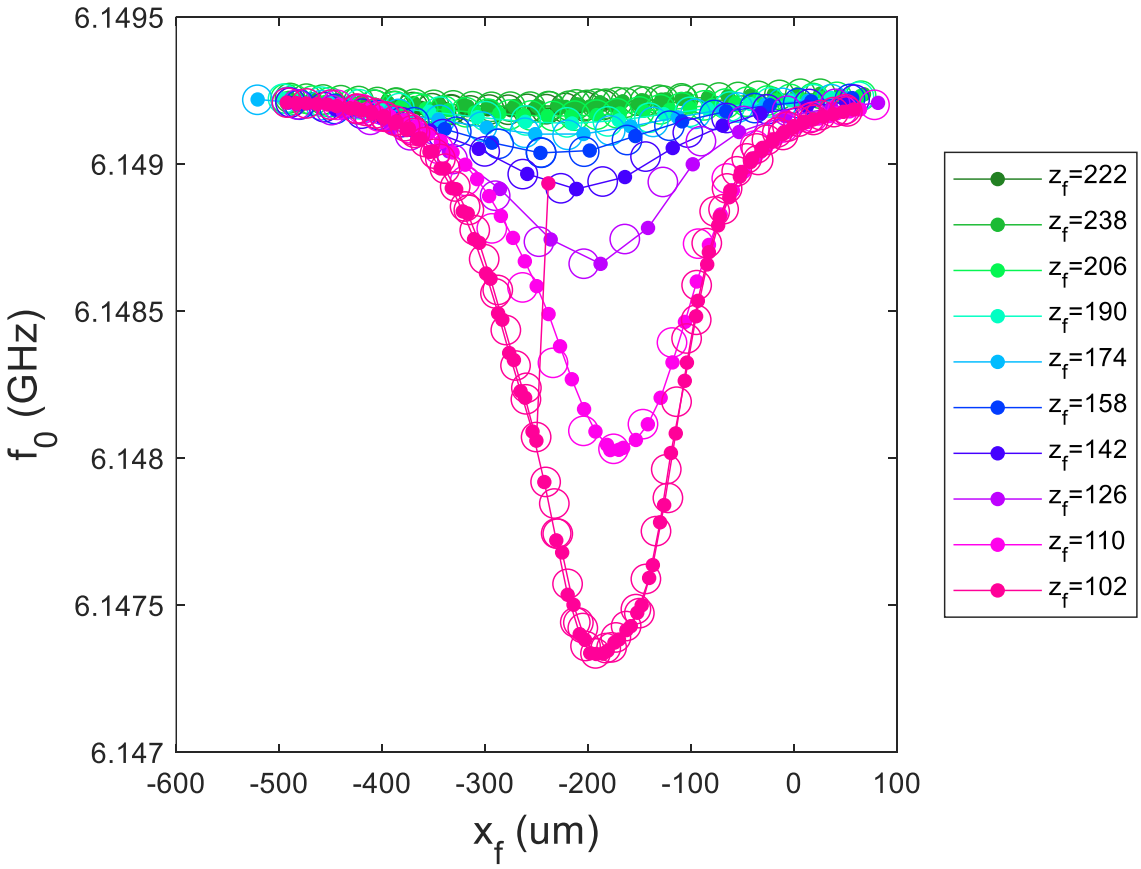

Fig. 7.5 - Resonance frequency f_0 of thin-film resonator LC3 plotted as a function of x_f for different fixed z_f. This data was taken for microfiber-chip experiment version 4, measured at 100 mK with no optical power applied to the fiber. The legend indicates z_f of the fiber in μm. Solid points indicate that the x attocube was extended between data points and open data points indicate that it was retracted.

from about 50 kHz to about 2 MHz, a factor of 40. I note that this is about 25 times larger than the 80 kHz-dip found to the right of the inductor in Fig. 7.3, and is consistent with the electric field being more concentrated near the interdigitated capacitor. Approaching the fiber even closer, Fig. 7.6 shows that additional features become apparent, suggesting that we are starting to resolve the structure of the capacitor banks (see inset in Fig. 7.6). From Fig. 7.6 we can see that the sweep at z_f = 72 μm (open green circles) has a minimum

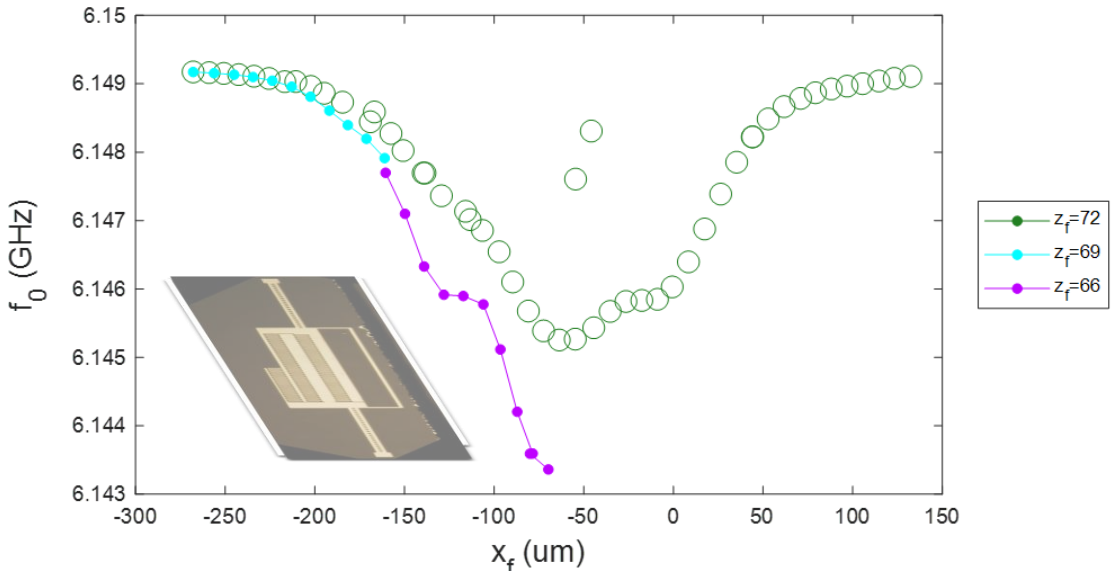

Fig. 7.6 - Resonance frequency f_0 of thin-film resonator LC3 plotted as a function of x_f for different fixed z_f. This data was taken on resonator LC3 for microfiber-chip experiment version 4 at 100 mK. The legend indicates z_f of the fiber in µm. Solid points indicate that the x attocube was extending between data points and open data points indicate that it was retracting. This was the closest approach of the fiber and it was able to resolve structure due to the capacitor banks in LC3 (inset).

frequency f_o at about x_f = -60 µm and a prominent shoulder near x_f = 0 µm, which is the nominal location of the inductor line in LC3. However, due to cumulative error in determining x_f, the inductor is probably near x_f = 200 µm for these sweeps. In other words, the minimum in f_0 is likely occurring over the middle capacitor bank or over the antenna (see inset). Similarly the shoulder near x_f = 0 µm likely corresponds to the capacitor bank nearest the inductor. The sweep closest to the surface of the chip at z_f = 66 µm shows another clear shoulder near x_f = -120 µm. This likely corresponds to the half capacitor bank that is farthest from the inductor line (see inset in Fig. 7.6).

Figure 7.7 shows the corresponding total quality factor Q of LC3 as a function of x_f for three sweeps that are relatively close to the surface of the chip. For z_f = 126 µm, the

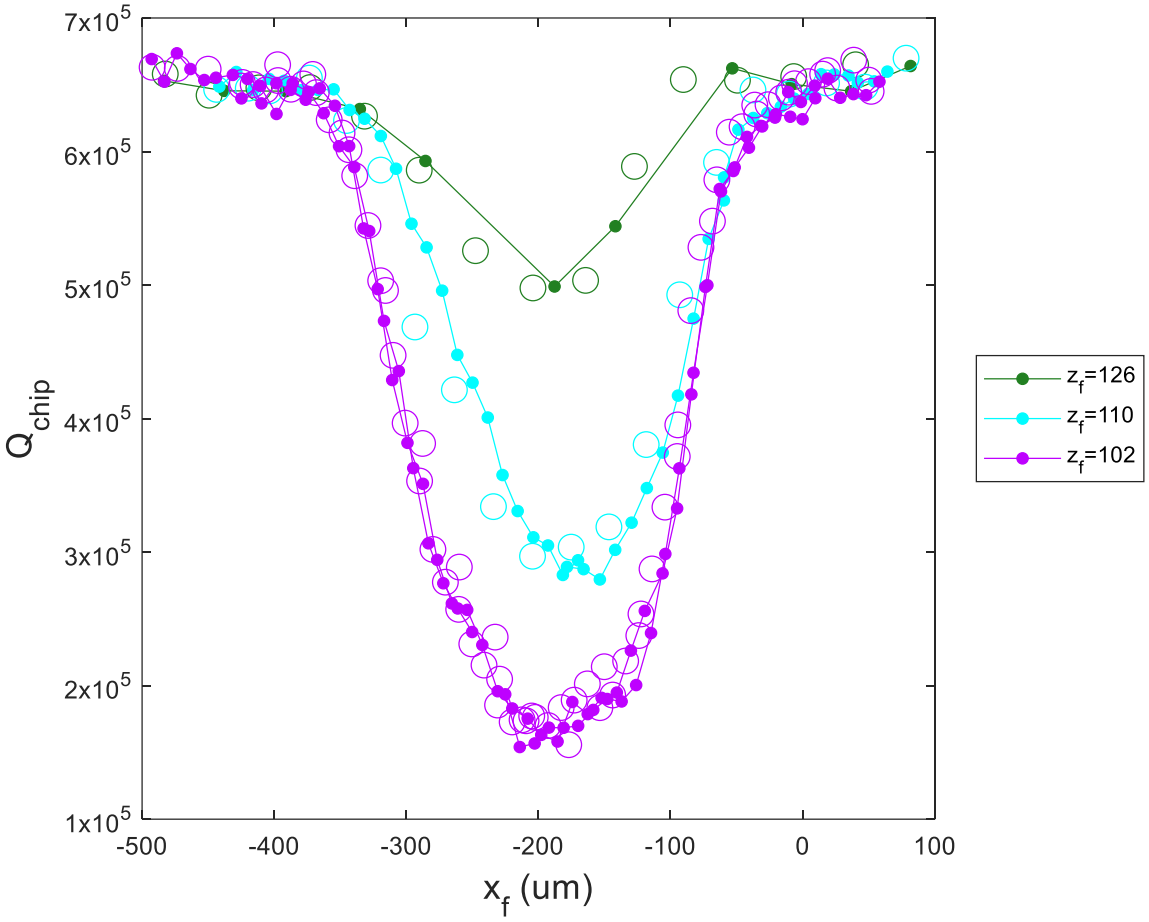

Fig. 7.7 - Plot of quality factor Q of resonator LC3 versus corrected position x_f of the microfiber for version 4 of the microfiber-chip experiment. No optical power was applied during these measurements. Legend indicates z_f of fiber in µm. Solid points indicate x attocube was extending between data points and open points indicate it was retracting. The decrease in Q may be due to dielectric loss in the fiber or may be due to inhomogeneous broadening of the resonance from vibrations of the fiber.

Q drops by a maximum of 25%, as it was swept over the capacitor. For comparison, at z_f = 102 µm above the chip, the Q dropped by about 75%. Note that these two scans differed in z_f by only 24 µm, which is almost equal to the 25 µm radius of the fiber. This behavior is consistent with a sharp fall-off of the electric field with distance from the capacitor and the increased loss when the fiber gets close to the resonator is consistent with dielectric

loss from two level systems in the fiber. However, it is also possible that the fiber is vibrating, causing rapid fluctuations (on the time scale of the measurement) of the resonance frequency. This would lead to inhomogeneous broadening of the measured resonance and an apparent reduction in the Q.

I note that this behavior shown in Fig. 7.6 for resonator LC3 in version 4 was different than what I observed for resonator LC2 in version 2. For LC2 I saw a sudden and unexplained drop in Q when attempting to move the fiber over the capacitor. This may have been due to contact between the fiber and the capacitor. Also, during z sweeps in version 2 to the right of the inductor (not shown here), the Q was fairly constant, indicating that the fiber did not impact the Q significantly in this region. This is beneficial because this is where the fiber will be located when coupling atoms to the resonator. I note that the Q values I report here were measured with a power of -88 dBm at the input of the 3D cavity and the maximum value of about $7x10^5$ in Fig. 7.6 is quite high for thin-film Al resonators.

I should also note that in a fully-realized hybrid system, we would use a nanofiber with a radius of about 250 nm. The cross-sectional area of a nanofiber would be 10,000 times smaller than that used in the microfiber experiment and the dielectric effects on Q and f_o would be proportionally smaller for the same separation from the capacitor. Nevertheless, the effects are quite large for the 25 μm diameter fiber and increase rapidly as the separation between the fiber and capacitor is reduced. This suggests that dielectric perturbations of the Q and f_o of the resonator will be small for a nanofiber, especially when the fiber is near the inductor, but visible for increased averaging and decreased separation between the chip and capacitor.

7.4 Cavity Response vs. Position - Without Optical Power

We also measured the transmission S_{21} through the 3D cavity near the TE_{101} resonance frequency f_{cav} of the cavity. For version 2, we used a power at the input of the cavity of -68 dBm and for version 4 we used -98 dBm. When the fiber was moved with respect to the chip, I observed small changes in the resonance frequency f_{cav} of the 3D cavity (see Fig. 7.8). This was most evident in version 2 of the fiber-chip experiment. Perturbation of the cavity resonance can be caused by direct perturbation of the electric field of the cavity by the fiber's dielectric or it can be due to the fiber perturbing the LC resonator, which in turn couples to and perturbs the cavity resonance. This indirect contribution is a level-repulsion effect and would produce a pattern for f_{cav} that was similar to that of f_o. As in Fig. 7.2, the indirect coupling would give a minimum in f_{cav} in the plane of the resonator closest to the inductor and a larger and roughly symmetric dip above the capacitor banks. In contrast, the direct perturbation of the cavity's electric field would yield relatively smooth changes in f_{cav}, on the scale of cavity dimensions, except for fringing fields near the edges of the mouse-hole and the chip.

Examining Fig. 7.8, we see that f_{cav} only shows smooth changes as the fiber is scanned, with a tendency for smaller frequencies near the chip. This looks more like direct perturbation of the cavity frequency as the fiber moves in the cavity electric field near the substrate. I note that the microfiber occupies about 10^{-5} of the 3D cavity volume and the max change we see in f_{cav} was ~6.7×10^{-6} f_0 . Given the dielectric constant of the fiber, this means that $\Delta f_{cav}/f_{cav}$ is about 10% of $\mathcal{E}_{fiber}/\mathcal{E}_{total}$. However, we are not removing the fiber from the cavity during the scan, we are displacing it in the cavity by a maximum of ~1 mm. If the cavity was empty, the electric field of the TE_{101} mode near the center of the cavity

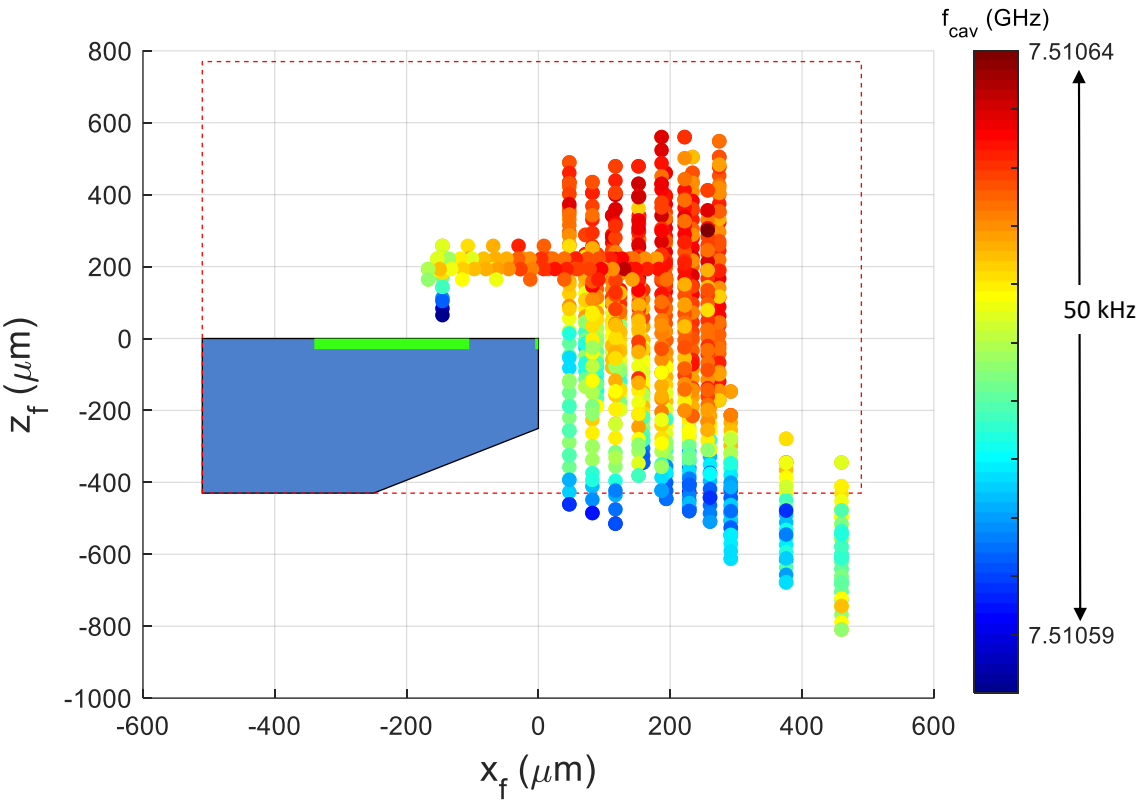

Fig. 7.8 - False color map showing frequency of the 3D cavity resonance f_{cav} (not the resonance of the thin-film resonator) as a function of the fiber's estimated position x_f and z_f. No light was transmitted through the fiber during these measurements. Data taken with device LC2 mounted inside the 3D cavity during the microfiber-chip experiment version 2, at 100 mK. The red dotted line indicates the estimated location of the hole in the 3D cavity. Blue polygon shows corresponding side-view of chip.

would not change much on a 1 mm scale. However, the cavity is not empty and the perturbation appears to be largest when the fiber is near the chip or the mouse-holes in the cavity wall; the weak spatial dependence in f_{cav} is likely due to perturbation of the cavity fringing fields near the chip edges and mouse-hole walls.

7.5 Resonator Response vs. Optical Power

Before discussing the behavior of the resonator when the fiber is moved and illuminating different parts of the resonator, it is helpful to first consider the simpler

situation where the fiber is held at a fixed location and the optical power is varied.

For these measurements the fiber was ~500 μm away from resonator LC2 and we measured what happened as we varied the optical power P_{opt} transmitted by the fiber from 0.0 to 4.0 mW. Of course, only a very small fraction of the light travelling down the fiber was Rayleigh scattered by the fiber and absorbed by the resonator. I estimate that just 0.1 ppm of the light applied to the fiber is incident on the resonator and only about 10% of this incident light would be absorbed, or about 40 pW at the maximum illumination used here.

Figures 7.9(a) and (b) show the magnitude and phase of S_{21} as a function of frequency for different optical powers in the fiber. This data was collected on resonator LC2 with the refrigerator at about 20 mK. Examining Fig. 7.9(a), we see a clear resonance in $|S_{21}|$ at about 6.14066 GHz and this shifts steadily to lower frequency and decreases in height as the optical power increases. This means that the resonance frequency f_0 and quality factor Q steadily decrease with increasing illumination, as expected from the generation of quasiparticles from optical absorption. Similarly, in Fig. 7.9(b) we see that the phase-vs-frequency curve shifts steadily to lower frequency as the optical power increases.

In version 2 of the microfiber-chip experiment, we used this simple behavior of the phase to quantify the optical response of the resonator. If we fix the frequency f at the unilluminated resonance frequency, as indicated by the dotted line in Fig. 7.9(b), the change $\delta\phi$ in the phase ϕ of S_{21} will be approximately proportional to the change δf_0 in the resonance frequency f_0, at least for sufficiently small shifts in f_0. Fitting a line to the linear portion of the ϕ vs f curve gave an approximate quantitative relation between δf_0 and $\delta\phi$.

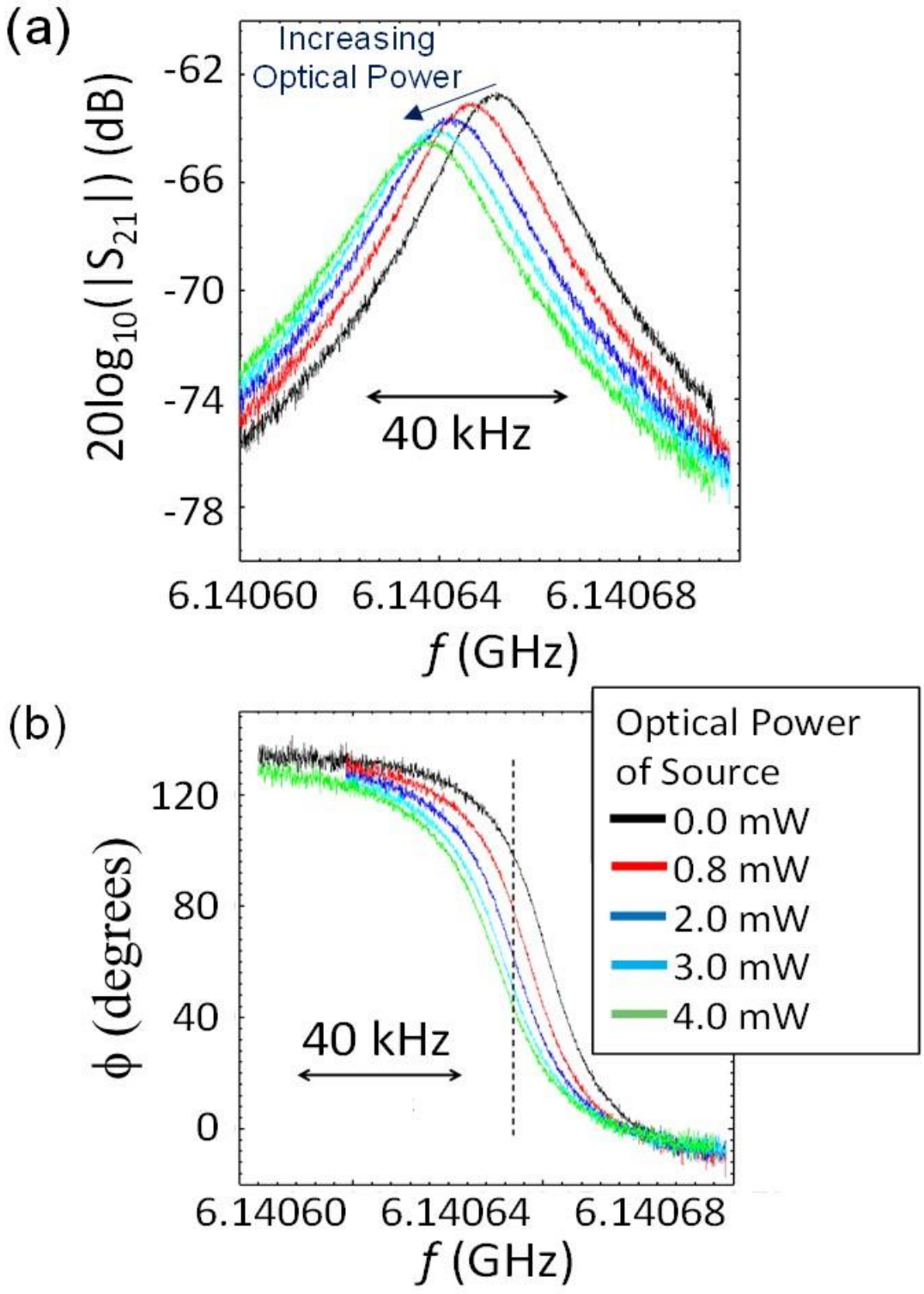

Fig. 7.9- (a) $|S_{21}|$ in units of dB versus frequency f for different applied optical source power for resonator LC2 at 20 mK. (b) Corresponding plot of the transmission phase ϕ versus frequency f for different applied optical source power.

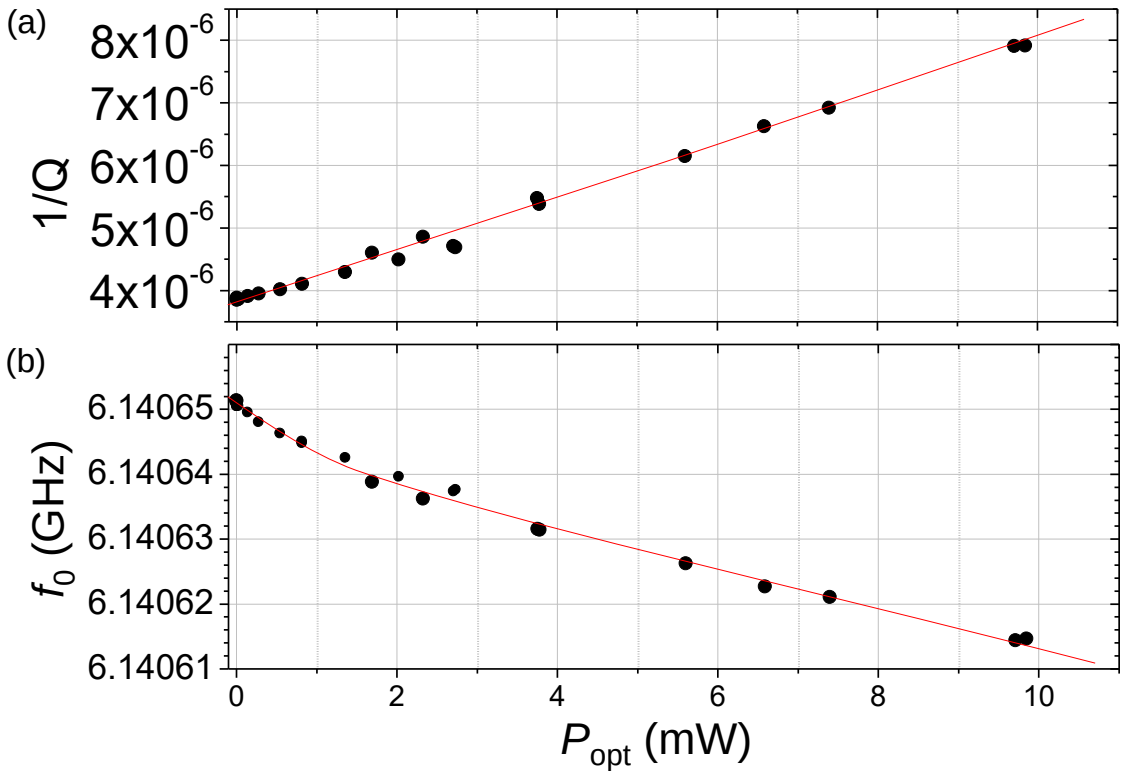

Fig. 7.10 - (a) Plot of inverse quality factor $1/Q$ versus applied source optical power P_{opt} for device LC2 at 20 mK. Red line is a guide for the eye, not a fit. (b) Corresponding plot of f_0 versus applied source optical power P_{opt}. Red curve is a guide for the eye.

As I describe below, this allowed me to monitor the phase in version 2 and extract the corresponding frequency shifts as we varied the illumination. For some measurements in version 2, I also extracted f_0 and Q of the resonance while illuminated by fitting to $S_{21}(f)$, using the same approach I discussed in Ch 5. In version 4, I measured $S_{21}(f)$ when the resonator was both illuminated and unilluminated, and then fit to the line shapes to extract the resonance frequencies.

Figure 7.10(a) shows a plot of the loss $1/Q$ versus P_{opt} from the measurements of resonator LC2 with the fiber 500 μm away. Notice that supplying 10 mW to the fiber caused $1/Q$ to double from the unilluminated value, which corresponds to Q decreasing

from about 250,000 at zero power to 125,000 at 10 mW in the fiber. Similarly, Fig. 7.10(b) shows a plot of f_0 versus P_{opt} from the measurements of resonator LC2 with the fiber 500 μm away. The curve clearly bends, rather than being straight, with a total shift of only 40 kHz at P_{opt} = 10 mW.

One complication of this particular data set was that during the measurements the mixing stage of the refrigerator heated to 60 mK. This temperature rise represents a heat load of about 55 μW at the cold stage of the fridge. Some of this heating was likely due to light that was leaving the fiber at the fiber tapers either due to mode mismatch or light that was left in the cladding after the mandrel wraps. Due to the geometry, this light would not be incident on the resonator [7.3, 7.4]. I note that the output power from the fiber was not measured at the time. If it were, it could have given a better lower bound on how much optical power was in the fiber as it passed near the resonator.

7.6 Resonator Response vs. Position - With Optical Power

The main data that I took on LC resonators involved mapping the change in resonance frequency δf_0 due to Rayleigh scattered light as a function of fiber position (x_f, z_f), where δf_0 was the difference between the resonance frequency when light was applied to the fiber and the resonance frequency when light was not applied to the fiber. I also simultaneously obtained maps of the change in loss $\delta(1/Q)$ due to the light.

There were three main reasons for generating these optical response maps. First, the response maps were essential for determining the relative position of the fiber with respect to the chip. Ultimately, a viable hybrid system will require position feedback on the attocubes and stable sensors to allow accurate positioning of the fiber. However, our

primary goal was locating the fiber with respect to the LC resonator, ultimately at the level of a few μm in both x and z. Even with perfect knowledge of the position at room temperature and the attocube stage position, one would still need to account for differential thermal contraction in the stages and fiber holder as the system cools. A better approach is to generate in situ response maps of δf_0 and $\delta(1/Q)$ and then use landmarks in the maps to reveal the relative fiber-chip position.

The other reason for generating optical response maps was that they helped me gauge the best location for the fiber (near the inductor and in the top-plane of the chip, at $z_f = 0$ μm) and determine how much loss and frequency shift we could expect with the fiber scattering light from that position. Third, as will be seen in Sec. 7.8, the response maps helped me model the distribution of quasiparticles in the resonator. In the future, this could help in designing a resonator and qubit that would be less affected by Rayleigh scattering of light from the fiber.

As I discussed above, in version 2 of the microfiber-chip experiment with resonator LC2, I found the optical response $|\delta f_0|$ from the change $\delta\phi$ in the phase of the transmitted microwave signal at frequency f_0 (see Sec. 7.4). Figure 7.11 shows an example where the microfiber was carrying 200 μW of transmitted optical power. As the fiber was swept in z, just to the right of the chip edge at $x_f = 0$, there is a local minimum at $z_f = 0$ as the fiber aligns with the chip surface and only illuminates the side of the 200 nm thick Al film. The minimum was distinct but non-zero.There was some inevitable misalignment of the fiber that tilted it out of the plane of the chip, which would have increased the exposed area of the chip even at $z_f = 0$. Note also that the pattern is roughly symmetric above and below $z_f = 0$ because the sapphire of the chip is transparent. However, scattering at the edge of

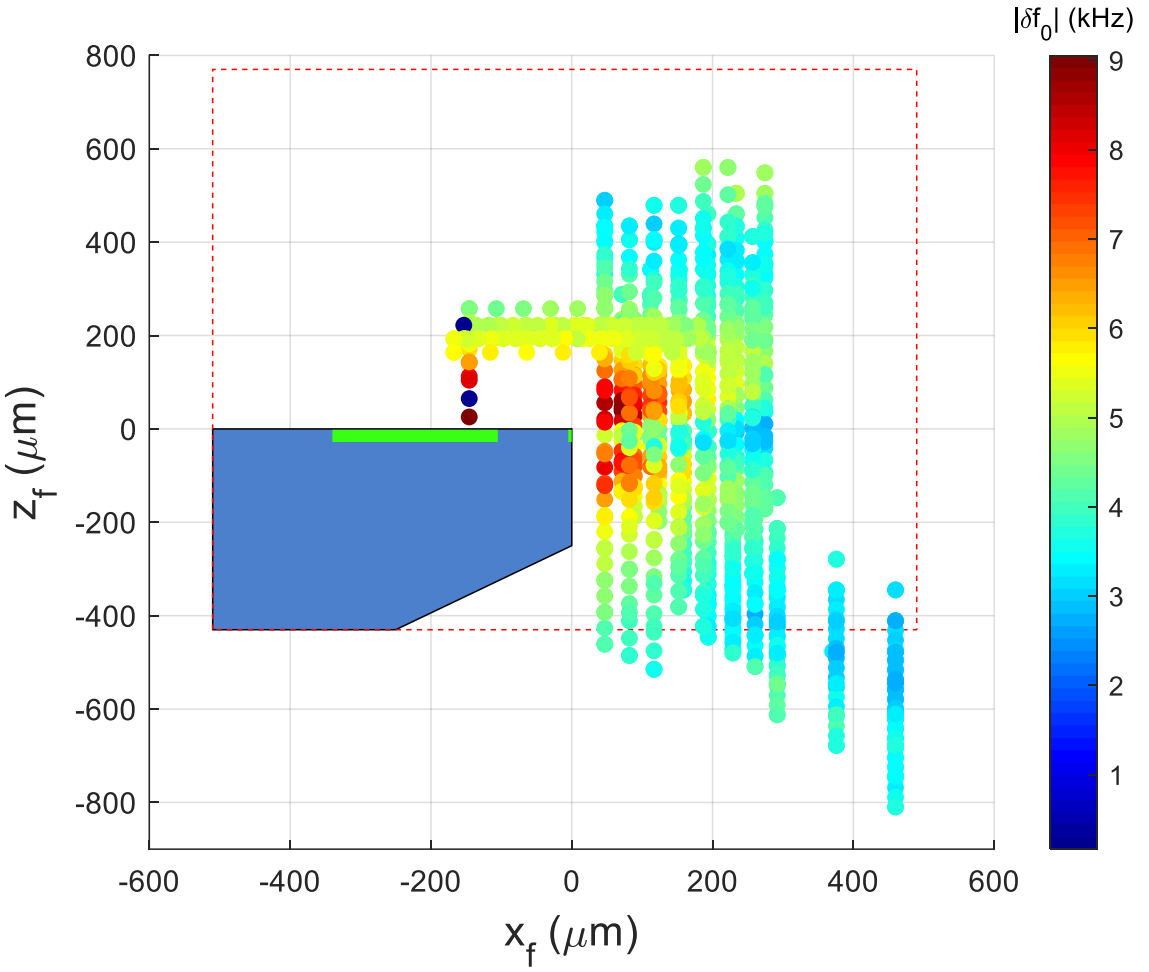

Fig. 7.11 - False color map of the optical response $|\delta f_0|$ due to light as a function of the fiber position (x_f, z_f). Data was taken on device LC2 at 100 mK during version 2 of the microfiber-chip experiment and was acquired during the same scans as the data shown in Figs. 7.2 and 7.8. Red dashed box indicates edge of hole in the wall of the 3D cavity. Some data points lie outside the red dotted lines likely due to cumulative error in the dead-reckoning process used for estimating (x_f, z_f).

the sapphire chip would reduce the amount of light reaching the resonator when the fiber was below the top-plane of the chip. This likely explains why the response is somewhat weaker for $z_f < 0$ than for $z_f > 0$. Just above and below the top-plane of the chip, $|\delta f_0|$ peaks because, taking the distance and angle of incidence into account, this is where the optical power incident on the top or bottom surface of the resonator is largest. Also, for

$|x_f|$ >100 μm and $|z_f|$ > 100 μm, $|\delta f_0|$ decreases steadily with $|z_f|$ and $|x_f|$ because the increasing distance from the resonator decreases the intensity of the incident light from the fiber.

Fig. 7.12(a) shows a plot of $|\delta f_0|$ versus z_f that more clearly displays details of the response shown in Fig. 7.11. For the sweep closest to the inductor (x_f = 71 μm), $|\delta f_0|$ dips to a minimum of about 5 kHz at z_f = 0 μm and rises to a maximum of about 9 kHz at z_f = 50 μm. Of course I adjusted the z-origin of the trace to place the minimum at z_f = 0 (see Appendix C for more discussion of the position calibration issues). For the sweep farthest from the inductor, at x_f = 460 μm, $|\delta f_0|$ is about 3 kHz, with a relatively weak dependence on z_f.

I can use this measured relationship between $|\delta f_0|$ and P_{opt} to estimate what $|\delta f_0|$ would be if the fiber were carrying 10 mW of power, which is about the level needed to trap atoms, rather than the 200 μW level used for the measurements in Fig. 7.12. At (x_f, z_f) = (70, 0) μm with P_{opt} = 200 uW the measured resonance-frequency shift is about $|\delta f_0| \approx 4$ kHz. If I assume that $P_{opt} \propto |\delta f_0|$, I find $|\delta f_0| \approx$ 200 kHz at 10 mW for the same location. This is a relatively small frequency shift, but it is for the case of the fiber being about 70 μm from the chip, which is farther than desirable for a hybrid system. Bringing the fiber to within 5 μm would increase the frequency shift by a factor of about 200 (purely from geometric considerations), to about 50 MHz, which is quite significant. Much of this residual level of optical response is likely due to tilting of the fiber, which could be reduced with better alignment.

Figure 7.12(a) shows two puzzling features. First, $|\delta f_0|$ increases for z_f > 300 μm and z_f < 400 μm. It is not clear why this is happening, but it may be due to light that is

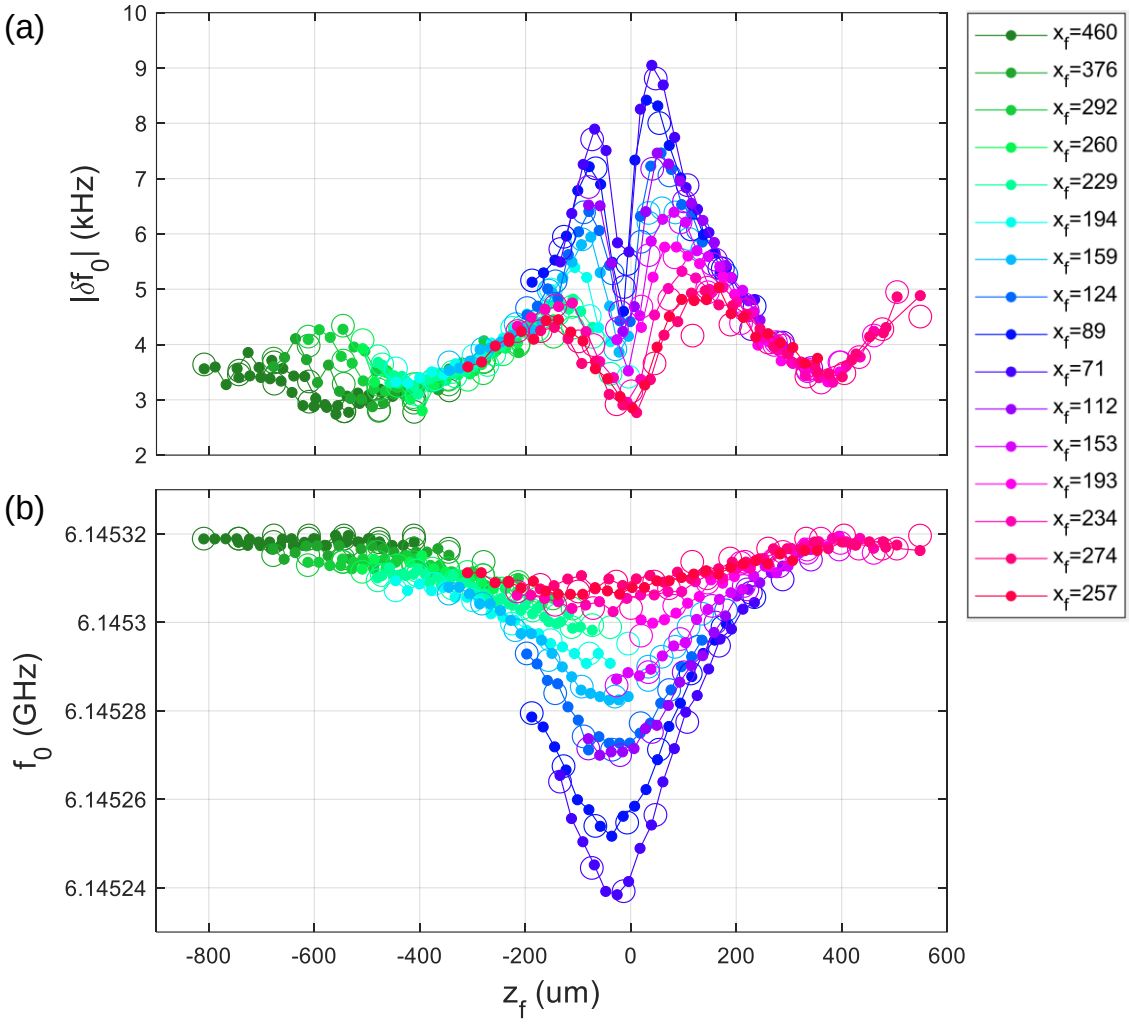

Fig. 7.12– (a) Magnitude of the shift $|\delta f_0|$ in resonance frequency due to Rayleigh scattered light versus the position z_f of the fiber. Data was taken on device LC2 at 100 mK during version 2 of the microfiber-chip experiment with about 200 μW being transmitted through the fiber. Different colored curves are for different x_f positions of the fiber, given in the legend in micrometers. Closed circles are for sweeps when the attocube was being extended and large open circles are for retracted sweeps. Note the prominent double-peak separated by a dip when the fiber is in line with the top-plane of the chip where the exposed area of the inductor is smallest. (b) Resonance frequency f_0 of the resonator LC2 versus z_f with no light transmitted through the fiber.

reflecting off the edges of the two holes in the 3D cavity and onto the resonator. Second, I note that the light blue sweep at x_f = 194 μm does not quite line up with the magenta curve, which was taken at an estimated x_f = 193 μm. This is most likely because of cumulative error in the positioning.

In Fig. 7.12(b), I plot the resonance frequency f_0 when no light is in the fiber versus z_f. This is the same data shown in Fig. 7.2. It was collected simultaneously with the optical response data in Fig. 7.12(a) and these changes in resonance frequency are due to the perturbation of the resonator's resonance frequency by the fiber's dielectric. Comparing the optical response of the resonator (Fig. 7.12 (a)) and the response of the resonator to the fiber dielectric (Fig. 7.12(b)), we see that both reveal *w*hen the z-coordinate of the fiber is aligned with the surface of the chip at z_f = 0. However, I note that the z-origin for each sweep in Fig. 7.12 (a) was adjusted such that the local minimum in $|\delta f_0|$ was situated at z_f = 0 μm. The same offset was used for each corresponding curve in Fig. 7.12(b), but when we compare some sweeps, especially x_f = 234, 274, and 257 μm in Fig. 7.12(b), we see that the minimum in $|\delta f_0|$ occurs close to but not exactly at z_f = 0 μm. This may be due to an asymmetry in the electric field due to the dielectric of the sapphire substrate, which could cause the maximum field strength to occur slightly below the z_f = 0 μm plane.

In version 2 of the fiber-chip experiment, we were only able to sweep the fiber part way over the capacitor (see Fig. 7.2). In version 4, we were careful to mount the chip so that we would be able to sweep the fiber all the way over the capacitor. In Figs. 7.13(a) and (b) I show plots of the optical response $|\delta f_0|$ and $\delta(1/Q)$ versus x_f for the two closest heights above the surface of the chip. Note that here $|\delta f_0|$ and $\delta(1/Q)$ are normalized by V_t/V_{t0} to account for laser drift, where V_t is the voltage of the photodiode measuring the transmitted

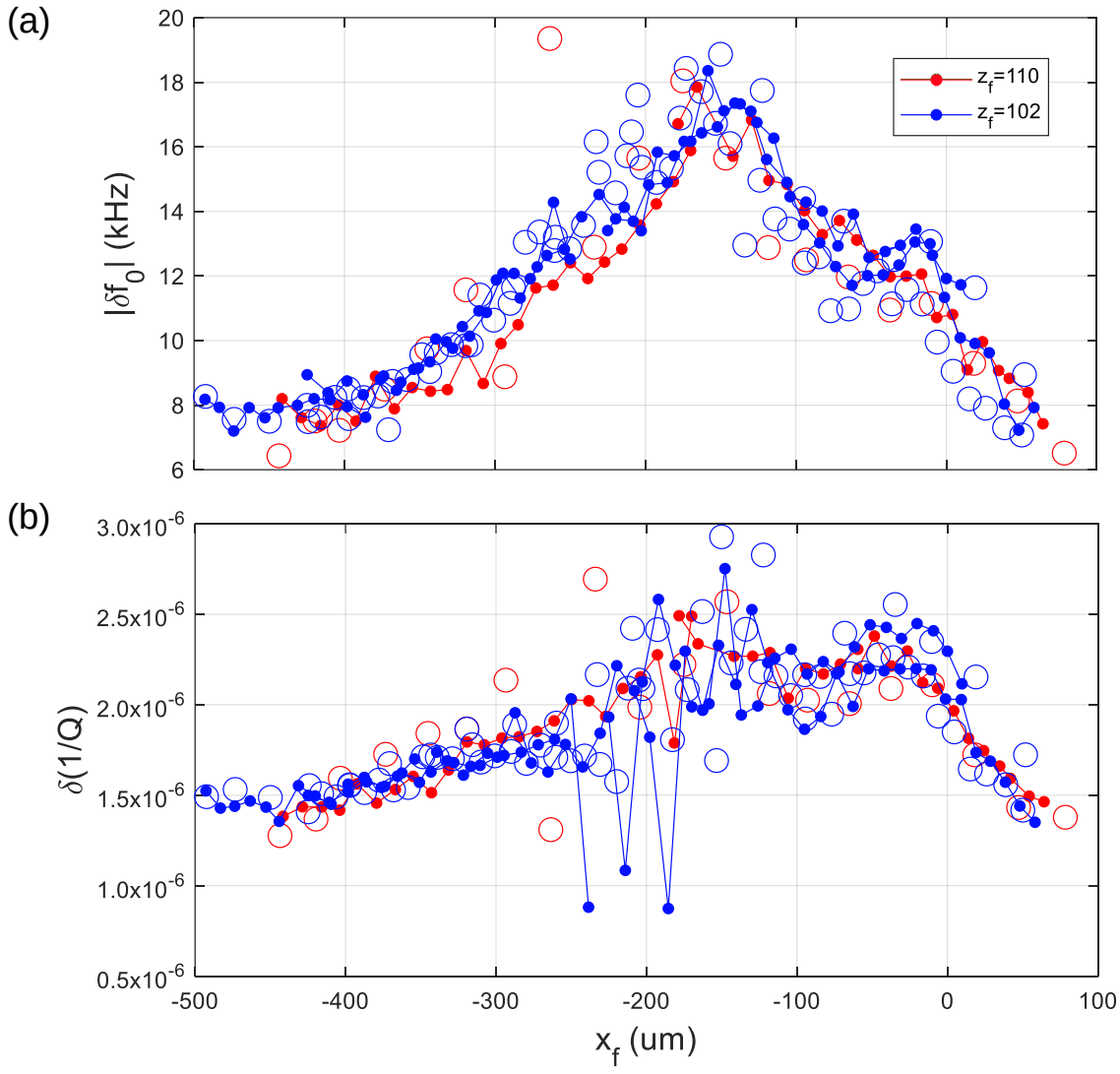

Fig. 7.13 - (a) Plot of $|\delta f_0|$ versus x_f above resonator LC3 for z_f = 102 μm (blue) and 110 μm (red). This data was taken at 100 mK in fiber-chip experiment version 4 on resonator LC3. Note the small bump near x_f = 0 μm for sweep at z_f = 102 μm. Closed circles are for sweeps where the attocube was extending and open circles are for when it was retracting. (b) Plot of $\delta(1/Q)$ in resonator LC3 due to Rayleigh scattering versus x_f for two z_f positions. The small bump near x_f = 0 μm is likely due to the number of quasiparticles in the inductor increasing when the fiber is over it.

optical power through the fiber and $V_{t0} = 0.733\ V$ is the value of V_t for the first data point (chronologically) shown in this plot. The variation in V_t is 2.3% at most over this range. In Fig. 7.13(a), both sweeps show a maximum response of about 18 kHz. This is about twice the response seen in Fig. 7.12(a) for device LC2, despite the fiber being further from the LC2 inductor. This may be due to the fact that these data sets were from two different resonators with somewhat different layout. It may also be that the relatively large response in LC3 was due to quasiparticles generated by the absorption of photons in the relatively large exposed area of the capacitor. I note that there is also a small broad bump near $x_f = 0$ μm. This is likely due to generation of quasiparticles in the inductor as the fiber is swept over it. I also note that the main peak in Fig. 7.13(a) is noticeably asymmetric, probably due to the asymmetric layout of the capacitor. Also, the quasiparticles will need to diffuse to the inductor to cause significant frequency perturbations, which would lead to an overall decrease in the response for large negative values of x_f.

In Fig. 7.13(b), I plot the corresponding change in loss $\delta(1/Q)$, due to Rayleigh scattering from the microfiber as a function of x_f. The two z sweeps show a small bump near $x_f = 0$ μm that we suspect is due to increased optically-induced quasiparticles in the inductor. This provides a possible reference point for the x position of the fiber, which would presumably be much more apparent if z_f was decreased further towards zero. While there is some resemblance between the plots in Fig. 7.12(a) and 7.12(b), the peak in the loss appears to be much broader. The reason for this is not clear, as we would expect both to be proportional to the same density of quasiparticles that are being generated. I note, however, that there is also more noise in $\delta(1/Q)$ for -300 μm < x_f < -100 μm, which is over

the capacitor. The shape of the LC3 resonance was also distorted in this region. This distortion may have been due to small vibrations of the fiber, which would cause inhomogeneous broadening of the resonance. This would be most noticeable over the capacitor, where the frequency depends most sensitively on the fiber position. In this case, the fitting routine produces less reliable values of Q, while still producing reliable f_0 values.

7.7 Model of the Optical Response

To better understand the position-dependent response that I discussed in the previous section, I did some detailed modelling of the expected response. Ultimately, the optical response is due to the absorption of optical photons in the superconductor, which breaks Cooper pairs and creates quasiparticles. A decrease in the number of pairs will increase the kinetic inductance and decrease the resonance frequency, while an increase in the number of quasiparticles will increase the loss, which decreases the internal quality factor Q_i.

The intensity of the Rayleigh-scattered light from a fiber can vary with azimuthal angle by about a factor of 2, depending on the light mode in the fiber [7.1]. However, for simplicity, I treat the fiber core as a line source of light that is isotropic in the azimuthal angle and that the light is emitted only perpendicular to the axis of the fiber. In addition, I assume the sapphire substrate is completely transparent to the 780 nm photons and ignore both absorption and scattering from the substrate surface or edges. I also assume that the reflectivity of the Al film is $R = 0.9$. The optical power absorbed in any region of the thin-film resonator can then be determined by the optical power scattered by the fiber, and the location and orientation of the fiber with respect to the resonator.

As discussed in Sec. 2.6, the two-dimensional density of quasiparticles n_{q2} obeys a diffusion equation

$$\dot{n}_{q2} = G_b + g_0 I_i + D_q \nabla^2 n_{q2} - R_q n_{q2}^2 - \Gamma_{tr} n_{q2} \tag{7.1}$$

where $G_b = G_t + G_n$ is the background areal rate at which quasiparticles are generated, G_t is the areal rate at which quasiparticles are generated thermally, and G_n is the areal rate at which non-equilibrium quasiparticles are generated, presumably by background infrared radiation or hot phonons. The spatially-dependent optical power absorbed in the resonator per unit area is $I_i(x,y)$, g_0 is the proportionality factor for creating quasiparticles from absorbed optical power, R_q is the areal recombination rate factor, and Γ_{tr} is the trapping rate of quasiparticles. For these simulations, I ignored trapping by setting $\Gamma_{tr} = 0$. I also assumed $G_t = 0$, as I was interested in temperatures T < 100 mK, which suppresses thermal generation.

With these assumptions the background generation rate of quasiparticles can be related to the background density of non-equilibrium quasiparticles by:

$$G_b = G_n = R_q n_{b2}^2 . \tag{7.2}$$

Experimental values for the 3D density of non-equilibrium quasiparticles appear to typically be about 1 to 100 μm^{-3} [7.5]. The density of non-equilibrium quasiparticles in our resonators was not known, but quite likely to be on the higher end of previously reported values given that there were two openings cut into the cavity wall. For simulations I assumed the 3D density of non-equilibrium quasiparticles was $n_b = 50\ \mu m^{-3}$. I converted this to an areal density n_{b2} by multiplying by the aluminum-film thickness d = 420 nm, giving $n_{b2} = 21\,\mu m^{-2}$.

Other studies have determined that the 3D recombination factor r_q is between

10 - 100 μm^3/s [7.6]. Here I will take r_q = 50 μm^3/s and divide by d to get an effective two-dimensional recombination factor R_q = 119 μm^2/s for our two-dimensional model. This then gives G_b = 5.25 x 10^{16} 1/(m^2·s) according to Eq. (7.2). I note also that $\Gamma_q = R_q n_{q2}$ is the effective decay rate of the quasiparticles to small perturbations in their number or areal density. For these values I find $\Gamma_q \sim 2x10^3$ /s.

From elementary statistical mechanics, the diffusion constant in a normal metal can be written as

$$D_n = \frac{v_{rms} d_o}{3} \tag{7.3}$$

where v_{rms} is the root-mean-square speed of the charge carriers and d_0 is the mean-free path of the charge carriers. I will ignore the energy dependence of v_{rms} and take it as the Fermi velocity v_f = 2.0 x 10^6 m/s in bulk aluminum [7.7]. The mean-free path in our sputtered aluminum film is not known, but as I argued in Ch. 3, we expect it is approximately d_0 = 19 nm based on the room temperature resistivity of the film. This is much less than the d = 420 nm film thickness and would imply the film is dirty. Plugging into Eq. (7.3) gives D_n = 0.01267 m^2/s. This is about a factor of two larger than what other researchers have reported in aluminum thin-films at cryogenic temperatures [7.9]. As discussed in Sec. 2.6, $D_q = D_q(E=\Delta+k_B T) = D_n\sqrt{1-\left(\Delta/(\Delta+k_B T)\right)^2}$ which becomes $D_q \approx 0.304 D_n$ for the T ~ 100 mK temperatures we are concerned with. Here I use the bulk value for the superconducting gap, Δ = 1.74 x 10^{-4} eV [7.7]. This results in a diffusion constant of D_q = 3.85067 x 10^{-3} m^2/s.

The second term on the right hand side of Eq. (7.1) determines the rate at which the local density of quasiparticles is generated by light. I can rewrite this as the rate at which

the optically generated quasiparticle density n_{opt} is created:

$$\dot{n}_{opt} = g_0 I_i \tag{7.4}$$

The local intensity I_i can also be written as the amount of power incident on the resonator δP_i per area $dx \cdot dy$ at location (x, y), or

$$I_i = \frac{d^2 P_i}{dx\, dy} \tag{7.5}$$

Integrating $I_i(x, y)$ over the area of the resonator gives the total power incident on the sample, which is P_i. The intensity I_i is due to the Rayleigh scattered light from the fiber. Figure 7.14 shows the configuration of the fiber and sample. The fiber is at height z above the sample and aligned parallel to the y-axis, while the sample is in the xy-plane. A small area $dA = dxdy$ on the sample at location $(x, y, 0)$ will have incident optical power

$$d^2 P_i = \frac{p_{RS}}{2\pi} d\theta dy\,, \tag{7.6}$$

where p_{RS} is the Rayleigh scattered optical power per unit length of the fiber and $d\theta$ is the angle subtended by dx. From Eqs. (7.5) and (7.6), I can write

$$I_i = \frac{d^2 P_i}{dxdy} = \frac{p_{RS}}{2\pi} \left| \frac{d\theta}{dx} \right| \tag{7.7}$$

Combining this with Eq. (7.4), I arrive at

$$\dot{n}_{opt} = \frac{g_0 p_{RS}}{2\pi} \left| \frac{d\theta}{dx} \right| . \tag{7.8}$$

Examining Fig. 7.14, the angle θ of Rayleigh scattered light incident on the resonator at location (x, y) is given by

$$\theta = \tan^{-1}\left(\frac{x - x_f}{|z_f|} \right) . \tag{7.9}$$

The derivative is then

$$\left|\frac{d\theta}{dx}\right| = \frac{\left|z_f\right|}{z_f^2 + \left(x - x_f\right)^2} \ . \tag{7.10}$$

Substituting Eq. (7.10) into Eq. (7.8) yields

$$\dot{n}_{opt} = \frac{g_0 p_{RS}}{2\pi} \frac{\left|z_f\right|}{z_f^2 + \left(x - x_f\right)^2} \tag{7.11}$$

The factor g_0 determines how many quasiparticles are generated by incident light and it depends on the superconducting energy gap Δ, the proportion η of the photon energy that goes into breaking Cooper pairs, and the reflectivity R of aluminum. I can write

$$g_0 = (1 - R)\frac{\eta}{\Delta} \tag{7.12}$$

Equation (7.11) then becomes

$$\dot{n}_{opt} = G_0 \frac{\left|z_f\right|}{z_f^2 + \left(x - x_f\right)^2}, \tag{7.13}$$

where

$$G_0 = \frac{\eta(1 - R)\, p_{RS}}{2\pi\, \Delta} \ . \tag{7.14}$$

To find a numerical value for G_0, I note that Day et al. has reported a value of $\eta = 0.57$ for Al [7.10]. Also, I will assume the Rayleigh scattering per unit length for the microfiber is the same as for a bulk fiber (<5 dB/km for 780 nm), which yields $p_{RS} = 2.4\text{x}10^{-7}$ W/m [7.11] for a source power of $P_{opt} = 200$ μW. I also take the reflectivity

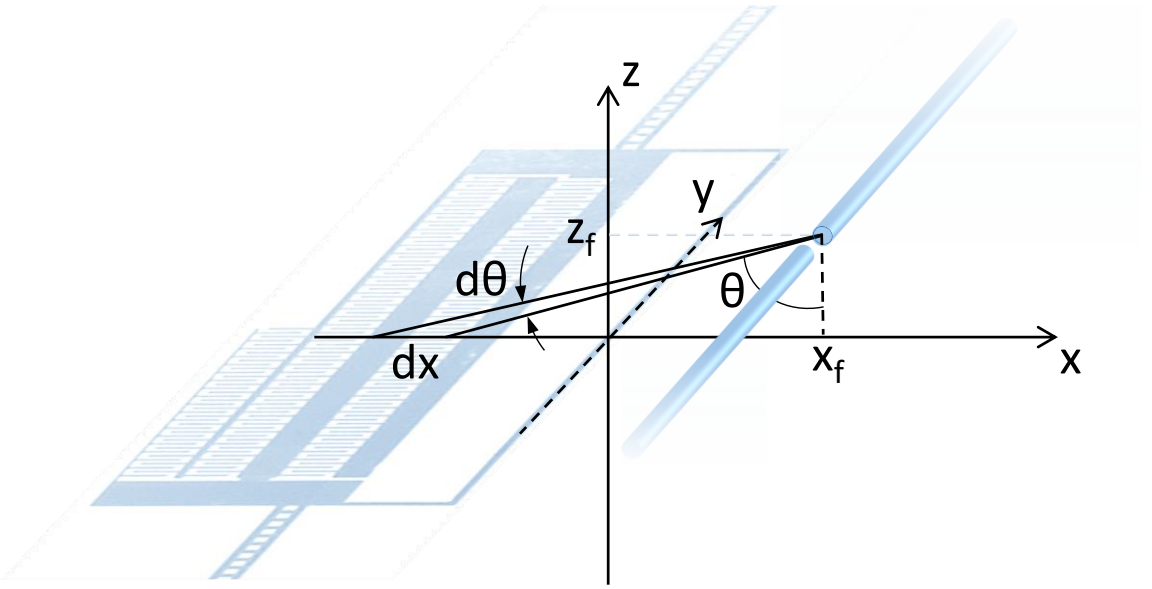

Fig. 7.14 - Coordinate system for the resonator and fiber. Position of a point on the resonator is given by (x, y, 0). The intensity of light depends on the perpendicular distance from the fiber. The angle of incident light on a given point of the resonator is θ.

of the aluminum film to be R = 0.9 [7.12]. Using the superconducting gap for bulk aluminum I find G_0 = 7.8 x10^{13} 1/(m·s).

Equation (7.1) can now be rewritten as:

$$\dot{n}_{q2} = G_b + G_0 \frac{|z_f|}{{z_f}^2 + (x - x_f)^2} + D_q \nabla^2 n_{q2} - R_q n_{q2}^2 \ . \tag{7.15}$$

The parameter values are summarized in Table 7.2. Additional parameters used to obtain the values in Table 7.2 are shown in Table 7.3.

Using Comsol modeling software [7.13], I built a 2D representation of the resonator and evaluated Eq. (7.15) to find the density of quasiparticles as a function of position in the resonator. Figure 7.15 shows results for resonator LC3 when the fiber was held at (x_f, z_f) = (200 μm, 200 μm), with the fiber running parallel to the inductor. Notice that the

Table 7.2 - Parameters in Eq. (7.15) and nominal values.

Parameter	**Description**	**Nominal value**
G_b	Rate of background quasiparticle density generation	5.25×10^{16} $(m^2 \cdot s)^{-1}$
G_0	Factor for optical quasiparticle generation for input fiber optical source power of 200 μW	7.8×10^{13} $(m \cdot s)^{-1}$
D_q	Quasiparticle diffusion coefficient [7.9]	3.85067×10^{-3} m^2/s
R_q	Recombination factor [7.6]	119 $\mu m^2/s$

Table 7.3 - Parameter values used to calculate parameters in Table 7.2.

Parameter	**Description**	**Nominal value**
R	Reflectivity of the Al film	0.9
Γ_{tr}	Trapping rate of quasiparticles	0
G_t	Thermal generation rate of quasiparticles	0
n_b	3D density of non-equilibrium quasiparticles	50 μm^{-3}
d	Al Film thickness	420 nm
n_{b2}	2D density of non-equilibrium quasiparticles	21 μm^{-2}
r_q	3D recombination factor	50 $\mu m^3/s$
Γ_q	Effective decay rate of quasiparticles	~ 10^3 /s
v_{rms}	Root-mean-square velocity of charge carriers in Al	2.0×10^6 m/s
v_f	Fermi velocity in Al	2.0×10^6 m/s
d_0	Mean-free path in Al at room temperature [7.8]	19 nm
D_n	Diffusion constant in normal Al at room temperature (Eq. (7.5))	0.013 m^2/s
Δ	Superconducting gap of bulk Al	1.74×10^{-4} eV
η	Fraction of pair-breaking photon energy [7.10]	0.57
p_{RS}	Rayleigh scattering power per unit length	2.4×10^{-7} W/m
P_{opt}	Optical power applied to fiber	200 μW
A	Fiber attenuation due to Rayleigh scattering at λ = 780 nm	<5 dB/km

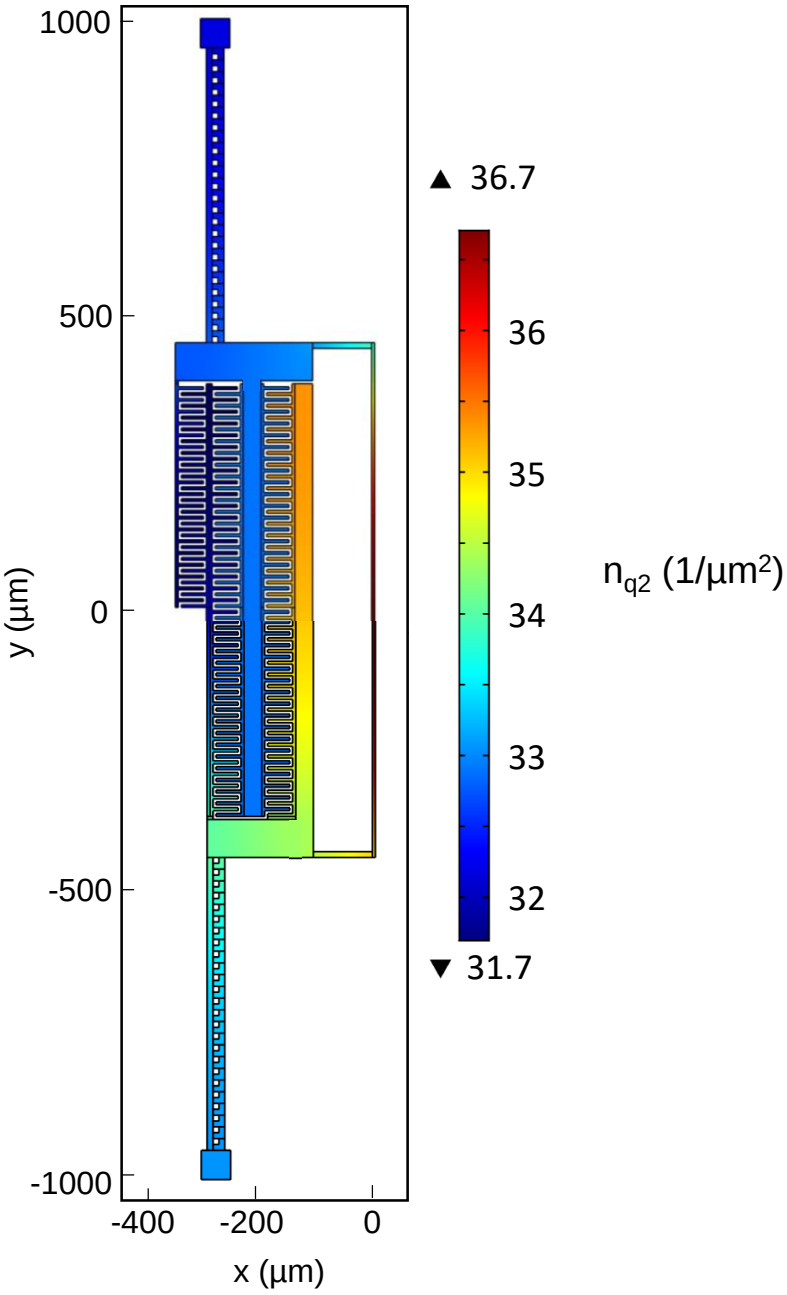

Fig. 7.15 - Simulated two-dimensional quasiparticle density map of the thin-film Al resonator LC3 with the fiber at location (x_f, z_f) = (200 µm, 200 µm), running parallel to the inductor line. The dark red represents all values above 36.7 μm^{-2} and the dark blue represents all values below 31.7 μm^{-2}.

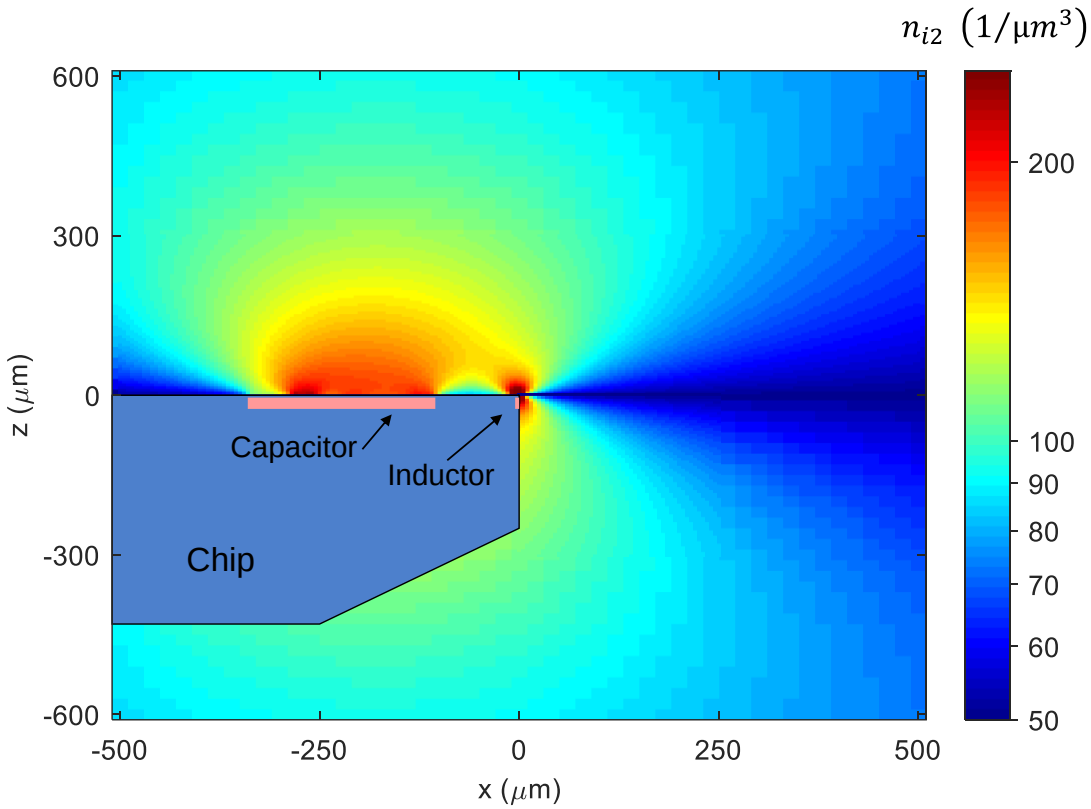

Fig. 7.16 – Side view of chip and false color plot showing simulation of the average volumetric density n_{i2} of quasiparticles in the resonator's inductor as a function of the position of the optical fiber. For small quasiparticles densities, the shift in resonance frequency is proportional to the quasiparticle density in the inductor.

quasiparticle density is highest in the inductor, which is the part of the resonator that is closest to the fiber.

Figure 7.16 shows another example from the simulation. The blue polygon represents the side view of the chip. The small and long pink lines on the top of the resonator represent the side view of the inductor and capacitor, respectively, although the thickness of these lines are not to scale (the capacitor and inductor consist of very thin-film aluminum). What this figure shows is how the response of the LC resonator depends on the fiber position. For each position of the fiber, I found the total number of quasiparticles

in the inductor. This number is a good figure of merit for the response because I expected the effect on the resonance frequency to be dominated by quasiparticles in regions where the resonant microwave current is highest, which is the inductor. For each point outside the chip, the color represents the average volumetric density of quasiparticles generated in the inductor when the fiber is at that point. The largest quasiparticle concentration (red) occurs in the inductor when the fiber is above the inductor. The response is roughly symmetric when the fiber is to either side of the inductor, but the response is greatest over the chip (i.e. on the left side) because the capacitor also absorbs light which generates quasiparticles that can diffuse into the inductor. The pattern is also symmetric about the z = 0 plane because our simple model does not account for the edge of the sapphire substrate's tendency to scatter light or the index of refraction. In practice, I expect the -z half-plane to resemble the +*z* half-plane, but for z < 0 the light from the fiber will be scattered and refracted somewhat as it passes through the polished edge of the sapphire chip.

In-line with the chip, at *z* = 0, the model indicates that the density of generated quasiparticles is n_{b2} because the thickness of the Al film is zero in the 2D model and thus absorbs no light. Since the actual film thickness is non-zero, and slight tilting of the fiber would prevent a true null, we expect the actual density of quasiparticles in the inductor when the fiber is in line with the chip surface to be greater than n_{b2}. In addition there will be some indirect light scattered from the chip and the 3D Al cavity walls.

7.8 Relating n_{qp} to f_0 and 1/Q using Gao's Equations

The simulations I described in the previous section give predictions for the areal density of quasiparticles as a function of the fiber's location. On the other hand, the

experiments involved measuring the change δf_0 in the resonance frequency f_0 and the change in the quality factor Q as a function of the fiber's location. To be able to compare the simulations to the data, I need a model for how Q and f_0 depend on the density of quasiparticles. The fractional change in resonance frequency $\delta f_0/f_0$ due to quasiparticles can be written in terms of the imaginary part σ_2 of the complex conductivity σ_1-iσ_2. For example, Gao *et al.* [7.14] write:

$$\frac{\delta f_0}{f_0} = -\frac{\alpha\gamma}{2}\frac{\delta\sigma_2}{\sigma_2}, \tag{7.16}$$

where $\alpha = L_k/L$ is the ratio of kinetic inductance L_k to geometric inductance L, and γ is a numerical factor that depends on whether the aluminum is clean (γ = -1/3) or dirty (γ = -1/2). The other key parameter that we measured was the quality factor Q or equivalently the total loss 1/Q which we can write as:

$$\frac{1}{Q} = \frac{1}{Q_i} + \frac{1}{Q_e} = \frac{1}{Q_{qp}} + \frac{1}{Q_{TLS}} + \frac{1}{Q_e} \tag{7.17}$$

where $1/Q_i$ is the internal loss, $1/Q_e$ is the coupling loss, and $1/Q_{TLS}$ is the loss due to TLSs. From R. Budoyo [7.15] we can write

$$\frac{1}{Q_{qp}} = \alpha\frac{\sigma_1}{\sigma_2} \tag{7.18}$$

In our situation, it is not easy to distinguish the coupling loss, the loss due to TLSs and the loss due to quasiparticles. However, we know that the change in loss when light is turned on is almost entirely due to the change in $1/Q_{qp}$. It is possible that there could be a contribution from the TLSs - if the temperature increases significantly when light is applied, this would cause the loss from TLSs to decrease. Ignoring this possible contribution we find from Eq. (7.17) that the change in the loss due to quasiparticles can

be written as:

$$\delta\left(\frac{1}{Q}\right)=\delta\left(\frac{1}{Q_{qp}}\right)=\alpha\frac{\delta\sigma_1}{\sigma_2}-\alpha\frac{\sigma_1\delta\sigma_2}{\sigma_2^2} \tag{7.19}$$

For a superconductor at temperatures such that $k_BT << \Delta$ and the frequency $f_0 << \Delta/h$, we will have $\sigma_1 << \sigma_2$ and the second term in Eq. (7.19) will be negligible compared to the first. Thus:

$$\delta\left(\frac{1}{Q}\right)\approx\alpha\frac{\delta\sigma_1}{\sigma_2} \tag{7.20}$$

To find $\alpha = L_k/L$, I need the kinetic inductance L_k. In principle, for a long straight line strip, this can be obtained from [7.16]:

$$L_k=\frac{\mu_0 l\lambda_{eff}}{2w\pi^2}\ln\left(\frac{4w}{d}\right) \tag{7.21}$$

where L_k is the resonator's kinetic inductance, l is the length of the inductor, λ_{eff} is the effective penetration depth for the inductor, w is the width of the inductor, and d is the film thickness. I estimate λ_{eff} to be 148 nm from [7.17]

$$\lambda_{eff}=\lambda_L\sqrt{1+\xi_0/d_0} \tag{7.22}$$

where λ_L is the London penetration depth, ξ_0 is the coherence length, and d_0 is the mean-free path. Note that the values of these and other essential parameters are given in Table 7.4. A difficulty with Eq. (7.21) is that it depends on λ_{eff}, which is admittedly not well-known. An alternative to finding L_k is to use instead

$$L_k=m_e l/\left(2n_{cp}e^2A_0\right) \tag{7.23}$$

where n_{cp} is the density of Cooper Pairs, m_e is the mass of an electron, and A_o is the effective cross-sectional area of inductor, i.e. the area that the current is flowing in. However, for all

Table 7.4 - Parameters to determine frequency response and loss due to illumination.

Parameter	Description	Value
f_0	Resonance frequency of resonator LC (depends on fiber position)	6.144118-6.145321 GHz
δf_0	Change in f_0 due to change in quasiparticle density n_{qp} (depends on fiber position)	2.5 to 12.4 kHz
L	Geometric inductance of resonator LC2	1.82 nH
L_k	Kinetic inductance of LC2: Eq. (7.21)	8.6 pH
A_0	Effective cross-sectional area of inductor	1.05 μm^2
α	L_k/L	4.73 x 10^{-3}
L	Length of the inductor of resonator LC2	1.1 mm
λ_{eff}	Effective superconducting penetration depth in the inductor of resonator LC2 at 100 mK	148 nm
W	Width of the inductor of resonator LC2	10 μm
D	Thickness of the Al thin film of resonator LC2	420 nm
λ_L	London penetration depth in bulk Al in the low-temperature limit	16 nm
ξ_0	Coherence length of superconducting Al	1.6 μm
d_0	Mean free path of charge carriers in superconducting Al	19 nm
γ	Local limit (-0.5) vs. anomalous limit (-1/3) parameter [7.14]	-0.33 or -0.5
σ_2	Imaginary part of complex conductivity of Al	--
$\delta\sigma_2$	Change in σ_2 due to optical illumination	--
Q_{TLS}	Inverse of the loss due to two-level systems (TLS)	--
Q_{qp}	Inverse of the loss due to quasiparticles	--
σ_1	Real part of complex conductivity of Al	--
$\delta\sigma_1$	Change in σ_1 due to optical illumination	--
σ_n	Normal conductivity	--
Δ_0	Superconducting gap energy of Al	1.74 x 10^{-4} eV
ω	Angular frequency of resonator LC2	3.86 x 10^{10} s^{-1}
N_0	Single-spin density of states in Al	1.07 x 10^{47} m^{-3}J^{-1}
T	Temperature	100 mK
ξ	$\xi = \hbar\omega / 2k_BT$	1.475
$I_0(\xi)$	Modified Bessel function of first kind, order 0.	1.622
$K_0(\xi)$	Modified Bessel function of second kind, order 0.	0.2209
A	$A = (\pi / 2N_0\hbar\omega)\left[1 + e^{-\xi} I_0(\xi)\sqrt{2\Delta_0 / \pi k_BT}\right]$	8.47 x 10^{-24} m^3
B	$B = (1/ N_0\hbar\omega)\sqrt{2\Delta_0 / \pi k_BT}\,\sinh(\xi) K_0(\xi)$	3.83 x 10^{-24} m^3
C	$C = (1/ 2N_0\Delta_0)\left[1 + e^{-\xi} I_0(\xi)\sqrt{2\Delta_0 / \pi k_BT}\right]$	3.82 x 10^{-25} m^3
D	$D = \pi\Delta_0 / \hbar\omega$	22.2
n_{q2}	2D density of quasiparticles	--
n_{qp}	3D density of quasiparticles	--
n_{b2}	2D unilluminated density of quasiparticles	--
n_b	3D unilluminated density of quasiparticles	--
n_{i2}	Average 2D density of quasiparticles in inductor	--

further calculations I use Eq. (7.21) for L_k.

I can now consider how the quasiparticle density n_{qp} determines the complex conductivity. Gao et al. [7.14] give the following three useful relationships:

$$\frac{\sigma_2(n_{qp},T)}{\sigma_n} = \frac{\pi\Delta_0}{\hbar\omega}\left[1-\frac{1}{2N_0\Delta_0}\left(1+\sqrt{\frac{2\Delta_0}{\pi k_B T}}e^{-\xi}I_0(\xi)\right)n_{qp}\right] \tag{7.24}$$

$$\frac{d\sigma_1}{dn_{qp}} = \sigma_n \frac{1}{N_0\hbar\omega}\sqrt{\frac{2\Delta_0}{\pi k_B T}}\sinh(\xi)K_0(\xi) \tag{7.25}$$

$$\frac{d\sigma_2}{dn_{qp}} = -\sigma_n \frac{\pi}{2N_0\hbar\omega}\left[1+\sqrt{\frac{2\Delta_0}{\pi k_B T}}e^{-\xi}I_0(\xi)\right] \tag{7.26}$$

where σ_n is the normal conductivity, Δ_0 is the superconducting energy gap, ω is the angular frequency of the resonator, N_0 is the single-spin density of states in aluminum, T is the temperature, and $\xi = \hbar\omega/2k_BT$. Here also, I_0 is the modified Bessel function of the first kind, with order 0, and K_0 is the modified Bessel function of the second kind, with order 0. I should also emphasize at this point that n_{qp} in these expressions is the 3D density of quasiparticles, while in the previous section I considered the areal density n_{q2} of quasiparticles - the two quantities are related by $n_{q2} = n_{qp}/d$, where d is the film thickness.

I define four temperature-dependent parameters to simplify Eqs. (7.24) - (7.26):

$$A = (\pi/2N_0\hbar\omega)\left[1+e^{-\xi}I_0(\xi)\sqrt{2\Delta_0/\pi k_B T}\right] \tag{7.27a}$$

$$B = (1/N_0\hbar\omega)\sqrt{2\Delta_0/\pi k_B T}\sinh(\xi)K_0(\xi) \tag{7.27b}$$

$$C = (1/2N_0\Delta_0)\left[1+e^{-\xi}I_0(\xi)\sqrt{2\Delta_0/\pi k_B T}\right] \tag{7.27c}$$

$$D = \pi\Delta_0/\hbar\omega \tag{7.27d}$$

This simplifies Eqs. (7.24) - (7.26) to:

$$\sigma_2 = D\left(1 - Cn_{qp}\right)\sigma_n \tag{7.28}$$

$$\delta\sigma_1 = B\sigma_n \delta n_{qp} \tag{7.29}$$

$$\delta\sigma_2 = -A\sigma_n \delta n_{qp} \tag{7.30}$$

At the low temperatures of interest, we expect $n_{qp} << 1/C$, and Eq. (7.28) simplifies to

$$\sigma_2 \approx D\sigma_n \ . \tag{7.31}$$

Combining Eqs. (7.16), (7.30), and (7.31), I find:

$$\frac{\delta f_0}{f_0} \approx \frac{A\alpha\gamma}{2D}\delta n_{qp} \ . \tag{7.32}$$

Similarly, by combining Eqs. (7.20), (7.29), and (7.31), I obtain the following expression relating $\delta(1/Q)$ to δn_{qp}

$$\delta\left(\frac{1}{Q}\right) = \frac{\alpha B}{D}\delta n_{qp} \tag{7.33}$$

Examining Eqs. (7.32) and (7.33), we see that according to this analysis the fractional change in frequency and the change in the loss should both be proportional to changes in the quasiparticle density. I can write the ratio of these two values as:

$$b = \frac{\delta(1/Q)}{\delta f_0 / f_0} = \frac{2B}{\gamma A} = \frac{4}{\gamma\pi}\frac{\sinh(\xi)K_0(\xi)}{\sqrt{\pi k_B T/2\Delta_0} + e^{-\xi}I_0(\xi)} \tag{7.34}$$

I note that this ratio depends on γ, which has the value -0.5 if the aluminum is in the local (or dirty) limit and -1/3 if the aluminum is in the anomalous (or clean) limit. Clearly, Eq. (7.34) also implies that the ratio b depends on temperature (see Fig. 7.17). Examination of Fig. 7.17, shows that the temperature dependence is fairly weak, but cannot be ignored. However, for fixed T we expect b to be constant and thus there will be a linear relation between the frequency shift and change in the loss:

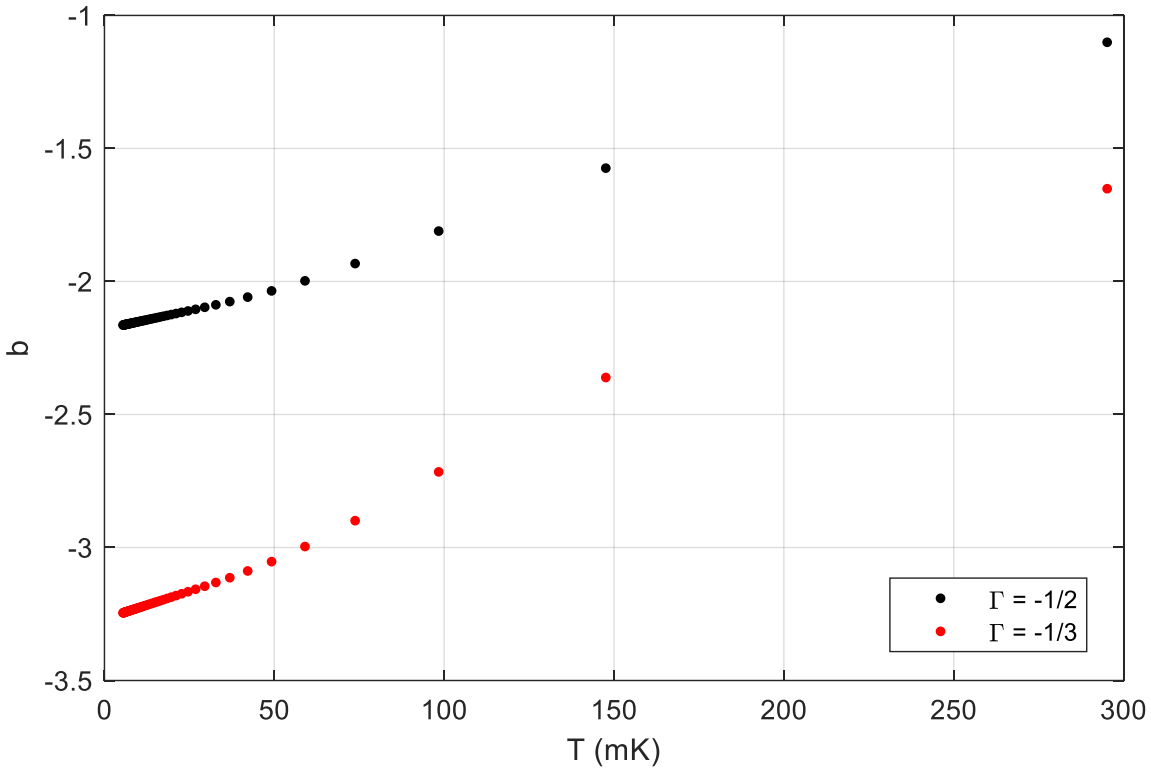

Fig. 7.17 - Plot of $b = \delta(1/Q)/(\delta f_0/f_0)$ from Eq. (7.35) as a function of the temperature *T*. Black curve and points are for γ = -0.5 (local or dirty limit) and red curve is for γ = -1/3 (anomalous or clean limit).

$$\delta\left(\frac{1}{Q}\right) = b\frac{\delta f_0}{f_0} \tag{7.35}$$

Note that this expression is only valid if the only thing changing is the quasiparticle density. If, for example, the temperature also changed, then this expression would fail.

This raises the question of whether our measurements of $\delta f_0/f_0$ and $\delta(1/Q)$ are consistent with Eq. (7.35). Figure 7.18 shows a plot of $\delta(1/Q)$ versus $\delta f_0/f_0$ taken from data I acquired during version 4 of the experiment resonator LC3 as the fiber moved around. Despite the scatter, there is a clear linear dependence. Ignoring the outliers, the slope of the

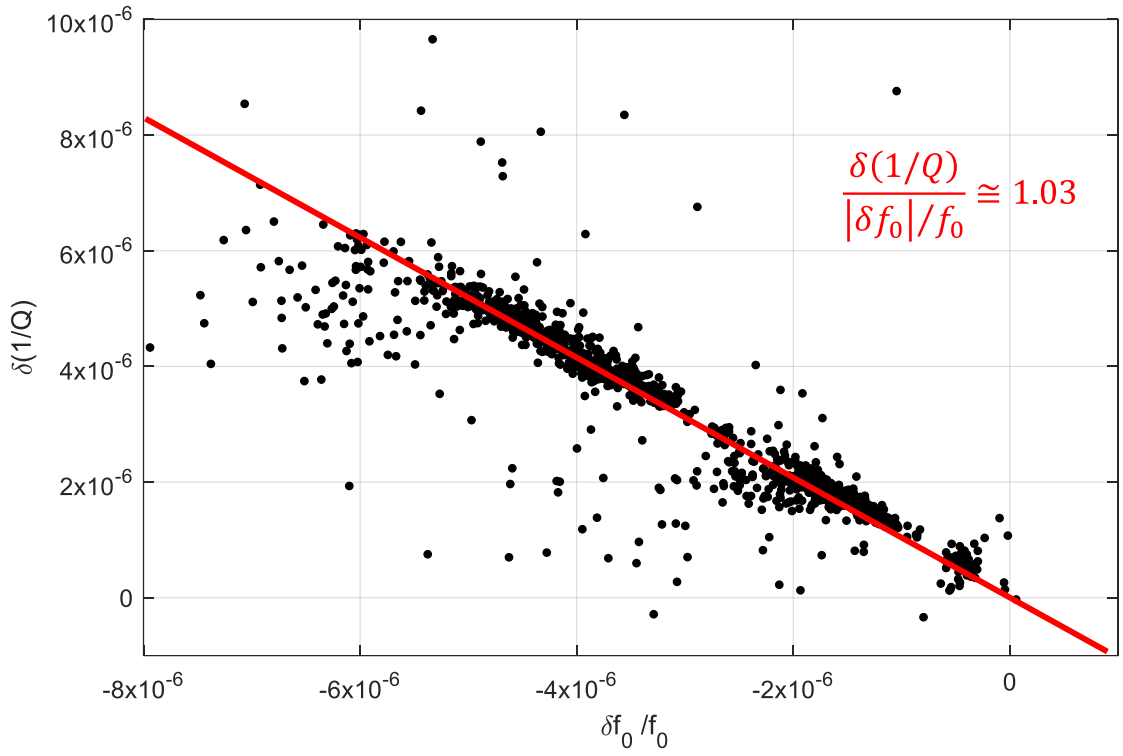

Fig. 7.18 - Scatter plot of the change in quality factor $\delta(1/Q)$ vs. the fractional frequency shift $\delta f_0/f_0$ for various positions of the light-carrying fiber in fiber-chip experiment version 4. Outliers and points where the fit to S_{21} were poor, have been omitted.

fit-by-eye line was b = -1.03. The minus sign indicates that, as expected, a decrease in the frequency corresponds to an increase in loss. This data was taken at T = 100 mK. Inspection of Fig. 7.17 shows that at T = 100 mK, we expect b = -2.7 in the clean or anomalous limit (γ = -1/3) and b = -1.8 in the dirty or local limit (γ = -0.5). My measured value of b = -1.03 from Fig. 7.18 is closer to the value of -1.8 expected in the dirty or local limit, but is about 43% smaller. Although we might have expected a sputtered Al film to be closer to the clean limit, as I noted above the film had a relatively high resistivity at room temperature and this gave a relatively short estimated mean free path. Another possible

explanation for the discrepancy is that when the resonator was illuminated, the temperature of the resonator and quasiparticles was somewhat higher than the temperature T of the mixing chamber. An overall increase to 300 mK would give good agreement in the dirty limit. However, as noted above, Eq. 7.35 assumed that the temperature does not change when the light is turned on and the discrepancy in the value of b suggests that we may be violating the assumption.

Another possible issue is evident in Fig. 7.18. At the highest illuminations, I find typical values of $\delta f_0/f_0 = -6\text{x}10^{-6}$ and $\delta(1/Q) = 6.2\text{x}10^{-6}$. Plugging values from Table 7.4 into Eq. (7.32) and considering a local quasiparticle temperature T = 300 mK, I find $\delta n_{qp} = 4.4\text{x}10^{3}$ μm^{-3} and $\delta n_{qp} = 1.7\text{x}10^{4}$ μm^{-3} from Eq. (7.33), where in both cases I have taken the dirty limit (γ = -1/2). The possible issue is that these densities are 50 to 1000 times larger than the expected background quasiparticle densities of 10-100 μm^{-3}. Of course this situation corresponds to the light being on (about 0.24 μW/m of scattered power, see Table 7.2), so it is not surprising that we appear to be getting density changes that are much larger than background. Never the less, these would correspond to quite large changes in the density for a well-shielded sample.

7.9 Comparison of the Measured Optical Response to the Model

In this section, I compare results from the model I described in the previous two sections to data from microfiber-chip experiment version 2 that I discussed in Sec. 7.6. Using the nominal parameters given above in Tables 7.1 and 7.2, I solved the diffusion equation Eq. (7.15) to find expected values for the areal quasiparticle density n_{q2} in all parts of the resonator with the fiber at a specific location and a specified level of Rayleigh scattered optical power. The response δf_0 due to quasiparticles will be dominated by

regions of the resonator where the resonator's oscillating current is highest, which is in the inductor, so n_{q2} in this region will determine the response. Thus for each fiber position (x_f, z_f), I found the average quasiparticle density n_{i2} in the inductor. Now in principle I could use Gao's equations to transform this into an equivalent expected values for the frequency shift, which could then be compared directly with the data. According to Eq. (7.32) we can write $\delta f_0 = (A\alpha\gamma f_0 / 2D)\,\delta n_{i2}/d$. However, not all the factors in the proportionality constant are well-known, so it is simplest to start by just arbitrarily scaling the simulated densities to see if they can match the frequency shift data when the fiber is moved.

Figure 7.19 shows an example of a comparison between the simulation and data acquired for version 2 of resonator LC2. The colored points show $|\delta f_0|$ versus z_f as the fiber is scanned through $z_f = 0$ just to the side of the inductor, with the $|\delta f_0|$ scale on the y-axis on the left. The different curves correspond to different values of x_f. The grey curves in Fig. 7.19 show the simulated values (converted to volumetric densities) of n_i as a function of z_f, with the n_i values given on the y-axis on the right. The different shades of grey correspond to different values of x_f.

Comparing results and simulations reveals that the proportionality constant between δn_i and f_0 is much different than Eq. (7.32) would suggest. For $|\delta f_0|$ = 9 kHz, Eq. (7.32) gives δn_{qp} = 3,200 μm^{-3} (in the dirty limit where gamma = -1/2), while the simulation with the nominal parameters of Table 7.2 gives δn_i = 60 μm^{-3} for the same $|\delta f_0|$. Given this discrepancy between the scales on the left and right y-axes of Fig. 7.19, which could be caused by an incorrect value for one or more of the parameters, I allow the proportionality factor to be a free variable for now. The minimum value of the right-hand

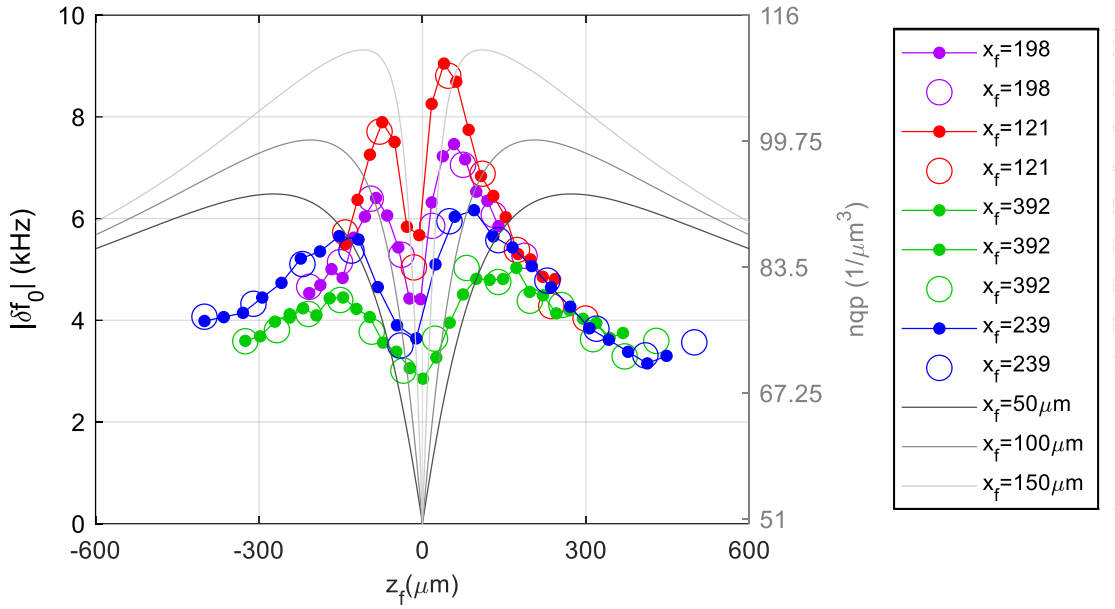

Fig. 7.19 - Colored dots and circles are measured frequency shifts of resonator LC2 from version 2 due to light $|\delta f_0|$ (left-hand y axis) as a function of the z position of the fiber z_f, where $z_f = 0$ has been determined by the "dip" feature in $|\delta f_0|$. The legend indicates the x position of the fiber, but still in the nominal coordinate system $x_{f,nom}$. The corresponding simulated densities of quasiparticles n_i (right-hand y axis) are shown in grey.

y axis is a free parameter that corresponds to n_i when no light is on the resonator (the resonator is a 2D surface in the simulation and absorbs no power when the fiber is at $z_f = 0$) and the maximum value of n_i is a free parameter that I chose to scale the simulation to the data.

Examination of Fig. 7.19 reveals obvious qualitative disagreements between the data and the simulation, even though we have allowed an arbitrary proportionality factor between δn_i and δf_0. For example, although both the data and the simulation show two peaks with a dip in the middle, the simulated peaks are much broader than the measured peaks. I address the possible causes for this disagreement below. Another difference is that the left peak in the data is lower than the right peak in the data, while the two peaks are the

same height in the simulation. The cause of this disagreement is clear. For $z_f < 0$, the fiber is below the plane of the resonator and must shine through the sapphire chip and its edge to illuminate the underside of the resonator, while for $z_f > 0$, the fiber is above the plane of the resonator and directly illuminates the topside of the resonator. In the actual device, for $z_f < 0$, scattering at the edge of the chip should tend to reduce the light reaching the resonator and decrease the frequency shift compared to when the fiber is in an analogous position above the plane. On the other hand, the simulation ignored scattering from the edge of the chip and thus did not accurately account for reduction in absorbed light for $z_f < 0$. Scattering at the chip's edge may also be the cause of another discrepancy. At $z_f = 0$, the simulated quasiparticle density reaches the background density because no light is absorbed when the fiber and ship surface are exactly aligned, and this would correspond to no change in the resonance frequency when light is turned on. However, in the real sample we see there is a substantial frequency shift at $z_f = 0$. Even if the fiber was well-aligned with the surface of the chip, scattering at the rough edge would cause some light to still reach the resonator and produce a frequency shift.

In addition to these qualitative disagreements, there is an important quantitative disagreement hiding in Fig. 7.19. The minimum quasiparticle density of about 51 μm^{-3} on the right-hand y-axis corresponds to the assumed background quasiparticle density when there is no light (at $z_f = 0$ in the simulation, the fiber and resonator are in the same plane and no light will be absorbed). However, the y-axis on the right has been stretched so that the maximum simulation value of $n_i = 110\ \mu m^{-3}$ corresponds to the maximum frequency shift. As I discussed above, this is equivalent to letting the proportionality between δf_0 and δn_i be a free variable, rather than fixed at a value of $A\alpha\gamma f_0 / 2D$ (from Eq. (7.32), where

δn_i and δn_{qp} are nominally the same parameter, as they both quantify 3D quasiparticle density in the high-current area of a resonator). Using the values in Table 7.4, I find a frequency shift of $|\delta f_0|$ = 9 kHz gives an expected δn_i = 3200 μm^{-3}. In contrast, Fig. 7.19 implies that a shift of $|\delta f_0|$ = 9 kHz corresponds to only δn_i = 60 μm^{-3}. What this means is that the simulation is producing too small of a change in the quasiparticle density. Or we could say that, if we incorporated the expected relationship between δf_0 and δn_i into the simulation, we would find that the simulated frequency shifts are about 50x smaller than the measured frequency shifts.

I now consider some of the possible causes of the qualitative disagreement that is causing the peaks in the simulation to be much broader than the peaks in the data. I can divide the possible causes into two categories, those that arise from errors in the experiment and those that arise from uncertainties or approximations made in the simulation.

Considering the possible experimental causes first, an obvious source of error in the data is that the attocube step size was only roughly known and tended to drift over time. If the attocube step size in the z-direction was smaller than expected by about a factor of 3, the agreement between the data and the simulation would be better, although still far from perfect. This is quite a large factor, probably unreasonably so, but as I discussed in Ch. 6 it cannot be completely ruled out because we did see significant changes in the step size. Another known source of uncertainty in the data was that, the phase ϕ of S_{21} varied due to drifting of the laser power by up to 10%. Since the frequency shift was determined from the phase shift, this effect would cause noise or drifting along the y-axis in Fig. 7.19. However, drifting of the phase could not explain broadening of the peaks, which corresponds to a stretching along the x-axis in Fig. 7.19. I should also note that the

relationship between δf_0 and $\delta\phi$ was approximately linear for small $\delta\phi$ but the approximation gets worse as $\delta\phi$ gets larger, with δf_0 increasing rapidly for large phase shifts. However, the phase shifts and corresponding frequency changes are too small for this to be an important effect. Furthermore the non-linearity would lead to an increased size of the largest frequency shifts on the experimental curves, rather than a flattening needed to get agreement with the simulation.

I next consider the possible causes in the qualitative disagreement due to possible uncertainties in the parameters or approximations made in the simulation. First, in arriving at the 2D diffusion equation, there were several approximations made. One important assumption was that the quasiparticles have a single speed, rather than an energy dependent dispersion relation. This simplifies the problem because it means I only needed to determine the spatial distribution of quasiparticles and did not need to also keep track at each location of the distribution of quasiparticles in energy. Further examination of the situation will be required to determine the impact of this approximation, but it appears to be a common simplifying assumption. Another issue with the simulation is that I set the trapping term $-\Gamma_{tr} n_{q2}$ to be zero (see Eq. (7.1)). Although there is no good physical reason to omit this term, and there is almost certainly trapping in the resonator at pinned flux vortices, recombination acts in a somewhat similar fashion to remove quasiparticles. In particular, if I use a somewhat larger value for the recombination rate constant R_q, this would tend to mimic the effect of a trapping term, especially if there is a background population of quasiparticles. Leaving out trapping appears to be an unlikely explanation for the discrepancy, but it can be checked qualitatively by trying larger values of R_q. Similarly, the thermal generation rate has been set to zero (see Table 7.2), which is

reasonable at 100 mK. However, if the resonator was heating up to 150 mK or higher when light was turned on, this could have caused a significant thermal population that depended on the location of the fiber. Finally, not all the parameters in the diffusion equation (G_b, G_0, D_q, and R_q) are well known. The most poorly known is G_b, which determines the background generation rate of non-equilibrium quasiparticles. This could be a factor of 10, 100 or 1000 times larger than the value in Table 7.2, which was used for the simulations in Fig. 7.19. Larger values are very plausible because the aluminum cavity had two holes cut into it which potentially allowed stray light to enter and generate background quasiparticles. Next, the optical generation rate G_0 could be significantly higher if the fiber had some light travelling in the cladding as well as in the core. This light should have been filtered out by the fiber mandrel wraps, but mismatch at the splices or insufficient filtering could have led to light in the cladding that was then ejected at the taper region and entered the cavity through the cavity hole. We note also that the quantitatively large frequency shifts seen in the data suggest a larger value for G_0. Next, the diffusion constant D_q depends on the cleanliness of the sputtered aluminum, which determines the quasiparticle mean free path, and this was not well-known. The value listed in Table 7.2 is actually a fairly small diffusion constant, as it is based on a relatively short mean free path of d = 19 nm. Although it is not impossible, it seems quite unlikely that D_q is much smaller than the assumed value. Finally, the recombination parameter was calculated from theory and is probably the best known of the parameters, but it actually will depend on the quasiparticle energy, which we have ignored because we have made a single speed approximation.

With differing levels of uncertainty in the parameters G_b, G_0, D_q, and R_q, it is important to have some intuition about how each parameter affects the simulation results.

Fig. 7.20 shows the same data as in Fig. 7.19, but now with different simulations where I have changed just one parameter while leaving the rest at the nominal values listed in Table 7.2.

Figure 7.20(a) is a reproduction of Fig. 7.19, which uses the nominal parameters for comparison. In Fig. 7.20(b), I show what happens when I increase G_0 by a factor of 100. Although this somewhat improves the agreement between the data and simulation, the data still appears considerably sharper than the simulation. Note, however, that this did increase δn_i by a factor of about 20 to 1,300 μm^{-3} and this gives better quantitative agreement with the measured frequency shifts - this density change would correspond to an expected frequency shift of about 4 kHz, which is still about 2 times smaller than observed but much closer. This behavior could suggest that the optical power was higher than the amount expected due to Rayleigh scattering from the core of the fiber.

In Fig. 7.20(c), I show what happens to the simulation when I decrease the diffusion constant D_q by a factor of 100. This results in much better qualitative agreement between data and simulation. However, notice also that δn_i increases to about 130 μm^{-3}, which is in the right direction, but still too small compared to the frequency shifts seen in the data. Also, it seems unlikely that D_q is even 10 times smaller than the nominal value, let alone 100 times smaller.

In Fig. 7.20(d), I show what happens when I increase R_q by a factor of 100. Again, we see much better qualitative agreement between the data and the simulation. However, notice that this increase in the recombination rate has led to a decrease in the maximum density change to just $\delta n_i = 10\ \mu m^{-3}$. Thus, while it is plausible that R_q could appear to be larger to account for trapping and this would improve the qualitative agreement between

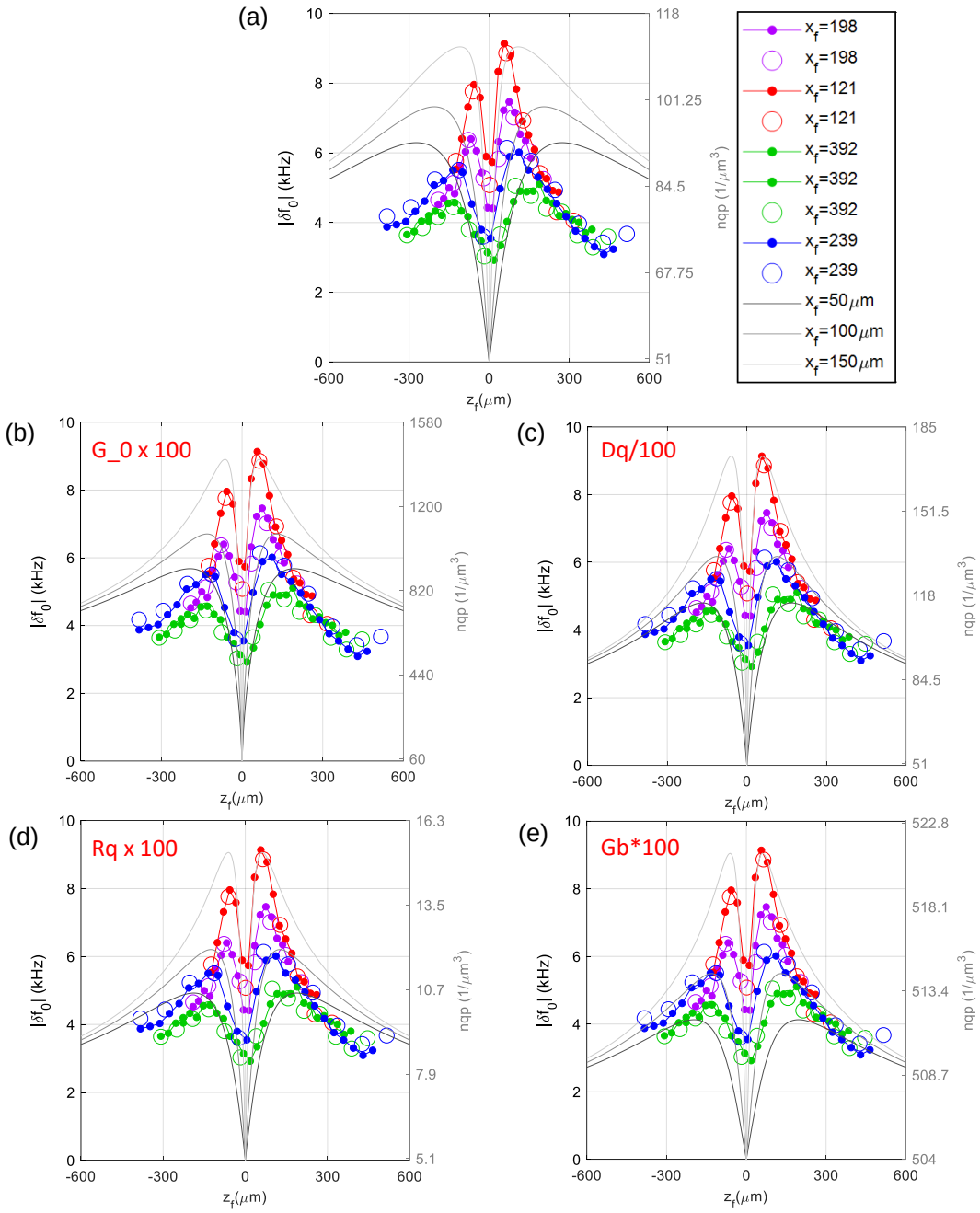

Fig. 7.20 - Comparison of data (color) and simulation (gray), changing one diffusion parameter at a time. (a) Same plot as Fig. 7.19 with simulation curves reflecting nominal diffusion parameters. (b) Increasing G_0 by two orders of magnitude does not improve the qualitative agreement between data and simulation very much, but it does increase δn_i closer to the values expected from the observed frequency shifts. (c) Decreasing D_q by two orders of magnitude appears to improve agreement. (d) Increasing R_q by two orders of magnitude improves qualitative agreement but reduces δn_i to of order 10, which is about 1000 times smaller than expected. (e) Increasing G_b by two orders of magnitude improves qualitative agreement but also decreases δn_i to values that are much smaller than expected.

the data and simulation, the resulting decrease in δn_i that is not consistent with the observed frequency shifts.

Finally, in Fig. 7.20(e), I show what happens when I increase the background generation rate G_b by a factor of 100. This again results in much better qualitative agreement between the data and the simulation. Notice also that the densities have all increased, which makes sense. However, the change in density between the minimum and maximum values of the simulation has actually decreased to $\delta n_i = 16\ \mu m^{-3}$, which would give far too small of a frequency change to be consistent with the data.

From the above discussion, we can get some important insights into the nature of the disagreement between the data and the simulation. First, we will need to make large adjustments in at least two parameters in the diffusion equation if we are going to get agreement. Second, by increasing G_0 substantially we can get better quantitative agreement between the data and the simulation. This seems to be the only parameter that can do this. Third, decreasing D_q or increasing R_q or G_b, all produce similar behavior, which is to sharpen the simulation, and give better qualitative agreement. This is because these three adjustments result in quasiparticles travelling less distance before they either scatter (D_q), recombine (R_q), or recombine with a high density of background quasiparticles (G_b). Essentially, these parameters affect the ability of the quasiparticles to leave the region where they are first generated. In contrast, if the quasiparticles can diffuse over the entire resonator, the response would be insensitive to the position of the fiber and the features would be very smeared out. A high trapping rate would cause a similar effect.

Based on these insights from Fig. 7.20, I tried changing some of the parameters in the diffusion equation (see Table 7.5) to see if I could get better agreement with the data.

Since G_b is the least well-known parameter, I allowed it to increase by a factor of 100, which we know will give better qualitative agreement, although it results in a less plausible δn_i. I also increased G_0 by a factor of 10 to increase δn_i. A factor of 100 increase would have given better quantitative agreement, although it seems unlikely that our estimates of light leakage from the fiber were off by more than a factor of 10. I also tried decreasing the diffusion constant D_q by a factor of 2 to improve the agreement. Finally, I left R_q unchanged because increasing it would decrease n_i to implausible values and decreasing it would reduce the qualitative agreement.

Figure 7.21 shows the new comparison plot, with the simulation curves found using the parameters listed in Table 7.5. The y-axis on the right side has been stretched so that the maximum value is 730 μm^{-3}, which gave good qualitative agreement with the data in the $z_f > 0$ region. This is the region where the scattering through the substrate was not important. Again, this is just one of many possible solutions. However, for this particular solution to the model, I can compare the x_f values for each sweep in the model, to the

Table 7.5 – Roughly optimized parameters used in Eq. (7.15) to produce plot in Fig. 7.21.

Parameter	**Factor Applied to Nominal Parameter**	**Description**	**Value**
G_b	x 100	Rate of background quasiparticle density generation	5.25×10^{18} $(m^2 \cdot s)^{-1}$
G_0	x 10	Optical quasiparticle generation rate factor for input fiber optical source power of 200 µW	7.8×10^{14} $(m \cdot s)^{-1}$
D_q	x 0.5	Quasiparticle diffusion coefficient [7.9]	1.93×10^{-3} m^2/s
R_q	x 1	Recombination factor [7.6]	1.19×10^{10} m^2/s

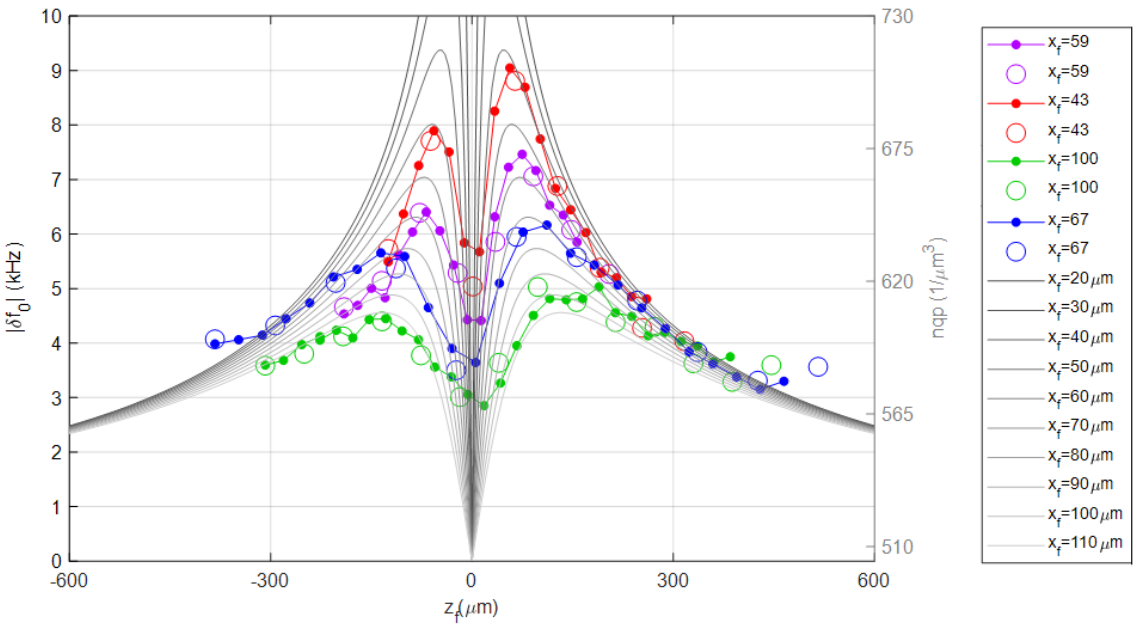

Fig. 7.21 - Comparison of measured $\delta f_0/f_0$ to simulated quasiparticle density n_{qi} in the inductor using roughly optimized parameters given in Table 7.5. Setting the maximum value on the right-hand-side y scale to 730 μm^{-3} and minimum to about 510 μm^{-3} gives good data-simulation agreement.

measured $|\delta f_0|$ z sweeps. The red sweep seems closest to the x_f = 40 µm simulation curve, the purple sweep corresponds to x_f = 55 µm, the blue matches x_f = 75 µm, and the green matches the x_f = 100 µm simulation curve. As expected, my original estimates x_f values (listed in the legend of Fig. 7.20) are not consistent with the simulation. These values have cumulative positioning errors and are based on the nominal x attocube step size given in Table 7.1. Fig. 7.21 shows the result of decreasing the x step size by a factor of 4.8 and setting the starting position of the fiber to x_{f0} = 117 µm to account for cumulative errors. The legend in Fig. 7.21 reflects these scaled x_f values. With these adjustments the red sweep would be at x_f = 43 µm, the purple sweep at x_f = 59 µm, the blue sweep at x_f = 67 µm, and the green sweep at x_f = 100 µm, and this brings the data close to the model curves.

Despite the good qualitative agreement, there is still a factor of 10 quantitative disagreement between the measured frequency shifts and the frequency shifts implied by the simulation - a density change of 140 μm^{-3} would correspond to only about a 0.5 kHz frequency shift. Of course this is just one of many possible solutions and further increases in G_0 would yield better quantitative agreement. Also, the rescaling in x by almost a factor of 5 was larger than expected. Improving the accuracy of the position sensing would be an essential next step in pinning down the nature of the discrepancy.

7.10 Conclusion

In this chapter, I discussed measurements of the response of a thin-film superconducting aluminum LC resonator to illumination by 780 nm light, at temperatures down to 100 mK. First, I discussed some of the positioning issues. Having closed-loop attocubes which record their position accurately would have helped to fix this problem. I next discussed the resonator response as a function of the fiber position with no applied optical power. The dielectric fiber perturbs the electric field of the resonator by as much as 2 MHz when the fiber was over the interdigitated capacitor and by as much as 80 kHz when the fiber was close to the inductor. This can be used to determine the relative position of the fiber with respect to the resonator. Next, I showed the change in resonance frequency of the cavity as a function of the fiber position. This measurement was also taken when the fiber was not carrying any optical power. In this case, the tuning effect appeared to be due to the fiber dielectric perturbing the electric field of the cavity, rather than indirect tuning of the cavity as the fiber tuned the resonator. The cavity was tuned by a maximum of about 50 kHz when the fiber was moved near the chip, which was harder to detect than the

perturbation of the chip resonator given the much lower *Q* of the cavity.

I then presented some data that showed the resonator response while it was illuminated by a stationary optical source. This was followed by my main results, which were measured shifts in resonance frequency and *Q* as a function of the fiber position when optical power was going through the fiber. The changes in the resonator's parameters were much larger than when the fiber did not have optical power running through it, as expected.

I next compared my measurements of the optical response to results from detailed simulations of the response. I discussed the unknown parameters in the simulation and the challenges in comparing the measured optical response to the expected response. It is important to be able to accurately model the response of the resonator because an understanding of this response is essential for constructing a working hybrid atom-to-superconducting-qubit system. Clearly, it would have been better to have all of the unknown parameters accurately determined in separate experiments. Also, for a good comparison between the data and model, it will be critical to determine the position of the fiber accurately and know the actual amount of scattered light from the fiber.

One way to reduce the uncertainties in the data is by significantly reducing uncertainty in position by using better calibrated position sensors, preferably without long-term drift or with closed loop control on the attocubes. The simulations could also be improved by including the trapping term in the diffusion equation, as in Eq. (2.52). Even better would be to determine the trapping rate and recombination rate through pulsed optical experiments. Furthermore, the model could be made more detailed by adding the optical power absorbed by the 420-nm-thick edge of the Al film, including scattering from the edge of the chip, and accounting for tilt of the fiber. Accurate measurements of the

diffusion parameter, the temperature of the quasiparticles, the reflectivity of the aluminum, the mean free path, and the Δ of the aluminum film would go a long way to reducing some of the unknowns.

A final open question is the disagreement between the δn_{qp} predicted in Sec 7.8 and δn_i simulated with the diffusion equation. As I discussed, there are several possibilities. Perhaps the fiber was scattering much more light than we expect based on Rayleigh scattering from the core. Another possibility is that quasiparticles are being preferentially trapped in a low-gap region in the inductor, which would also give a larger than anticipated quasiparticle density in the inductor for a given illumination. Further experiments would be needed to sort out whether the possible explanation, or whether something else is going on. It should be emphasized that if the cause can be identified and removed, this would decrease the response of the resonator to light, which would improve the performance in a hybrid system.

Despite the challenges, overall my results demonstrate the feasibility of positioning an optical fiber in close proximity to a thin-film superconducting resonator at 15 mK, even while the fiber is carrying enough optical power to trap atoms as proposed for use in a hybrid quantum system.

Chapter 8: Conclusions

8.1 Summary of Main Results

In this thesis I described my research into the development of a hybrid quantum system. In Chapter 1, I began by describing the challenges of building a hybrid qubit that was based on coupling neutral atoms to a superconducting qubit at millikelvin temperatures. I then introduced the proof-of-principle system that I built and measured, which consisted of a superconducting resonator coupled to a moveable tapered optical microfiber.

In Chapter 2, I briefly described relevant theory for the electrical behavior of superconducting resonators, including resonance frequency f_0, quality factor Q, and transmission S_{21}. I also described the effects produced by TLSs coupled to the resonator and loss due to quasiparticles, which are typically the two main sources of loss in my resonators.

In Chapter 3, I outlined the design, fabrication, and characterization of our LC microwave resonators and 3D cavity. Resonator LC1 was wire-bonded to a PCB and used in the resonator-tuning experiment described in Chapter 4 and the two-level system experiment described in Chaper 5. The 3D cavity that housed resonators LC2 and LC3 had a resonance frequency that was more than a GHz higher than the LC resonators' to reduce loss from the Purcell effect. Resonators LC2 and LC3 were both used in different versions of the microfiber-chip experiment.

In Chapter 4, I first introduced the physics behind tuning a superconducting thin-film resonator at 12 mK and then presented the experimental setup and the data Dr. Kim

and I collected on the tuning of resonator LC1. We were able to tune the resonance frequency of resonator LC1 through the ^{87}Rb hyperfine-splitting with a precision of a few kHz. We also demonstrated an overall tuning range of 137 MHz with an increase in Q by a factor of 4, for high RF powers, when the wings of the tuning pin made contact with the chip. This was important for the hybrid system because it meant the resonator could be tuned to within the linewidth of the ^{87}Rb hyperfine-splitting. Resonators with designs similar to LC2 and LC3, which had a single straight line inductor instead of the meandering inductor in LC1, would be easier to tune and to couple to atoms because the straight line layout of the inductor allows us to tune with the pin further away. With the pin further away, the resonator was also less sensitive to TLSs on the pin.

In Chapter 5, I discussed our method for detecting dipole-coupled two-level systems in a thin-film superconducting microwave resonator (Resonator LC1). I presented our experimental setup and discussed our observations of fluctuations in the transmission spectrum. I then argued that the fluctuations appeared to be due to thermally activated capacitive TLSs (cTLSs), rather than standard dipole-coupled TLSs.

In Chapter 6, I described the design and integration of a tapered optical microfiber with a superconducting resonator, the first step toward realizing our proposed hybrid quantum system. I discussed the design constraints, the design and fabrication of the tapered optical microfiber, and the assembly used to align the LC resonator and microfiber. I also described several other components, including the low-temperature translation stages (attocubes), the position sensors, and the laser and other optical components used to send light through the microfiber. Finally, I described the assembly and alignment of all these components.

In Chapter 7, I presented data from the setup described in Chapter 6. I began by describing our method for determining the relative position of the fiber with respect to the chip. I then discussed the response of the LC resonator and 3D cavity to the position of the optical fiber when there was no applied optical power, and compared this with the expected qualitative response due to the fiber dielectric perturbing the electric field near the resonator. I then presented data on the LC resonator's response (change in resonance frequency and change in $1/Q$) when optical power was applied to the fiber and the change in the resonator's optical response with the position of the fiber. I finished by comparing the data with simulations that accounted for the geometry of the LC resonator and the behavior of quasiparticles generated in the resonator by the incident light. Qualitative agreement was obtained, but only after adjusting key parameters in the model.

8.2 Suggestions for Future Work

The main question left from Chapter 5 is whether the fluctuations in resonance frequency were really due to cTLSs or some other mechanism, such as coupled two-level systems [8.2]. Further measurements and analysis of both models will be needed to resolve this question. Specifically, time resolved measurements of S_{21} on resonance while two-level fluctuators are active would allow us to gather better statistics on the excited state population of a given TLF. Examining the behavior of the fluctuators with temperature and static applied voltage would also be interesting. These data could tell us about the temperature of the TLS and whether the capacitance fluctuator model or the two-coupled TLS model describes it better.

The microfiber-chip experiment can be improved and expanded upon in several

ways. First, the position sensors described in Chapter 6 and 7 only had a precision of about 10 μm and this limited the resolution of our maps of the resonator response as a function of fiber position. Improving the precision, accuracy and repeatability of the position sensors would greatly improve the microfiber-chip experiment. The easiest way to do this is would be to use closed-loop attocubes [8.1] that can monitor the motion with sub-μm resolution.

The design of the microfiber-chip experiment could also be improved to allow for easier and faster assembly. Specifically, one could try to reduce the probability that the fiber breaks when tensioning the fiber and gluing a tensioned fiber to the fiber holder fork. Finding a more controlled way to measure the fiber-holder-fork compression would help. A design which allows transfer of the fiber to the fiber plate, without relying on steady hands, would also be helpful. It would also be beneficial to design a better way to attach the position sensors more quickly and precisely, and without risking breaking the fiber. Finally, the legs that attach the fiber plate to the fridge, originally designed with a lot of wiggle room, could be redesigned with tighter tolerances, and thus speed up the assembly process.

Of course the main item left for future work is the actual demonstration of an atom-superconductor hybrid system. There are several major steps left. Getting atoms trapped on a nanofiber in the dilution refrigerator is clearly one of the most difficult steps. One must find a way to operate a MOT in a cryogenic environment without causing too many problems (radiation, heat leaks, and magnetic fields) for the milliKelvin superconducting parts of the experiment. The MOT, which typically takes up several cubic square feet of space on a room temperature optics table, must be redesigned to fit inside a dilution

refrigerator. Alternatively, it could be placed in a cryogenic chamber immediately adjacent to the dilution refrigerator at the height of the fiber plate. In either case, cold atoms must be transferred from the MOT to the fiber, and then moved down the fiber to the resonator. The time that atoms can remain trapped on the fiber is another issue, as this is not very long at present.

Another interesting question is the actual temperature of the fiber in the cryogenic section of the experiment and how this depends on the optical power. Given the very low thermal conductance of the fiber (glass), it is likely that the fiber is well above 1 K even for relatively low applied optical power. We also saw some scans where the fiber may have been touching the resonator and this caused a large change in the response. This is likely a side issue for a hybrid qubit experiment, but if the temperature is too high, we may encounter additional loss or dephasing due to black-body radiation.

Short of putting atoms onto the fiber, the superconducting qubit side of the experiment also needs further development. A large next step would be to couple a long-lived transmon to the capacitor of my thin-film resonator, while the optical fiber is coupled to the inductive section of the resonator. The transmon will also be sensitive to quasiparticles, heating and induced loss in the resonator, and likely to the position of the fiber. One would need to find a design that minimizes these effects while maximizing the effective coupling between the fiber and the transmon. The qubit may also need to be tunable, but the magnetic screening approach I described in Ch. 4 to tune the resonator is not applicable to transmons because they do not store significant energy in a magnetic field. In principle a similar approach could be used to perturb the electric field and achieve tuning by changing the effective capacitance of the transmon. However, one would have to make

sure that the means to tune the qubit would not negatively affect the transmon or atoms.

To maintain a high Q in the resonator, it would help to find a geometric design or choice of materials that reduces the number of quasiparticles in the inductor, where the current is highest. The addition of quasiparticle traps would help. Another possibility would be to make the inductor out of a pure superconductor with a higher gap than the rest of the device. Quasiparticles would tend to accumulate in the low-gap parts of the device, rather than in the high-gap inductor, which would reduce the loss.

Finally, for the experiments I described in Chapter 7, improved position data and better knowledge of the actual level of radiated optical power comparison with the simulations and more accurate extraction of parameters, including the quasiparticle generation rate, the background density of non-equilibrium quasiparticles, the recombination rate and the diffusion constant. These parameters are essential for understanding the limitations of the setup, improving the design, and evaluating possible modifications such as adding quasiparticle traps or altering the materials.

Appendix A: MATLAB Code

The code below was used to fit S_{21} data of microwaves sent through a 3D cavity to a Lorentzian. It expects a file where the first 3 columns of data are the frequency (Hz), the S_{21} magnitude, and the phase of S_{21}.

```
function result = ComplexNotch_rpb_readarray_CONSEC2Im(file)

tic;
% RPB 021313
%
% A modification of Moe Khalil's ComplexNotch.m file that
% he uses to fit Qe and Qi to lumped element resonator
% peaks.
%
% 3d Cavities have transmission peaks instead of absorption
% peaks. Here I followed Sergey Novikov's 3d cavity fit
% Mathematica notebook (ReIm simultaneous fitting v1.1.nb)
%
%
% The input file format is changed as well, to be a
% tab-delimited file with frequency, S_21, and phase
% columns instead.
%
% reads out of a (corrected) data array instead of a
% tab-delimited file. This is to be used in conjunction
% with semiAutoCavityFit.m script.
%
% Fit bounds and tolerances are not fixed, and one can play
% around with them to find the best looking fit.
%
% Typical fit bounds: rangecoefficient=3-4
% Typical tolerances:
% Fast iterations: Tolx & TolFun 1e-20,
%                  MaxIter & MaxFunEvals 30000
% Slower iterations": Tolx & TolFun 1e-30,
%                     MaxIter & MaxFunEvals 100000
```

```
%%%%%
% Read data

data=dlmread(file,'\t',0,0);
d1 = size(data);

start=data(1,1);
inc=data(2,1)-data(1,1);

freq= data(:,1)/1e9; % Keep frequencies in GHz
Pow=data(:,2);
Phase= data(:,3)*pi/180; % In radians!

PowSmear = smear(Pow, 23);  %change this to account for
                    %traces with smaller number
                    %of pts. e.g. data with
                    %only 20 pts would not be
                    %fit

Powlin=10.^(Pow./10);
VRe=(10.^(Pow./20)).*cos(Phase);
VIm=(10.^(Pow./20)).*sin(Phase);

%#########################################################
%Lorentzian fit

temp=[freq, Pow];
S21lin=[freq, Powlin];


d1 = size(S21lin);

S21linGuess = S21lin;
%S21linGuess is a smoothed our version of the data and will
% be used to estimate the resosnace and quality factors.
% 03/03/09 by Moe
S21linGuess(:,2) = smear(S21lin(:,2), 5);
S21linpk=S21linGuess;

%#######################################
%Guessing good start values

S21linpk(:,2)=S21linGuess(:,2);   %redundant. fix this.

%frindex is the index for the maximum S21 in S21linpk
```

```
[maxAmpl,frindex]=max(S21linpk(:,2));
fr0=S21linpk(frindex,1); %find the frequency that gives
                    %maximum amplitude

tempS21linpk = S21linpk(:,2);

%find at which frequency the half maximum occur

halfmaxcandidate = [];
halfmaxcandidateindex=[];
l=1;
factor = 1e-20; % oldfactor=.0001
while size(halfmaxcandidateindex) == 0
   maxAmpl;     %unecessary
   tempdepth = maxAmpl - (tempS21linpk(1)+ ...
      tempS21linpk(2)+tempS21linpk(3)+tempS21linpk(4) ...
      +tempS21linpk(5)+tempS21linpk(6)+ ...
      tempS21linpk(7)+tempS21linpk(8)+tempS21linpk(9) ...
      +tempS21linpk(10))/10;   %rough estimate of bkgnd
   % tempdepth is the power difference between the
   % on-resonance frequency and the average of the lowest
   % ten frequencies.  03/03/09 by Moe
   depth = (tempdepth+maxAmpl)/2;      % rough guess for
                                % peak height minus
                                % bkgnd
  %depth is the average of tempdepth and maxAmpl.
  %03/03/09 by Moe

  % just to go through the frequency up to the peak
  % frequency
  for k=1:frindex
   % find data points that are different by 0.01 or less
   % to calculated half maximum from the peak among the
   % linearized raw data
     % if index is within close range of index of left
     % side of FWHM....
     if abs(depth./2 - tempS21linpk(k)) < factor
        halfmaxcandidate(l) = tempS21linpk(k);
        halfmaxcandidateindex(l) = k; % record the index
        l=l+1;
     end
  end
  %if didn't find any halfmaxcandidate, increase tolerance
  %and repeat while loop
  factor = factor*10;
end
```

```
if factor>.2  %this is incase factor got too big before
          %it found the halfmax, so it iterates slower.
          %03/03/09 by Moe
   halfmaxcandidate = [];
   halfmaxcandidateindex=[];
   l=1;
   factor = .01;
   while size(halfmaxcandidateindex) == 0
      tempdepth = maxAmpl - (tempS21linpk(1)+ ...
         tempS21linpk(2)+tempS21linpk(3)+ ...
         tempS21linpk(4)+tempS21linpk(5)+ ...
         tempS21linpk(6)+tempS21linpk(7)+ ...
         tempS21linpk(8)+tempS21linpk(9)+ ...
         tempS21linpk(10))/10;
       % tempdepth is the power difference between the
       % on-resonance frequency and the average of the
       % lowest ten frequencies.  03/03/09 by Moe
      depth = (tempdepth+maxAmpl)/2;
      %depth is the average of tempdepth and maxAmpl.
      %03/03/09 by Moe

      for k=1:frindex % just to go through the frequency
                  % up to the peak frequency
         %find data points that are different by 0.01
         %or less to calculated half maximum from the
         %peak among the linearized raw data
         if abs(depth./2 - tempS21linpk(k)) < factor
            halfmaxcandidate(l) = tempS21linpk(k);
            % record the index
            halfmaxcandidateindex(l) = k;
            l=l+1;
         end
      end
      factor = factor*2;
   end
end

% find minimum among the candidates for the half max data
% points
[halfmax,index] = min(abs(frindex - halfmaxcandidateindex));
% find the index for the half max point
HWindex = halfmaxcandidateindex(index);

dfr0 = 2*abs(S21linpk(HWindex,1) - fr0);   %dfr0 = FWHM
Q0=fr0/dfr0;      %ending with '0' means initial guess
```

```
Qe0 = Q0./(sqrt(maxAmpl));

QInv0=1/Q0;
QeInv0=1/Qe0;

phi0=Phase(HWindex);
%sqrt of power S21 to get offset in units of voltage S21
off0=sqrt(tempS21linpk(1));
offIm0=0;
% QeInvIm0=0;

%###################################
% Set up the range of fitting

datafitf = S21lin(:,1);
datafitP = S21lin(:,2);
rawdatafitP = temp(:,2);        %not smoothed

%rangecoeff = 2; used all data before 2009/1/27
%rangecoeff = 2
rangecoeff =4;
% The minimum frequency for fit is set at "rangecoeff"
% times half-max width lower from the resonance frequency.
% But the maximum calculated here is below the minimum
% measurement frequency, the minimum frequency for
% fitting is determined as measurement minimum frequency.
if fr0 - rangecoeff*dfr0 < S21lin(1,1)
   ffitmin = S21lin(1,1);
else
   ffitmin = fr0 - rangecoeff*dfr0;
end


% The maximum frequency for fit is set at "rangecoeff" times
% half-max width higher from the resonance frequency.  But the
% maximum calculated here exceeds the maximum measurement
% frequency, the maximum frequency for fitting is determined as
% measurement maximum frequency.
if fr0 + rangecoeff*dfr0 > S21lin(d1(1),1) %
   ffitmax = S21lin(d1(1),1);
else
   ffitmax = fr0 + rangecoeff*dfr0;
end


% Adjust the range of the data for fit to within the frequency
```

```
% range determined above.

%#############
%fr0 = 4*fr0*Q0^2*Qe0*sin(phi0)/(Q0^2-2*Q0*Qe0*cos(phi0)+Q0
%     *sqrt(Q0^2+4*Qe0^2-4*Q0*Qe0*cos(phi0))+4*Q0^2*Qe0
%     *sin(phi0))
%#############

datafitf = ...
   datafitf( ffitmin < S21lin(:,1) & S21lin(:,1) < ffitmax);
datafitP = ...
   datafitP( ffitmin < S21lin(:,1) & S21lin(:,1) < ffitmax);
rawdatafitP = ...
   rawdatafitP( ffitmin < S21lin(:,1) & S21lin(:,1) < ffitmax);
datafitVRe = ...
   VRe( ffitmin < S21lin(:,1) & S21lin(:,1) < ffitmax);
datafitVIm = ...
   VIm( ffitmin < S21lin(:,1) & S21lin(:,1) < ffitmax);
format long;
datafitVComplex = datafitVRe + i * datafitVIm;

%##############################
% 02/21/13 RPB: Changed the fitting routines to fit 3d cavity
% resonance peaks.
% fit the real and imaginary part separately.
%##############################

% ADJUST THESE PARAMETERS TO CONTROL TOLERANCE OF FIT AND
RUNTIME
options= optimset('Tolx',1e-20,'TolFun',1e-20,'MaxIter',300000,'MaxFunEvals',3000);

% THIS IS THE EQUATION THE DATA IS FIT TO
% (The RE and Im are treated as 2 equations)
ftype=inline('[real((fp(2)/fp(1)).*exp(i*fp(4))./(1+(2*i*(x-
fp(3))./(x.*fp(1))))+fp(5)+i*fp(6))-re,  imag((fp(2)/fp(1)).*exp(i*fp(4))./(1+(2*i*(x-
fp(3))./(x.*fp(1))))+fp(5)+i*fp(6))-im]',  'fp','x','re','im');

% % [real( (fp(2)/fp(1)) .* exp(i*fp(4)) ...
% %                  ./ ...
% %       (1+ (2*i*(x-fp(3)) ./ (x.*fp(1)) )) ...
% %       +fp(5) + i*fp(6)                    ) -re,...

% % [real( Q/Qe .* exp(i*phi) ...
% %           ./ ...
% %       (1+ (2*i*(x-fr)*Q ./ x )) ...
% %       +off + i*offIm                    ) -re,...
```

```
f0=[QInv0 QeInv0 fr0 phi0 off0 offIm0];
% [f1,f1norm,f1resid,f1exit,f1output,f1lambda,f1Jacobi] =
%     lsqnonlin(ftype,f0,[],[],options,datafitf,datafitVRe,
%     datafitVIm,datafitP);
% lsqnonlin is matlab func. It optimize fit to both Re and Im at
% the same time:
[f1,f1norm,f1resid,f1exit,f1output,f1lambda,f1Jacobi]=lsqnonlin(ftype,f0,[],[],options,dat
afitf,datafitVRe,datafitVIm);

QInv0=f1(1);
QeInv0=f1(2);
fr0 = f1(3);
phi0 = f1(4);
off0 =f1(5);
offIm0= f1(6);

%##############################
% output
%f1 = [Q ReffoverRt fr off phi]
coeff=f1;
% if isempty(f1resid) == 0;
% if lsqnonlin outputs f1resid, it is possible to calculate
% error:
   error=nlparci(f1,f1resid,'jacobian',f1Jacobi,'alpha',.317);
% else
%     error = zeros(6,2)
% end

%makes vector to plot resulting plot shape
compfitfunc=notchT3_2Im(coeff, datafitf);

QInv=coeff(1);
dQInvp=error(1,2)-QInv;      %plus error (upper bound)
dQInvm=QInv-error(1,1);      %minus error (lower bound of
                        %unceratinty)
dQInv=(dQInvp+dQInvm)/2; % estimate the error as symmetric

QeInv=coeff(2);
dQeInvp=error(2,2)-QeInv;
dQeInvm=QeInv-error(2,1);
dQeInv=(dQeInvp+dQeInvm)/2;

fres = coeff(3);
dfresp=error(3,2)-fres;
dfresm=fres-error(3,1);
```

```
dfres=(dfresp+dfresm)/2;

phi = coeff(4);
dphip=error(4,2)-phi;
dphim=phi-error(4,1);
dphi=(dphip+dphim)/2;

offsetRe = coeff(5);
doffsetRep=error(5,2)-offsetRe;
doffsetRem=offsetRe-error(5,1);
doffsetRe=(doffsetRep+doffsetRem)/2;

offsetIm = coeff(6);
doffsetImp=error(6,2)-offsetIm;
doffsetImm=offsetIm-error(6,1);
doffsetIm=(doffsetImp+doffsetImm)/2;

losstan=QInv-QeInv; %internal Q
Qi=1/losstan;
dlosstan=sqrt(dQInv.^2+dQeInv.^2);
dQi=dlosstan/losstan^2;

%fractional errors:
e1=dQInv/QInv;
e2=dQeInv/QeInv;
e3=dfres/fres;
e4=dphi/phi;
e5=doffsetRe/offsetRe;
e6=doffsetIm/offsetIm;
e7=dQi/Qi;

Q = 1/QInv;
Qe = 1/QeInv;
dQ = dQInv/QInv^2;
dQe = dQeInv/QeInv^2;

% Saving results in structure

result.f = temp(:,1);
result.raw = temp(:,2);
result.rawPow = S21lin(:,2);
result.rawVRe = VRe;
result.rawVIm = VIm;

result.fitf = datafitf;
result.fitdataP = rawdatafitP;
```

```
result.fitdataPlin = datafitP;
result.fitdataVRe = datafitVRe;
result.fitdataVIm = datafitVIm;

result.fitfunclin = compfitfunc.Pow;
result.fitfuncVRe = compfitfunc.VRe;
result.fitfuncVIm = compfitfunc.VIm;
% result.goodnessoffit = gof;

result.QInv = QInv;
result.dQInv = dQInv;
result.Q = Q;
result.dQ = dQ;
result.QeInv = QeInv;
result.dQeInv = dQeInv;
result.Qe = Qe;
result.dQe = dQe;

result.Qi = Qi;
result.dQi = dQi;
result.losstan = losstan;
result.dlosstan = dlosstan;
result.fres = fres;
result.dfres = dfres;
result.offsetRe = offsetRe;
result.doffsetRe = doffsetRe;
result.offsetIm = offsetIm;
result.doffsetIm = doffsetIm;
result.phi = phi;
result.dphi = dphi;
result.peakpower = maxAmpl;

%############################

% Plot power
% figure(201);
figure;
plot(result.fitf, result.fitfunclin,'r', 'LineWidth',1.5);
hold on;
plot(result.f, result.rawPow,'b', 'LineWidth',1.2);
set(gcf,'Color',[1,1,1]);
set(gca,'FontSize',14,'FontName','Arial','LineWidth',2,'TickLength',[.02 .02]);
box on
xlabel('\fontname{Arial}{\fontsize{14}{\rm{f}} {\rm{(GHz)}}}');
ylabel('\fontname{Arial}{\fontsize{14}{\rm{|S_{21}|}}}');
```

```
% Plot real part
figure(202);
plot(result.f, result.rawVRe,'b', result.fitf, result.fitfuncVRe,'r');
set(gcf,'Color',[1,1,1]);
set(gca,'FontSize',20,'FontName','Times New Roman','LineWidth',2,'TickLength',[.02
.02]);
box on
xlabel('\fontname{Times New Roman}{\fontsize{25}{\rm{f}} {\rm{(GHz)}}}');
ylabel('\fontname{Times New Roman}{\fontsize{25}{\rm{Re(S_{21})}}}');

% Plot imaginary part
figure(203);
plot(result.f, result.rawVIm,'b', result.fitf, result.fitfuncVIm,'r');
set(gcf,'Color',[1,1,1]);
set(gca,'FontSize',20,'FontName','Times New Roman','LineWidth',2,'TickLength',[.02
.02]);
box on
xlabel('\fontname{Times New Roman}{\fontsize{25}{\rm{f}} {\rm{(GHz)}}}');
ylabel('\fontname{Times New Roman}{\fontsize{25}{\rm{Im(S_{21})}}}');

% Plot real vs. imaginary part
figure(204);
%find index of the raw data point closest to peak
[Pkf,fresi] = min(abs(result.f - result.fres));
plot(result.rawVRe, result.rawVIm,'b', result.fitfuncVRe, result.fitfuncVIm,'r',
result.rawVRe(fresi), result.rawVIm(fresi), '.g');
set(gcf,'Color',[1,1,1]);
set(gca,'FontSize',12,'FontName','Times New Roman','LineWidth',2,'TickLength',[.02
.02]);
box on;
grid on;
axis equal;
xlabel('\fontname{Times New Roman}{\fontsize{12}{\rm{Re(S_{21})}}}');
ylabel('\fontname{Times New Roman}{\fontsize{12}{\rm{Im(S_{21})}}}');

   toc




function smeared = smear(clean, Nsmear, index1, index2)

% smeared = smear(in, Nsmear, index1, index2)
% This averages every 'Nsmear' points in 'clean'.  'clean' and
```

```
% 'smeared' are of the same length.  'Nsmear' should be odd.  If
% the last two optional arguments are passed in, then the smearing
% is performed between indices 'index1' and 'index2' -- the
% elements outside of these are untouched. created 8/13/04
% modified 1/12/06

if nargin == 4
  fullclean = clean;
  clean = clean(index1 : index2);
end

% Round to nearest odd number
Nsmear = (floor(Nsmear / 2) + 0.5) * 2;
Nsmear2 = (Nsmear - 1) / 2;

for i = 1 : Nsmear2
  smeared(i) = mean(clean(1 : i+Nsmear2));
end

for i = Nsmear2+1 : length(clean)-Nsmear2
  smeared(i) = mean(clean(i-Nsmear2 : i+Nsmear2));
end

for i = length(clean)-Nsmear2+1 : length(clean)
  smeared(i) = mean(clean(i-Nsmear2 : end));
end

if nargin == 4
  temp = smeared;
  smeared = fullclean;
  smeared(index1 : index2) = temp;
end
```

Appendix B: Supplementary Material for Ch. 5

Accounting for Background in S_{21} Lorentzian Fit

I define the background transmission K as the transmission S_{21} that would exist if there were no coupling to the LC resonator. I fit the following equation

$$K = Re(K_0) + i * Im(K_0) + r_0 * \ e^{-i\gamma*(f-f_o)} \tag{B.1}$$

to $S_{21}(f)$ over a frequency span that is many linewidths wider than the linewidth of the LC resonator, while excluding a region that is within several linewidths of the LC resonator. Equation (B.1) describes a circle in the complex plane with center at K_0 and radius r_0, where γ is the phase unwinding, and f_o is a reference frequency.

The black curve in Fig. B.1(a) and (b) shows a plot of the measured transmission $S_{21}(f)$ at 15 mK over a 30 MHz range. The red curve is the result from fitting Eq. (B.1) to this data set in the complex plane. For comparison, the gray curve shows the transmission within several linewidths of the resonance frequency (6.81571 GHz), i.e. the region omitted from the fit.

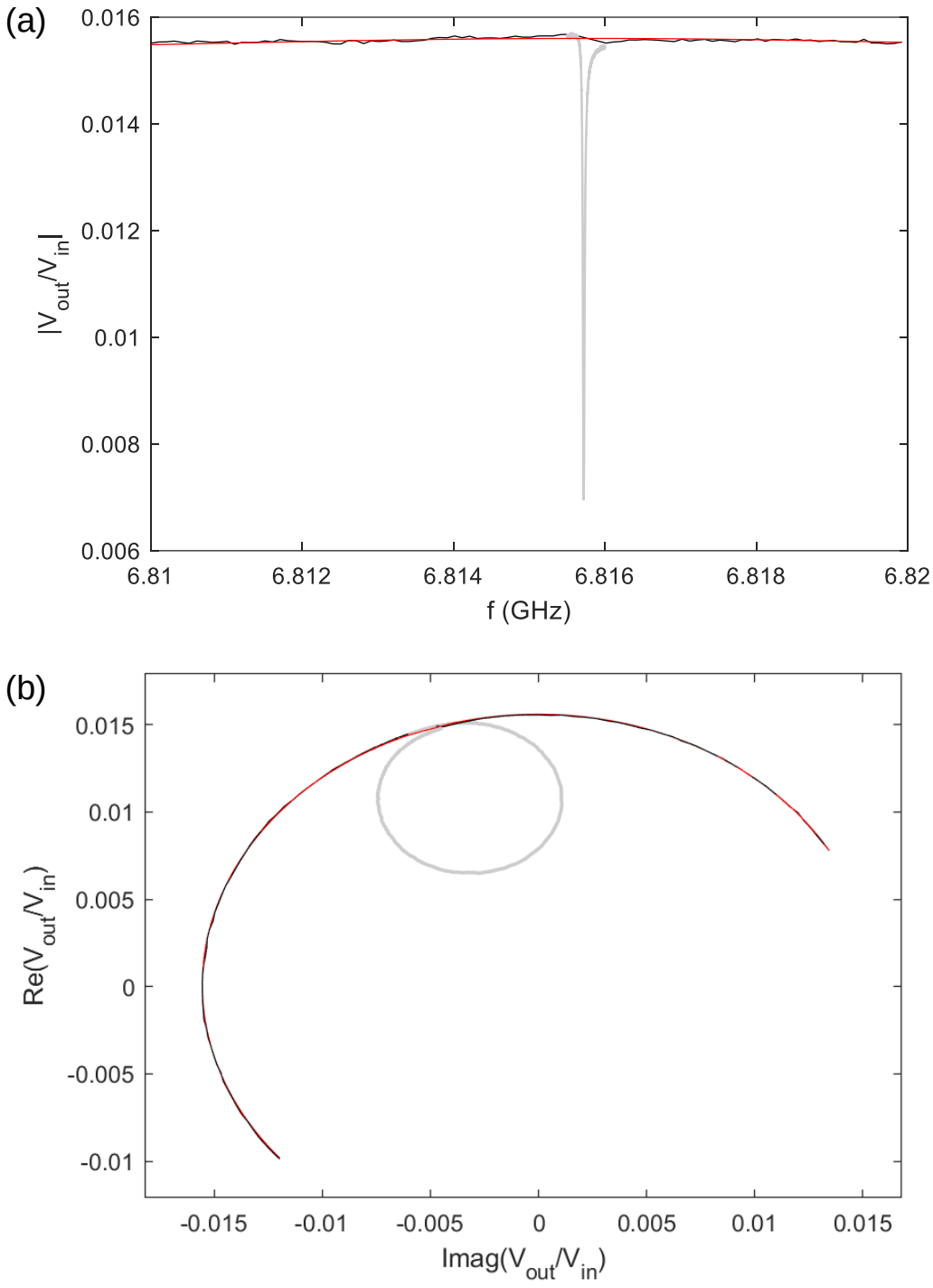

Fig. B.1. (a) The black curve shows a plot of the magnitude of the measured transmission $|V_{out}/V_{in}|$ vs frequency f over a 30 MHz span. The gray curve shows the magnitude of the measured transmission $|V_{out}/V_{in}|$ vs f near the resonance. The red curve shows the result from fitting background transmission Eq. (B.1) to the measured S_{21} in the complex plane (points on the gray curve were omitted). (b) The same three curves shown in the complex plane.

Lorentzian fit details

To calculate uncertainty in each data point of the real part of $S_{21} = V_{out}/V_{in}$ vs. f, I fit a line to the first 100 pts of the trace and took the standard deviation of the residuals. We assume this number is the uncertainty for each data point. I similarly determined the uncertainty for the imaginary part of $S_{21} = V_{out}/V_{in}$. For Figs. 5.5, 5.6, 5.7, and 5.10, we determined the uncertainty of each trace and plot it in Fig. B.2(a) and (b). The distribution of uncertainties is shown in Fig. B.2(c) and (d) with the standard deviation of the

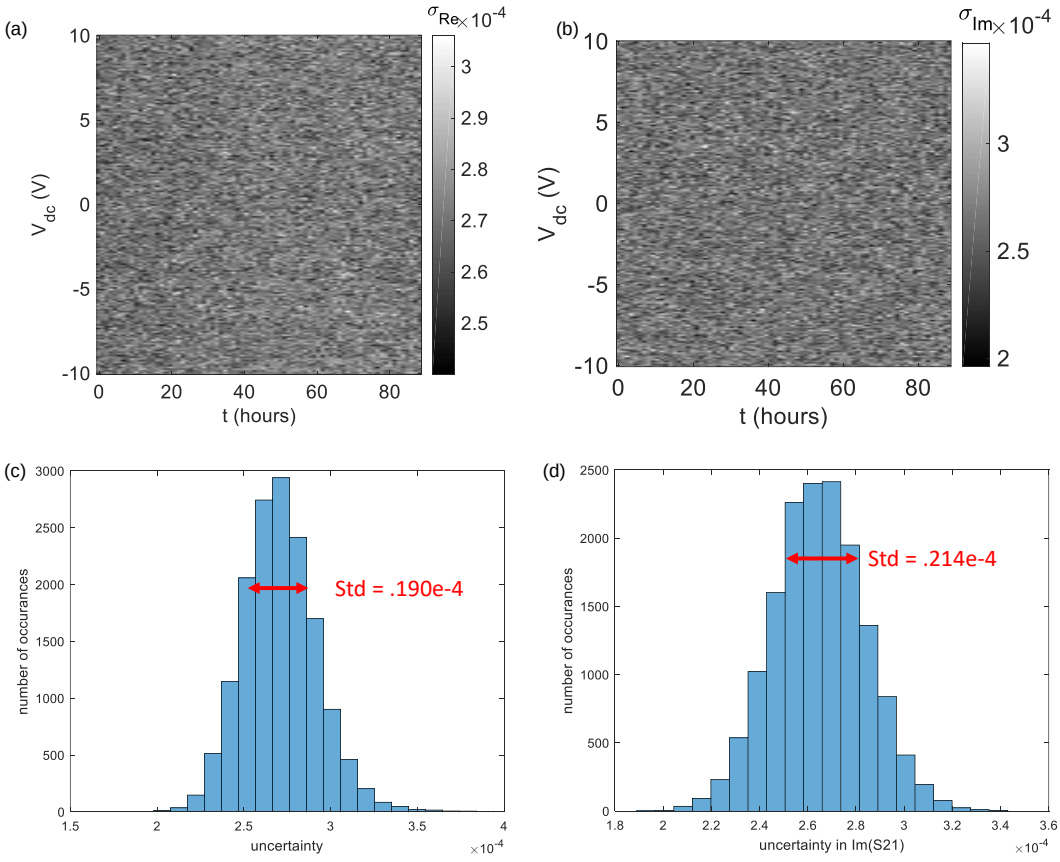

Fig. B.2 - (a) Each pixel in this plot represents the uncertainty σ_{re} in every data point of the real part of S_{21} vs. f. (b)Each pixel in this plot represents the uncertainty σ_{im} in every data point of the imaginary part of S_{21} vs. f. (c) Histogram of the data in (a) showing the spread of uncertainties. (d) Histogram of the data in (b) showing the spread of uncertainties.

uncertainties being indicated in red. To calculate χ^2, we use the mean of all uncertainties in Fig. B.2(a) as the uncertainty in the real part of S_{21}, $\sigma_{re} = 2.71 \times 10^{-4}$, for every point in every trace. Similarly, we use the mean of Fig. B.2(b) as the uncertainty in the imaginary part of S_{21}, $\sigma_{im} = 2.66 \times 10^{-4}$.For Figs. 5.5, 5.6, 5.7, and 5.10, we obtained the fitting parameters by fitting the data to Eq. 5.29. We used the reduced χ^2 method and simultaneously fit real and imaginary data by defining χ^2 as a sum of χ^2 of the real part of S_{21} added to χ^2 of the imaginary part of S_{21}.

$$\chi^2 = \sum_j \frac{\left(V_{\mathrm{Re},\,Data} - V_{\mathrm{Re},\,Fit}\right)^2}{\sigma_{\mathrm{Re}}^2} + \sum_j \frac{\left(V_{\mathrm{Im},\,Data} - V_{\mathrm{Im},\,Fit}\right)^2}{\sigma_{\mathrm{Im}}^2} \qquad \text{(B.2)}$$

Additional fitting parameters

Table B.1 shows the additional background fit parameters not shown in Table 5.1, S_o and θ, for the four curves shown in Fig. 5.8.

Table B.1. - Background fit parameters S_o and θ for the four $S_{21}(f)$ fit curves shown in Fig. 5.8.

	Red	Green	Blue	Magenta
S_o	0.984	0.971	0.969	0.964
θ	5.4°	6.5 °	7.6 °	8.8 °

Details About χ^2 of S_{21} Lorentzian Fit

Figure B.3 shows a histogram of the χ^2 values displayed in Fig. 5.7. The peak occurs at around 3600 which is significantly larger than the degrees of freedom (3196) indicating that most of the fits are not good. Switching events can cause the outliers with much higher χ^2 values.

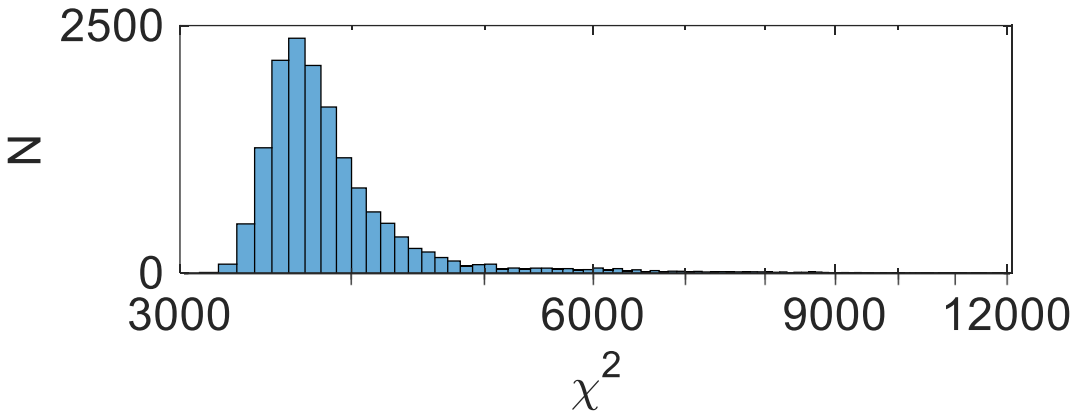

Fig. B.3. - Histogram of χ^2 values displayed in Fig. 5.7.

Additional Fitting Parameters vs V_{dc} and *t*

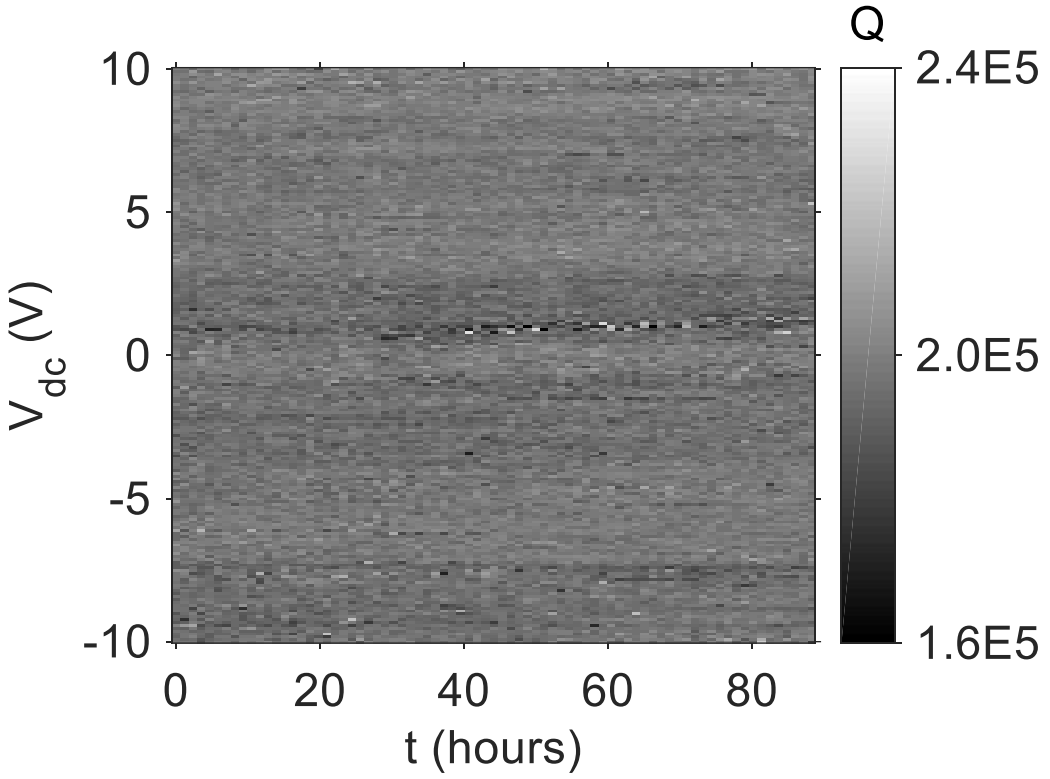

Fig. B.4 - Quality factor *Q* vs. V_{dc} and time *t*.

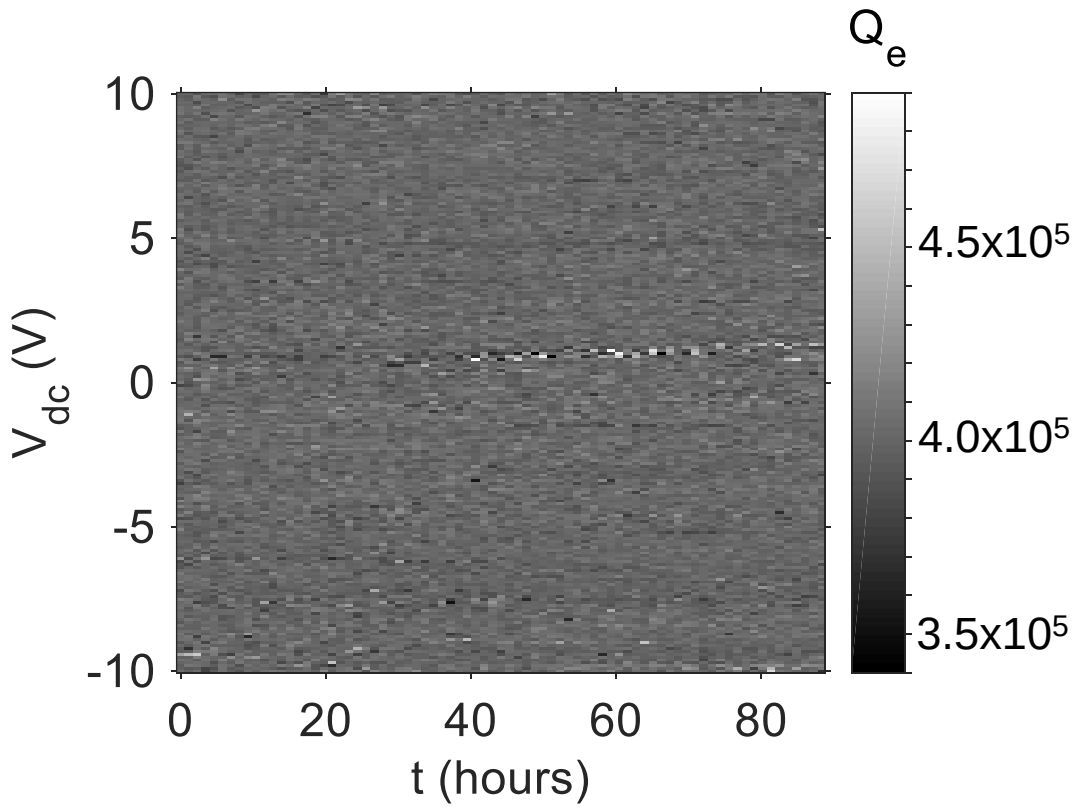

Fig. B.5 - External quality factor Q_e vs. V_{dc} and time t.

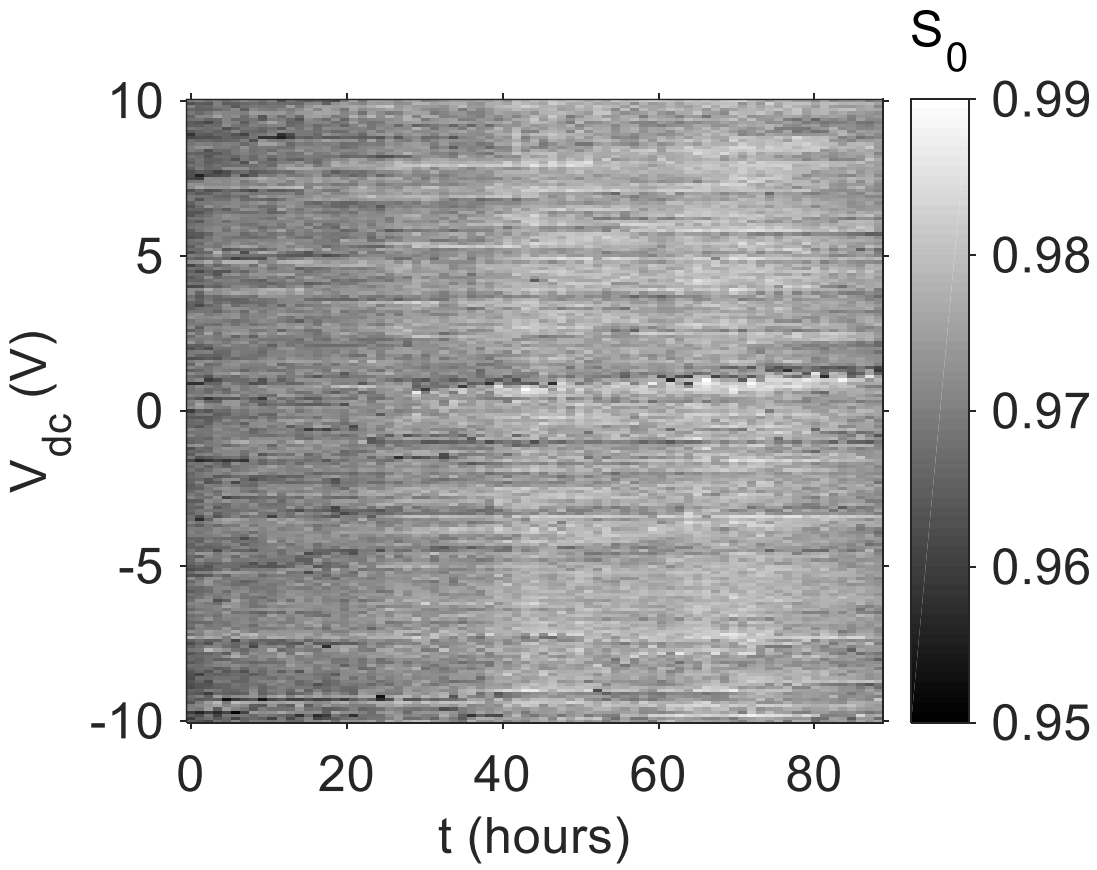

Fig. B.6- S_0 vs. V_{dc} and time t.

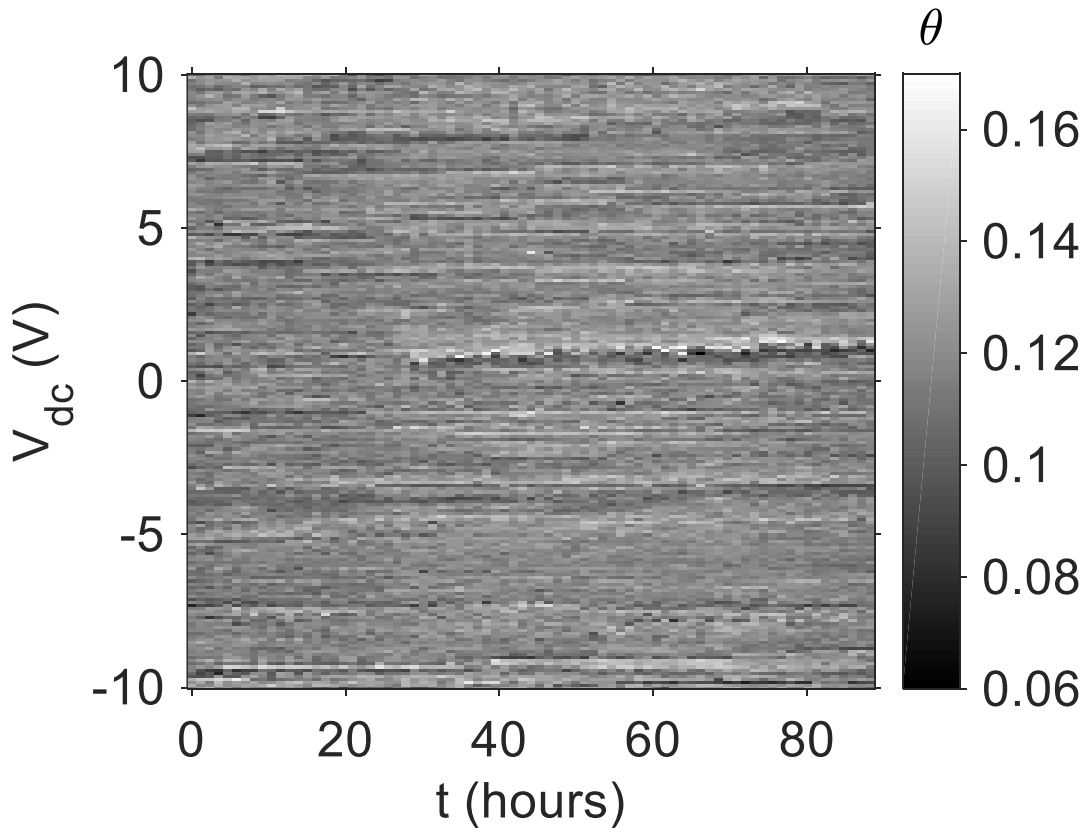

Fig. B.7- θ vs. V_{dc} and time *t*.

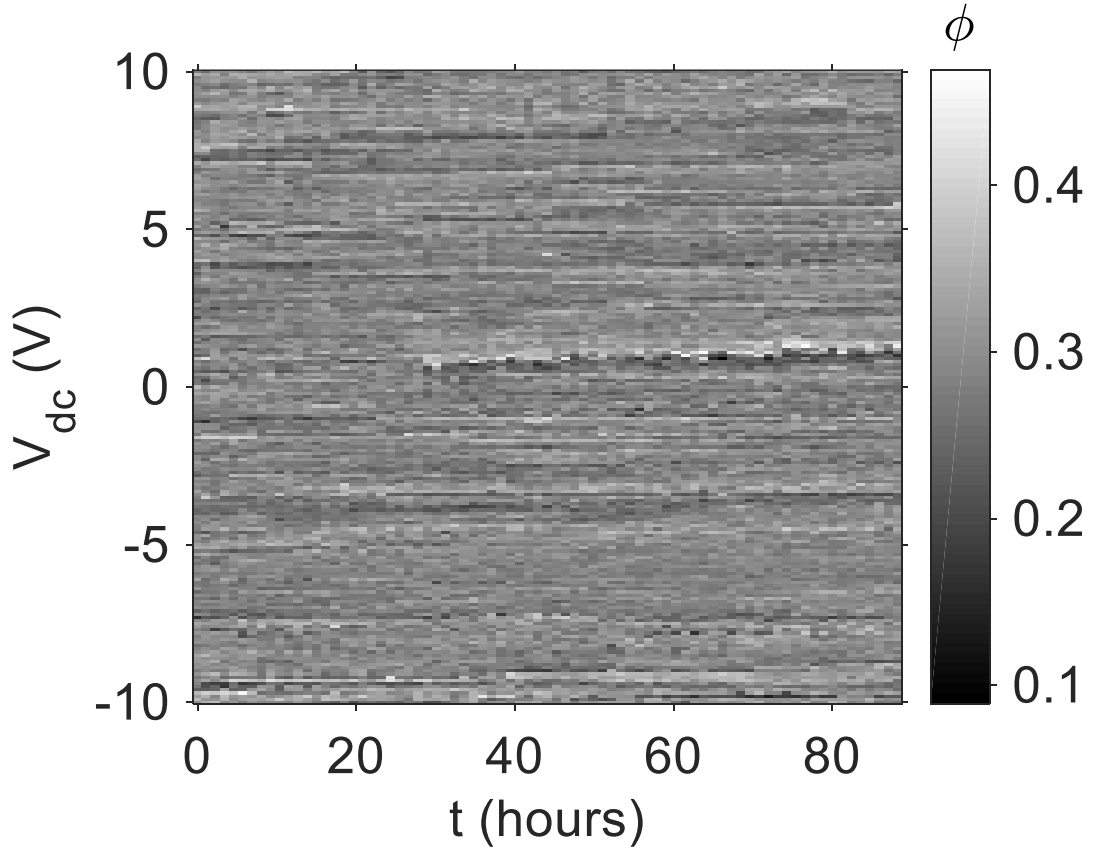

Fig. B.8 - ϕ vs. V_{dc} and time *t*.

Additional Evidence of cTLS

Figure B.10 shows the transmitted power through the resonator as a function of the input frequency with a 1.0 V dc bias applied at about t = 72 hours. The input frequency was swept over a period of about 1 second. During the course of the sweep, there is sudden switching between several different resonance curves. The sweep begins at the lower frequency in Fig. 5.10 in region

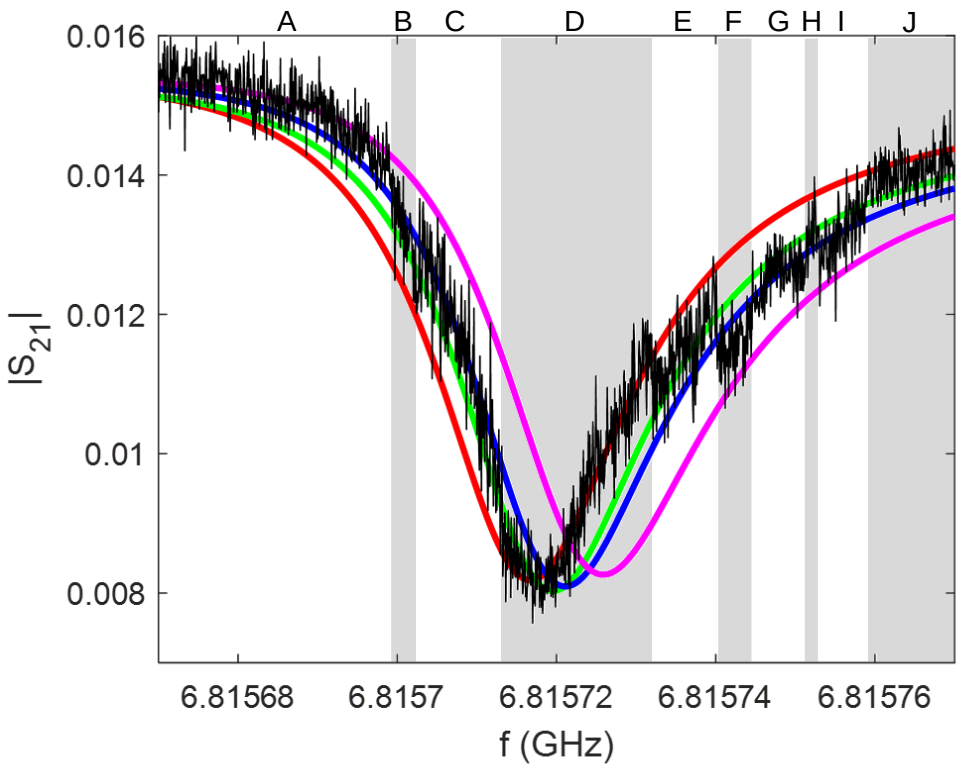

Fig. B.10 - Magnitude of S_{21} as a function of frequency f from run #62 with a dc voltage applied to the center of the transmission line Vdc = 1.0 V, taken around t = 72 hrs is shown in black. Also, a fit to data-runs #63, #18, #23, and #30 (taken at t = 73.1, 20.9, 26.7, and 34 hrs respectively) are shown in red, green, blue, and magenta, respectively. Throughout the 1.5 second scan of run #62, which sweeps the frequency from low frequency to high frequency, we see S_{21} appear to 'switch' between several resonance curves, denoted by the gray boxes, similar to the fits from data-runs #63, #18, #23, and #30. This supports evidence of two or more TLSs coupled to the resonator.

A where it appears that the resonator is in the 'magenta' state. Then switches into the 'blue' state in region B. In region C, it is less clear precisely which state the resonator is in. It looks like it could be either the 'blue' state or the 'green' state but the noise makes it difficult to resolve. Alternatively, there could be a rapid switching between these two states, in this region. In region D, the resonator seems to clearly in the 'red' state, whereas region E the state of the resonator seems less clear. It appears to be between the 'blue' and 'magenta' state. This could mean rapid switching between these two states or another state not shown here as there are many possible configurations of microscopic terrain and the

charged two-level systems therein. In region G, there is again ambiguity as to whether the resonator is in the ‘blue’ or ‘green’ state, or

Appendix C: Method for Estimating Relative Fiber-Chip Position

As I discussed in Sec. 6.5, the x and z attocubes did not move a consistent repeatable distance upon repeated application of identical voltage pulses. Also, the average length of an extend step typically did not equal the average length of a retract step. Furthermore, the ratio between the length of extend steps and retract steps seemed to drift over time. As I discussed in Chap. 6, I estimated the average step size by taking the step size measured at room-temperature (see Table 6.3) and assuming that it shrunk at 100 mK by a factor of $D = 4.6$ (see Table 6.4). A summary of the resulting nominal step sizes at 100 mK is shown in the first 2 lines of Table C.1. The calibration of step size is critical because the resonator response data was collected in "sweeps", in which one attocube was extended or retracted a certain number of steps, the system was given time to cool back down to 100 mK, the resonator response was measured, and the procedure repeated for each subsequent data point in the sweep. I assumed that the attocube step size did not change much within a given sweep. The data sweeps should be repeatable, but they were not if plotted using

Table C.1 - Nominal estimates for attocube step sizes for both version 2 and version 4 of the fiber-chip experiment and best estimates for version 4 of the fiber-chip experiment.

Version	Δx_{ext} (μm/step)	Δx_{rtr} (μm/step)	Δz_{ext} (μm/step)	Δz_{rtr} μm/step)
2 (nominal)	0.48	0.42	0.32	0.40
4 (nominal)	0.45	0.48	0.32	0.37
4 (best estimate)	0.45	0.37	0.32	0.315

the nominal step size. We concluded that the attocube step sizes ($\Delta_{x,ext}$, $\Delta_{x,rtr}$, $\Delta_{z,ext}$, $\Delta_{z,rtr}$) changed over time by a significant amount. This behavior was not surprising because the attocubes employ a stick-and-slip motion that relies on friction and is affected by loading.

To deal with the uncertainty in the relative fiber-chip position, we added x and z position sensors, as discussed in Sec. 6.6. In version 2 of the microfiber-chip experiment, we used air-core inductive sensors but they did not have sufficient sensitivity for accurate positioning. In version 4, I used spiral sensors on a PCB to get improved sensitivity. They had inconsistencies when used over long time periods due to cable drift, but yielded accurate results for data sets taken over sufficiently short time. While these later sensors showed promise, our data from version 2 lacked consistently accurate positioning. Nevertheless, I was able to put together a cohesive picture for version 2 by making manual corrections to the attocube step size using two different methods.

In both correction methods, I assumed that the *z* attocube moved independently of the *x* attocube and vice versa. However, it may be possible that their movements were somewhat coupled as the movable cavity was connected to the refrigerator by semi-flexible coax lines. These lines could pull slightly on the cavity. The degree to which this happens would likely change as the apparatus cooled down. With the version 2 sensors, it was difficult to know for each attocube whether the extend size, the retract size, or both, changed over time. For consistency in method 1, I assumed that the retract size for each attocube was fixed and the extend size drifted in an uncontrolled manner. I also approximate that all the data points within a sweep have the same step size.

In the first correction method, I compared data from two or more $z(x)$ sweeps taken at a constant x (z) position. Figure C.1(a) shows $|\delta f_0|$ for sweep 126 and 127 vs the nominal

position ($x_{f,nom}$, $z_{f,nom}$), which assumes nominal step sizes $\Delta_{z,ext,nom}$ = 0.322 μm/step and $\Delta_{z,rtr,nom}$ = 0.402 μm/step for all sweeps. The extend data points do not align with the retract data points. In Fig. C.1(b), I adjusted the z extend size to be $\Delta_{z,ext}$ = 0.278 μm/step, which roughly aligns the two data sweeps. I note that I applied this method to all sweeps before sweep 126, which changed the starting position of sweep 126.

I used the second method to align z sweeps in which there was a characteristic "dip" in $|\delta f_0|$ appears when the fiber is in line with the plane of the chip (see Fig. C.2). At the dip, the fiber was positioned such that only the thin cross-section of the aluminum was directly illuminated as opposed to the entire face of the resonator when the fiber is above or below the plane of the chip. Figure C.2(a) shows $|\delta f_0|$, for several sweeps, as a function of the nominal position $z_{f,nom}$ for different $x_{f,nom}$ values. The effect of cumulative errors in z is clear. This form of "dead reckoning" with incorrect step sizes shifts each subsequent sweep to lower z_f even though these dips should occur at roughly the same z_f position.

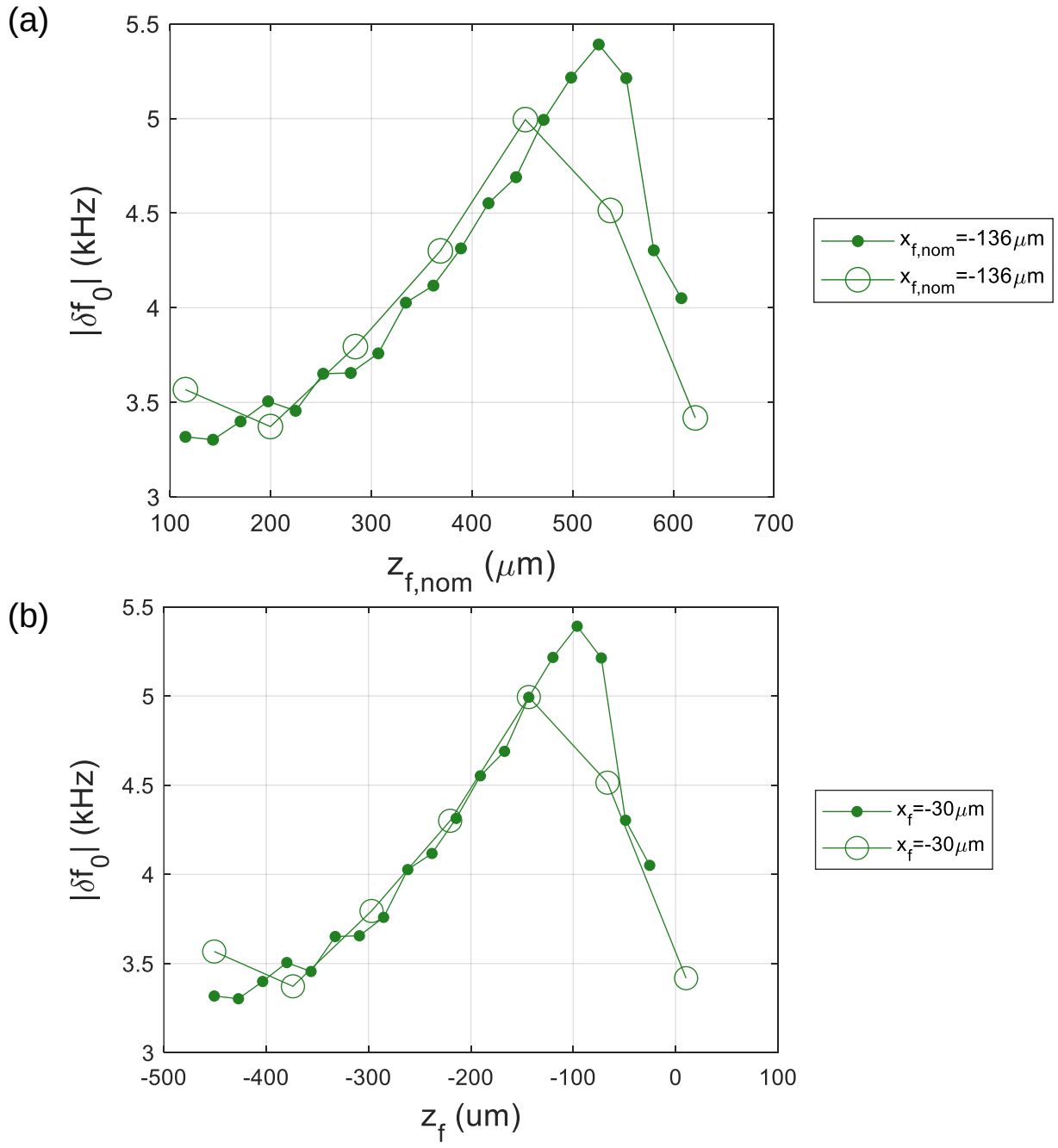

Fig. C.1 - (a) Plot of $|\delta f_0|$ as a function of the nominal z position, before making adjustments to attocube step size estimates. Solid circles were measured when the attocube was extended and open circles were measured when the attocube was retracted. Mismatch between these two sweeps indicates that the ratio of the z extend and retract step-sizes is varying over time. (b) Plot of $|\delta f_0|$ as a function of the best estimate z position, after using method 1 to adjust the z attocube extend step size.

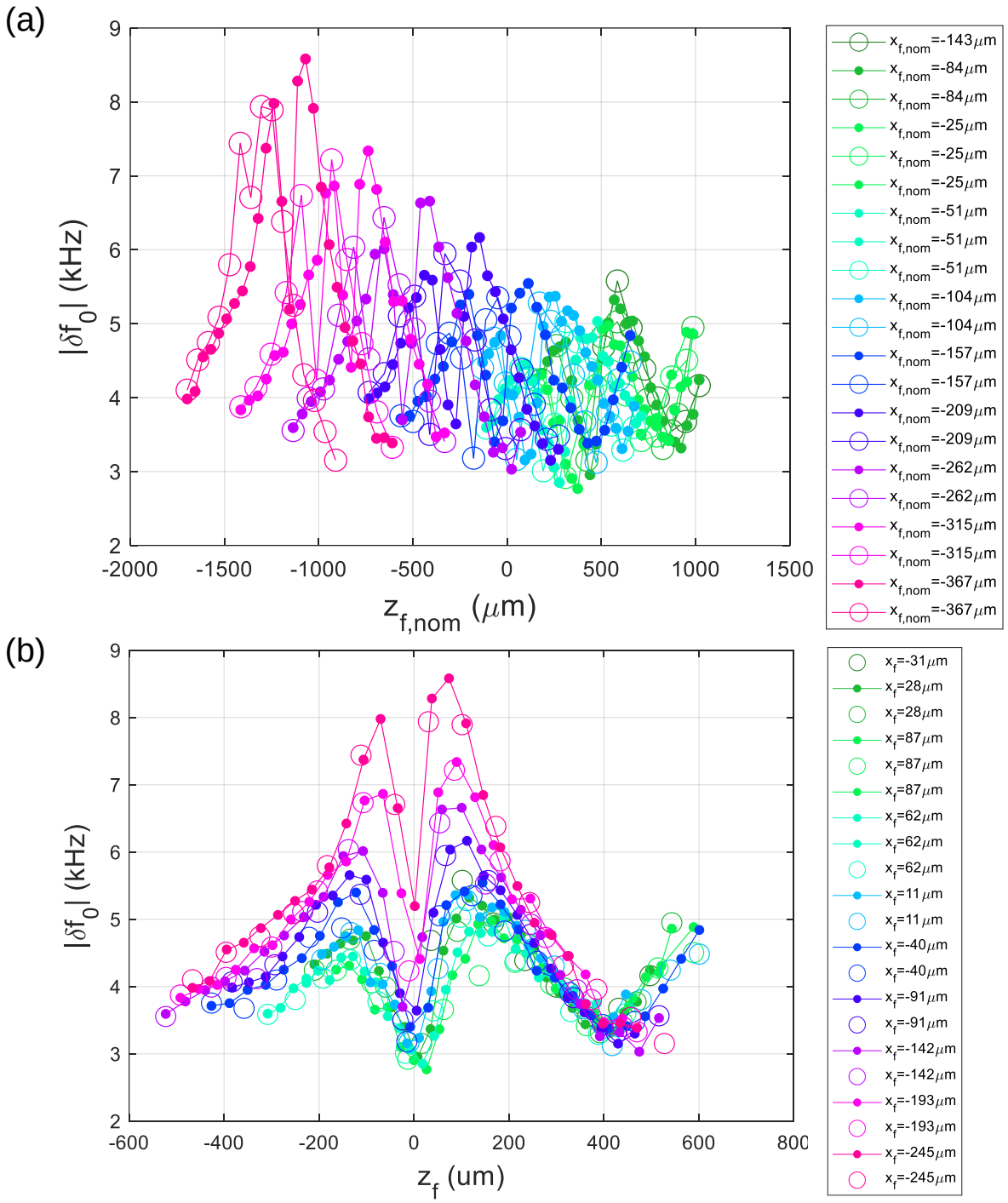

Fig. C.2 - (a) Plot of $|\delta f_0|$ as a function of $z_{f,nom}$ before making adjustments to attocube step size. Solid points were measured when the attocube was extended and open points were measured when the attocube was retracted. Each sweep has a "dip" that should occur at $z = 0$. The error in the attocube step size is cumulative and shifts each subsequent sweep to falsely lower z_f values. (b) Plot of $|\delta f_0|$ as a function of the best estimate z position z_f, after using method 2 to adjust the z attocube extend step size.

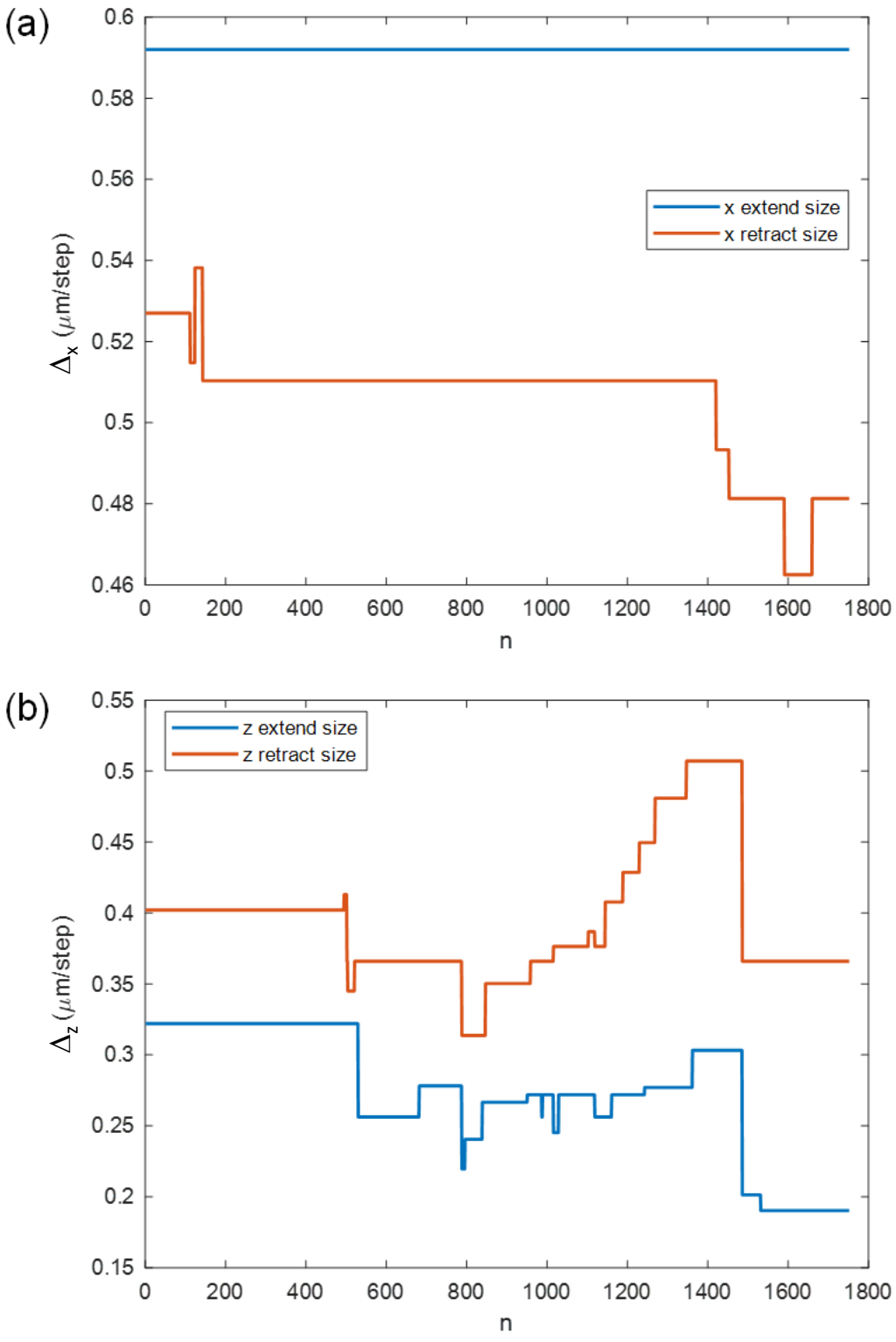

Fig. C.3 - (a) Adjusted step sizes, in version 2, for x attocube as a function of data point *n*. Step sizes at $n = 1$ are nominal. Subsequent step sizes are determined by applying either method 1 or method 2. (b) Adjusted step sizes for z attocube.

Figure C.2(b) shows $|\delta f_0|$ as a function of the adjusted position z_f, using the second method. This provides a clear qualitative correction to the drift as demonstrated by the overlapping dip position about $z_f = 0$. Here, both the extend and retract step sizes are adjusted by choosing s such that the "dip" occurs at $z_f = 0$ μm for each sweep. The nominal starting position, in version 2 was $(x_{0,nom}, z_{0,nom}) = (145\ \mu m, 151\ \mu m)$, which was found from images taken before cooldown. From Fig. C.2(b), I estimated the new starting position for the fiber to be $(x_{f0}, z_{f0}) = (325\ \mu m, -430\ \mu m)$, such that the first sweep with a dip was aligned at $z_f = 0$ μm. However, a starting point of $z_{f0} = -430$ μm is non-physical (too far to be physically allowed) and indicates that there are still calibration errors in the position. Figure C.3 shows the step sizes for both the x and z attocubes, as a function of data point number, estimated using methods 1 and 2.

To determine the position for version 4 of the fiber-chip experiment, I was able to make use of some of the data from the inductive position sensors (see Sec. 6.6). However, I was only able to measure one sensor at a time. Additionally, there were some sensor measurements that were inconsistent due to intermittent wiring issues. To estimate the position of the attocubes in version 4 I used a hybrid method of determining the position, using the sensor data when available and using dead reckoning from the nominal steps taken when sensor data was not available. The nominal measurements for the attocube stepsizes for version 4 given in the second line of Table C.1 do not produce a ratio which aligns extend and retract sweeps. Therefore I took extend step sizes to be fixed and used method 1 to determine starting retract step sizes. An x retract step size of $\Delta_{x,rtr} = 0.37$ μm aligns sweeps 17 and 18. A z retract step size of $\Delta_{z,rtr} = 0.37$ μm aligns sweeps 64 and 65. The starting value of step sizes used in version 4 is shown in the third line of Table Cs.1.

I also filtered out inconsistent position sensor values. To do so, we measured the sensor value before and after each data point. I quantified the sensor stability by looking at the absolute value of the change in sensor frequency δf_x after one data point and before the next. After filtering out outliers, the values of δf_x were roughly centered about zero and the mean of their magnitudes was 0.50 kHz. Between data points, we moved the x attocube 5 to 40 μm at a time. This corresponded to changes of about 2 to 15 kHz in the x sensor, which was sufficient sensitivity to resolve the change in position. For any sensor values f_{xf} whose δf_{xf} (either before or after that data point) was greater than 1.5 kHz, I instead used the nominal positions to estimate the distance between those data points.

Similarly, I quantified the z sensor stability by looking at the absolute value of the change in sensor value δf_z after one data point and before the next (i.e. two measurements with the attocube at the same location). The values of δf_z were roughly centered about zero and the mean of their absolute value was 0.80 kHz. Between data points, we moved the z attocube 4 to 18 μm at a time. This corresponded to changes of about 0.8 to 3.6 kHz in the z sensor, which was sufficient sensitivity to resolve the larger z steps. In this analysis, I filtered out any sensor values whose δf_z (either before or after that data point) was greater than 1.5 kHz.

We found that the nominal step sizes measured for version 4 at room temperature did not yield repeatable measurements of f_0 or $|\delta f_0|$, which was not unexpected by this time. Instead, I used a method similar to method 1: I kept Δx_{ext} at its nominal value and set Δx_{rtr} = 0.37 μm/step, such that forward and backward x sweeps were aligned (specifically sweeps 17 and 18). Similarly, I chose to keep Δz_{ext} at its nominal value and Δz_{rtr} = 0.315 μm/step, such that forward and backward z sweeps were aligned (specifically sweeps 64

and 65).

In version 4 the nominal x position of the fiber $x_{f,nom}$ was then determined by cumulatively adding the nominal number of attocube steps multiplied by the best-estimate step size (see Table C.1). Figure C.4 shows a plot of $x_{f,nom}$ as a function of f_{xf}. The red data points were taken before a "jump" in the resonance frequency of the sensor due to cable issues and the blue data points were taken after. For the red data, the first data line was fit to a quadratic variation of frequency with position (shown by a black curve). I assumed that this first data line most accurately represents the true sensor position, as subsequent data lines were subject to drift in the attocube step size. Similarly, I fit the first line of the blue data to a quadratic curve (also shown by a black line). I used these two fits, with fit values shown in the inset of Fig. C.4, to estimate the x-position.

I used a similar approach to convert z sensor frequency values to z positions. Figure C.4 shows $z_{f,nom}$ as a function of the sensor frequency f_{zf}. Again, I assumed that the initial data (red points) most accurately represents the sensor position, because subsequent data were subject to drift in the attocube step size. I fit this initial data to a line (shown by a red line on the figure). Using this fit, whose value is shown as an inset in Fig. C.5, I estimated the z-position.

To determine the 'adjusted' position of the fiber (x_f, z_f) I chose a starting point of (x_{f0}, z_{f0}) = (-365 μm, 222 μm) such that the peak in f_0 is roughly over the capacitor for the first 100 x sweeps and so that z sweeps 143 through 159 had their minimum in f_0 aligned at z_f = 0 μm. I chose these sweeps because they best display the dip in f_0. To this starting point, I cumulatively added changes in f_{xf} and f_{zf}, that were measured and viable, and I added the estimated change in x_{nom} and z_{nom}, respectively if they were not viable.

It should be noted that these positions would be affected by any error in the fiber-chip alignment. For simplicity, I assumed that the fiber was parallel to the plane of the chip. However, in practice the fiber was not exactly parallel to the plane of the chip. For version 4, I estimated the fiber exited the cavity with a (δx, δz) = (200, -100) μm offset from where the fiber entered the cavity. This measurement was made at room temperature and the

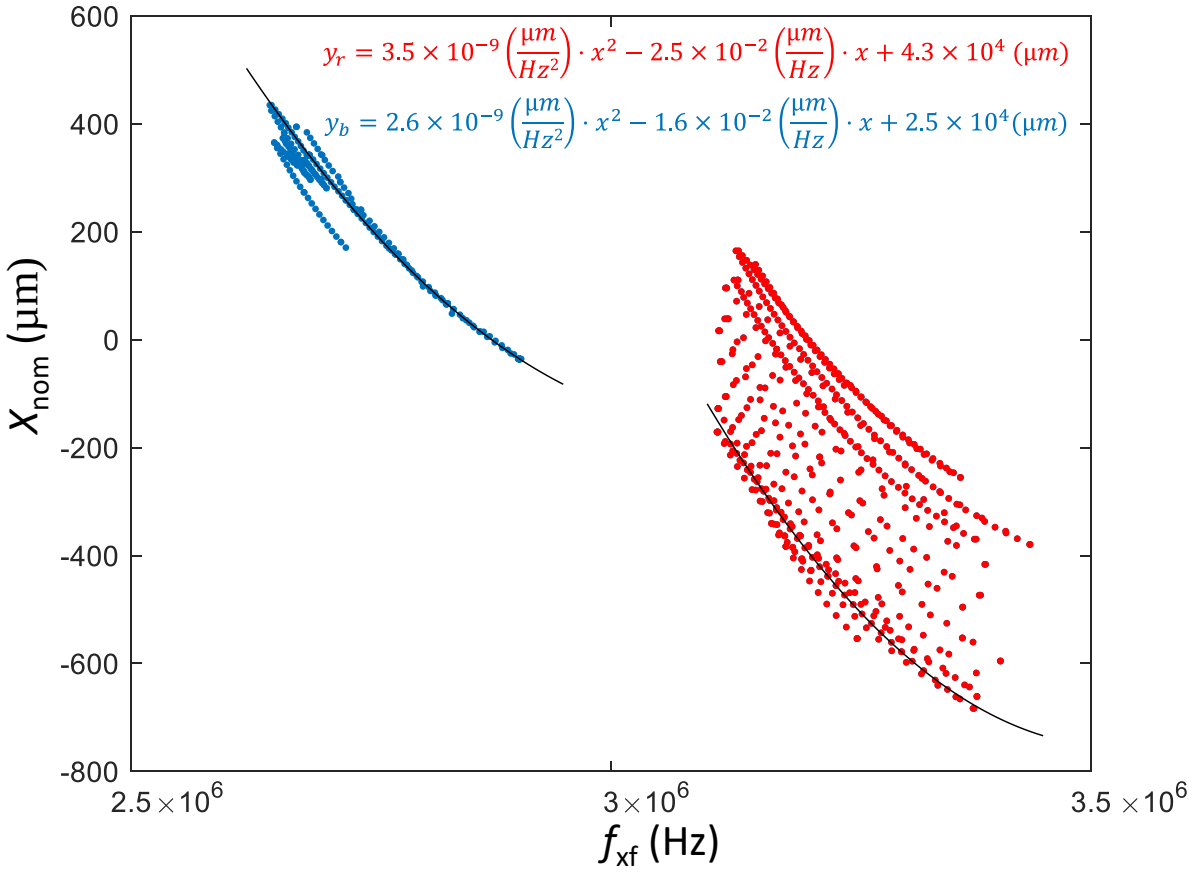

Fig. C.4 - The nominal position $x_{f,nom}$ as a function of sensor resonance frequency f_{xf}. The sensor resonance jumped between the red and blue data. The red values are before the jump, and the blue values are after the jump. Note that bad x sensor values have been filtered out. Solid curves are quadratic fits.

cooldown likely changed this offset.

Despite the additional complexities posed by the uncertainty in the fiber-chip positioning, the calibration schemes provided qualitative and quantitative corrections to the relative fiber-chip position. Future hybrid system experiments would benefit from using upgraded translation stages with integrated position tracking or improved sensors, which should greatly reduce the fiber-chip positioning uncertainty. While some of the position data has hard-to-quantify systemic uncertainty, particularly in versions 1-3, it still provides important qualitative information.

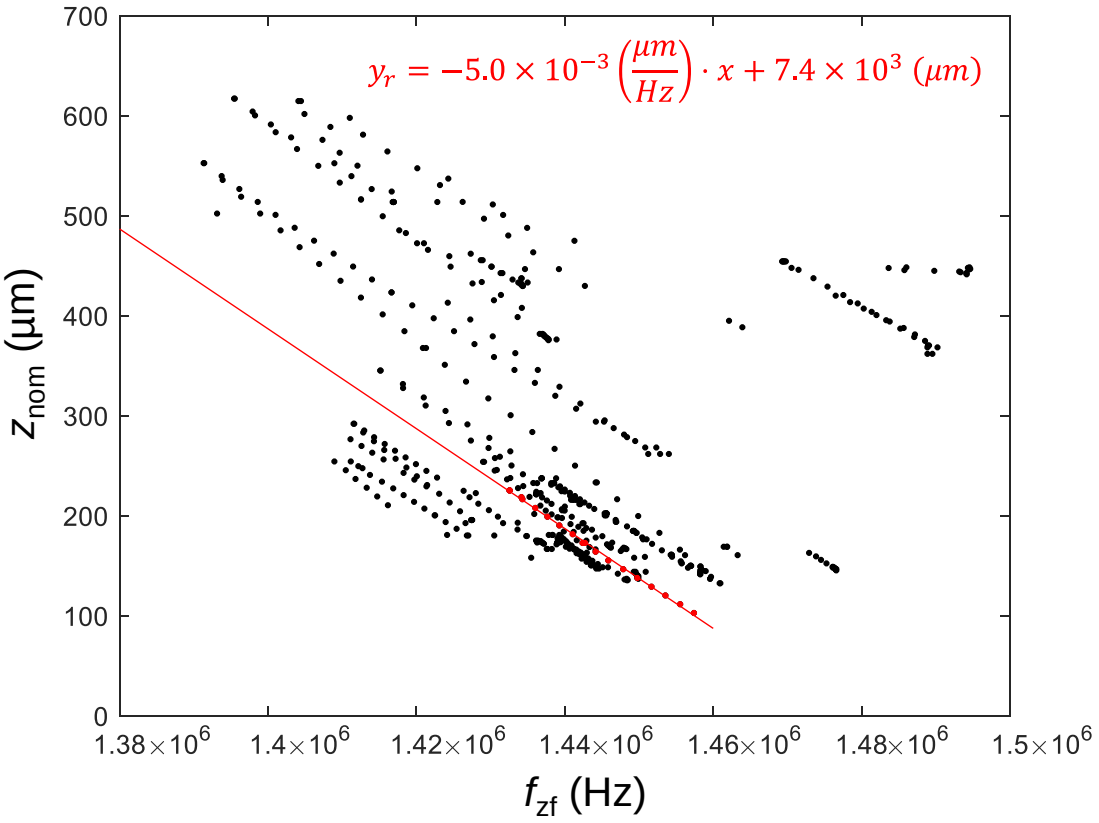

Fig. C.5 - The nominal z position as a function of z sensor frequency f_{zf}. Data points are shown in black. Note that erroneous z sensor values have been filtered out. Red line shows a linear fit to the initial data (red dots).

Bibliography

[1.1] R. P. Feynman, “Simulating physics with computers”, Intl. J. Theor. Phys. **21**, 467 (1982).

[1.2] A. Perdomo-Ortiz, N. Dickson, M. Drew-Brook, G. Rose, and A. Aspuru-Guzik, “Finding low-energy conformations of lattice protein models by quantum annealing”, Sci. Rep. **2**, 571 (2012).

[QC27] I. M. Georgescu, S. Ashhab, and F. Nori, “Quantum simulation”, Rev. Mod. Phys. **86**, 153 (2014).

[1.3] P. W. Shor, “Polynomial-time algorithms for prime factorization and discrete logarithms on a quantum computer”, SIAM Review **41**, 303 (1999).

[1.4] A. K. Lenstra and H. W. Lenstra, eds., “The development of the number field sieve”, Lecture Notes in Mathematics 1554 (Springer-Verlag, Berlin, 1990).

[1.5] L. K. Grover, “Quantum mechanics helps in searching for a needle in a haystack” , Phys. Rev. Lett. **79**, 325 (1997).

[1.6] J. M. Raimond, M. Brune, and S. Haroche, “Manipulating quantum entanglement with atoms and photons in a cavity”, Rev. Mod. Phys. **73**, 565 (2001).

[1.7] J. I. Cirac and P. Zoller, “Quantum Computations with Cold Trapped Ions,” Phys. Rev. Lett. **74**, 4091 (1995).

[1.8] G. K. Brennen, C. M. Caves, P. S. Jessen, and I. H. Deutsch, “Quantum Logic Gates in Optical Lattices,” Phys. Rev. Lett. **82**, 1060 (1999).

[1.9] R. Hanson and D. D. Awschalom, “Coherent manipulation of single spins in semiconductors”, Nature **453**, 1043 (2008).

[1.10] A. A. Clerk, M. H. Devoret, S. M. Girvin, F. Marquardt, and R. J. Schoelkopf,

"Introduction to quantum noise, measurement, and amplification", Rev. Mod. Phys. **82**, 1155 (2010).

[1.11] K. Saeedi, S. Simmons, J. Z. Salvail, P. Dluhy, H. Riemann, N. V. Abrosimov, P. Becker, H.-J. Pohl, J. J. L. Morton, M. L. W. Thewalt, "Room-Temperature Quantum Bit Storage Exceeding 39 Minutes Using Ionized Donors in Silicon-28", Science **15**, 830 (2013).

[1.12] N. Ofek, et al., "Extending the lifetime of a quantum bit with error correction in superconducting circuits", Nature **536**, 7617 (2016).

[1.13] L. B. Nguyen, Y.-H. Lin, A. Somoroff, R. Mencia, N. Grabon, and V. E. Manucharyan, "High-Coherence Fluxonium Qubit", Phys. Rev. X **9**, 041041 (2019).

[1.14] M. Kjaergaard, M. E. Schwartz, J. Braumüller, P. Krantz, J. I. J. Wang, S. Gustavsson, and W. D. Oliver, "Superconducting Qubits: Current State of Play", arXiv preprint arXiv:1905.13641v2 (2019).

[1.15] K. Hammerer, A. S. Sørensen, and E. S. Polzik, "Quantum interface between light and atomic ensembles", Rev. Mod. Phys. **82**, 1041 (2010).

[1.16] E. Knill, R. Laflamme, and G. J. Milburn, "A scheme for efficient quantum computation with linear optics", Nature **409**, 46 (2001).

[1.17] J. I. Cirac and P. Zoller, "A scalable quantum computer with ions in an array of microtraps", Nature **404**, 579 (2000).

[1.18] R. Blatt and D. Wineland," Entangled states of trapped atomic ions", Nature **453**, 1008 (2008).

[1.19] M. D. Lukin, "Colloquium: trapping and manipulating photon states in atomic ensemble", Rev. Mod. Phys. **75**, 457 (2003).

[1.20] D. Loss and D. P. DiVincenzo, “Quantum computation with quantum dots”, Phys. Rev. A **57**, 120 (1998).

[1.21] N. A. Gershenfeld and I. L. Chuang, “Bulk spin-resonance quantum computation”, Science **275**, 350 (1997).

[1.22] M. H. Devoret and R. J. Schoelkopf, "Superconducting circuits for quantum information: an outlook", Science **339**, 1169 (2013).

[1.23] D. P. DiVincenzo, “The physical implementation of quantum computation”, Prog. Phys. **48**, 771 (2000).

[1.24] P. W. Shor, “Scheme for reducing decoherence in quantum computer memory,” Phys. Rev. A **52**, R2493 (1995).

[1.25] A. Steane, “Multiple-Particle Interference and Quantum Error Correction,” Proc. R. Soc. London Ser. A **452**, 2551 (1996).

[1.26] E. Knill and R. Laflamme, “Theory of quantum error-correcting codes,” Phys. Rev. A **55**, 900 (1997).

[1.27] D. Gottesman, “Stabilizer Codes and Quantum Error Correction,” Ph.D. dissertation, California Institute of Technology (1997).

[1.28] C. Monroe, D. M. Meekhof, B. E. King, W. M. Itano, and D. J. Wineland, “Demonstration of a fundamental quantum logic gate.” Phys. Rev. Lett. **75**, 4714 (1995).

[1.29] G. Sagué, A. Baade, and A. Rauschenbeutel, “Blue-detuned evanescent field surface traps for neutral atoms based on mode interference in ultrathin optical fibres,” New Journal of Physics **10**, 113008 (2008).

[1.30] H. Paik, D. I. Schuster, L. S. Bishop, G. Kirchmair, G. Catelani, A. P. Sears,

B. R. Johnson, M. J. Reagor, L. Frunzio, L. I. Glazman and S. M. Girvin, "Observation of high coherence in Josephson junction qubits measured in a three-dimensional circuit QED architecture", Phys. Rev. Lett. **107**(24), 240501 (2011).

[1.31] D. A. Steck, "Rubidium 87 d line data", available online, http://steck.us/alkalidata, revision 2.1.5 (July 2020).

[1.32] J. Koch, T. M. Yu, J. Gambetta, A. A. Houck, D. I. Schuster, J. Majer, A. Blais, M. H. Devoret, S. M. Girvin, and R. J. Schoelkopf, "Charge-insensitive qubit design derived from the Cooper pair box", Phys. Rev. A **76**, 042319 (2007).

[1.33] A. Wallraff, D. I. Schuster, A. Blais, L. Frunzio, R.- S. Huang, J. Majer, S. Kumar, S. M. Girvin, and R. J. Schoelkopf, "Strong coupling of a single photon to a superconducting qubit using circuit quantum electrodynamics", Nature **431**, 162 (2004).

[1.34] E. Vetsch, S. T. Dawkins, R. Mitsch, D. Reitz, P. Schneeweiss, and A. Rauschenbeutel, "Nanofiber-based optical trapping of cold neutral atoms," IEEE Jour. of Selected Topics in Quant. Elect. **18**, 1763 (2012).

[1.35] J. M. Martinis, M. Ansmann, and J. Aumentado, "Energy decay in superconducting Josephson-junction qubits from nonequilibrium quasiparticle excitations", Phys. Rev. Lett. **103**, 097002 (2009).

[1.36] M. Lenander, H. Wang, R. C. Bialczak, E. Lucero, M. Mariantoni, M. Neeley, A. D. O'Connell, D. Sank, M. Weides, J. Wenner, T. Yamamoto, Y. Yin, J. Zhao, A. N. Cleland, and J. M. Martinis, "Measurement of energy decay in superconducting qubits from nonequilibrium quasiparticles", Phys. Rev. B **84**, 024501 (2011).

[1.37] G. Catelani, R. J. Schoelkopf, M. H. Devoret, and L. I. Glazman, "Relaxation and

frequency shifts induced by quasiparticles in superconducting qubits", Phys. Rev. B **84**, 064517 (2011).

[1.38] R. P. Budoyo, J. B. Hertzberg, C. J. Ballard, K. D. Voigt, Z. Kim, J. R. Anderson, C. J. Lobb, and F. C. Wellstood, " Effects of nonequilibrium quasiparticles in a thin-film superconducting microwave resonator under optical illumination", Phys. Rev. B **93,** 024514 (2016).

[1.39] D. J. Goldie and S. Withington, "Non-equilibrium superconductivity in quantum-sensing superconducting resonators", Supercond. Sci. Technol. **26**, 015004 (2013).

[1.40] F. Le Kien, V. I. Balykin, and, K. Hakuta, "Atom trap and waveguide using a two-color evanescent light field around a subwavelength-diameter optical fiber", Phys. Rev. A **70,** 063403 (2004).

[1.41] J. E. Hoffman, "Optical Nanofiber Fabrication and Analysis Towards Coupling Atoms to Superconducting Qubits" Ph.D. dissertation, University of Maryland, (2014).

[1.42] J. Lee, J. A. Grover, L. A. Orozco, and S. L. Rolston, "Sub-Doppler cooling of neutral atoms in a grating magneto-optical trap", J. Opt. Soc. Am. B **30**, 11 (2013).

[1.43] P. Schneeweiss, S. T. Dawkins, R. Mitsch, D. Reitz, E. Vetsch, and A. Rauschenbeutel, "A nanofiber-based optical conveyor belt for cold atoms," Appl. Phys. B **110**, 279 (2013).

[1.44] M. Tavis and F. W. Cummings, "Exact solution for an N-molecule-radiation-field Hamiltonian", Phys. Rev. **170**, 379 (1968).

[1.45] M. Tavis and F. W. Cummings, "Approximate solutions for an N-molecule-radiation-field Hamiltonian", Phys. Rev. **188**, 692 (1969).

[1.46] J. E. Hoffman, J. A. Grover, Z. Kim, A.K. Wood, J.R. Anderson, A. J. Dragt, M. Hafezi, C. J. Lobb, L. A. Orozco, S. L. Rolston, J. M. Taylor, C. P. Vlahacos, and F. C. Wellstood, "Atoms talking to SQUIDs", Revista Mexicana De Fisica **57**, 3 (2011).

[1.47] A. W. Snyder, J. D. Love, "Optical Waveguide Theory", Springer, Boston, MA (1983).

[1.48] S. Ravets, J. E. Hoffman, P. R. Kordell, J. D. Wong-Campos, S. L. Rolston, and L. A. Orozco, "Intermodal energy transfer in a tapered optical fiber: optimizing transmission", J. Opt. Soc. Am. A **30**, 2361 (2013).

[1.49] J. E. Hoffman, F. K. Fatemi, G. Beadie, S. L. Rolston, and L. A. Orozco, "Rayleigh scattering in an optical nanofiber as a probe of higher-order mode propagation," Optica **2**, 416 (2015).

[1.50] R. Budoyo, "Effects of Optical Illumination on Superconducting Quantum Devices", Ph.D. dissertation, University of Maryland - College Park, MD (2015).

[1.51] P. J. de Visser, S. J. C. Yates, T. Guruswamy, D. J. Goldie, S. Withington, A. Neto, N. Llombart, A. M. Baryshev, T. M. Klapwijk, and J. J. A. Baselmans, "The non-equilibrium response of a superconductor to pair-breaking radiation measured over a broad frequency band"**,** Appl. Phys. Lett. **106**, 252602 (2015).

[1.52] P. Schneeweiss, S. T. Dawkins, R. Mitsch, D. Reitz, E. Vetsch, and A. Rauschenbeutel, "A nanofiber-based optical conveyor belt for cold atoms," Appl. Phys. B **110**, 279 (2013).

[1.53] F. Le Kien, V. I. Balykin, and, K. Hakuta, "Atom trap and waveguide using a two-color evanescent light field around a subwavelength-diameter optical fiber", Phys.

Rev. A **70**, 063403 (2004).

[1.54] E. Vetsch, D. Reitz, G. Sagué, R. Schmidt, S. T. Dawkins, and A. Rauschenbeutel, "Optical interface created by laser-cooled atoms trapped in the evanescent field surrounding an optical nanofiber", Phys. Rev. Lett. **104**, 203603 (2010).

[1.55] A. Goban, K. S. Choi, D. J. Alton, D. Ding, C. Lacroûte, M. Pototschnig, T. Thiele, N. P. Stern, and H. J. Kimble, "Demonstration of a state-insensitive, compensated optical nanofiber trap", Phys. Rev. Lett. **109**, 033603 (2012).

[1.56] T. Barwicz and H. A. Haus, "Three-dimensional analysis of scattering losses due to sidewall roughness in microphotonic waveguides", J. Lightwave Technol. **23**, 2719 (2005).

[1.57] A. Stiebeiner, R. Garcia-Fernandez, and A. Rauschenbeutel, "Design and optimization of broadband tapered optical fibers with a nanofiber waist," Opt. Express **18**, 22677(2010).

[1.58] A. Megrant *et al.*, "Planar superconducting resonators with internal quality factors above one million." Appl. Phys. Lett. **100**, 113510 (2012).

[1.59] Attocube Product Catalog 2016 & 2017, vol. 15.

[2.1] Agilent E5071C Vector Network Analyzer, Agilent, Inc.

[2.2] D. M. Pozar, *Microwave Engineering*, 3rd Ed., (John Wiley & Sons, Inc., 2005), p. 271.

[2.3] M. S. Khalil, M. J. A. Stoutimore, F. C. Wellstood, and K. D. Osborn. "An analysis method for asymmetric resonator transmission applied to superconducting devices." J. Appl. Phys **111**, 054510 (2012).

[2.4] R. Budoyo, "Effects of Optical Illumination on Superconducting Quantum Devices",

Ph.D. dissertation, University of Maryland - College Park, MD (2015).

[2.5] J. M. Martinis, *et al.*, "Decoherence in Josephson qubits from dielectric loss", Phys. Rev. Lett. **95**, 210503 (2005).

[2.6] M.S. Khalil, "A study of two-level system defects in dielectric films using superconducting resonators," Ph.D. dissertation, University of Maryland, College Park (2013).

[2.7] B. Sarabi, "Cavity quantum electrodynamics of nanoscale two-level systems" Ph.D. dissertation, University of Maryland, College Park, (2014).

[2.8] W. A. Phillips, "Two-level states in glasses" Rep. Prog. Phys. **50** (12), 1657 (1987).

[2.9] A. M. Holder, K. D. Osborn, C. J. Lobb, and C. B. Musgrave, "Bulk and surface tunneling hydrogen defects in alumina", Phys. Rev. Lett. **111**(6), 065901 (2013).

[2.10] J. Lisenfeld, G. J. Grabovskij, C. Müller, J. H. Cole, G. Weiss, and A. V. Ustinov, "Observation of directly interacting coherent two-level systems in an amorphous material." Nature Commun. **6**, 6182 (2015).

[2.11] M. Neeley, M. Ansmann, R. C. Bialczak, M. Hofheinz, N. Katz, E. Lucero, A. O'Connell, H. Wang, A. N. Cleland & John M. Martinis, "Process tomography of quantum memory in a Josephson-phase qubit coupled to a two-level state", Nature Phys. **4**, 523 (2008).

[2.12] E. T. Jaynes and F. W. Cummings, "Comparison of quantum and semiclassical radiation theories with application to the beam maser", Proc. IEEE. **51**, 89 (1963).

[2.13] C. Cohen-Tannoudji, B. Diu, F. Laloe, *Quantum Mechanics*, Vol. 1 (John Wiley, Paris, France, 1977), p. 555ff.

[2.14] See for example: H. Haken, *Quantum Field Theory of Solids an Introduction* (North-

Holland, New York, 1976), p. 40ff.

[2.15] C. Cohen-Tannoudji, B. Diu, F. Laloe, *Quantum Mechanics*, Vol. 1 (John Wiley, Paris, France, 1977), p. 407ff.

[2.16] A. Rothwarf and B. N. Taylor, "Measurement of recombination lifetimes in superconductors", Phys. Rev. Lett. **19**, 1 (1967).

[2.17] W. H. Parker and W. D. Williams, "Photoexcitation of quasiparticles in nonequilibrium superconductors", Phys. Rev. Lett. **29**, 14 (1972).

[2.18] C. S. Owen and D. J. Scalapino, "Superconducting state under the influence of external dynamic pair breaking", Phys. Rev. Lett. **28**, 24 (1972).

[2.19] M. Dressel, "Electrodynamics of metallic superconductors", Adv. in Cond. Matt. Phys., pp. 104379, (2013).

[2.20] F. Marsili *et al.*, "Detecting single infrared photons with 93% system efficiency", Nat. Photon. **7**, 3 (2013).

[2.21] G. N. Gol'tsman *et al*., "Picosecond superconducting single-photon optical detector", Appl. Phys. Lett. **79**, 6 (2001).

[2.22] P. K. Day, H. G. Leduc, B. A. Mazin, A. Vayonakis, and J. Zmuidzinas, "A broadband superconducting detector suitable for use in large arrays", Nature **425**, 817 (2003).

[2.23] B. A. Mazin, "Microwave kinetic inductance detectors: The first decade", AIP Conf. Proc. **1185**, 1 (2009).

[2.24] B. A. Mazin, M. E. Eckart, B. Bumble, S. Golwala, P. K. Day, J. Gao, and J Zmuidzinas, "Optical/UV and x-ray microwave kinetic inductance strip detectors," J. Low T. Phys. **151**, 1 (2008).

[2.25] J. Zmuidzinas, “Superconducting microresonators: Physics and applications”, Annu. Rev. Condens. Matter Phys. **3**, 169 (2012).

[2.26] R. Barends, J. Wenner, M. Lenander, Y. Chen, R. C. Bialczak, J. Kelly, E. Lucero, P. O'Malley, M. Mariantoni, D. Sank, H. Wang, T. C. White, Y. Yin, J. Zhao, A. N. Cleland, J. M. Martinis, and J. J. A. Baselmans, “Minimizing quasiparticle generation from stray infrared light in superconducting quantum circuits”, Appl. Phys. Lett. **99**, 113507 (2011).

[2.27] I. Nsanzineza and B. L. T. Plourde, “Trapping a single vortex and reducing quasiparticles in a superconducting resonator”, Phys. Rev. Lett. **113**, 117002 (2014).

[2.28] S. Friedrich, K. Segall, M. Gaidis, C. Wilson, D. Prober, A. Szymkowiak, and S. Moseley, “Experimental quasiparticle dynamics in a superconducting, imaging x-ray spectrometer”, Appl. Phys. Lett. **71**, 3901 (1997).

[2.29] P. J. de Visser, S. J. C. Yates, T. Guruswamy, D. J. Goldie, S. Withington, A. Neto, N Llombart, A. M. Baryshev, T. M. Klapwijk, and J. J. A. Baselmans, “The non-equilibrium response of a superconductor to pair-breaking radiation measured over a broad frequency band”**,** Appl. Phys. Lett. **106**, 252602 (2015).

[2.30] D. J. Goldie and S. Withington, “Non-equilibrium superconductivity in quantum-sensing superconducting resonators”, Supercond. Sci. Technol. **26**, 015004 (2013).

[2.31] P. J. de Visser, S. Withington, and D. J. Goldie, “Readout-power heating and hysteretic switching between thermal quasiparticle states in kinetic inductance detectors”, J. Appl. Phys. **108**, 114504 (2010).

[2.32] R. P. Budoyo, J. B. Hertzberg, C. J. Ballard, K. D. Voigt, Z. Kim, J. R. Anderson, C. J. Lobb, and F. C. Wellstood, “Effects of nonequilibrium quasiparticles in a thin-

film superconducting microwave resonator under optical illumination", Phys. Rev. B **93,** 024514 (2016).

[3.1] Z. Kim, C. P. Vlahacos, J. E. Hoffman, J. A. Grover, K. D. Voigt, B. K. Cooper, C. J. Ballard, B. S. Palmer, M. Hafezi, J. M. Taylor, J. R. Anderson, A. J. Dragt, C. J. Lobb, L. A. Orozco, S. L. Rolston, and F. C. Wellstood, "Thin-film superconducting resonator tunable to the ground-state hyperfine splitting of ^{87}Rb", AIP Advances **1**, 042107 (2011).

[3.2] K. C. Gupta, "Microstrip Line and Slotlines", Artech House, Inc., Norwood, MA, 2nd ed. (1996).

[3.3] Kyocera Industrial Ceramics Co.

[3.4] M. S. Khalil, M. J. A. Stoutimore, F. C. Wellstood, and K. D. Osborn. "An analysis method for asymmetric resonator transmission applied to superconducting devices." J. Appl. Phys. **111**, 054510 (2012).

[3.5] H. Paik, D. I. Schuster, L. S. Bishop, G. Kirchmair, G. Catelani, A. P. Sears, B. R. Johnson, M. J. Reagor, L. Frunzio, L. I. Glazman and S. M. Girvin, "Observation of high coherence in Josephson junction qubits measured in a three-dimensional circuit QED architecture", Phys. Rev. Lett. **107**(24), 240501 (2011).

[3.6] E. M. Purcell, "Spontaneous emission probabilities at radio frequencies", Phys. Rev. **69**, 681 (1946).

[3.7] Transene Company, Inc., Danvers Industrial Park, 10 Electronics Avenue, Danvers, MA 01923.

[3.8] Resist Remover PG is manufactured by MicroChem, 1254 Chestnut Street, Newton, MA 02464.

[3.9] A. Megrant *et al.*, "Planar superconducting resonators with internal quality factors above one million." Appl. Phys. Lett. **100**, 113510 (2012).

[4.1] G. Hernandez, J. Zhang, and Y. Zhu, "Collective coupling of atoms with cavity mode and free-space field," Optics Express **17**, 4798 (2009).

[4.2] B. Sarabi, "Cavity quantum electrodynamics of nanoscale two-level systems" Ph.D. dissertation, University of Maryland, College Park, (2014).

[4.3] B. Sarabi, A. N. Ramanayaka, A. L. Burin, F. C. Wellstood, and K. D. Osborn, "Cavity quantum electrodynamics using a near-resonance two-level system: Emergence of the Glauber state", App. Phys. Lett., **106**, 172601 (2015).

[4.4] B. Sarabi, A. N. Ramanayaka, A. L. Burin, F. C. Wellstood, and K. D. Osborn, "Projected dipole moments of individual two-level defects extracted using circuit quantum electrodynamics", Phys. Rev. Lett. **116**, 167002 (2016).

[4.5] M. S. Khalil, F. C. Wellstood, and K. D. Osborn, "Loss dependence on geometry and applied power in superconducting coplanar resonators", IEEE Trans. App. Supercond. **21**, 879 (2011).

[4.6] M. J. Morrissey, K. Deasy, Y. Wu, S. Chakrabarti, and S. Nic Chormaic. "Tapered optical fibers as tools for probing magneto-optical trap characteristics", Rev. of Sci. Instrum. **80**, 053102 (2009).

[4.7] Z. Kim *et al.*, "Thin-film superconducting resonator tunable to the ground-state hyperfine splitting of ^{87}Rb", AIP Advances **1**, 042107 (2011).

[4.8] Attocube Product Catalog 2016 & 2017, vol. 15.

[4.9] ANSYS, 3D Electromagnetic Field Simulator Software, HFSS, (ANSYS Inc. 2020).

[4.10] The situation is equivalent to two coils that have uncoupled inductances L_a and L_b

that are coupled together with mutual inductance $M = k\sqrt{L_a L_b}$, where k is the coefficient of coupling. The screened inductance $L_a^{'}$ of the first coil is $L_a(1-k^2)$ and the screened inductance of the second coil is $L_b(1-k^2)$. See for example R. P. Giffard, R. A. Webb, and J. C. Wheatley, J. Low Temp. Phys. **6**, 533 (1972).

[4.11] Agilent E5071C Vector Network Analyzer, Agilent, Inc.

[4.12] J. B. Johnson, "Thermal Agitation of Electricity in Conductors", Phys. Rev. **29**, 367 (1927).

[4.13] H. Nyquist, "Thermal Agitation of Electric Charge in Conductors", Phys. Rev. **32**, 110 (1928).

[4.14] Miteq Low Noise Amplifier LNA-30-02001200-33-20P, 30 dBm.

[4.15] FS725 frequency standard, Stanford Research Systems.

[4.16] M. S. Khalil, M. J. A. Stoutimore, F. C. Wellstood, and K. D. Osborn, "An analysis method for asymmetric resonator transmission applied to superconducting devices." J. Appl. Phys **111**, 054510 (2012).

[4.17] J. M. Martinis, et al., "Decoherence in Josephson qubits from dielectric loss", Phys. Rev. Lett. **95**, 210503 (2005).

[4.18] A. D. O'Connell, M. Ansmann, R. C. Bialczak, M. Hofheinz, N. Katz, E. Lucero, C. McKenney, M. Neeley, H. Wang, E. M. Weig, A. N. Cleland, and J. M. Martinis, "Microwave dielectric loss at single photon energies and millikelvin temperatures", Appl. Phys. Lett. **92**, 112903 (2008).

[4.19] Microwave Office, circuit design software, (AWR Corporation, Cadence Design Systems, Inc. 2020).

[4.20] A. Megrant *et al.*, "Planar superconducting resonators with internal quality factors

above one million", Appl. Phys. Lett. **100**, 113510 (2012).

[5.1] W. A. Phillips, "Tunneling states in amorphous solids", Jour. of Low Temp. Phys. 7, 351 (1972).

[5.2] P. W. Anderson, B. I. Halperin, and C. M. Varma, "Anomalous low-temperature thermal properties of glasses and spin glasses", Phil. Mag. **25**, 1 (1972).

[5.3] M. Von Schickfus, and S. Hunklinger. "Saturation of the dielectric absorption of vitreous silica at low temperatures." Phys. Lett. A **64** 144-146 (1977).

[5.4] S. Hunklinger and A. K. Raychaudhuri, "Chapter 3: Thermal and Elastic Anomalies in Glasses at Low Temperatures", Prog. Low. Temp. Phys. **9**, 265 (1986).

[5.5] W. A. Phillips, "Two-level states in glasses" Rep. Prog. Phys. **50**(12), 1657 (1987).

[5.6] P. Macha, S. H. W. van der Ploeg, G. Oelsner, E. Il'ichev, and H.-G. Meyer, "Losses in coplanar waveguide resonators at millikelvin temperatures" Appl. Phys. Lett. **96**, 062503 (2010).

[5.7] J. M. Martinis, *et al.*, "Decoherence in Josephson qubits from dielectric loss", Phys. Rev. Lett. **95**, 210503 (2005).

[5.8] R. W. Simmonds, K. M. Lang, D. A. Hite, S. Nam, D. P. Pappas, and John M. Martinis, "Decoherence in Josephson Phase Qubits from Junction Resonators", Phys. Rev. Lett. **93**, 077003 (2004).

[5.9] L. Ku and C. C. Yu, "Decoherence of a Josephson qubit due to coupling to two-level systems", Phys. Rev. B **72**, 024526 (2005).

[5.10] E. Paladino, Y. M. Galperin, G. Falci, and B. L. Altchhuler,"1/f noise: Implications for solid-state quantum information", Rev. Mod. Phys. **86**, 361 (2014).

[5.11] See Fig. 4(a) in C. Müller, J.H. Cole, and J. Lisenfeld, "Towards understanding two-

level-systems in amorphous solids-Insights from quantum devices", arXiv preprint arXiv:1705.01108 (2017).

[5.12] J. Zmuidzinas, "Superconducting microresonators: Physics and applications", Annu. Rev. Condens. Matter Phys. **3**, 169 (2012).

[5.13] Z. Kim, C. P. Vlahacos, J. E. Hoffman, J. A. Grover, K. D. Voigt, B. K. Cooper, C. J. Ballard, B. S. Palmer, M. Hafezi, J. M. Taylor, J. R. Anderson, A. J. Dragt, C. J. Lobb, L. A. Orozco, S. L. Rolston, and F. C. Wellstood, "Thin-film superconducting resonator tunable to the ground-state hyperfine splitting of ^{87}Rb", AIP Advances **1**, 042107 (2011).

[5.14] H. Paik, D. I. Schuster, L. S. Bishop, G. Kirchmair, G. Catelani, A. P. Sears, B. R. Johnson, M. J. Reagor, L. Frunzio, L. I. Glazman and S. M. Girvin, "Observation of high coherence in Josephson junction qubits measured in a three-dimensional circuit QED architecture", Phys. Rev. Lett. **107**, 240501 (2011).

[5.15] P. K. Day, H. G. Leduc, B. A. Mazin, A. Vayonakis, and J. Zmuidzinas, "A broadband superconducting detector suitable for use in large arrays", Nature **425**, 817 (2003).

[5.16] B. A. Mazin, "Microwave Kinetic Inductance Detectors", Ph.D. dissertation, California Institute of Technology, Pasadena, CA (2004).

[5.17] J. Baselmans, "Kinetic inductance detectors", J. Low Temp. Phys. **167**, 292 (2012).

[5.18] A. D. O'Connell, M. Ansmann, R. C. Bialczak, M. Hofheinz, N. Katz, E. Lucero, C. McKenney, M. Neeley, H. Wang, E. M. Weig, A. N. Cleland, and J. M. Martinis, "Microwave dielectric loss at single photon energies and millikelvin temperatures", Appl. Phys. Lett. **92**, 112903 (2008).

[5.19] A. M. Holder, K. D. Osborn, C. J. Lobb, and C. B. Musgrave, "Bulk and surface tunneling hydrogen defects in alumina", Phys. Rev. Lett. **111**, 065901 (2013).

[5.20] H. Paik and K. D. Osborn, "Reducing quantum-regime dielectric loss of silicon nitride for superconducting quantum circuits", Appl. Phys. Lett. **96**, 072505 (2010).

[5.21] M. S. Khalil, S. Gladchenko, M. J. A. Stoutimore, F. C. Wellstood, A. L. Burin, and K. D. Osborn, "Landau-Zener population control and dipole measurement of a two-level-system bath", Phys. Rev. B **90**, 100201 (2014).

[5.22] M. S. Khalil, M. J. A. Stoutimore, S. Gladchenko, A. M. Holder, C. B. Musgrave, A. C. Kozen, G. Rubloff, Y. Q. Liu, R. G. Gordon, J. H. Yum, S. K. Banerjee, C. J. Lobb, and K. D. Osborn, "Evidence for hydrogen two-level systems in atomic layer deposition oxides", Appl. Phys. Lett. **103**, 162601 (2013).

[5.23] M.S. Khalil, "A study of two-level system defects in dielectric films using superconducting resonators," Ph.D. dissertation, University of Maryland, College Park (2013).

[5.24] J. Gao, M. Daal, A. Vayonakis, S. Kumar, J. Zmuidzinas, B. Sadoulet, B. A. Mazin, P. K. Day, and H. G. Leduc, "Experimental evidence for a surface distribution of two-level systems in superconducting lithographed microwave resonators", Appl. Phys. Lett. **92**, 152505 (2008).

[5.25] S. Machlup, "Noise in semiconductors: spectrum of a two-parameter random signal", Jour. of Appl. Phys. **25**, 341 (1954).

[5.26] C. T. Rogers and R. A. Buhrman, "Characterization of individual electron traps in amorphous Si by telegraph noise spectroscopy", Appl. Phys. Lett. **49**, 1107 (1986).

[5.27] B.Sarabi, , A.N. Ramanayaka, A.L. Burin, F.C. Wellstood, and K.D. Osborn,

"Projected dipole moments of individual two-level defects extracted using circuit quantum electrodynamics", Phys. Rev. Lett. **116**, 167002 (2016).

[5.28] G. J. Grabovskij, T. Peichl, J. Lisenfeld, G. Weiss, and A. V. Ustinov, "Strain Tuning of Individual Atomic Tunneling Systems Detected by a Superconducting Qubit", Science **338**, 232 (2012).

[5.29] T. A. Palomaki, S. K. Dutta, R. M. Lewis, A. J. Przybysz, H. Paik, B. K. Cooper, H. Kwon, J. R. Anderson, C. J. Lobb, F. C. Wellstood, and E. Tiesinga, "Multilevel spectroscopy of two-level systems coupled to a dc SQUID phase qubit", Phys. Rev. B **81**, 144503 (2010).

[5.30] P. W. Anderson and Y. B. Kim, "Hard Superconductivity: Theory of the Motion of Abrikosov Flux Lines", Rev. Mod. Phys. **36**, 39 (1964).

[5.31] T. T. M. Palstra, B. Batlogg, R. B. V. Dover, L. F.Schneemeyer, and J. V. Waszczak, "Dissipative flux motion in high-temperature superconductor", Phys. Rev. B **41**, 6621 (1990).

[5.32] M. J. Ferrari, J. J. Kingston, F. C. Wellstood, and J. Clarke, "Flux noise from superconducting $YBa_2Cu_3O_{7-x}$ flux transformers", Appl. Phys. Lett. **58**, 1106 (1991).

[5.33] M. Tinkham, *Introduction to Superconductivity*, 2nd Ed., (Dover, New York, 1996).

[5.34] B. Savo, F. C. Wellstood, and J. Clarke, "Low-frequency excess noise in Nb-Al_2O_3-Nb Josephson tunnel junctions", Appl. Phys. Lett. **50**, 1757 (1987).

[5.35] D. J. Van Harlingen, T. L. Robertson, B. L. T. Plourde, P. A. Reichardt, T. A. Crane, and J. Clarke, "Decoherence in Josephson-junction qubits due to critical-current fluctuations", Phys. Rev. B **70**, 064517 (2004).

[5.36] J. Eroms, L. C. van Schaarenburg, E. F. C. Driessen, J. Plantenberg, K. Huizinga, R. N. Schouten, A. H. Verbruggen, C. J. P. M. Harmans, and J. E. Mooij, "Low-frequency noise in Josephson junctions for superconducting qubits", Appl. Phys. Lett. **89**, 122516 (2006).

[5.37] M. Constantin and C. C. Yu, "Microscopic Model of Critical Current Noise in Josephson Junctions", Phys. Rev. Lett. **99**, 207001(2007).

[5.38] R. C. Bialczak, R. McDermott, M. Ansmann, M. Hofheinz, N. Katz, E. Lucero, M. Neeley, A. D. O'Connell, H. Wang, A. N. Cleland, and J. M. Martinis, "1/f Flux Noise in Josephson Phase Qubits", Phys. Rev. Lett. **99**, 187006 (2007).

[5.39] P. Kumar, S. Sendelbach, M. A. Beck, J. W. Freeland, Z. Wang, H. Wang, Clare C. Yu, R. Q. Wu, D. P. Pappas, and R. McDermott, "Origin and Reduction of 1/f Magnetic Flux Noise in Superconducting Devices", Phys. Rev. Applied **6**, 041001 (2016).

[5.40] S. E. de Graaf, A. A. Adamyan, T. Lindström, D. Erts, S. E. Kubatkin, A. Ya. Tzalenchuk, and A. V. Danilov, "Direct identification of dilute surface spins on Al_2O_3: Origin of flux noise in quantum circuits", Phys. Rev. Lett. **118**, 057703 (2017).

[5.41] F. C. Wellstood, C. Urbina, and J. Clarke, "Low-frequency noise in dc superconducting quantum interference devices below 1 K", Appl. Phys. Lett. **50**, 772 (1987).

[5.42] See for example: E. Merzbacher, *Quantum Mechanics*, 2nd Ed. (John Wiley, New York, 1970), p. 65ff.

[5.43] J. D. Jackson, *Classical Electrodynamics*, 2nd Ed. (John Wiley, New York, 1975),

p. 51.

[5.44] M. Kenyon, J. L. Cobb, A. Amar, D. Song, N. M. Zimmerman, C. J. Lobb, and F. C. Wellstood, "Dynamics of a Charged Fluctuator in an Al–AlO_x–Al Single-Electron Transistor", J. Low Temp. Phys. **123**, 103 (2001).

[5.45] R. C. Ashoori, H. L. Stormer, J. S. Weiner, L. N. Pfeiffer, S. J. Pearton, K. W. Baldwin, and K. W. West, "Single-electron capacitance spectroscopy of discrete quantum levels", Phys. Rev. Lett. **68,** 3088 (1992).

[5.46] R. C. Ashoori, H. L. Stormer, J. S. Weiner, L. N. Pfeiffer, K. W. Baldwin, and K. W. West, "N-electron ground state energies of a quantum dot in magnetic field", Phys. Rev. Lett. **71,** 613 (1993).

[5.47] D. Berman, N. B. Zhitenev, R. C. Ashoori, H. I. Smith, and M. R. Melloch, "Single-electron transistor as a charge sensor for semiconductor applications", J. Vac. Sci. Technol. **B15,** 2844 (1997).

[5.48] S. H. Tessmer, P. I. Glicofridis, R. C. Ashoori, L. S. Levitov, and M. R. Melloch, "Subsurface charge accumulation imaging of a quantum Hall liquid", Nature **392,** 51 (1998).

[5.49] O. E. Dial, R. C. Ashoori, L. N. Pfeiffer, and K. W. West, "High-resolution spectroscopy of two-dimensional electron systems", Nature **448,** 176 (2007).

[5.50] Agilent E5071C Vector Network Analyzer, Agilent, Inc.

[5.51] FS725 frequency standard, Stanford Research Systems.

[5.52] 0.1 to 60 GHz Anritsu V250 bias T.

[5.53] Miteq Low Noise Amplifier LNA-30-02001200-33-20P, 30 dBm.

[5.54] B. Sarabi, "Cavity quantum electrodynamics of nanoscale two-level systems" Ph.D.

dissertation, University of Maryland, College Park, (2014).

[5.55] M. S. Khalil, M. J. A. Stoutimore, F. C. Wellstood, and K. D. Osborn. "An analysis method for asymmetric resonator transmission applied to superconducting devices." J. Appl. Phys 111, 054510 (2012).

[6.1] G. Sagué, A. Baade, and A. Rauschenbeutel, "Blue-detuned evanescent field surface traps for neutral atoms based on mode interference in ultrathin optical fibres", New Journal of Physics **10**, 113008 (2008).

[6.2] E. Vetsch, "Optical Interface Based on a Nanofiber Atom-Trap", Ph.D. dissertation, Johannes Gutenberg University of Mainz, (2010).

[6.3] J. Wenner, *et al*., "Excitation of superconducting qubits from hot nonequilibrium quasiparticles", Phys. Rev. Lett. **110**, 150502 (2013).

[6.4] J.-H. Yeh, J. LeFebvre, S. Premaratne, F. C. Wellstood, and B. S. Palmer, "Microwave attenuators for use with quantum devices below 100 mK", Journal of Appl. Phys. **121**, 224501 (2017).

[6.5] J. Lee, J. A. Grover, L. A. Orozco, and S. L. Rolston, "Sub-Doppler cooling of neutral atoms in a grating magneto-optical trap", J. Opt. Soc. Am. B **30**, 11 (2013).

[6.6] R. Budoyo, "Effects of Optical Illumination on Superconducting Quantum Devices", Ph.D. dissertation, University of Maryland - College Park, MD (2015).

[6.7] R. Barends, J. J. A. Baselmans, S. J. C. Yates, J. R. Gao, J. N. Hovenier, and T. M. Klapwijk, "Quasiparticle relaxation in optically excited high-Q superconducting resonators", Phys. Rev. Lett. **100**, 257002 (2008).

[6.8] R. Barends, J. Wenner, M. Lenander, Y. Chen, R. C. Bialczak, J. Kelly, E. Lucero, P. O'Malley, M. Mariantoni, D. Sank, H. Wang, T. C. White, Y. Yin, J. Zhao, A. N.

Cleland, J. M. Martinis, and J. J. A. Baselmans, “Minimizing quasiparticle generation from stray infrared light in superconducting quantum circuits”, Appl. Phys. Lett. **99**, 113507 (2011).

[6.9] J. M. Martinis, M. Ansmann, and J. Aumentado, “Energy decay in superconducting Josephson-junction qubits from nonequilibrium quasiparticle excitations”, Phys. Rev. Lett. **103**, 097002 (2009).

[6.10] M. Lenander, H. Wang, R. C. Bialczak, E. Lucero, M. Mariantoni, M. Neeley, A. D. O'Connell, D. Sank, M. Weides, J. Wenner, T. Yamamoto, Y. Yin, J. Zhao, A. N. Cleland, and J. M. Martinis, “Measurement of energy decay in superconducting qubits from nonequilibrium quasiparticles”, Phys. Rev. B **84**, 024501 (2011).

[6.11] G. Catelani, R. J. Schoelkopf, M. H. Devoret, and L. I. Glazman, “Relaxation and frequency shifts induced by quasiparticles in superconducting qubits”, Phys. Rev. B **84**, 064517 (2011).

[6.12] J. Hoffman, S. Ravets, J. Grover, P. Solano, P. Kordell, J. Wong-Campos, L. Orozco, and S. Rolston, “Ultrahigh transmission optical nanofibers”, AIP Adv. **4**, 067124 (2014).

[6.13] Fibercore spec sheet: “SM Fiber for Visible Through to Near IR”, https://www.newport.com/medias/sys_master/images/images/h9c/hac/8797262512158/SM-Fiber-for-Visible-Through-to-Near-IR.pdf.

[6.14] P. W. Anderson, B. I. Halperin, and C. M. Varma, “Anomalous low-temperature thermal properties of glasses and spin glasses”, Philos. Mag. **25**, 1 (1972).

[6.15] Fibercore spec sheet: “SM Fiber for Visible Through to Near IR” https://www.newport.com/medias/sys_master/images/images/h9c/hac/8797262512

158/SM-Fiber-for-Visible-Through-to-Near-IR.pdf.

[6.16] C. Wuttke and A. Rauschenbeutel, "Thermalization via Heat Radiation of an Individual Object Thinner than the Thermal Wavelength", Phys. Rev. Lett. **111**, 024301, (2013)

[6.17] A. Yariv, "Optical Electronics", The Oxford Series in Electrical and Computer Engineering Series Oxford University Press, (1990).

[6.18] J. E. Hoffman, "Optical Nanofiber Fabrication and Analysis Towards Coupling Atoms to Superconducting Qubits", Ph.D. dissertation, University of Maryland, (2014).

[6.19] R. Grimm, M. Weidemuller, and Y. B. Ovchinnikov, "Optical dipole traps for neutral atoms", Adv. At. Mol. Opt. Phys. **42**, 95 (2000).

[6.20] G Brambilla, "Optical fibre nanowires and microwires: a review", Journal of Optics **12**, 043001 (2010).

[6.21] Z. Kim *et al.*, "Thin-film superconducting resonator tunable to the ground-state hyperfine splitting of ^{87}Rb", AIP Advances **1**, 042107 (2011).

[6.22] Attocube Product Catalog 2016 & 2017, vol. 15.

[6.23] J. A. Grover, "Atom-Trapping and Photon-Counting Experiments with Optical Nanofibers", Ph.D. dissertation, University of Maryland (2015).

[7.1] J. E. Hoffman, "Optical Nanofiber Fabrication and Analysis Towards Coupling Atoms to Superconducting Qubits" Ph.D. dissertation, University of Maryland, (2014).

[7.2] D. A. Steck, "Rubidium 87 d line data", available online, http://steck.us/alkalidata, revision 2.1.5 (July 2020).

[7.3] J. Hoffman, S. Ravets, J. Grover, P. Solano, P. Kordell, J. Wong-Campos, L. Orozco, and S. Rolston, "Ultrahigh transmission optical nanofibers", AIP Adv. 4, 067124 (2014).

[7.4] S. Ravets, J. E. Hoffman, P. R. Kordell, J. D. Wong-Campos, S. L. Rolston, and L. A. Orozco, "Intermodal energy transfer in a tapered optical fiber: optimizing transmission", J. Opt. Soc. Am. A 30, 2361 (2013).

[7.5] R. Barends, *et al*., "Minimizing quasiparticle generation from stray infrared light in superconducting quantum circuits", Appl. Phys. Lett. **99**, 113507 (2011).

[7.6] J. N. Ullom, P. A. Fisher, and M. Nahum, "Magnetic field dependence of quasiparticle losses in a superconductor", Appl. Phys. Lett. **73**, 2494 (1998).

[7.7] C. Kittel, *Introduction to Solid State Physics*, 5th Edition, (Wiley, New York, 1976).

[7.8] D. Gall, "Electron mean free path in elemental metals", J. Appl. Phys. **119**, 085101 (2016).

[7.9] I. Nsanzineza and B. L. T. Plourde, "Trapping a single vortex and reducing quasiparticles in a superconducting resonator", Phys. Rev. Lett. **113**, 117002 (2014).

[7.10] P. K. Day, H. G. Leduc, B. A. Mazin, A. Vayonakis, and J. Zmuidzinas, "A broadband superconducting detector suitable for use in large arrays", Nature **425**, 817 (2003).

[7.11] Fibercore spec sheet: "SM Fiber for Visible Through to Near IR" https://www.newport.com/medias/sys_master/images/images /h9c/hac/ 8797262512158/SM-Fiber-for-Visible-Through-to-Near-IR.pdf.

[7.12] G. Hass, "Filmed surfaces for reflecting optics", J. Opt. Soc. Am. **45**, 945 (1955).

[7.13] Comsol Mulitphysics® Modeling Software, (Comsol Inc. 2020).

[7.14] J. Gao, J. Zmuidzinas, A. Vayonakis, P. Day, B. Mazin, and H. Leduc, "Equivalence of the effects on the complex conductivity of superconductor due to temperature change and external pair breaking", J. Low Temp. Phys. **151**, 557 (2008).

[7.15] R. Budoyo, "Effects of Optical Illumination on Superconducting Quantum Devices", Ph.D. dissertation, University of Maryland - College Park, MD (2015).

[7.16] R. Meservey and P. M. Tedrow, "Measurements of the Kinetic Inductance of Superconducting Linear Structures", J. Appl. Phys. **40,** 2028 (1969).

[7.17] M. Tinkham, *Introduction to Superconductivity*, 2nd Ed., (Dover, New York, 1996).

[8.1] Attocube Product Catalog 2016 & 2017, vol. 15.

[8.2] J. Lisenfeld, G. J. Grabovskij, C. Müller, J. H. Cole, G. Weiss, and A. V. Ustinov, "Observation of directly interacting coherent two-level systems in an amorphous material", Nature Commun. **6**, 6182 (2015).